The Materials Research Society Series

Masako Kato
Kazuyuki Ishii *Editors*

Soft Crystals

Flexible Response Systems with High Structural Order

OPEN ACCESS

The Materials Research Society Series

The Materials Research Society Series covers the multidisciplinary field of materials research and technology, publishing across chemistry, physics, biology, and engineering. The Series focuses on premium textbooks, professional books, monographs, references, and other works that serve the broad materials science and engineering community worldwide. Connecting the principles of structure, properties, processing, and performance and employing tools of characterization, computation, and fabrication the Series addresses established, novel, and emerging topics.

Masako Kato · Kazuyuki Ishii
Editors

Soft Crystals

Flexible Response Systems with High Structural Order

MRS MATERIALS RESEARCH SOCIETY®

Springer

Editors
Masako Kato
Department of Applied Chemistry
for Environment
Kwansei Gakuin University
Sanda, Japan

Kazuyuki Ishii
Institute of Industrial Science
The University of Tokyo
Tokyo, Japan

ISSN 2730-7360 ISSN 2730-7379 (electronic)
The Materials Research Society Series
ISBN 978-981-99-0259-0 ISBN 978-981-99-0260-6 (eBook)
https://doi.org/10.1007/978-981-99-0260-6

The translation was done with the help of artificial intelligence (machine translation by the service DeepL.com). A subsequent human revision was done primarily in terms of content.

© The Editor(s) (if applicable) and The Author(s) 2023. This book is an open access publication.
Open Access This book is licensed under the terms of the Creative Commons Attribution 4.0 International License (http://creativecommons.org/licenses/by/4.0/), which permits use, sharing, adaptation, distribution and reproduction in any medium or format, as long as you give appropriate credit to the original author(s) and the source, provide a link to the Creative Commons license and indicate if changes were made.
The images or other third party material in this book are included in the book's Creative Commons license, unless indicated otherwise in a credit line to the material. If material is not included in the book's Creative Commons license and your intended use is not permitted by statutory regulation or exceeds the permitted use, you will need to obtain permission directly from the copyright holder.
The use of general descriptive names, registered names, trademarks, service marks, etc. in this publication does not imply, even in the absence of a specific statement, that such names are exempt from the relevant protective laws and regulations and therefore free for general use.
The publisher, the authors, and the editors are safe to assume that the advice and information in this book are believed to be true and accurate at the date of publication. Neither the publisher nor the authors or the editors give a warranty, expressed or implied, with respect to the material contained herein or for any errors or omissions that may have been made. The publisher remains neutral with regard to jurisdictional claims in published maps and institutional affiliations.

This Springer imprint is published by the registered company Springer Nature Singapore Pte Ltd.
The registered company address is: 152 Beach Road, #21-01/04 Gateway East, Singapore 189721, Singapore

Preface

You may imagine crystals are hard and stable materials like diamond and quartz that are distinct from liquids and polymers. However, "soft crystals" respond to gentle stimuli such as vapor exposure and rubbing, but maintain their structural order and exhibit remarkable visual changes in their shape, color, and luminescence. In the context of recent successive discovery of stimuli-responsive crystals, we started the project entitled "Soft Crystals: Science and Photofunctions of Flexible-response Systems with High Order" as a Japanese national project, KAKENHI, Scientific Research on Innovative areas in 2017; and for five years until March 2022, we have promoted the project intensively. More than 100 researchers including 11 planned research groups and 31 publicly offered research groups participated in this project collaborating with each other to develop the science of soft crystals. In this project, we particularly focus on the photofunctionality of soft crystals.

This book summarizes the achievements of the project. You will see that soft crystals are fascinating and promising materials. In part I, we describe the historical background and basic concepts. Then, interesting examples and recent remarkable developments of soft crystals as well as various approaches to understand the characteristic phenomena and properties of soft crystals will be described in part II. In part III, we summarize the science of soft crystals systematically and prospects toward applications of soft crystals. Throughout the book, readers will find a new concept of materials that have the characteristics of stimulus-sensitive soft matter and finely controlled crystals.

We express our sincere thanks to all the members of the Soft Crystals project for their endeavors to develop the research area based on the collaboration, especially, the authors of this book who are responsible for the big achievements. We are also

grateful to Mr. Shinichi Koizumi and Mr. Rammohan Krishnamurthy at Springer Nature for their helpful suggestions, support, and patience.

We hope you enjoy the materials world of soft crystals through this open access book.

Tokyo, Japan — Kazuyuki Ishii
Sanda, Japan — Masako Kato
December 2022

Contents

Part I Introduction

1 Background and Overview 3
Kazuyuki Ishii and Masako Kato

2 Classification and Definition of "Soft Crystals" 13
Kazuyuki Ishii and Masako Kato

3 Theoretical Background of Photophysical Properties 23
Kazuyuki Ishii and Masako Kato

Part II Various Soft Crystals Categorized by Stimulus-Response

4 Vapochromic Soft Crystals Constructed with Metal Complexes 39
Masako Kato

5 Luminescent Mechanochromism and the Photosalient Effect of Aryl Gold(I) Isocyanide Complexes 53
Tomohiro Seki and Hajime Ito

6 Elastic and Plastic Soft Crystals with Superelasticity, Ferroelasticity, and Superplasticity 87
Satoshi Takamizawa and Masako Kato

7 Triboluminescence of Lanthanide Complexes 105
Miki Hasegawa and Yasuchika Hasegawa

8 Thermosalient Phenomena in Molecular Crystals: A Case Study of Representative Molecules 131
Yoshinori Yamanoi, Kenichiro Omoto, Toyotaka Nakae, and Masaki Nishio

9 Soft Crystal Chemiluminescence Systems Using Organic Peroxides 155
Takashi Hirano and Chihiro Matsuhashi

10 Molecular Crystal Calculation Prospects for Structural Phase Transitions 179
Naofumi Nakayama and Hitoshi Goto

11 Approach of Electronic Structure Calculations to Crystal 209
Naoki Nakatani, Jia-Jia Zheng, and Shigeyoshi Sakaki

Part III Scope

12 Toward the Applications of Soft Crystals 259
Kazuyuki Ishii and Masako Kato

Part I
Introduction

Chapter 1
Background and Overview

Kazuyuki Ishii and Masako Kato

Abstract In this chapter, the characteristics and potentials of "soft crystals" are compared with those of conventional hard crystals after providing a historical background. In addition, representative examples of "soft crystals" are discussed, and their thermodynamic models are qualitatively described.

Keywords Soft crystals · Crystal structure · Phase transition · Stimulus response · Photofunction

1.1 Background and Significance

Crystals are solid structures with regularly arranged atoms, molecules, or ions that exhibit anisotropic properties unlike randomly oriented amorphous solids. The characteristic properties of crystals have been utilized to develop materials that require fine tuning of their electrical, magnetic, optical, and other parameters.

Historically, Max Theodor Felix von Laue from Germany observed X-ray diffraction from crystals in 1912, which confirmed that X-rays were electromagnetic waves. In 1913, William Henry Bragg and his son William Lawrence Bragg from England discovered Bragg's law, which formulated the relationship between the X-ray diffraction wavelength and the distance between diffracting planes in crystals. Based on this law, we can determine not only the structures of natural crystals such as minerals, but also those of single crystals consisting of artificially synthesized compounds. Similarly, the structures of complex biomolecules, such as proteins and deoxyribonucleic acids, were elucidated by preparing their single crystals. Thus, crystals and their analytical methods played important roles not only as functional materials

K. Ishii
Institute of Industrial Science, The University of Tokyo, 4-6-1 Komaba, Tokyo 153-8505, Japan
e-mail: k-ishii@iis.u-tokyo.ac.jp

M. Kato (✉)
Department of Applied Chemistry for Environment, Kwansei Gakuin University, 1 Gakuen Uegahara, Sanda 669-1330, Japan
e-mail: katom@kwansei.ac.jp

© The Author(s) 2023

M. Kato and K. Ishii (eds.), *Soft Crystals*, The Materials Research Society Series,
https://doi.org/10.1007/978-981-99-0260-6_1

with regular arrangements and/or anisotropic characteristics but also as materials that helped achieve a better understanding of various biological phenomena.

According to the definition provided by the International Union of Crystallography in 1992, "crystal" denotes any solid that produces an essentially discrete diffraction pattern [1]; however, many people think that crystals should be hard and stable like diamonds. The hardness of crystals mainly originates from stable interatomic bonds, which are regularly arranged in three dimensions. Meanwhile, in the past decade, a group of crystals with characteristic molecular rearrangements in the solid state caused by gentle external stimuli have attracted considerable attention from researchers. For example, single crystal ↔ single crystal phase transitions accompanied by color changes occurred in response to specific volatile organic compounds. In addition, remarkable photoluminescent color changes were detected during mechanical grinding. These phenomena were observed in a wide range of materials mainly consisting of molecules, such as organic and inorganic molecules, metal complexes, and coordination polymers. In contrast to the previously known crystals, which are thermodynamically stable and rigid, these new materials are classified based on their ability to undergo structural transformations in response to macroscopic gentle external stimuli, while their stable crystals can be synthesized. The class of these materials, which are different from conventional and liquid crystals, was named "soft crystals", and their concept paper was published in 2019 [2]. Typical examples of "soft crystals" are provided in Fig. 1.1.

How can macroscopic gentle external stimuli change the solid-state nanometer-scaled molecular assembled structures? This apparent conundrum cannot be solved by conventional science and is similar to the initial stages of previous scientific discoveries. The first example includes the discovery of liquid crystals serving as intermediates between liquid and crystals. F. Reinitzer, a botanist in Austria, discovered an unusual phenomenon, two melting points, when studying the functions of cholesterol in plants. In 1888, he wrote a letter to O. Lemann, a physicist in Germany, about this phenomenon, which was a landmark in the development of liquid crystals. After a press release about the birth of a liquid crystal display (LCD) was issued by RCA Laboratories in U.S.A. in 1968, more than 100 million LCD monitors per year have been manufactured in recent years. Another example is the discovery of metal complexes constituting various soft crystals. In the late nineteenth century, it was believed that salts consisted of atoms with simple ratios or their multiples; however, many exceptions from this rule were observed. Later, these exceptions were assigned to the metal complexes named "complex salts" because of their initial complexity. The first step in the discovery of coordination bonds and coordination chemistry was the systematization of the coordination theory by Alfred Werner in Switzerland. With the further development of metal complexes and supramolecules, organic light-emitting materials were constructed owing to the strong phosphorescence of metal complexes. Compared to the development of liquid crystals or metal complexes, which produced a significant impact on the society, "soft crystals" are expected to become a class of materials strongly influencing future technological innovations. Thus, it is extremely important to summarize, classify, and systematize their main properties.

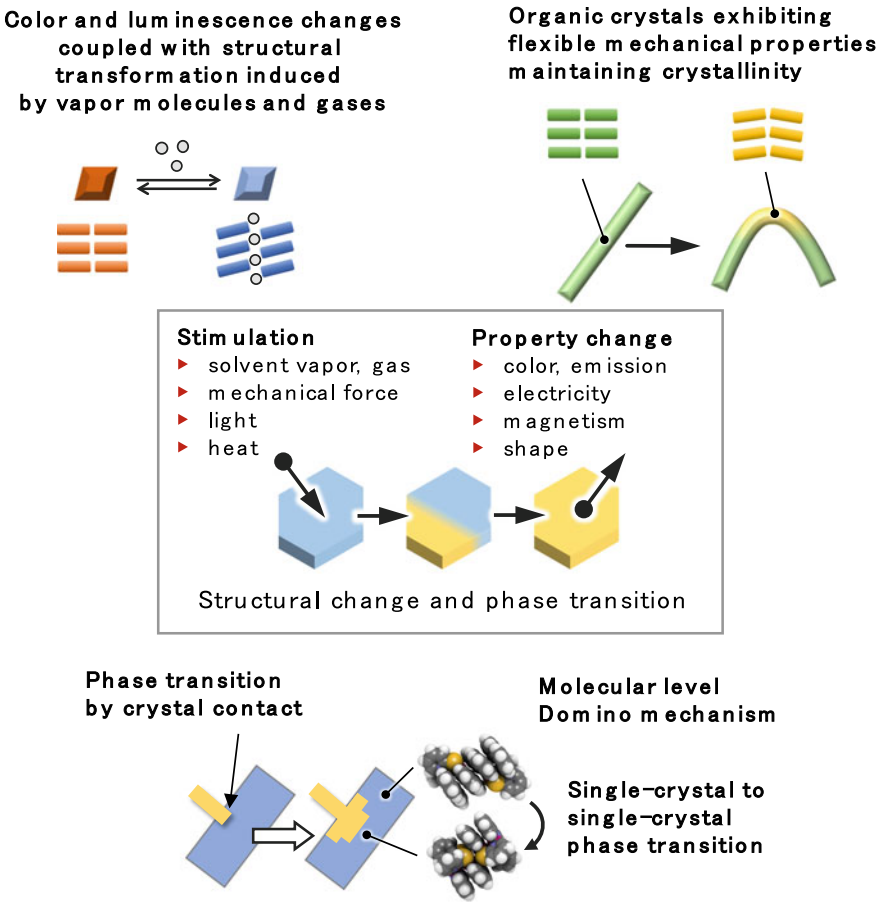

Fig. 1.1 Typical examples of "soft crystals". Reprinted with permission from ref. [2]

1.2 Structure of This Book

This is the first book focusing on the science of "soft crystals" by classifying and systematizing various soft crystals' phenomena because it is scientifically important to present new ways of interpreting newly discovered data. The syntheses of molecular crystals, which contain not only various types of atoms but also a mixture of "strong intramolecular atomic bonds" and "weak but non-negligible intermolecular atomic interactions", are very complex and continue to depend on serendipity and screening. Therefore, because to clarify and control the formation and phase transitions of molecular crystals has remained the most challenging issue in molecular science and technology in recent decades, this book intends to address them to contribute to the future development of related fields.

The next Sect. 1.3 provides an overview of the initial representative examples of "soft crystals", and their thermodynamic properties are qualitatively described in Sect. 1.4. In Chap. 2, "soft crystals" are compared with other materials and defined more precisely. In Chap. 3, the photophysical properties of molecules and molecular crystals are briefly explained by considering their colors or luminescence colors. In Part II, the latest studies on various "soft crystals" are discussed in detail. In Part III, potential applications of "soft crystals" as future functional materials are discussed with reference to boundary region studies related to soft matter and/or device engineering.

1.3 Soft Crystals: An Overview

If you search for "soft crystals" online, you will find multiple papers. Even hard metal crystals such as iron soften and eventually melt at high temperatures. Crystals near the melting point can be called soft crystals, which have been the subject of recent research studies because of their unique properties such as atomic diffusion [3]. We might even say that rock salt, i.e., the ionic crystal of sodium chloride, is soft compared to those of metal crystals because they shatter when crushed even at room temperature. Crystals of organic molecules or metal complexes are also weak in terms of mechanical strength. In particular, crystals composed of neutral molecules have low melting points and are relatively soft. In the field of liquid crystals, the soft crystal phase located at the boundary of the crystal phase was proposed as one of the smectic liquid crystal phases [4]. In addition, the flexible properties and mechanical functions of organic molecular crystals formed by van der Waals forces and hydrogen bonds have attracted considerable attention [5]. Metal–organic frameworks (MOFs) undergo flexible structural changes due to the adsorption and desorption of gas molecules; therefore, they are called porous soft crystals or flexible MOFs [6]. In the following sections, we discuss some specific examples that enabled defining certain materials as soft crystals and describe their properties.

1.3.1 Vapochromic Crystals

The reversible color change induced by organic vapors such as alcohol and ether or inorganic gases such as hydrogen chloride and sulfur dioxide is called vapochromism. As an example, a luminescent vapochromic platinum dinuclear complex discovered by Kato et al. in their early work is shown in Fig. 1.2 [7]. When a crystal of this compound is exposed to organic vapors, its color change occurs between bright red and dark red, and a visual ON–OFF change of luminescence is detected (Fig. 1.2b). This phenomenon is observed only for the structure depicted in Fig. 1.2a (which is called a *syn*-type isomer) and not for isomers with different arrangements of bridging ligands (*anti* type). The color change is caused by the crystal structural transformation

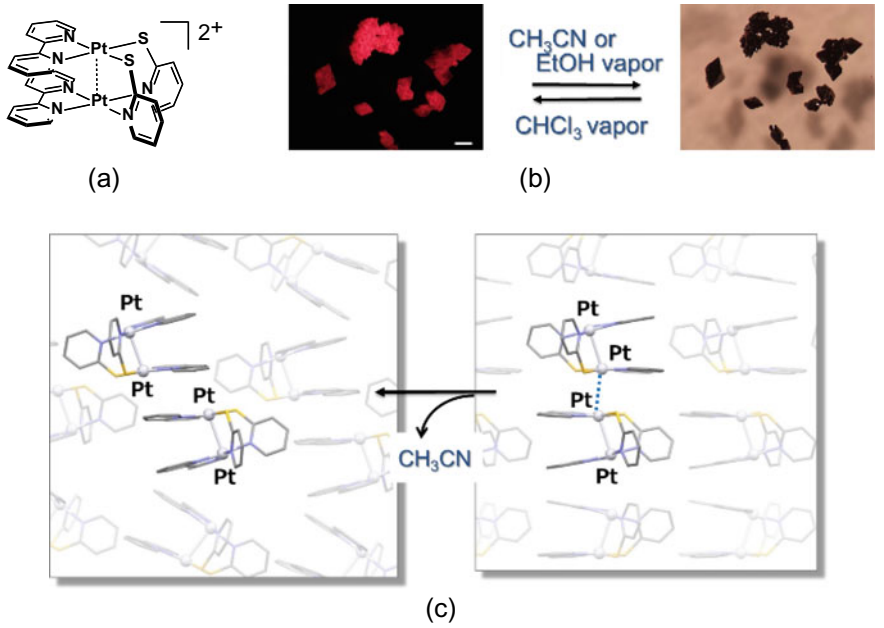

Fig. 1.2 **a** Structural formula of the *syn*-isomer of a dinuclear Pt(II) complex. **b** Vapochromic behavior of crystals (the white scale bar in the left photograph has a length of 100 μm). **c** Vapor-induced structural transformation of the dimer-of-dimer. Reprinted with permission from ref. [7]

induced by the entry and exit of vapor molecules. An analysis of the structural changes caused by the single crystal-to-single crystal conformational transition revealed that the arrangement of two dinuclear complexes in the crystal switched from a close arrangement between intermolecular Pt atoms (the right panel in Fig. 1.2c) to a distant arrangement between them (the left panel in Fig. 1.2c) upon the release of the enclosed crystalline solvent molecules (left). Vapochromism has attracted significant attention as a process that can be potentially used to easily and sensitively detect volatile organic compounds (which are considered the cause of a sick building syndrome) and acidic exhaust gases representing environmental pollutants. Since 2000, various vapochromic crystal systems have been developed [8]. Vapochromism is also scientifically important as an emergent phenomenon of solid–gas interactions.

1.3.2 Mechanochromic Crystals

The color change of solid materials in response to weak mechanical stimuli such as touch, grinding, or scratching is called mechanochromism [9]. Sometimes, the terms tribochromism (friction) and piezochromism (pressure) are also used to describe similar phenomena. Mechanochromism has been known for a long time, and related

processes such as the color change due to pulling and glowing caused by pressing occur not only in crystals but also in polymers and inorganic solid powders [10]. In recent years, the number of publications on mechanochromic crystals has increased dramatically because the recent advances in X-ray structural analysis methods have allowed easy determination of the three-dimensional structures of even very small crystals by synthetic chemists. As one of the starting points of this trend, the luminescent mechanochromic Au(I) complex synthesized by Ito et al. is shown in Fig. 1.3a [11]. A crystalline powder of this complex emits blue-colored luminescence under UV light; however, after gently grinding with a spatula, the luminescence color changes to yellow (Fig. 1.3b). This phenomenon is caused by the structural change from the crystalline to amorphous phase, and the observed luminescence color change is attributed to the change in the interactions between gold atoms (Fig. 1.3c). The luminescence returns to the original crystalline blue state after the dropwise addition of solvent. Araki et al. found that the luminescence color changed from blue to green after rubbing or pressing the crystalline sample of a tetraphenylene derivative and returned to the original crystalline state after heating, which were attributed to the changes in intermolecular interactions (Fig. 1.4) [12].

1.3.3 Organic Crystals Exhibiting Superelasticity or Ferroelasticity

Superelasticity, a property in which a material is deformed by mechanical loading but returns to its original state upon removing the load, had been observed only for a limited number of metal alloys such as Ni–Ti. Takamizawa et al. reported the first superelastic crystal of an organic compound in 2014 [13]. As shown in Fig. 1.5a, a terephthalamide crystal is deformed by pressing the crystal's right side with a needle tip but returns to its original shape after releasing the load. In the deformed area, the optical property of the crystal is changed because of the phase transition. The authors also found the shape memory effect of an ionic organic crystal that was plastically deformed but returned to the original crystalline shape after heating (Fig. 1.5b) [14]. Furthermore, crystals possessing ferroelasticity [15] or superplasticity [16] were reported as well. They undergo macroscopic morphological changes upon weak mechanical stimuli, which are literally soft crystals. Recently, the characteristic properties owing to microscopic structural changes in bent or twisted organic molecular crystals have attracted significant interest from organic crystal researchers worldwide [17]. In addition to crystallographic studies, a superelastic chromic crystal that changes luminescence color upon pressing the crystal has recently been discovered, and the functionalization of organic superelastic crystals is expected to be developed [18].

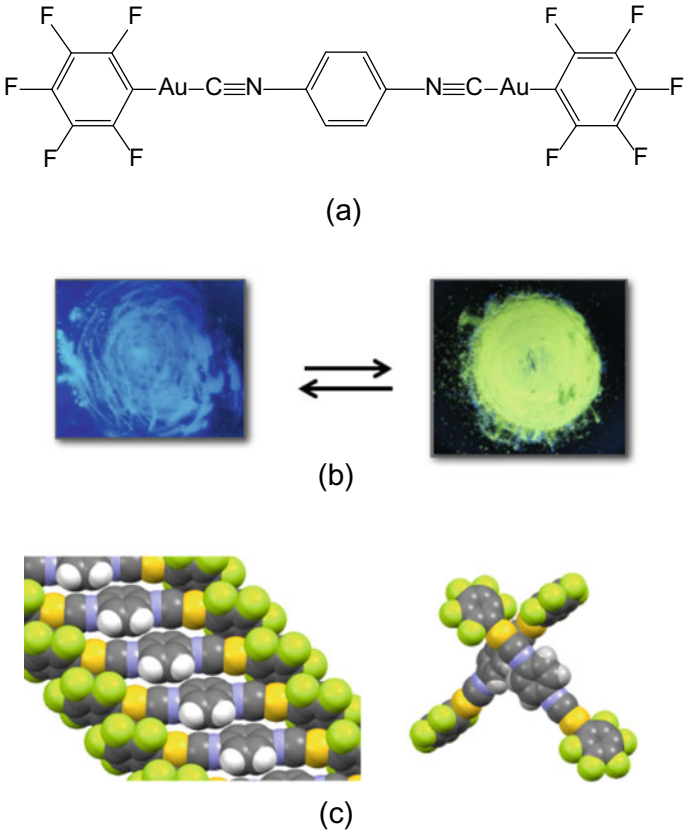

Fig. 1.3 Mechanochromic luminescence of a Au(I) complex. **a** Structural formula of the Au(I)-isocyanide complex and **b** luminescence color change accompanied by **c** the crystal-to-amorphous transformation during grinding. Reprinted with permission from reference [11]

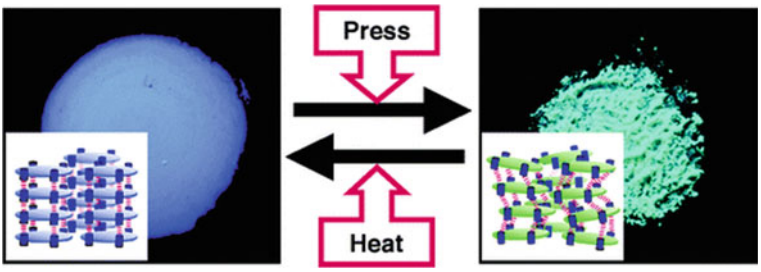

Fig. 1.4 Piezochromic luminescence of a tetraphenylpyrene derivative. Reprinted with permission from reference [12]

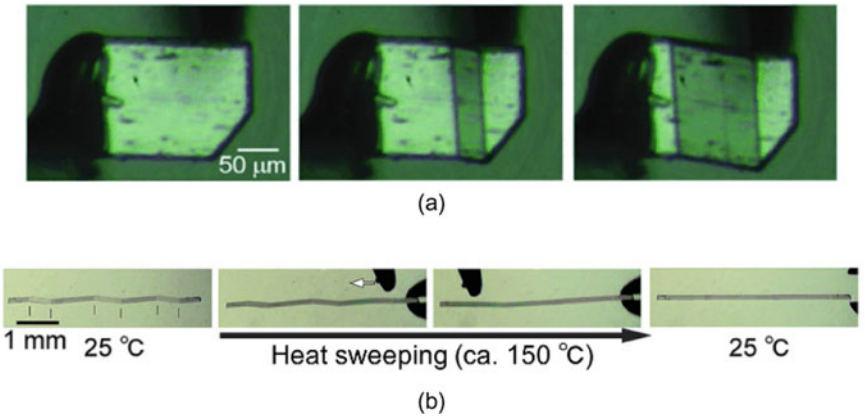

Fig. 1.5 **a** Structural transformation followed by phase transition upon the application of slight shear stress to a telephthalamide single crystal. **b** Shape recovery of the deformed zigzag tetrabutyl-*n*-phosphonium tetraphenylborate crystal induced by heat sweeping. Reprinted with permission from ref. [13, 14]

1.4 Thermodynamic Images: Stimulus Versus Potential Energy

When studying soft crystals that undergo structural transformations in response to macroscopic gentle external stimuli, it is important to thermodynamically consider potential energy changes corresponding to these transformations. For vapochromism, mechanochromism, and superelasticity, the qualitative images of potential energy changes are shown in Fig. 1.6.

The left panel of Fig. 1.6 qualitatively illustrates the vapochromic behavior of a crystal. Here, the horizontal q_1, vertical, and the third q_2 axes denote the uptake of vapor molecules by the crystal, Gibbs free energy of the entire system, and intermolecular arrangement, respectively. This indicates that the uptake of vapor molecules by the crystal leads to structural transformations including both

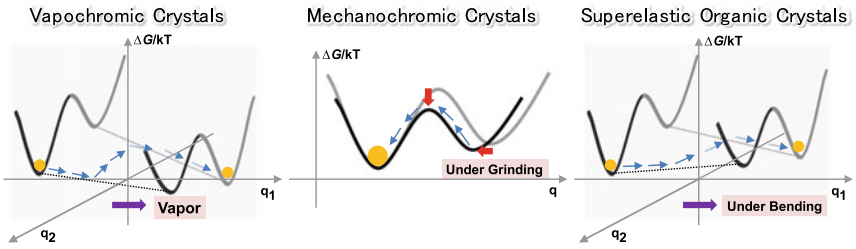

Fig. 1.6 Schematic potential energy diagrams constructed for the models of vapochromic, mechanochromic, and superelastic crystals

intramolecular structural changes and intermolecular rearrangements accompanied by color and/or luminescence color changes. The middle panel of Fig. 1.6 thermodynamically describes typical mechanochromic behavior. Here, the horizontal and vertical axes denote the intermolecular arrangement and Gibbs free energy, respectively, and the initial potential energy surface (gray line) is compared with that obtained during macroscopic mechanical grinding (black line). In this model, the local minimum structure is varied under gentle grinding, after which structural transformations accompanied by color and/or luminescence color changes occur even without an additional heat energy because of the decrease in activation energy. The right panel of Fig. 1.6 shows the superelasticity of a crystal. Here, the horizontal q_1, vertical, and the third q_2 axes denote the bending of the crystal, the Gibbs free energy, and intermolecular arrangement, respectively. The molecular crystal is flexibly bended throughout structural transformations because the energy relationship between the two local minimum structures is changed under bending.

Importantly, "soft crystals" may undergo structural transformation even at room temperature ($\Delta G^{\ddagger}/kT \sim 1$) (i.e., approximately 2.5 kJ mol^{-1}) under intrinsic gentle external stimuli, although the as-synthesized crystals are stable without these stimuli. Thus, they can be potentially used as the next-generation stimuli-responsive materials with highly ordered structures for sensors and luminescent and/or electronic devices. In the next chapter, the question "what are soft crystals?" is addressed.

References

1. (a) (1992) Acta Crystallogr A48:922–946; (b) Authier A, Chapuis G (2014) A little dictionary of crystallography. International Union of Crystallography, Chester
2. Kato M, Ito H, Hasegawa M, Ishii K (2019) Chem Eur J 25:5105–5112
3. Taubera J, Higlera R, Sprakela J (2016) Proc Natl Acad Sci USA 113:13660–13665
4. Ren Y, Kan WH, Henderson MA, Bomben PG, Berlinguette CP, Thangadurai V, Baumgartner T (2011) J Am Chem Soc 133:17014–17026
5. (a) Annadhasan M, Agrawal AR, Bhunia S, Pradeep VV, Zade SS, Reddy CM, Chandrasekar R (2020) Angew Chem Int Ed Engl 59:13852–13858; (b) Karothu DP, Halabi JM, Ahmed E, Ferreira R, Spackman PR, Spackman MA, Naumov P (2022) Angew Chem Int Ed Engl 61:e202113988
6. Horike S, Shimomura S, Kitagawa S (2009) Nat Chem 1:695–704
7. Kato M, Omura A, Toshikawa A, Kishi S, Sugimoto Y (2002) Angew Chem Int Ed 41:3183–3185
8. (a) Kato M (2007) Bull Chem Soc Jpn 80:287–294; (b) Wenger OS (2013) Chem Rev 113:3686–3733; (c) Zhang X, Li B, Chen Z-H, Chen Z-N (2012) J Mater Chem 22:11427–11441
9. (a) Seki T, Ito H (2016) Chem Eur J 22:4322–4329; (b) Kobayashi A, Kato M (2017) Chem Lett 46:154–162
10. (a) Sagara Y, Kato T (2009) Nat Chem 1:605–610; (b) Xu C-N, Watanabe T, Akiyama M, Zheng X-G (1999) Appl Phys Lett 74:2414
11. Ito H, Saito T, Oshima N, Kitamura N, Ishizaka S, Hinatsu Y, Wakeshima M, Kato M, Tsuge K, Sawamura M (2008) J Am Chem Soc 130:10044–10045
12. Sagara Y, Mutai T, Yoshikawa I, Araki K (2007) J Am Chem Soc 129:1520–1521
13. Takamizawa S, Miyamoto Y (2014) Angew Chem Int Ed Engl 53:6970–6973
14. Takamizawa S, Takasaki Y (2016) Chem Sci 7:1527–1534

15. Mir SH, Takasaki Y, Engel ER, Takamizawa S (2017) Angew Chem Int Ed Engl 56:15882–15885
16. Takamizawa S, Takasaki Y, Sasaki T, Ozaki N (2018) Nat Commun 9:3984
17. (a) Varughese S, Kiran MS, Ramamurty U, Desiraju GR (2013) Angew Chem Int Ed Engl 52:2701–2712; (b) Panda MK, Ghosh S, Yasuda N, Moriwaki T, Mukherjee GD, Reddy CM, Naumov P (2015) Nat Chem **7**:65–72
18. Mutai T, Sasaki T, Sakamoto S, Yoshikawa I, Houjou H, Takamizawa S (2020) Nat Commun 11:1824

Open Access This chapter is licensed under the terms of the Creative Commons Attribution 4.0 International License (http://creativecommons.org/licenses/by/4.0/), which permits use, sharing, adaptation, distribution and reproduction in any medium or format, as long as you give appropriate credit to the original author(s) and the source, provide a link to the Creative Commons license and indicate if changes were made.

The images or other third party material in this chapter are included in the chapter's Creative Commons license, unless indicated otherwise in a credit line to the material. If material is not included in the chapter's Creative Commons license and your intended use is not permitted by statutory regulation or exceeds the permitted use, you will need to obtain permission directly from the copyright holder.

Chapter 2
Classification and Definition of "Soft Crystals"

Kazuyuki Ishii and Masako Kato

Abstract "Soft crystals" typically undergo structural transformations in response to weak stimuli while maintaining the crystalline structural order. These transformations are often manifested as visible phenomena, such as changes in optical properties (color and/or luminescence color). In this chapter, the structural order, activation energy, and softness of "soft crystals" are compared with those of conventional hard crystals and soft materials, including liquid crystals and gels. Based on the results of this comparison, "soft crystals" are defined more precisely.

Keywords Soft crystals · Crystal structure · Phase transition · Stimulus response · Photofunction

2.1 What Are "Soft Crystals"?

How are "soft crystals" characterized and defined? When the main features of "soft crystals", such as vapochromism, mechanochromism, and superelasticity/ferroelasticity, were discussed, their key characteristics were typically extracted as follows: "many crystal polymorphs can be formed"; "phase transition and/or structural transformation can occur even under gentle stimuli at room temperature"; "because of the various intermolecular electronic interactions, such as d–π, d–d, or π–π ones, intermolecular rearrangements are accompanied by color and/or luminescence color changes"; "there are large voids in crystals"; "crystals with flexible molecular structures and substituents tend to exhibit mechanochromism"; and "energy changes during phase transitions and/or structural transformations should

K. Ishii
Institute of Industrial Science, The University of Tokyo, 4-6-1 Komaba, Tokyo 153-8505, Japan
e-mail: k-ishii@iis.u-tokyo.ac.jp

M. Kato (✉)
Department of Applied Chemistry for Environment, Kwansei Gakuin University, 1 Gakuen Uegahara, Sanda 669-1330, Japan
e-mail: katom@kwansei.ac.jp

© The Author(s) 2023

M. Kato and K. Ishii (eds.), *Soft Crystals*, The Materials Research Society Series,
https://doi.org/10.1007/978-981-99-0260-6_2

be gradual". Furthermore, "adsorption/desorption of large molecules", "chemical conversion", and "chemical reaction-based chemiluminescence" can be also observed for such crystals.

Considering these key characteristics from various points of view, we will attempt to define "soft crystals" in this chapter.

2.2 Crystal Polymorphisms

In crystals of molecules composed of various atoms, many kinds of intermolecular interactions can lead to the formation of several crystal structures with different molecular arrangements. This phenomenon is called crystal polymorphisms. "Soft crystals" mainly consisting of organic molecules and metal complexes are characterized by the (1) existence of various crystal polymorphs and (2) occurrence of phase transitions between these polymorphs under gentle stimuli. In this section, a historical background of polymorphism in molecular crystals is briefly described.

Controlling crystal polymorphism is an important task, especially in the research and development of drugs (Note 1) because their stability, solubility, and dissolution rate depend on the crystalline form, which can strongly influence drug efficacy. The second example is crystal polymorphs of phthalocyanine pigments in relation to photo- and electronic properties. Phthalocyanine crystals are practically used as near-infrared light-active photoconductors in photocopiers and laser beam printers, and their photoconductivity is considerably influenced by the crystal structures (Note 2). In spite of these social demands, the engineering of molecular crystals, which aims to achieve a desired molecular arrangement, has long been dependent on serendipity and screening. In recent decades, international blind tests for predicting molecular crystal structures have been performed, and various prediction methods based on theoretical calculations of crystal structures are rapidly developing [1].

Note 1: Crystal polymorphism is a widely observed phenomenon, which has been investigated by crystal scientists for a long time. In this book, vapochromic molecular crystals are also discussed as important structures, and pseudo-polymorphs, such as solvated crystals and hydrated crystals, are considered crystal polymorphs in a broad sense. First, crystal polymorphism is utilized in the field of pharmaceutical manufacturing. Pharmaceuticals in commercial formulations and/or at the development stage are mainly produced in the crystalline form, and 70–80% of all pharmaceuticals have crystal polymorphs owing to their complex and/or flexible molecular structures. The physicochemical properties of polymorphic pharmaceuticals are dependent on their crystal forms, which affect the pharmacokinetics of solid dosages, such as solubility and biocompatibility. Because of the necessity to control the quality and stability of products at their manufacturing stage, the solubility, dissolution kinetics, and storage stability of various crystal polymorphs are investigated in pharmaceutical industries.

Note 2: Phthalocyanine pigments have been used in GaAsAl laser printers or copiers as near-infrared light-active photoconductors; however, they produced different

crystal polymorphs whose photoconductivity strongly depended on the crystal structure. Therefore, it is important to elucidate the relationship between crystal polymorphs and their photoconductivity and control their crystal structures when manufacturing printers and copiers. This aspect is briefly discussed in Chap. 3.

2.3 Comparison of "Soft Crystals" with Conventional "Hard Crystals" and "Soft Materials"

According to the principles of basic chemistry, the hardness and softness of materials depend on the type of their atomic bonds. In contrast to conventional hard crystals consisting of covalent and/or ionic bonds, the characteristic feature of "soft crystals" is the coexistence of "strong intramolecular atomic bonds" and "weak but non-negligible intermolecular atomic interactions", which are summarized as follows.

Diamond crystals composed solely of carbon–carbon covalent bonds (357 kJ mol^{-1}) are known as the kings of stable hard crystals. However, diamond is a metastable state at room temperature and atmospheric pressure, and its conversion to graphite is thermodynamically spontaneous (the Gibbs free energy difference between these two states is $\Delta G^\circ = -2.9$ kJ mol^{-1}). Fortunately, diamond exhibits its eternal brilliance due to the very large activation Gibbs free energy of $\Delta G^\ddagger \sim 1.0 \times 10^3$ kJ mol^{-1} under ambient pressure. Intermolecular hydrogen bonds (10–20 kJ mol^{-1}) and van der Waals interactions (10–30 kJ mol^{-1}) in molecular crystals are much weaker than the covalent and ionic bonds (e.g., NaCl: 785 kJ mol^{-1}) in hard crystals; therefore, the lattice enthalpies (<100 kJ mol^{-1}) of molecular crystals formed by van der Waals interactions and hydrogen bonds are much smaller than those of typical ionic crystals (≥several 100 kJ mol^{-1}) [2]. Thus, the state of atomic bonding strongly contributes to the enthalpy terms of $\Delta G^\ddagger$ values for solid-state structural transformations, such as phase transitions. Meanwhile, the existence of large voids and/or flexible substituents is also characteristic of "soft crystals", which facilitates solid-state structural transformations and may decrease their $\Delta G^\ddagger$ values by increasing the entropy terms.

In contrast to soft materials, "soft crystals" produce discrete X-ray diffraction patterns, indicating a long-range structural order. Figure 2.1a displays the relationship between the activation energy of a structural change ($\Delta G^\ddagger$) and the structural order of different forms of condensed matter, such as "Crystals", "Liquid Crystals", "Gel", "Glass", and "Liquid" [3]. As the degree of structural order increases in the series "Liquid" < "Gel" < "Liquid Crystals" < "Crystals", the $\Delta G^\ddagger$ value tends to increase, which impedes structural transformations. In this figure, amorphous solid materials, such as "Glass", are stiff but less ordered; therefore, they should be located in the lower right part of Fig. 2.1a. "Soft crystals", which contain highly ordered structures but undergo structural transformations at low $\Delta G^\ddagger$ values (Fig. 2.1b), are classified as unexplored and placed in the upper left part (opposite to "Glass") in Fig. 2.1a.

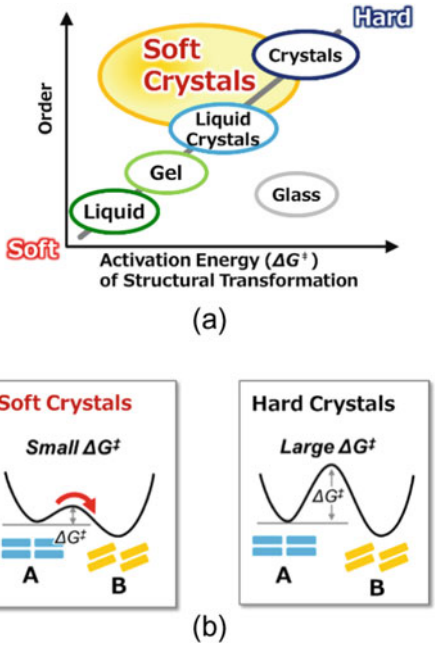

Fig. 2.1 Schematic drawings showing the **a** structural order in condensed matter and activation energy of structural transformation ($\Delta G^{\ddagger}$) and **b** energetic characteristics of soft crystals and conventional hard crystals. Reprinted with permission from reference [3]

Therefore, "soft crystals" can undergo structural transformations accompanied by changes in electronic properties at room temperature upon gentle stimuli. Thus, they may be potentially used as next-generation materials because their structural transformations cause visible changes in morphology and/or optical properties, such as color and luminescence. Meanwhile, as compared with soft materials or polymers, "soft crystals" exhibit smaller structural fluctuations, and their solid-state structures are ordered in the long range, making them suitable for the transport/delocalization of electrons or excitons.

2.4 Comparison of "Soft Crystals" with "Liquid Crystals" and "Plastic Crystals"

Molecular crystals generally possess optically anisotropic properties (anisotropic crystals) because of the ordered centers of gravity and orientations of their constituent molecules. When molecular crystals are melted by heating, they become an optically isotropic liquid. However, in the case of pseudo-spherical molecules, a solid-state phase transition occurs before melting owing to the molecular reorientational motion around the molecular centers of gravity. This state is called "isotropic crystals" or "plastic crystals" (Note 3). In the case of rod-like or disk-like molecules, even when the order of the molecular center of gravity is destroyed, the crystals sometimes

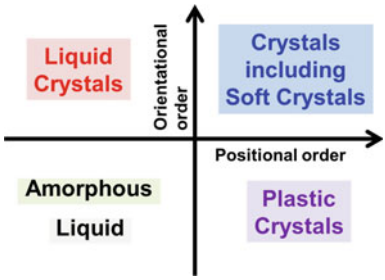

Fig. 2.2 Positional/orientational order-based relationship between the amorphous state, liquid state, liquid crystals, plastic crystals, and crystals including soft crystals

remain anisotropic because of the partial restriction of the molecular reorientational motion. This state is called "liquid crystals" (Note 4). Figure 2.2 classifies different states of condensed matter, such as "Crystals including soft crystals", "Amorphous", "Liquid", "Liquid crystals", and "Plastic crystals" in terms of their orientational order and positional order (center of gravity). In Fig. 2.2, the structural order presented in Fig. 2.1 is divided into two parts (the orientational order and positional order), and "soft crystals" are clearly classified into "crystals" with respect to the existing liquid and plastic crystals.

Note 3: Phase transitions due to the restricted rotation or reorientation of molecules in their crystalline states have been known for a long time. Simon and von Simpson discussed their possibility and reported a phase transition caused by the reorientation of tetrahedral NH_4^+ ions in NH_4Cl crystals (ref. [4]).

Note 4: Because liquid crystals exhibit optically anisotropic properties, such as dielectric constant and refractive index, owing to the difference between their molecular long and short axes, they have been applied in displays with electrically modulated optical characteristics.

2.5 Mechanical Softness of Molecular Crystals

As mentioned in Chap. 1, molecular crystals sometimes exhibit superelasticity or ferroelasticity. How can the mechanical softness of molecular crystals be characterized? Naumov et al. performed global analyses of the mechanical properties of organic molecular crystals, such as strength and toughness, and compared them with those of various engineering materials, including polymers, ceramics, and metals [5]. In their work, Young's modulus (E), a proportionality constant between strain and stress widely utilized for elastic materials, and hardness (H), served as a measure of resistance to deformation and scratching, were focused on. By plotting these parameters versus material density, the softness of organic molecular crystals was compared with those of other materials (Fig. 2.3).

Because the red areas in Fig. 2.3 representing molecular crystals contain only organic compounds, they should be expanded towards higher densities by adding

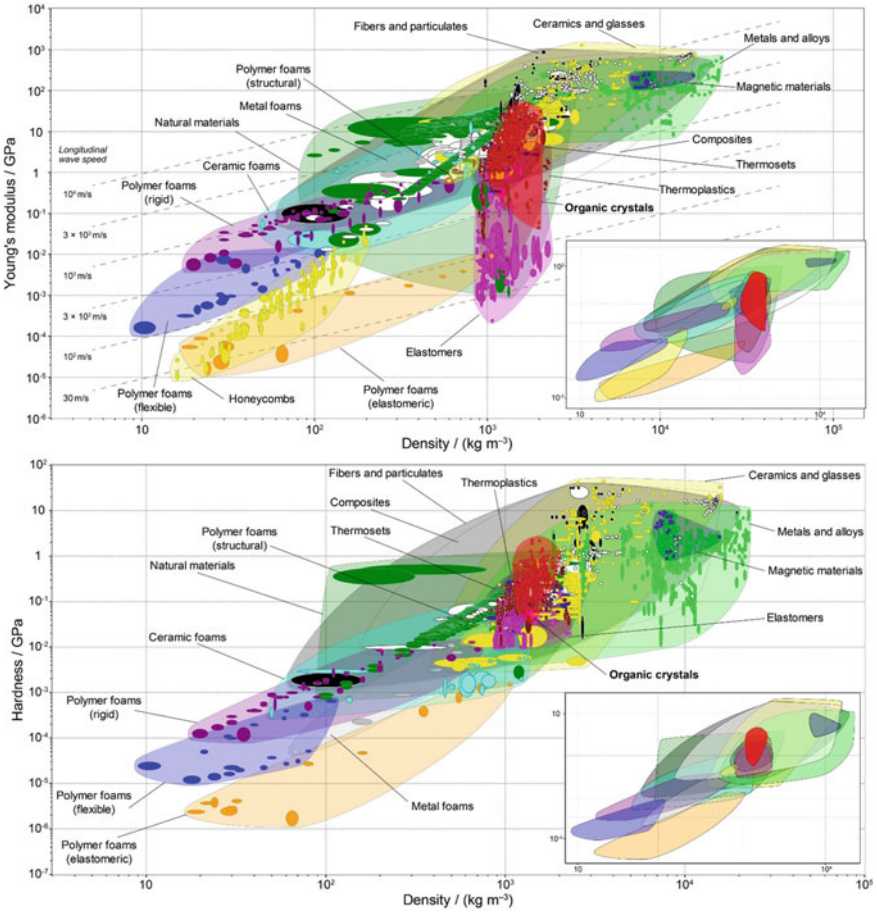

Fig. 2.3 Young's modulus (E)–density (top) and hardness (H)–density (bottom) plots constructed for organic crystals and other classes of materials. The opaque bubbles represent ranges of performance indices determined for particular materials, while the larger translucent envelopes enclose points obtained for a given class of materials. Reprinted with permission from ref. [5]

metal complexes. Although it may be possible to discover softer molecular crystals in the future, we can determine the positions of molecular crystals in a wide range of materials. Even at this stage, organic molecular crystals with high mechanical properties have been reported, and their softness enables the utilization of these materials in devices requiring high flexibility and mechanical compliance. Because the horizontal axis denotes the density of materials, the red area corresponding to organic molecular crystals partially overlaps with the region representing polymers. This means that molecular crystals are much lighter than ceramics and metals, which has an important advantage in the functionalization of organic materials. Meanwhile, in contrast to polymers, the long-range structural order and anisotropy in molecular crystals are

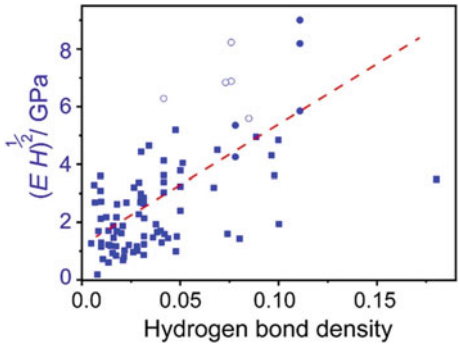

Fig. 2.4 Correlation of the number and strength of hydrogen bonds with the mechanical properties of organic crystals. Dependence of the combined measure of softness, $(EH)^{1/2}$, on the hydrogen bond density. Reprinted with permission from ref. [5]

their distinct advantages that outweigh disadvantages, such as the difficulty of mass production.

The combination of multiple strong hydrogen bonds oriented along a particular direction can provide guidance for the design of flexible molecular crystals. Naumov et al. reported the rough relationship between hydrogen bonding and softness in organic crystals (Fig. 2.4), which was derived from the detailed analysis of hydrogen bonds in well-characterized crystal structures, i.e., the properties of "soft crystals". This relationship may be potentially used for designing not only molecular crystals but also various types of soft molecular materials, such as gels and polymers whose structures cannot be determined precisely. This analysis focused on strong and designable hydrogen bonds; however, similar analyses may be performed for other intermolecular interactions.

Gong proposed the intrinsic correlation between the elastic moduli of crystals and their lattice constants (Fig. 2.5). The elastic modulus G, which represents the energy density for causing material deformation, is expressed by the formula U/b^3, where b and U denote the lattice constant and the deformation energy of the lattice, respectively. According to this equation, the energy density decreases with increasing the lattice constant, which in turn increases the crystal softness. This is consistent with the fact that "soft crystals" whose crystal lattices are composed of ~1 nm-sized molecules or supramolecules, can exhibit softness in contrast to the extremely hard diamond crystal lattice composed of ~0.1 nm-sized atoms. By increasing the lattice constant, flexible molecular structures and/or large voids can be introduced, and thus, the crystals can be softened. Gong et al. successfully prepared macroscopically oriented lipid molecular films with a period of approximately 100 nm by polymerizing and fixing lipids in a hydrogel [6]. The gels can be easily deformed by applying a very weak pressure, and their structural color is varied by changing the periodic distance. Although the formation of crystal structures becomes difficult with increasing the lattice constant, the gels exhibiting discrete diffraction patterns of ultrasmall-angle X-rays are regarded as one-dimensional crystals with a lattice constant of 100 nm. Thus, this proposal illustrates how to not only extend the concept of "soft crystals" but also increase crystal softness.

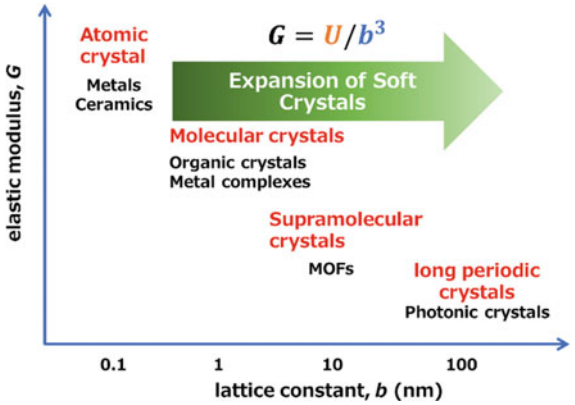

Fig. 2.5 Conceptual image of the correlation between the elastic moduli of crystals and their lattice constants

2.6 Definition of "Soft Crystals"

Various phenomena related to "soft crystals", such as vapochromism and mechanochromism, have been extensively studied in recent years. Mechanochromism corresponding to the single crystal → amorphous structural transformation is induced by gently grinding crystals. Meanwhile, the organic vapor-induced crystallization of amorphous solids, which accompanies vapochromism, has been reported as well. Therefore, to accurately characterize the properties of "soft crystals", this book describes not only representative "soft crystals" with discrete X-ray diffraction patters but also various related processes.

In Sect. 2.3, "soft crystals" are compared with conventional hard crystals and soft materials in terms of their activation energy and structural order. In Sect. 2.4, "crystals including soft crystals" are compared with liquid crystals and plastic crystals from the viewpoint of the orientational order and positional order. Thus, "soft crystals" are clearly distinguishable from liquid crystals in terms of their positional order and from conventional hard crystals in terms of their activation energy. However, "soft crystals" can be stably prepared and isolated despite their ability to undergo structural transformations at room temperature after applying weak but specific stimuli. In Fig. 2.6, the qualitative activation energy $\Delta G^{\ddagger}$ is plotted along the vertical axis against the positional order (the horizontal axis) and orientational order (the third axis), which are displayed in Fig. 2.2. Importantly, "soft crystals" are stable at room temperature in the absence of specific stimuli (similar to conventional crystals) because the $\Delta G^{\ddagger}$ value is significantly larger than the thermal energy. However, in contrast to conventional hard crystals, the structural transformations of "soft crystals" are caused by weak but specific stimuli because of the decrease in $\Delta G^{\ddagger}$. In other words, "soft crystals" can be defined in a narrow sense as crystals that are normally stable but undergo structural transformations in the presence of specific stimuli, which decrease the $\Delta G^{\ddagger}$ value.

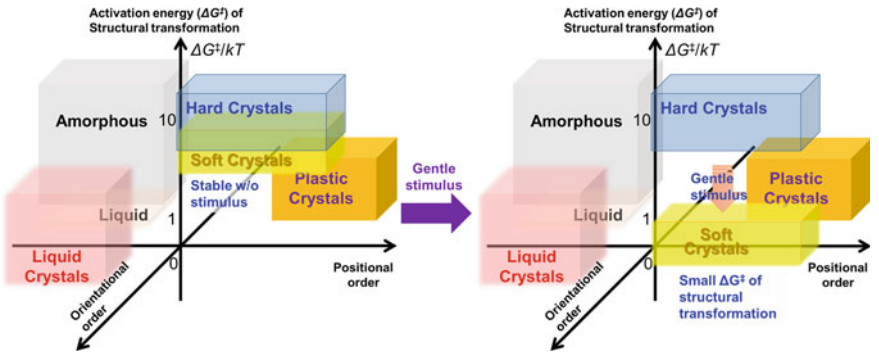

Fig. 2.6 Schematic diagrams illustrating the positional/orientational orders in condensed matter and the activation energies of structural transformations ($\Delta G^{\ddagger}$) before (left) and after (right) applying a gentle stimulus

References

1. (a) Maddox J (1988) Nature 335:201. (b) Reilly AM, et al (2016) Acta Crystallogr B 72:439–459; (c) Price SL (2018) Proc R Soc A 474:20180351
2. (a) Beran GV (2016) Chem Rev 116:5567–5613; (b) Liu D, Zhang S, Wu Z (2003) Inorg Chem 42:2465–2469
3. Kato M, Ito H, Hasegawa M, Ishii K (2019) Chem Eur J 25:5105–5112
4. Simon F, von Simson C (1924) Z Phys 21:168
5. Karothu DP, Halabi JM, Ahmed E, Ferreira R, Spackman PR, Spackman MA, Naumov P (2022) Angew Chem Int Ed Engl 61:e202113988
6. (a) Yue Y, Kurokawa T, Haque MA, Nakajima T, Nonoyama T, Li X, Kajiwara I, Gong JP (2014) Nat Commun 5:4659; (b) Li X, Kurokawa T, Takahashi R, Haque MA, Yue Y, Nakajima T, Gong JP (2015) Macromolecules 48:2277–2282

Open Access This chapter is licensed under the terms of the Creative Commons Attribution 4.0 International License (http://creativecommons.org/licenses/by/4.0/), which permits use, sharing, adaptation, distribution and reproduction in any medium or format, as long as you give appropriate credit to the original author(s) and the source, provide a link to the Creative Commons license and indicate if changes were made.

The images or other third party material in this chapter are included in the chapter's Creative Commons license, unless indicated otherwise in a credit line to the material. If material is not included in the chapter's Creative Commons license and your intended use is not permitted by statutory regulation or exceeds the permitted use, you will need to obtain permission directly from the copyright holder.

Chapter 3
Theoretical Background of Photophysical Properties

Kazuyuki Ishii and Masako Kato

Abstract In this chapter, we aim to explain the chromic phenomena observed in "soft crystals". Accordingly, the basic principles for comprehending the fundamental photophysical properties of molecular monomers, such as electronic absorption spectra and luminescence properties, are introduced. Moreover, the photophysical properties of molecular dimers and molecular crystals are explained in terms of intermolecular interactions in excited states.

Keywords Soft crystals · UV-vis absorption · Luminescence · Photophysical properties

3.1 Background and Significance

Color and/or luminescence color changes, called chromism, with structural changes in molecular crystals are one of essential characteristics of soft crystals [1]. In recent decades, in the case of molecular monomers, theoretical quantum calculations have been developed to be able to reproduce the photophysical properties experimentally evaluated. On the other hand, although Davidov splitting, which results from exciton interactions, has long been recognized as the important photophysical property of molecular crystals [2], even at this stage, it is difficult to comprehend the photophysical properties of molecular crystals using similar approaches. This originates from the coexistence of intramolecular interactions based on strong interatomic bonds and non-negligible electronic intermolecular interactions in molecular crystals, which are different from the molecular monomers or inorganic crystals. In this chapter, molecular photophysical properties are explained in terms of molecular monomers,

K. Ishii (✉)
Institute of Industrial Science, The University of Tokyo, 4-6-1 Komaba, Meguro-Ku, Tokyo 153-8505, Japan
e-mail: k-ishii@iis.u-tokyo.ac.jp

M. Kato
Department of Applied Chemistry for Environment, Kwansei Gakuin University, 1 Gakuen Uegahara, Sanda 669-1330, Japan
e-mail: katom@kwansei.ac.jp

© The Author(s) 2023

M. Kato and K. Ishii (eds.), *Soft Crystals*, The Materials Research Society Series,
https://doi.org/10.1007/978-981-99-0260-6_3

dimers, and crystals. First, we explain the basic photophysical properties of molecular monomers, such as electronic absorption spectra, fluorescence and phosphorescence spectra, luminescence lifetimes, and luminescence yield, focusing on the π-π* and metal-to-ligand charge transfer (MLCT) excited states, which are essential for the chromism of organic molecules and metal complexes. Next, the photophysical properties of molecular dimers are briefly described using intermolecular interactions, such as exciton interactions and charge transfer interactions, in addition to metal–metal-to-ligand charge transfer which are crucial in soft crystals based on metal complexes. Finally, we introduce the theoretical analysis on photoconductive molecular crystals using exciton and charge transfer interactions.

3.2 Photophysical Properties of Diamagnetic Molecular Monomers

This chapter focuses on the photophysical properties of molecules showing diamagnetism in the ground state, which are the majority of luminescent organic molecules and metal complexes.

Figure 3.1 depicts the photophysical processes occurring in diamagnetic molecules [3]. Here, the singlet ground (S_0) state, the lowest excited singlet (S_1) state, and the lowest excited triplet (T_1) state are considered. Although the actual excited states are represented as a result of configuration interaction between several excited configurations, the S_1 and T_1 states are approximately represented here as the transition states from the highest occupied molecular orbital (HOMO) to the lowest unoccupied molecular orbital (LUMO). The general photophysical processes are: (1) spin-allowed singlet–singlet (S_0–S_n) absorption, (2) $S_1 \rightarrow S_0$ fluorescence, (3) $T_1 \rightarrow S_0$ phosphorescence, (4) spin-forbidden thermal deactivation processes, i.e., $S_1 \rightarrow T_1$ or $T_1 \rightarrow S_0$ intersystem crossing (ISC), and (5) spin-allowed thermal deactivation process i.e., $S_1 \rightarrow S_0$ internal conversion (IC). The detail procedures (1)–(4) are described in the following sections.

3.3 Electronic Absorption and Luminescence of π–π* Transitions

In diamagnetic organic compounds and metal complexes containing metal ions with d^0 or d^{10} electron configuration, excited configurations, such as (π–π*), (n–π*), (σ–π*), (π–σ*), and (σ–σ*), are considered. Because the σ (or σ*) orbitals are highly stabilized (or destabilized), (σ–π*), (π–σ*), and (σ–σ*) are typically observed in the UV region or higher energies region. Thus, the electronic absorption bands originating from (π–π*) and (n–π*) are frequently observed in the visible region. Because the molar absorption coefficient (ε) of (n–π*) transitions is much smaller than that of

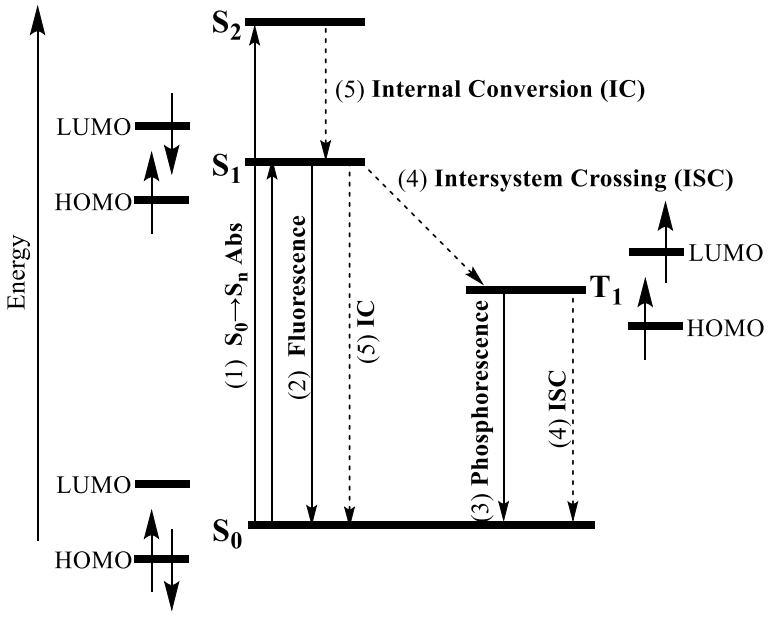

Fig. 3.1 Photophysical processes of a typical diamagnetic molecule

(π–π*) transitions, the (π–π*) transitions are mainly responsible for the coloration of molecules. For metal complexes containing transition metal ions with the d^n (n = 1–9) electron configuration, the (d–π*) (or MLCT) configuration is crucial. In this and the following sections, we discuss (π–π*) and MLCT, using phthalocyanines, which are practically used as blue or green dyes and pigments, as well as for photoconducting materials in laser-beam printers and photocopiers [4].

Figure 3.2 depicts the electronic absorption, fluorescence, and phosphorescence spectra of a zinc phthalocyanine complex (the diamagnetic central metal is Zn^{2+} with the d^{10} electron configuration) showing a typical (π–π*) transitions.

In the UV-vis spectrum, a sharp and strong absorption band attributed to the $S_0 \rightarrow S_1$ transition is seen at approximately 680 nm, which is called as the Q band. In contrast, the absorption band centered around 350 nm is referred to as the Soret band, which originates from the $S_0 \rightarrow S_2$ transition. These S_1 and S_2 states corresponding to ^{1}(π–π*) consist primarily of HOMO(π) → LUMO(π*) and HOMO−1(π) → LUMO(π*), respectively (Fig. 3.3).

The electronic transition probability of a $S_0 \rightarrow S_n$ transition is expressed by the oscillator strength f, which is expressed to be proportional to the integral of the experimental absorption coefficient ε, as follows:

$$f_{Sn \leftarrow S0} = 4.32 \times 10^{-9} \int \varepsilon(\tilde{\nu}) d\tilde{\nu} \tag{3.1}$$

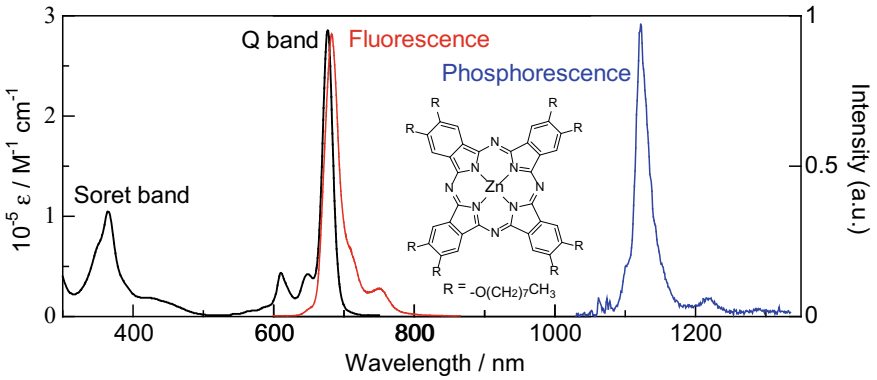

Fig. 3.2 UV-vis absorption (black line), fluorescence (red line), and phosphorescence (blue line) spectra of a zinc phthalocyanine complex [4]

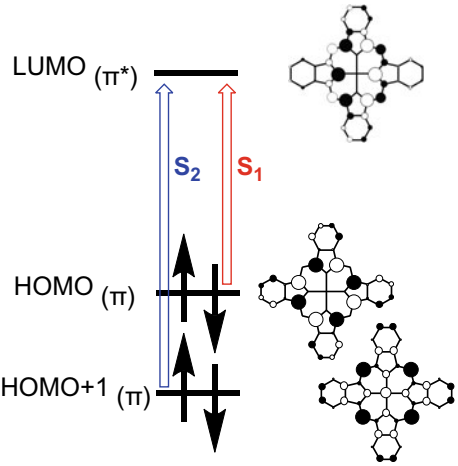

Fig. 3.3 Four frontier π MOs of ZnPc. Only one LUMO is shown, although two LUMOs are degenerated for ZnPc

The oscillator strength f is expressed by the theoretically calculated electric dipole strength as follows.

$$f_{Sn \leftarrow S0} = \left(\frac{8\pi^2 m_e \nu}{3he^2}\right) \left| \left\langle S_n \left| \sum_i er_i \right| S_0 \right\rangle \right|^2 \tag{3.2}$$

The (π–π*) transition is distinguished by the fact that ε is frequently large (10^3–10^5 M^{-1} cm^{-1}) when it is the electric dipole allowed transition. For example, the ε value of the Q band of zinc(II) phthalocyanine is very large (~3 × 10^5 M^{-1} cm^{-1}). In addition, vibronic bands, which are based on the misalignment of the most stable structure between the ground and excited states and reflect the vibrational structures

in the excited state, can be observed because of the sharp absorption bands (the full width at half maximum (FWHM) of the Q band of zinc(II) phthalocyanine is 450 cm^1).

As depicted in Fig. 3.2, the $S_1 \rightarrow S_0$ fluorescence of zinc(II) phthalocyanine is observed around 700 nm, which is the mirror image of the Q band. The peak difference (Stokes shift) between the absorption and fluorescence is small, which is characteristic of the $^1(\pi–\pi^*)$ transition and reflects the small structural change caused by photoexcitation. The phosphorescence of zinc(II) phthalocyanine is observed at approximately 1100 nm and 77 K, where non-radiative deactivation is suppressed.

Using the excited state lifetime (τ_F: fluorescence lifetime, τ_P: phosphorescence lifetime), luminescence efficiency (Φ_F: fluorescence quantum yield, Φ_P: phosphorescence quantum yield), and triplet yield (Φ_T), the excited state dynamics in the S_1 and T_1 states is experimentally defined as follows.

$$\tau_F = 1/(k_F + k_{IC} + k_{ISC}), \tag{3.3a}$$

$$\tau_P = 1/\left(k_P + k'_{ISC}\right), \tag{3.3b}$$

$$\Phi_F = k_F/(k_F + k_{IC} + k_{ISC}), \tag{3.3c}$$

$$\Phi_T = k_{ISC}/(k_F + k_{IC} + k_{ISC}), \tag{3.3d}$$

$$\Phi_P = \Phi_T \times k_P/\left(k_P + k'_{ISC}\right), \tag{3.3e}$$

where, k_F and k_P are the radiative decay rate constants in fluorescence and phosphorescence, k_{IC} is the internal conversion rate constant, and k_{ISC} and $k_{ISC'}$ are the intersystem rate constants. When no compensation in the condensed system is considered, k_F is expressed as follows.

$$k_F = \left(\frac{\nu_F^2}{1.5}\right) f_{S0\rightarrow S1}. \tag{3.4}$$

k_F is proportional to the oscillator strength, similarly to the electronic absorption coefficient ε. Therefore, the k_F value is high when the ε value is large. For instance, in the case of metal phthalocyanines (central metal/axial ligand = Mg, Al, Zn, Ga, Cd, In), the k_F value is less dependent on the central metal, since the fluorescence is derived from $(\pi–\pi^*)$ of the phthalocyanine ligand.

On the other hand, the main non-radiative decay process is the intersystem transition from the S_1 state to the T_1 state. The intersystem crossing is governed by the spin–orbit coupling on the central atom, and consequently the fluorescence is strongly dependent on the central atom. In terms of the periodic table, we compare the τ_F and Φ_F of phthalocyanines as an example, either unsubstituted or substituted with *tert*-butyl groups. In the case of phthalocyanine containing the first and second

periodic elements (central atoms = 2H, 2Li, Mg, Al, Si), τ_F is relatively long, ranging from 3.8 to 9.0 ns, and Φ_F is also high, ranging from 0.57 to 0.85. For the third periodic elements (central atom = Zn, Ga), τ_F and Φ_F decreases to 3.15–4.73 ns and 0.30–0.37, respectively. In addition, for the fourth-period elements (central atoms = Cd, In, and Sb), τ_F significantly becomes short (0.37–0.6 ns) and Φ_F significantly decreases (0.03–0.08). Since the spin–orbit coupling is stronger for heavier atoms, the reduction in τ_F and Φ_F for heavier atoms can be interpreted as a strengthening of the intersystem crossing.

In Mg, Zn, and Cd phthalocyanine complexes, since the spin–orbit coupling is not large, Phosphorescence has been observed with extremely low Φ_P ($<10^{-3}$) and primarily measured at low temperatures, such as 77 K. Also, their triplet lifetimes at room temperature are relatively long and approximately a few hundred μs.

3.4 Electronic Absorption and Luminescence of (d–π*) (= MLCT) Transitions

Next, we describe a summary of MLCT transitions. Figure 3.4 depicts the UV–vis absorption and room temperature phosphorescence spectra of RuPc(CO)(py) and $RuPc(py)_2$ [5].

Similar to ZnPc, RuPc(CO)(py) with CO as an axial ligand displays a sharp and strong Q band attributed to (π–π*). In contrast, $RuPc(py)_2$ demonstrates a broad Q band, which can be explained by the admixture between (d–π*) (= MLCT) and

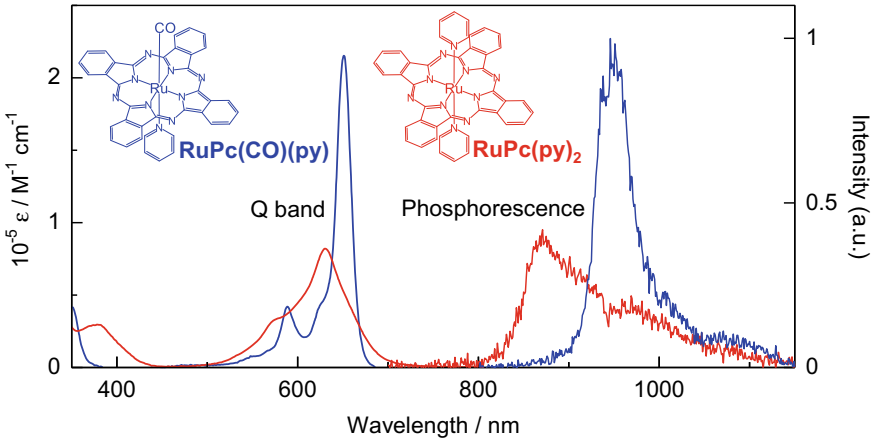

Fig. 3.4 UV-vis absorption and phosphorescence spectra of RuPc(CO)(py) (blue line) and $RuPc(py)_2$ (red line) at room temperature [5]. Here, four *tert*-butyl substituents in molecular structures are omitted for clarify

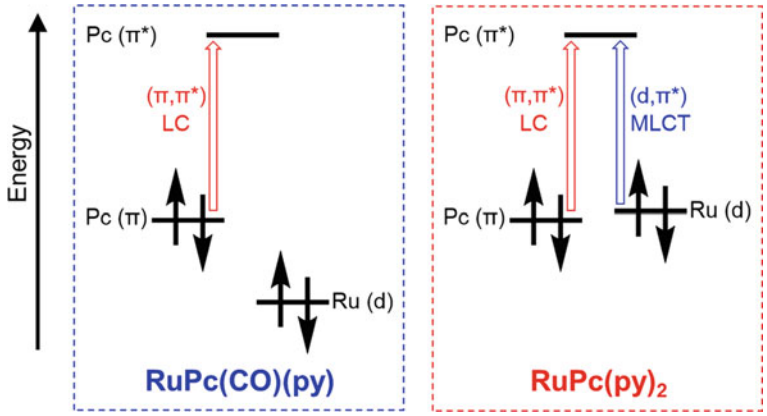

Fig. 3.5 Frontier MOs of RuPc(CO)(py) (left) and $RuPc(py)_2$ (right)

(π–π*) (= ligand center, LC). MLCTs are distinguished by a broad absorption bands and typically possess relatively large absorption coefficients ε (10^3–10^4 M^{-1} cm^{-1}).

The CO ligand is responsible for the distinction between RuPc(CO)(py) and $RuPc(py)_2$: CO is highly electron-withdrawing, and the π* orbital of CO strongly interacts with the d_π orbital of the metal, stabilizing the d_π orbital of ruthenium to a greater extent than the π orbital of the Pc ligand (π-back donation). Consequently, the Q band attributed to (π–π*) is observed in RuPc(CO)(py). On the other hand, in $RuPc(py)_2$, the energy of the d_π(Ru) orbital is of the same level as the π(Pc) orbital; thus, the MLCT contribution is more prominent (Fig. 3.5).

RuPc(CO)(py) and $RuPc(py)_2$ exhibit strong phosphorescence at room temperature. The T_1 state is attributed to (π–π*) because of the sharp spectrum and relatively long lifetime (10 μs). In contrast, the phosphorescence spectrum of $RuPc(py)_2$ is broad and the phosphorescence lifetime is short (160 ns at 293 K), experimentally indicating that the MLCT contributes to the T_1 state as in the Q band.

Thus, metal phthalocyanine complexes containing second or third transition metal ions (especially those with d^6 or d^8 electron configuration) can exhibit efficient phosphorescence at room temperature; the phosphorescence radiation rate k_P between the T_1 and S_0 states can be expressed as follows.

$$k_P \propto \left|\left\langle \Phi_{S0}^{N} \middle| \Phi_{T1}^{N} \right\rangle\right|^2 \left(\left| \left\langle \Phi_{Sn}^{ES} \middle| \sum_k \sum_i \xi_{ki} l_i s_i \middle| \Phi_{T1}^{ES} \right\rangle \right|^2 \Big/ \left(E(S_n) - E(T_1)\right) \right) \left| \left\langle \Phi_{S0} \middle| \sum_i e r_i \middle| \Phi_{Sn} \right\rangle \right|^2, \quad (3.5)$$

where, $E(S_n)$ and $E(T_1)$ are the energies of S_n and T_1, respectively, $\left| \left\langle \Phi_{Sn}^{ES} \middle| \sum_k \sum_i \xi_{ki} l_i s_i \middle| \Phi_{T1}^{ES} \right\rangle \right|^2$ is the spin–orbit coupling (SOC) between the T_1 and S_n states, and $\left| \left\langle \Phi_{S0} \middle| \sum_i e r_i \middle| \Phi_{Sn} \right\rangle \right|^2$ is the transition electric dipole moment between the S_n and S_0 states. In other words, the phosphorescence gains intensity by borrowing the

transition electric dipole moment between the S_n and S_0 states via the SOC between the T_1 and S_n states. In the case of the second or third transition metal ions, the SOC constant, ξ, is large, causing high k_P and room temperature phosphorescence.

3.5 Photophysical Properties of Molecular Dimers

In molecular crystals, their photophysical properties are relatively complex because of the coexistence of strong interatomic bonds in molecules and non-negligible intermolecular electronic interactions. Therefore, firstly, we describe the photophysical properties of molecular dimers as a model in terms of intermolecular electronic interactions.

When considering the photophysical properties of molecular dimers, there are two types of methods, as in the case of molecular hydrogen: (1) the Valence Bond (VB) method, which first constructs the excited states of the consisting monomer units and then considers the interaction between units [6]. (2) the Molecular Orbital (MO) method, which considers the molecular orbitals of the dimer itself and its excited states [7]. The VB method can easily visualize the interaction between units, whereas the MO method can accurately represent the interactions when the interaction is substantial. These two methods are different from the viewpoint of starting points, but should provide similar results under the same approximations. In this section, we will discuss the exciton and charge-transfer interactions under the VB method using the phthalocyanine dimer as a model, as well as the metal–metal-to-ligand charge transfer (MMLCT) state under the MO method using Pt diimine complexes [8].

Using the phthalocyanine dimer as an example, we discuss the basic theory of homodimers composed of the same monomer units. The UV–vis absorption spectra of monomer and dimer of silicon phthalocyanine are depicted in Fig. 3.6 [9]. As compared to the monomer, the Q band of the dimer shifts to the blue-side (a shift to higher energy). This blue shift can be explained by the energy-transfer type, exciton interaction between two phthalocyanine units. Figure 3.7 illustrates the relationship between the dimeric configurations and exciton interactions. The energy splitting caused by the exciton interaction is approximately proportional to the transition electric dipole moment, and therefore, the exciton interaction is crucial in the phthalocyanine dimers because the Q band of phthalocyanines has a large transition electric dipole moment, as mentioned in Sect. 3.1.

In the case of a face-to-face type dimer, the excited state is destabilized when the transition electric dipoles are aligned in the same direction, while it is stabilized when the transition electric dipoles are aligned in the opposite direction. Thus, the transition from the S_0 state to the high-energy exciton state is allowed because of the sum of two transition electric dipoles, whereas the transition to the low-energy exciton state is forbidden.

For the head-to-tail type dimer, the transition to the high-energy exciton state is forbidden, whereas the transition to the low-energy exciton state is allowed. The transitions to the high-energy exciton and low-energy exciton states are allowed to

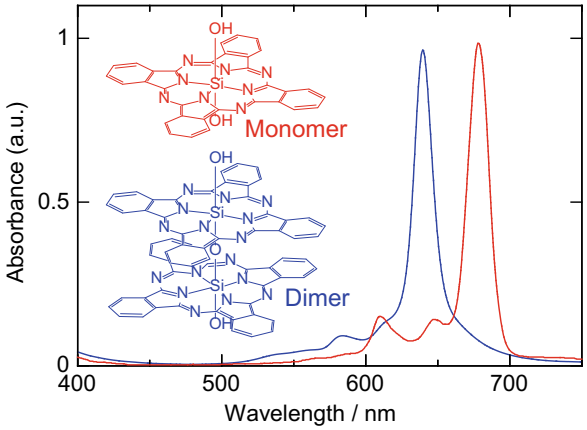

Fig. 3.6 UV-vis absorption spectra of the SiPc monomer (red line) and dimer (blue line) [9]. Here, four *tert*-butyl substituents in the molecular structures are omitted for clarity

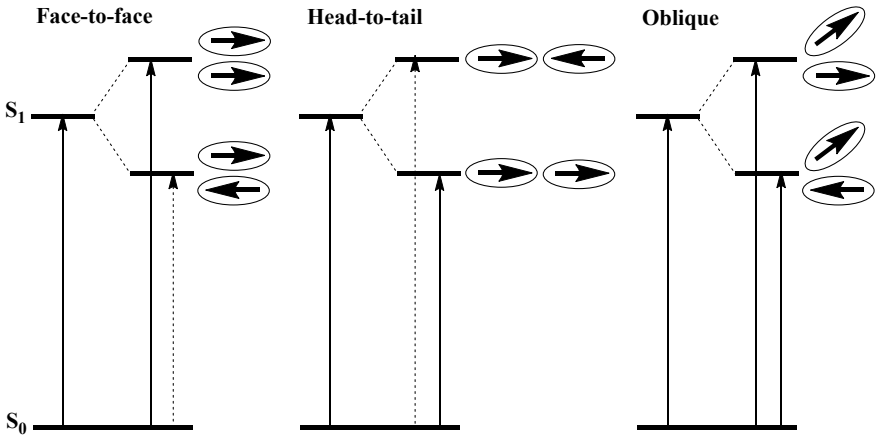

Fig. 3.7 Exciton interactions in various dimeric configurations

some extent for the oblique dimer, but their intensity is dependent on the dihedral angle of the Pc plane. The dimeric configuration can be estimated by analyzing its absorption spectrum based on this principle.

The electronic configuration describing the exciton interaction can be expressed as follows.

$$\Phi_{EX}(\pm) = \left(\varphi_A^*\varphi_B \pm \varphi_A\varphi_B^*\right)/\sqrt{2}, \tag{3.7}$$

where $\varphi_A{}^*$ indicates the A unit in the S_1 (or T_1) state, and the + and − signs indicate the two exciton states.

In the face-to-face dimer, when the distance between constituting units is less than approximately the sum of the van der Waals radii, the low-energy exciton state significantly shifts to the red-side in comparison to the blue-shift of the high-energy exciton state. For instance, the SiPc dimer depicted in Fig. 3.6 exhibits a significant red-shifted fluorescence peak near 940 nm [9]. This large red-shift of over 200 nm cannot be explained only by the exciton interaction. Accordingly, it is explained by the contribution of the charge-transfer interactions in terms of the VB method. The electronic configuration of the charge resonance that reflects the charge transfer interaction can be described as follows.

$$\Phi_{\mathrm{CR}}(\pm) = \left(\varphi_{\mathrm{A}}^{+}\varphi_{\mathrm{B}}^{-} \pm \varphi_{\mathrm{A}}^{-}\varphi_{\mathrm{B}}^{+}\right)/\sqrt{2}, \tag{3.8}$$

where $\varphi_{\mathrm{A}}{}^{+}$ and $\varphi_{\mathrm{A}}{}^{-}$ denote the A units in the cationic and anionic states, respectively. When the distance between the constituting units is short, the exciton and charge resonance configurations can be mixed, the wavefunction of the excited state of the dimer is expressed as

$$\Phi_{\mathrm{DM}}(\pm) = \Phi_{\mathrm{EX}}(\pm) + \Phi_{\mathrm{CR}}(\pm). \tag{3.9}$$

The interaction with the energetically higher charge resonance configuration results in a substantial red-shift of the low-energy exciton state. Such a significant red-shift owing to dimerization is observed not only in the $S_1 \rightarrow S_0$ fluorescence, but also in the $T_1 \rightarrow S_0$ phosphorescence.

The exciton interactions are incredibly essential when the constituting dyes in the dimer have large transition electric dipole moments. In contrast, even when the exciton interaction is negligible, the charge-transfer interactions are applied when the distance between the constituting units is short. In such molecules, the MO method is effective. Here, we describe the MMLCT excited state using Pt(II) diimine complexes as a typical example [8]. When Pt(II) diimine complexes form aggregates or crystalline states with a close contact between Pt(II) ions, the electronic absorption band and luminescence are observed at longer wavelengths (Fig. 3.8). This is explained by the formation of the σ and σ* orbitals due to the interaction between the $d_z{}^2$ orbitals of Pt ions, and the transition from the σ* orbital to the π* orbital of the diimine ligand appears on the lower energy side (longer wavelength side) (Fig. 3.9). This (σ*–π*) is called as MMLCT, which is a crucial photophysical property in molecular crystals consisting of integrated metal complexes.

3.6 Photophysical Properties of Molecular Crystals

As described in Sect. 3.5, there are two methods, i.e., VB and MO methods, for understanding the photophysical properties of dimers or oligomers. The MO method leads to the band theory, wherein the valence and conduction bands are formed as a results of the interactions between the HOMOs of constituents and those between

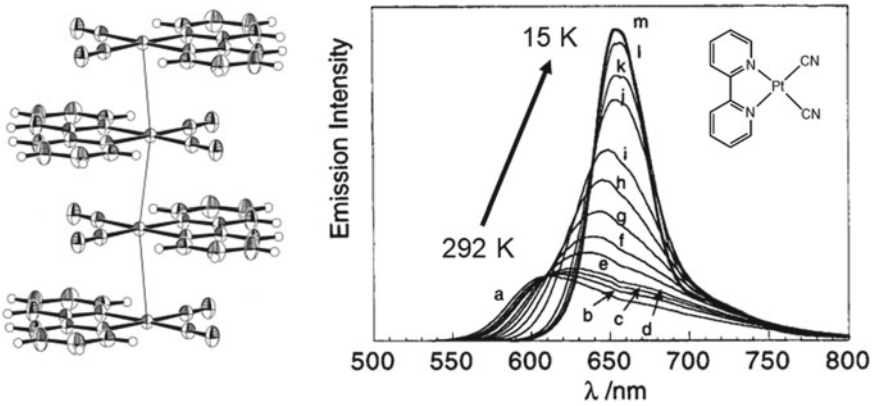

Fig. 3.8 Stacking structure of the red form of [Pt(bpy)$(CN)_2$] and the ^{3}MMLCT emission spectra at different temperatures: **a** 292, **b** 260, **c** 240, **d** 220, **e** 180, **f** 160, **g** 140, **h** 120, **I** 100, **j** 60, **k** 45, **l** 30, **m** 15 K [8]

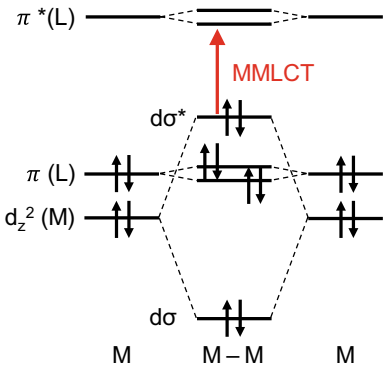

Fig. 3.9 Explanation of the MMLCT transition using the molecular orbital diagram of the dimer model

the LUMOs of constituents, respectively. This approach is useful for discussing the conductivity of crystals but it has a disadvantage of difficulty about the direct comparison of the band theory with the photophysical properties of molecular monomers, which have been accumulated by the spectroscopic measurements of molecules in solution and their theoretical calculations. Thus, for instance, the MMLCT luminescence observed in the molecular crystal of a metal complex is explained by the MO method, using the comparison between the monomer and the dimer. In contrast, the VB method is based on the photophysical properties of molecular monomers and takes into account exciton and charge-transfer interactions as the intermolecular interactions, although it is weak to correctly consider the strong intermolecular interactions. Thus, historically, Davydov splitting, which reflects exciton interaction, had been developed as the first theoretical approaches for explaining the spectral broadening of molecular crystals.

In this section, in order to show the example connecting between the monomer to the molecular crystals, we briefly illustrate the VB method-based analyses on photophysical properties of oxotitanium phthalocyanine (OTiPc) crystals, including both exciton and charge-transfer interactions [10]. OTiPc forms a few crystal structures, i.e., crystal polymorphisms such as phases I, II, and Y (phases I and II are also called β and α phases, respectively). One of them, phase II, has been practically utilized as near-infrared light-active photoconductors in GaAsAl laser printers and photocopiers because their photoconductivities are highly dependent on their crystal structures. Also, in contrast to the sharp Q absorption band in solution, the electronic absorption spectra of OTiPc thin films are significantly broadened and shift to longer wavelength side; the broadening and red-shift are dependent on the crystal structures.

The electronic absorption spectra of OTiPc thin films in phases I and II are shown in Fig. 3.10. In phase I, a broad absorption band between 650 and 800 nm is observed, whereas in phase II, it exceeds 800 nm. The electroabsorption measurements indicated that the charge transfer band was assigned to the 800 nm-region for the thin films in the phases II and Y. In the charge transfer band, the mixture of the exciton and charge-transfer configurations is essential; the absorbance of the charge-transfer band is caused by a contribution of the transition electric dipole-allowed exciton configuration, while the magnitude of the charge-transfer character correlates with the photocurrent and photocharge generation efficiency.

After molecular orbital calculations and configuration interactions for each molecule, the photophysical properties of OTiPc crystals are theoretically calculated by considering the exciton and charge-transfer electron configurations as intermolecular interactions. The theoretical calculations demonstrate that (1) the large red-shift in phase II is caused by the exciton interaction between OTiPc constituents, and (2) the

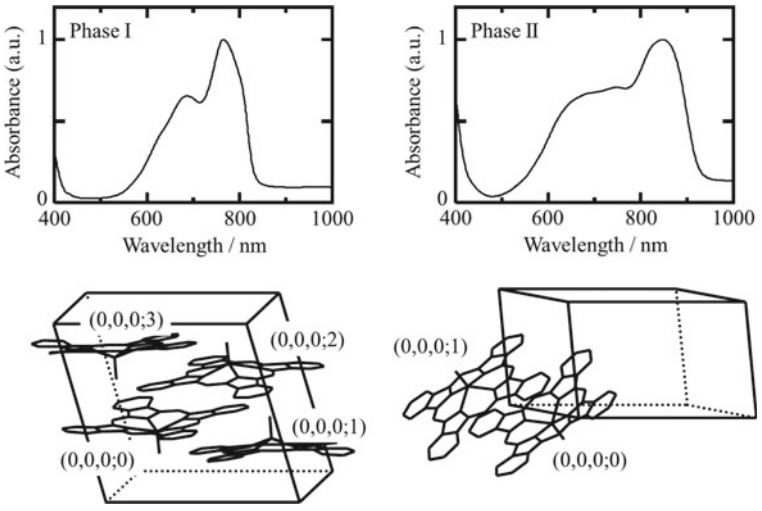

Fig. 3.10 UV-vis absorption spectra of OTiPc crystals in phases I (left) and II (right) and their crystal structures [10]

charge transfer band and the high photoconductivity observed in phase II are highly dependent on the intermolecular resonance integrals, which are well-correlated with the orbital overlaps. In other words, the electronic absorption spectroscopic properties can be tuned by manipulating the excitation energy of constituting molecules and the exciton interactions between constituents. Further, the design of molecular crystals to increase the intermolecular resonance integrals is crucial for achieving high photoconductivity.

References

1. Kato M, Ito H, Hasegawa M, Ishii K (2019) Chem Eur J 25:5105–5112
2. Davydov AS (1964) Sov Phys Usp 7:145–178
3. Turro NJ (1991) Modern molecular photochemistry. University Science Books, New York
4. (a) Ishii K, Kobayashi N (2003) The porphyrin handbook, eds Kadish K, Smith RM, Guilard R, vol 16. Academic Press, San Diego, pp 1–42. (b) Ishii K, Kitagawa Y (2014) Handbook of porphyrin science, vol 32, ed by Kadish K, Smith RM, Guilard R. World Scientific Publishing, Singapore, Chapter 168, pp 173–270. (c) Miwa H, Ishii K, Kobayashi N (2004) Chem Eur J 10:4422–4435
5. (a) Wang M, Ishii K (2022) Photochemical properties of phthalocyanines with transition metal ions. Coord Chem Rev 468:214626. (b) Ishii K, Shiine M, Shimizu Y, Hoshino S, Abe H, Sogawa K, Kobayashi N (2008) J Phys Chem B 112:3138–3143.
6. (a) Ishii K, Yamauchi S, Ohba Y, Iwaizumi M, Uchiyama I, Hirota N, Maruyama K, Osuka A (1994) J Phys Chem 98:9431–9436. (b) Ishii K, Ohba Y, Iwaizumi M, Yamauchi S (1996) J Phys Chem 100:3839–3846. (c) Ishikawa N, Ohno O, Kaizu Y, Kobayashi H (1992) J Phys Chem 96:8832–8839
7. Bilsel O, Rodriguez J, Milam SN, Corlin PA, Girolami GS, Suslick KS, Holten D (1992) J Am Chem Soc 114:6528–6538
8. Kato M (2007) Bull Chem Soc Jpn 80:287–294
9. (a) Ishii K, Sakai N (2010) Phys Chem Chem Phys 12:15354–15357. (b) Oddos-Marcel L, Madeore F, Bock A, Neher D, Ferencz A, Rengel H, Wegner G, Kryschi C, Trommsdorff HP (1996) J Phys Chem 100:11850–11856
10. (a) Nakai K, Ishii K, Kobayashi N, Yonehara H, Pac C (2003) J Phys Chem B 107:9749–9755. (b) Saito T, Sisk W, Kobayashi T, Suzuki S, Iwayanagi T (1993) J Phys Chem 97:8026–8031. MM+

Open Access This chapter is licensed under the terms of the Creative Commons Attribution 4.0 International License (http://creativecommons.org/licenses/by/4.0/), which permits use, sharing, adaptation, distribution and reproduction in any medium or format, as long as you give appropriate credit to the original author(s) and the source, provide a link to the Creative Commons license and indicate if changes were made.

The images or other third party material in this chapter are included in the chapter's Creative Commons license, unless indicated otherwise in a credit line to the material. If material is not included in the chapter's Creative Commons license and your intended use is not permitted by statutory regulation or exceeds the permitted use, you will need to obtain permission directly from the copyright holder.

Part II
Various Soft Crystals Categorized by Stimulus-Response

Chapter 4
Vapochromic Soft Crystals Constructed with Metal Complexes

Masako Kato

Abstract Vapochromism, a phenomenon in which the color or luminescence color of a substance changes in response to gaseous molecules, has potential for developing sensor materials to detect harmful substances in the environment. In addition, vapochromism is scientifically interesting for the direct visualization of interactions between gases and solids. The crystals of metal complexes involve diverse and flexible electronic interactions, such as metal–metal and metal–ligand interactions. It is expected that slight structural changes in such crystals will lead to distinct color or emission color changes, thus achieving highly sensitive and selective vapochromic responses. Consequently, highly ordered and flexible response systems (i.e., soft crystals) can be constructed. This chapter introduces the interesting and attractive features of vapor-responsive soft crystals by discussing platinum complexes that show color and luminescence changes in dilute vapor atmospheres while maintaining an ordered structure, nickel(II) complexes that change magnetic properties in conjunction with a color change, and copper(I) complexes that change luminescence color in response to N-heteroaromatic vapors.

Keywords Vapochromism · Luminescence · Chromic metal complex · Chemical sensor · Vapor-induced structural transformation

4.1 Introduction

We live by responding to various stimuli sensitively, adapting to the environment, and communicating with other people. Biosystems have various wonderful stimuli-responsive functions to be living matters. Various efforts have focused on developing materials that mimic how living systems interact with the environment. In the material world, crystals may look like far from biosystems. However, soft crystals, that show visible and distinct color and luminescence changes in response to weak stimuli while maintaining structural order are attracting increasing attention as new

M. Kato (✉)
Department of Applied Chemistry for Environment, Kwansei Gakuin University, 1 Gakuen Uegahara, Sanda 669-1330, Japan
e-mail: katom@kwansei.ac.jp

© The Author(s) 2023

M. Kato and K. Ishii (eds.), *Soft Crystals*, The Materials Research Society Series,
https://doi.org/10.1007/978-981-99-0260-6_4

stimuli-responsive systems [1]. Various external stimuli, such as heat, light, pressure, chemicals, and mechanical stimuli, can change the structure and properties of crystals, and a wide range of stimuli-responsive materials are known, including metals, polymers, and liquid crystals. Soft crystals are expected to offer new possibilities because their structures and properties can be transformed by mild stimuli while maintaining three-dimensional order, and the original order can also be recovered. This chapter focuses on metal complex crystals that respond to gaseous molecules, such as water vapor, organic vapor, and inorganic gases, by changing their color or emission color.

4.2 Soft Crystals and Vapochromism

Vapochromism involves the color change of a material in response to gas molecules. This phenomenon is relatively new compared with other types of chromism, such as thermochromism, photochromism, and piezochromism. Many systems showing chromism have flexible structures that undergo structural transformations and exhibit multichromic properties in response to various external stimuli. It has long been known that platinum complexes exhibit temperature- and pressure-dependent color changes in the solid state. However, the term vapochromism was not used until the end of the twentieth century to describe double-salt-type platinum(II) complexes that change color when exposed to chloroform or alcohol vapors [2]. Subsequently, various systems have been constructed as volatile organic compound (VOC) sensors to visually detect the vapor of harmful organic solvents [3]. Vapochromism is also of considerable scientific interest as a visible manifestation of the interaction between a gas and a solid. Vapochromic materials are not limited to crystals, with amorphous materials, liquid crystals, and ionic liquids also known to show color changes in response to vapor. However, the highly ordered three-dimensional nature of crystals enables this phenomenon to be traced at the molecular level.

4.3 Interactions Between Vapor Molecules (Gases) and Crystals

The interactions between gases and crystals are commonly exploited in gas storage materials. Palladium is used for hydrogen purification owing to its high hydrogen mobility and excellent hydrogen storage capacity. In this case, stable hydrides form via interactions between small hydrogen molecules and palladium metal crystals. In addition, inorganic porous materials such as zeolites, metal–organic frameworks (MOFs), and porous coordination polymers (PCPs) have been extensively studied. Porous materials have attracted attention as rigid and stable materials with nanospaces. However, some porous materials undergo structural changes as the

framework expands and contracts with gas adsorption and desorption, and the mechanism of structural change in such soft porous crystals has been studied [4]. Materials containing nanospaces, including supramolecular and covalent structures, have been widely developed to have not only gas storage properties but also novel physical properties such as conductivity and magnetism. Furthermore, the nanospaces in such materials have been used to modulate reactivity. Here, we focus on vapor-responsive photofunctional crystals that show distinct visible changes in color or luminescence [5]. Although such vapochromic crystals are found in coordination polymers (so-called flexible MOFs), more flexible systems with electronic interactions, such as supramolecular crystals constructed using weak intermolecular interactions and molecular crystals constructed using van der Waals forces, are the main targets. Vapor can also affect soft matter and thin-film surfaces. For example, it has been reported that vapor exposure can induce a liquid-crystalline-to-crystalline phase transition, and such vapor annealing has attracted attention as a strategy for constructing highly ordered systems [6].

To achieve vapochromism, a gas molecule must induce a change in the electronic state of a crystal that results in a change in color or luminescence. In metal complex crystals, the effects of gas molecules on vapochromism can be classified into three main categories (Fig. 4.1). First and most commonly, a new crystalline phase is formed by the inclusion of gas molecules (Fig. 4.1a). In this case, the color change is caused by a structural change in the complex, and the included gas molecules are involved in stabilizing the new crystal phase, which is similar to a solvate in the crystallization from a solution. If the molecules are released by heating or decompressing, the original structure is recovered. Second, gas molecules are directly coordinated to the metal center (Fig. 4.1b). Here, the mobility of the gas molecules in the crystal is critical for changing the crystalline state. There is an interesting example reported recently for manganese(II)-halide complexes which shows reversible tetrahedral-octahedral geometrical change by water–vapor exposure and heating, followed by the luminescence color change between green and red [7]. Third, the vapor molecules change the crystalline environment (dielectric constant, pressure, etc.), which induces a crystal phase transformation, but are not incorporated into the crystal (Fig. 4.1c). It can be said to be real polymorphism induced by vapor, although those cases are not so many compared with the others [8]. In all cases, the crystal phase transition should be easily induced under mild conditions. In other words, soft crystals with low activation barriers for structural changes and crystal polymorphism should be designed. In the next section, typical vapochromic metal complex crystals are introduced as representative examples of these cases.

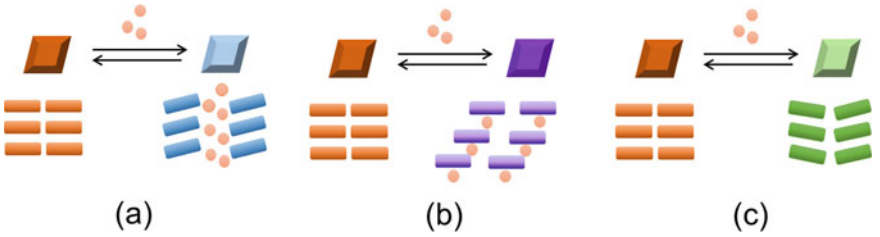

Fig. 4.1 Schematic of the effects of gas molecules on vapochromism

4.4 Vapochromic Metal Complexes

4.4.1 Vapochromism in Integrated Luminescent Platinum(II) Complexes

Commonly, d^8 and d^{10} metal complexes containing soft metal ions show unique coloration and luminescence. In particular, the luminescence properties of planar tetracoordinated platinum(II) complexes have long been studied. The luminescence originates from electronic interactions between stacked platinum(II) complexes. The stacking of platinum(II) complexes with appropriate π-conjugated ligands results in the overlap of platinum ion d_{z^2} orbitals, which split into dσ and dσ* states. Consequently, a metal–metal-to-ligand charge transfer (MMLCT) state is formed, which has the lowest energy transition, and luminescence occurs from the excited triplet state (^{3}MMLCT) (Fig. 4.2) [9]. Because the structure constructed by weak metal–metal interactions is flexible, the MMLCT transition energy is sensitive to small changes caused by external stimuli. Unsurprisingly, MMLCT-derived platinum and gold complexes have recently been reported to have excellent stimuli-responsive properties and remain the subject of active research. Incidentally, aggregation-induced emission (AIE) has attracted much attention in organic crystals and organic polymers [10]. AIE is a phenomenon in which the luminescence of organic molecules is switched on and off using orientation changes caused by hydrogen bonding, π–π interactions, CH–π interactions, etc. Here, the luminescence based on metal–metal interactions caused by the accumulation of complexes is called assembly-induced emission and is considered distinct from aggregation-induced emission.

As a typical vapochromic platinum(II) complex, *syn*-$[Pt_2(pyt)_2(bpy)_2](PF_6)_2$ (pyt = pyridine-2-thiolate, bpy = 2,2′-bipyridine) (Chap. 1, Fig. 1.2), which exhibits reversible on/off luminescence in response to vapor molecules such as ethanol, was introduced in Chap. 1 [11]. In this dinuclear complex, vapochromism is accompanied by a structural transition between a dark-red form with incorporated vapor molecules and a light-red form without vapor molecules. The two stable configurations of this complex (tetranuclear platinum interaction configuration and stacked bpy ligand configuration) are easily converted by vapor molecules, providing a guideline for interaction conversion in soft crystals.

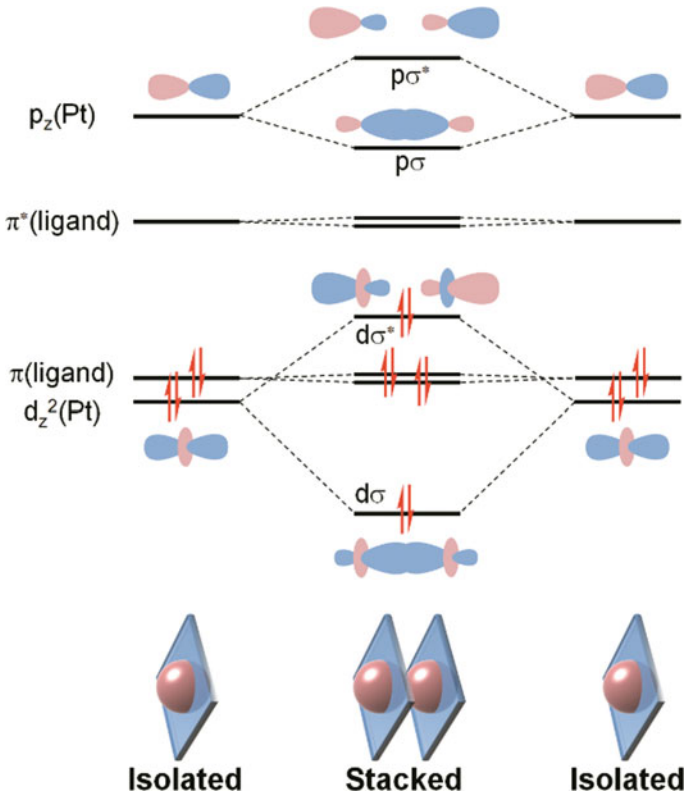

Fig. 4.2 Schematic MO diagram for Pt(II) complexes with aromatic ligands showing effective Pt···Pt electronic interactions by stacking. Reprinted with permission from ref. [9]

Mononuclear platinum(II) complexes with planar structures can self-assemble and form Pt···Pt interactions. Complexes that are colorless when dispersed in dilute solution often show bright colors and luminescence when crystallized via self-assembly. A typical example is the platinum(II) complex [Pt(bpy)$(CN)_2$], which comprises bpy, a typical aromatic bidentate chelate ligand, and cyanide ligands that provide a strong ligand field. Two forms of this complex can be produced by a slight change in the stacking structure (Fig. 4.3): a red hydrated crystal and a yellow anhydrous crystal [12]. Interestingly, this complex shows environmental sensitivity. When the yellow form (monohydrate) is exposed to organic solvents such as DMF or ethanol, it instantaneously changes to the red form (anhydrate), whereas the red form returns to the yellow form upon exposure to water. This change can be controlled using water vapor and is accompanied by a change in the luminescence color, which is typical of vapochromic platinum complexes. The color change has been attributed to changes in the interplatinum interactions, as shown in the stacking structures of the crystals. The correlation between the interplatinum distance and the MMLCT transition energy has been studied in detail based on temperature-dependent data [13], but this is not

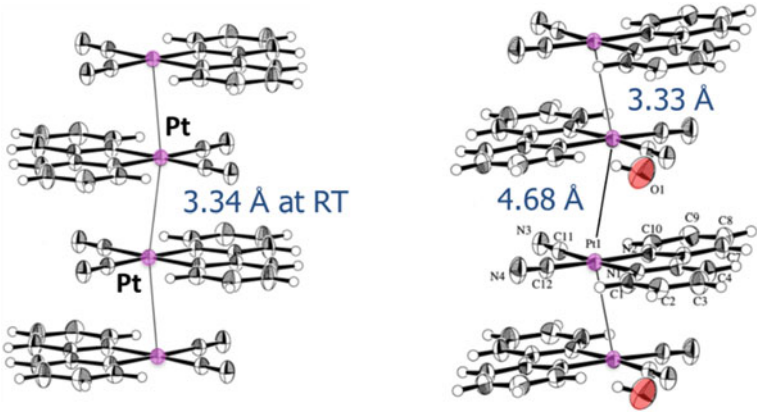

Fig. 4.3 Stacking structures of the red and yellow forms of [Pt(bpy)$(CN)_2$]. Reprinted with permission from ref. [12]

discussed here. Note that the correlation between the interplatinum distance and the excited state energy in the ground state can be explained by the delocalization of the excited state. The theoretical interpretation of the emission state change is given in Chap. 11.

To develop a distinct vapochromic response using platinum interactions, it is effective to construct a soft crystal structure in which vapor molecules can easily form gaps to allow their entry and exit. Based on this strategy, a variety of vapochromic platinum(II) complexes with long-chain alkyl groups or bulky substituents have been reported [3]. In the author's group, a hydrogen-bonded network structure was constructed using a complex with carboxy groups, [Pt$(CN)_2(H_2$dcbpy)] (H_2dcbpy = 4,4′-dicarboxy-2,2′-bipyridine), which produced a variety of colors ranging from white to yellow, red, blue, and purple depending on the vapor type (Fig. 4.4a) [14]. Figure 4.4b shows a schematic of the response of this system to vapor. Vapor molecules incorporated in the crystal pores affect the three-dimensional framework of the platinum complexes, which induces changes in the Pt···Pt interactions and causes the ^{3}MMLCT luminescence color to change. Interestingly, the supramolecular framework is stable enough to retain its structure upon the release of enclosed water molecules and the emission color remains essentially unchanged. However, the framework structure is easily collapsed by macroscopic mechanical abrasion, and the sample shows a distinct color change related to changes in intermolecular interactions. Moreover, the collapsed framework structure can be reconstructed by exposure to methanol vapor, thus restoring the original red luminescent crystals. The process of crystal structure construction by the penetration of gas molecules from the surface was analyzed in detail using super-resolution microscopic luminescence observations of single particles [15]. Thus, this system is notable for exhibiting both

mechanochromism (structural destruction) and vapochromism (structural restoration and self-healing phenomena). Chromic luminescence based on similar metal–metal interactions has also been observed in gold(I) complexes. The vapochromic phenomena of gold(I) complexes are introduced together with their mechanochromic phenomena in the next chapter (Chap. 5).

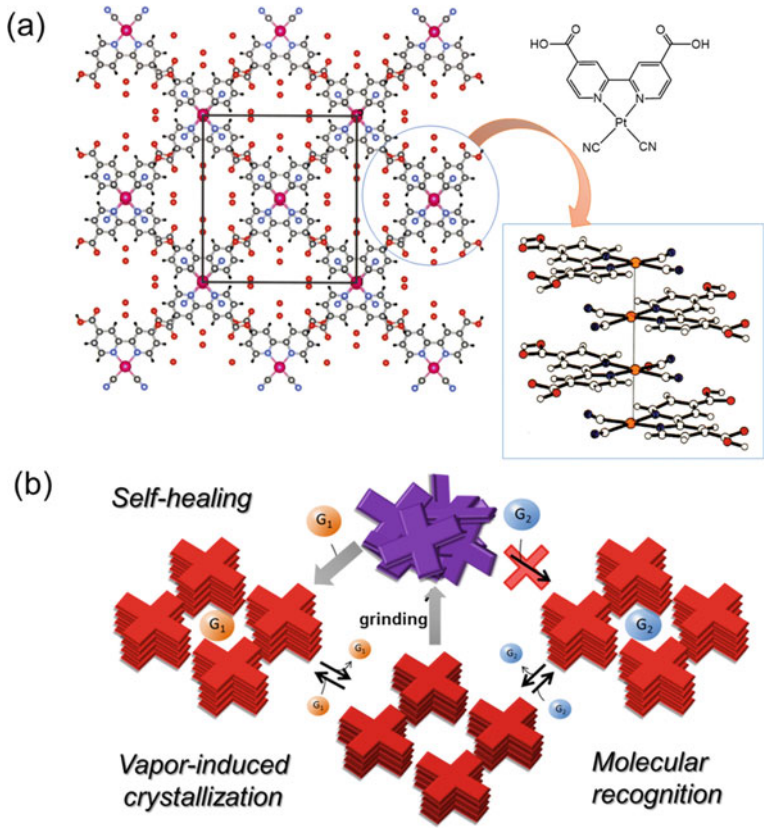

Fig. 4.4 **a** Porous supramolecular structure of $[Pt(CN)_2(H_2dcbpy)]$ crystals, and **b** schematic diagram of vapochromic behavior, including vapor-induced crystallization, self-healing, and molecular recognition, depending on the state. G_1 and G_2 represent guest molecules. Reprinted with permission from refs. [14a, b]

4.4.2 Vapochromism and Single-Crystal-To-Single-Crystal Structural Transitions

As mentioned above, the energy of ^{3}MMLCT luminescent state formed via platinum interactions depends on the strength of the interaction between the metal d_{z^2} orbitals, but the relationship with the energy level of the ligand π* orbital, which is the LUMO, must also be considered. In platinum(II) complexes with ^{3}MMLCT emission, diimine and cyclometalating ligands have been successfully used as aromatic ligands. As shown in Fig. 4.2, the ^{3}MMLCT transition energy based on Pt···Pt interactions is lower in energy than the π–π* (LC) and d–π* (MLCT) transitions of a mononuclear complex. Thus, for conventional systems, ^{3}MMLCT emission generally occurs in the red region. An assembled system with very weak Pt···Pt interactions and an unstable LUMO could realize MMLCT emission at a higher energy. However, the precise control of weak Pt···Pt interactions is difficult in flexible media such as solutions and even in crystals. An integrated system with yellow to green ^{3}MMLCT emission has been reported using platinum complexes with *N*-heterocyclic carbene (NHC) ligands, which make the LUMO level relatively unstable; however, shorter-wavelength blue emission could not be realized. Recently, the author's group found that the emission color can be controlled from red to blue by systematically changing the substituents of the NHC ligands. This realization of strong blue ^{3}MMLCT luminescence breaks with conventional wisdom [16]. Specifically, a series of Pt(II)-NHC complexes, [Pt(CN)$_2$(R-impy)] (R-impyH$^+$ = 1-alkyl-3-(2-pyridyl)-1*H*-imidazolium, R = Me, Et, ^{i}Pr, ^{t}Bu), form similar stacking structures (Fig. 4.5a) with average interplatinum distances varying systematically from 3.2 Å (R = Me) to 3.5 Å (R = ^{t}Bu). All these crystals show high luminescence quantum yields (ϕ = 0.5–0.7), and the monotonic spectral shapes suggest that the emission originates from charge-transfer-type luminescence (Fig. 4.5b). Single-crystal X-ray diffraction measurements revealed that the Pt···Pt distance decreases with decreasing temperature from room temperature (298 K) to 77 K. This trend is similar to that observed in self-assembled platinum complexes and corresponds to the anisotropic shrinkage of the crystal lattice at lower temperatures. Therefore, the Pt···Pt interaction is expected to become stronger at lower temperatures. However, the temperature dependence of the emission spectra was found to depend on the substituent. For all four complexes, the average interplatinum distance (R_{ave}) increases with increasing temperature from 77 to 298 K, whereas the ^{3}MMLCT luminescence energies show different behavior, with decreasing slope of the emission energy against the distance (R_{ave}) from the R = Me complex to the Et and ^{i}Pr complexes, and no emission spectral shift occurs for the R = ^{t}Bu complex (Fig. 4.5c). This important result, which is related to the nature of integrated luminescence, reveals the specific limits of interplatinum interactions. Although the relative energy difference cannot be changed using conventional ligands, changing the substituents of the NHC ligands allows the Pt···Pt interactions to be systematically controlled, and consequently, the luminescence can be modulated.

Interestingly, in such a system with controlled platinum interactions, a vapochromic phenomenon based on a single-crystal-to-single-crystal (SCSC) structural

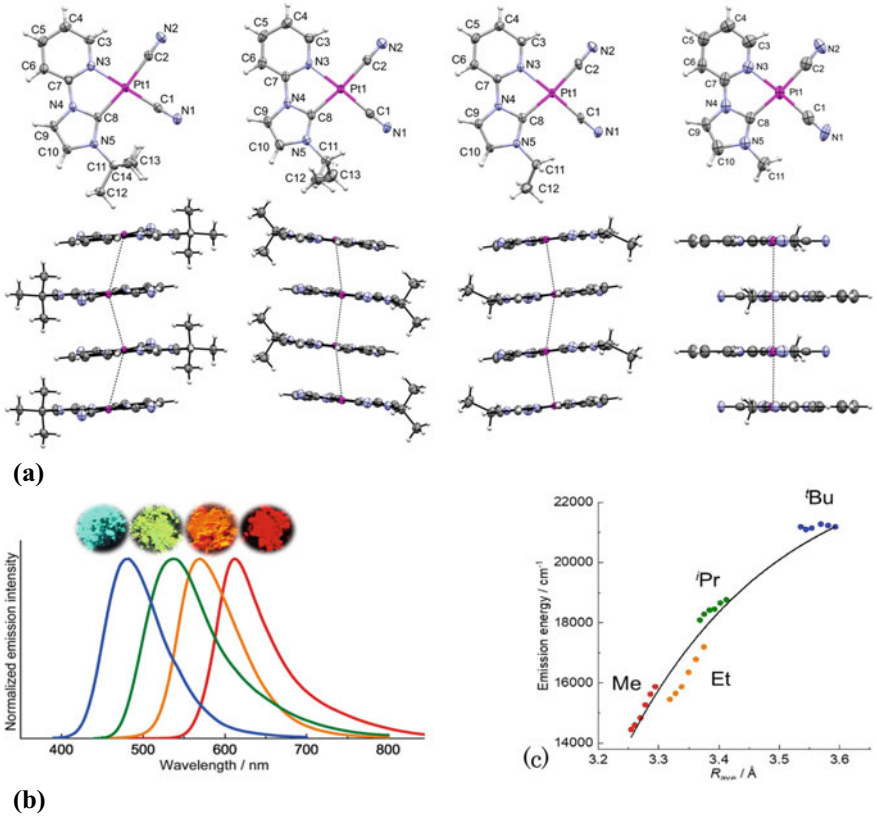

Fig. 4.5 **a** Stacking structures of platinum(II)-NHC complexes, **b** photographs of luminescent crystalline powders and corresponding emission spectra at RT, and **c** correlation between the emission energy and average Pt···Pt distance (R_{ave}). Reprinted with permission from ref. [16]

transformation has been observed [17]. The blue-emitting crystal (R = ^{t}Bu), which is a trihydrate, is stable in a sealed environment but immediately releases water upon exposure to air, and forms a yellowish-green-emitting anhydrous crystals when dried under reduced pressure (Fig. 4.6). Upon exposure to water vapor to the anhydrous form, a dihydrate is formed at saturated water vapor pressure. Through in-situ tracking of single-crystal X-ray diffractions, it was found that an atmospheric pressure environment is necessary to return to the original trihydrate. Notably, all these changes occur while maintaining a single-crystal structure. In the present system, the self-assembled platinum complexes can change flexibly in response to the movement of water molecules by reconstructing hydrogen bonds, which is considered to enable the SCSC structural transformation.

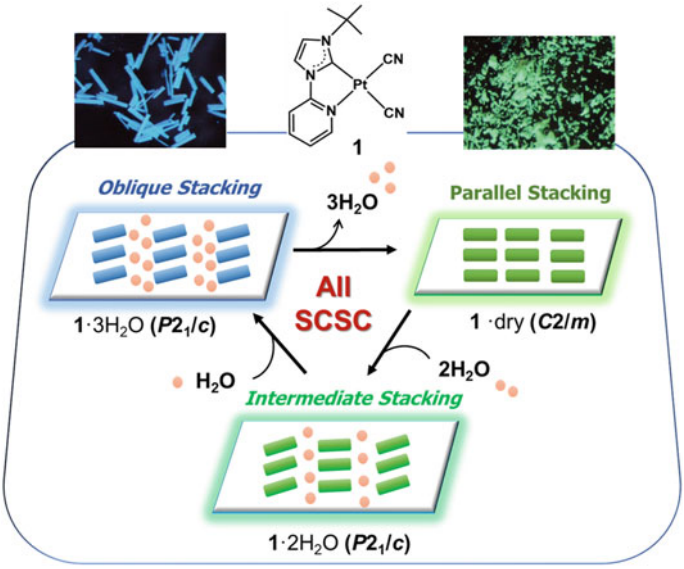

Fig. 4.6 Vapor-induced reversible and stepwise single-crystal-to-single-crystal (SCSC) transformations of [Pt(CN)$_2$(^{t}Bu-impy)] (^{t}Bu-impyH$^+$ = 1-^{t}Bu-3-(2-pyridyl)-1*H*-imidazolium) crystals. Reprinted with permission from ref. [17]

4.4.3 Cooperation Between Vapochromism and Spin-State Changes in a Nickel(II) Complex

Nickel(II)-quinonoid complexes show distinct changes in physical properties in conjunction with vapochromism [18]. Quinonoid compounds have also attracted attention as redox-active ligands, and various noninnocent metal complexes have been constructed in which the electronic states are spread between the ligand and the metal. The nickel(II)-quinonoid complex [Ni(HLMe)$_2$] (H_2LMe = 4-methylamino-6-methyliminio-3-oxocyclohexa-1,4-dien-1-olate) has been found to selectively respond to methanol vapor with a distinct purple to orange color change (Fig. 4.7). This phenomenon is caused by methanol molecules coordinating to nickel ions in the supramolecular crystal structure of the complex, which is an example of the direct coordination of gaseous molecules. The color change is caused by a perturbation of the electronic state of the quinonoid by the coordination of a methanol molecule to the axial position of nickel. Interestingly, the spin state of the nickel ion also changes upon coordination and desorption of the methanol molecule. The low-spin square-planar four-coordinated nickel(II) complex is diamagnetic and purple in color, whereas methanol molecule coordination induces a high-spin state of the nickel(II) ion, resulting in the orange crystal being paramagnetic (Fig. 4.7). Although several examples of the vapor-induced spin-switching of nickel complexes have been previously reported, they were based on ionic liquids or liquid crystals. In

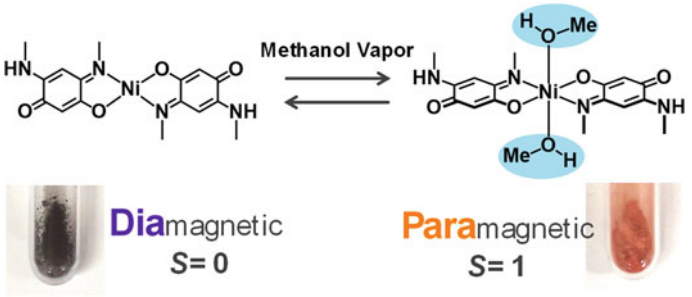

Fig. 4.7 Coordination-induced spin-state switching of a Ni-quinonoid complex by methanol vapor. Reprinted with permission from ref. [18]

the present system, the selective response to methanol was achieved by a structural transformation between crystal states that retain precise arrangements. This system provides a new direction for developing highly ordered, flexible, and multifunctional vapochromic complexes.

4.4.4 Strongly Luminescent Copper(I) Complexes

Most strongly luminescent metal complexes contain noble metals such as platinum, iridium, gold, and europium, or rare earths. The development of highly luminescent complexes using copper, which is an abundant and inexpensive element, is of great interest from both academic and elements strategy points of view. Luminescent copper(I) complexes have long been known to show temperature-dependent luminescence color changes, and recently, strongly luminescent copper(I) complex crystals that exhibit vapor responsivity have been constructed [19]. For example, a mononuclear copper(I) complex with a phosphine ligand and an *N*-heteroaromatic compound, $[CuI(PPh_3)_2L]$ (L = *N*-heteroaromatic compound), is strongly luminescent and can be easily synthesized by simply mixing and grinding. Moreover, the ligand can be changed by exposure to the vapor of various *N*-heteroaromatic compounds. This ligand-substitution behavior is accompanied by a change in the luminescence color change (Fig. 4.8) [20]. This phenomenon is attributed to the direct exchange of coordinated vapor molecules, which is unique to these ligand-substituted copper(I) complexes.

Fig. 4.8 Reversible luminescence color changes of $[CuCl(PPh_3)_2(L)]$ based on ligand exchange reactions with *N*-heteroaromatic vapors. Reprinted with permission from ref. [20]

4.5 Conclusion

Recently, vapochromic phenomena have been reported in not only complex crystals but also organic crystals and liquid crystals [3e]. Thus, it may be possible that any soft crystal or soft material with color and luminescence properties can exhibit vapochromism. However, to verify this suggestion, research on this phenomenon must advance from the stage of serendipitous discoveries and observations. Soft crystals are advantageous because they enable the precise elucidation of three-dimensional structures, including dynamic structural changes, at the molecular level. In addition, they exhibit visually perceptible changes in properties such as color and luminescence, which can be precisely evaluated spectroscopically. Thus, the information about small molecule–solid-state interactions obtained through soft crystal studies may provide useful molecular insights into more complex systems, for example, into the interactions and mechanisms of enzyme–protein–substrate systems.

From the viewpoint of function, various advances can be expected for vapor-responsive crystalline materials. High selectivity and high sensitivity are important issues for humidity and VOC sensors. Vapor-selective vapochromism as well as high-sensitivity and fast-response vapochromism have been achieved via the skillful molecular design of MOFs and supramolecules [21]. However, further development is needed to realize high-precision devices utilizing the characteristics of crystalline materials. Multifunctional vapochromic materials, in which other physical properties change simultaneously with color or luminescence changes are also attracting attention. The aforementioned nickel complex is a good example of such a system, in which concurrent changes in color and spin state are induced by methanol vapor. As a stimuli-responsive material that can undergo stable spin state changes in a wide temperature range, this complex is expected to be applicable to memory functions. Vapochromism is a visible manifestation of the interaction between a gas and a

solid, which is of broad interest. A multifaceted approach based on the observation of bulk changes combined with the tracking of microscopic and dynamic behavior can advance the understanding of these complex phenomena. Such insights are expected to lead to the development of novel materials with outstanding functions.

References

1. Kato M, Ito H, Hasegawa M, Ishii K (2019) Chem Eur J 25:5105–5112
2. C. C. Nagle, U. S. Patent No. 4826774, **1989**
3. (a) Kato M (2007) Bull Chem Soc Jpn (Accounts) 80:287; (b) Wenger OS (2013) Chem Rev 113:3686; (c) Zhang X, Li B, Chen Z-H, Chen Z-N (2012) J Mat Chem 22:11427; (d) Kobayashi A, Kato M (2014) Eur J Inorg Chem 4469; (e) Li E, Jie K, Liu M, Sheng X, Zhua W, Huang F (2020) Chem Soc Rev 49:1517
4. Horike S, Shimomura S, Kitagawa S (2009) Nat Chem 1:695–704
5. Kato M, Yoshida M, Sun Y, Kobayashi A (2022) J Photochem Photobio C 51:100477
6. (a) Sinturel C, Vayer M, Morris M, Hillmyer MA (2013) Macromolecules 46:5399–5415; (b) Higashi T, Ohmori M, Ramananarivo MF, Fujii A, Ozaki M (2015) APL Mater 3:126107
7. Jiang C, Luo Q, Luo C, Lin H, Peng H (2022) J Phys: Condens Matter 34:154001
8. Yuan M-S, Wang D-E, Xue P, Wang W, Wang J-C, Tu Q, Liu Z, Liu Y, Zhang Y, Wang J (2014) Chem Mater 26:2467
9. Yoshida M, Kato M (2018) Coord Chem Rev 355:101–115
10. Hong Y, Lam JW, Tang BZ (2011) Chem Soc Rev 40:5361–5388
11. (a) Kato M, Omura A, Toshikawa A, Kishi S, Sugimoto Y (2002) Angew Chem, Int Ed 41:3183; (b) Ohba T, Kobayashi A, Chang H-C, Kato M (2013) Dalton Trans 42:5514
12. Kishi S, Kato M (2002) Mol Cryst Liq Cryst 379:303–308
13. Kato M, Kosuge C, Morii K, Ahn JS, Kitagawa H, Mitani T, Matsushita M, Kato T, Yano S, Kimura M (1999) Inorg Chem 38:1638–1641
14. (a) Kato M, Kishi S, Wakamatsu Y, Sugi Y, Osamura Y, Koshiyama T, Hasegawa M (2005) Chem Lett 34:1368–1369; (b) Shigeta Y, Kobayashi A, Ohba T, Yoshida M, Matsumoto T, Chang H-C, Kato M (2016) Chem Eur J 22:2682–2690
15. Ishii K, Takanohashi S, Karasawa M, Enomoto K, Shigeta Y, Kato M (2021) J Phys Chem C 125:21055
16. Saito D, Ogawa T, Yoshida M, Takayama J, Hiura S, Murayama A, Kobayashi A, Kato M (2020) Angew Chem Int Ed 59:18723
17. Saito D, Galica T, Nishibori E, Yoshida M, Kobayashi A, Kato M (2022) Chem Eur J 28:e202200703
18. Kar P, Yoshida M, Shigeta Y, Usui A, Kobayashi A, Minamidate T, Matsunaga N, Kato M (2017) Angew Chem Int Ed 56:2345
19. Kobayashi A, Kato M (2017) Chem Lett 46:154
20. Ohara H, Ogawa T, Yoshida M, Kobayashi A, Kato M (2017) Dalton Trans 46:3755–3760
21. (a) Bryant MJ, et al (2017) Nat Commun 8:1800; (b) Li Y, Chen L, Ai Y, I-long EY, Chan AK, Yam VW (2017) J Am Chem Soc 139:13858–13866

Open Access This chapter is licensed under the terms of the Creative Commons Attribution 4.0 International License (http://creativecommons.org/licenses/by/4.0/), which permits use, sharing, adaptation, distribution and reproduction in any medium or format, as long as you give appropriate credit to the original author(s) and the source, provide a link to the Creative Commons license and indicate if changes were made.

The images or other third party material in this chapter are included in the chapter's Creative Commons license, unless indicated otherwise in a credit line to the material. If material is not included in the chapter's Creative Commons license and your intended use is not permitted by statutory regulation or exceeds the permitted use, you will need to obtain permission directly from the copyright holder.

Chapter 5
Luminescent Mechanochromism and the Photosalient Effect of Aryl Gold(I) Isocyanide Complexes

Tomohiro Seki and Hajime Ito

Abstract A study of stimuli-responsive molecules that can change their physical properties or external shape owing to variations in the external environment has attracted much attention owing to potential application in sensors and actuators. Our group has intensively studied aryl gold(I) isocyanide complexes to develop stimuli-responsive molecular crystals that can show luminescent mechanochromism and crystal jumping through phase transitions induced by mechanical stimulation or photoirradiation. Interestingly, some of our gold(I) isocyanide complexes have crystalline or even single crystalline characteristic both before and after mechano-induced emission color changes or photoinduced crystal jump. Based on the detailed information on molecular arrangements of the aryl gold(I) isocyanide complexes, the underlying mechanism of the responses can be clearly identified. In the Sect. 5.2 of this chapter, we review luminescent mechanochromic aryl gold(I) isocyanide complexes that has unique characteristic such as multiple emission colors, infrared emission, and noncentrosymmetry/centrosymmetry switching. Section 5.3 describes the mechano-induced single-crystal-to-single-crystal phase transitions of aryl gold(I) isocyanide complexes with red- and blue-shifted emission color changes or reversibility. In Sect. 5.4, the photoinduced phase transition of a gold(I) complex which accompanied by mechanical motion, i.e., crystal jump is described.

Keywords Luminescent mechanochromism · Photosalient effect · Gold(I) isocyanide complex · Photoluminescence · Phase transition

T. Seki
Department of Chemistry, Shizuoka University, 836 Ohya, Shizuoka 422-8529, Japan
e-mail: seki.tomohiro@shizuoka.ac.jp

H. Ito (✉)
Institute for Chemical Reaction Design and Discovery, Division of Applied Chemistry, Hokkaido University, Sapporo 060-8628, Japan
e-mail: hajito@eng.hokudai.ac.jp

© The Author(s) 2023

M. Kato and K. Ishii (eds.), *Soft Crystals*, The Materials Research Society Series,
https://doi.org/10.1007/978-981-99-0260-6_5

5.1 Introduction

Molecules that change their physical properties or external shape owing to variations in the external environment are collectively called stimuli-responsive molecules. For example, azobenzene [1–3] and diarylethene [4, 5] exhibit photochromism when irradiated with ultraviolet light, which results in a change in the color of the solution or crystal. This color change is attributed to the photoisomerization of the molecule caused by light irradiation, which changes the molecular structure, especially the π-conjugation length. However, when photoisomerization occurs in these molecules in crystals or polymers, changes in the morphology, such as bending of crystals or polymers, may be observed in addition to changes in the molecular structure. This phenomenon is called the photomechanical effect because it involves the conversion of light energy into mechanical motion [6, 7]. Molecules that exhibit this effect, when viewed as bulk materials, have a simple structure consisting of a single type of molecule or its dispersion in a polymer. Since these molecules have the ability to "move," they have great potential to serve as microscopic actuators. This is in contrast to conventional actuators, which are made up of multiple elements such as gears and motors, and have miniaturization limitations.

Recently, luminescent mechanochromic molecules, one type of stimuli-responsive molecule, have been extensively studied [8–12]. Luminescent mechanochromism refers to a phenomenon in which the photoluminescence properties of solid and liquid crystalline materials are altered by the application of mechanical stimuli, such as rubbing or crushing. The mechanism that causes the luminescence color to change is often attributed to molecular rearrangement in the material. Mechanochromism occurs when the pattern of intermolecular interactions is altered and the excitation energy level varies as the molecular arrangement changes. In the case of this phenomenon, it is noteworthy that macroscopic mechanical stimuli exerted by human intervention can alter the microscopic molecular arrangement and intermolecular interactions, which are essential to the luminescence properties of a material. Although this type of luminescent mechanochromism has been intermittently reported since 1990 (e.g., in molecules **1** [13] shown in Fig. 5.1), it did not attract much attention at the time. In contrast, from 2000 to 2010, the luminescence property and color changes induced by mechanical stimulation in several molecules resulted in an increased interest in this phenomenon. Crystalline solid samples of a gold complex **2** reported by Eisenberg et al. showed a change in luminescence intensity in response to a mechanical stimulus [14]. In 2007, Sagara, Araki et al. reported the luminescent mechanochromism of pyrene derivatives **3** [15]. In 2008, the mechanochromism of a gold(I) isocyanide complex **4** was reported [16]. The mechano-induced color change of **4** from blue to yellow and the reversibility by solvent addition was reported [16]. In the same year, Weder et al. reported the luminescence color change of an organic dye molecule **5** [17]. A visible red shift was observed by grinding the powdered form of the dye **5** using a mortar and pestle or by clasping and compressing it into infrared (IR) pellets. Moreover, in 2010, Fraser reported the mechanochromism of a boron complex **6** [18]. The luminescence color

was also reported to be altered by mechanical stimulation, and further changes in color were observed over time. These mechanochromic molecules shown in Fig. 5.1 are only a few examples, and many others have been reported up to 2010 [19–25]. These molecules have no clear similarity in terms of molecular structures. Thus, it is widely recognized that luminescent mechanochromism can be found in solid materials composed of organic molecules and metal complexes. Consequently, since 2010, many researchers have reported the luminescent mechanochromism of several organic molecules, metal complexes, and polymers.

With the increased number of investigations, many characteristic mechanochromic molecules have been reported. Mechanochromic molecules with multicolor luminescence (Fig. 5.2a) [26–30], those that can be coated onto glass or polymer surfaces to impart mechanochromic properties (Fig. 5.2b) [31], and those that exhibit altered luminescence owing to crystal-to-liquid–crystal phase transitions induced by mechanical stimuli (Fig. 5.2c) [27, 32] were reported. The spontaneous recovery or transition of mechanochromic molecules to a new phase after a change in luminescence color upon mechanical stimulation has also been reported (Fig. 5.2d) [33–37]. Moreover, the successful control of the direction of the luminescence shift was achieved by an extensive screening of the substituents of mechanochromic molecules (Fig. 5.2e) [38]. Additionally, a novel material was developed that exhibits luminescent mechanochromism in a specific temperature

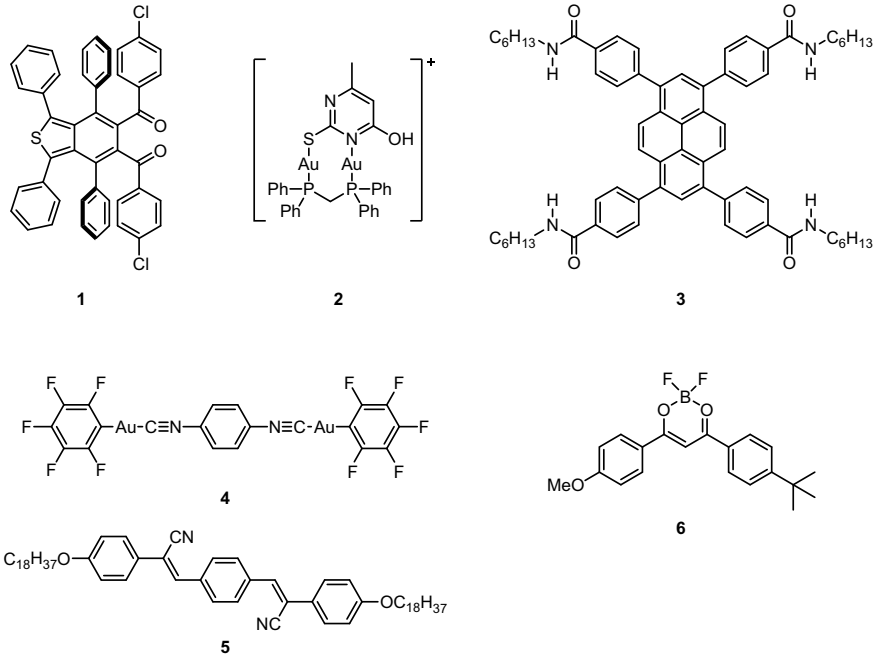

Fig. 5.1 Structures of pioneering mechanochromic molecules

range (Fig. 5.2f) [33, 39, 40], and a mechanochromic material was fabricated that utilizes the reversibility of rotaxane to realize instantaneous, reversible, and repeatable chromic properties in response to the application of mechanical stress (Fig. 5.2g) [41, 42]. Furthermore, elastochromic luminescent materials, in which the luminescence change is induced by stress-responsive crystal deformation, have been reported recently (Fig. 5.2h) [43–45].

Our group has extensively investigated luminescent mechanochromism and the related stimuli-responsivity of the gold complexes. It is noteworthy that anisotropic mechanical stimuli on a macroscopic scale to mechanochromic molecules can induce changes in the molecular arrangements on a microscopic scale. The phenomenon of luminescent mechanochromism has also clearly showed that such microscopic molecular arrangements play a significant role in the bulk properties and functions. Therefore, we have considered that inducing perturbations in the molecular coordination and arrangement of a material by applying external stimuli, including mechanical force and other stimuli, can cause the generation of luminescent mechanochromism, and impart various functions and response properties to the material. Accordingly, we have prepared a number of aryl gold(I) isocyanide complexes, analogues of **4**. As a result, a number of aryl gold(I) isocyanide complexes with mechanochromism have been developed, many of which exhibited attractive features. Moreover, gold(I) complexes that exhibit external stimuli responsiveness, that is, phase transitions in response to changes in light or temperature has been successfully developed. The phase transition is also accompanied by a mechanical response, i.e., crystal jump, and the relationship between the behaviors of molecular arrangement changes and mechanical properties has also been elucidated.

In this chapter, we review the aryl gold(I) isocyanide complexes that have been developed thus far. These gold(I) complexes can extend the π-conjugated system and incorporating various substituents to the aromatic rings covalently connected with gold(I) atom and the aromatic rings of the ligand moiety. A slight difference in the molecular structure of the aromatic moiety of these gold(I) complexes can alter the crystal structure and response properties of a material in various ways, and thereby many luminescent mechanochromism and mechanical responses have been successfully developed. In Sect. 5.2, the luminescent mechanochromism of gold(I) isocyanide complexes is discussed. In particular, a series of complexes that exhibit luminescent mechanochromism with unique characteristic that general mechanochromic molecules does not have is described. In Sect. 5.3, the series of the mechanically stimulated single crystal-to-single crystal (SCSC) phase transition is discussed. The origin of the luminescence change is successfully elucidated based on the detailed crystal structure information. We achieved the control of the direction of the shift of the luminescence change through the trend of the aurophilic interaction change. We also achieved to bestow the nature of the reversibility. In Sect. 5.4, the crystal phase transition of the gold(I) complexes induced by light irradiation is discussed in detail, especially their response mechanism. Additionally, the mechanical response of the crystal and jumps (that is, the photosalient effect) that are triggered by the phase transition is described.

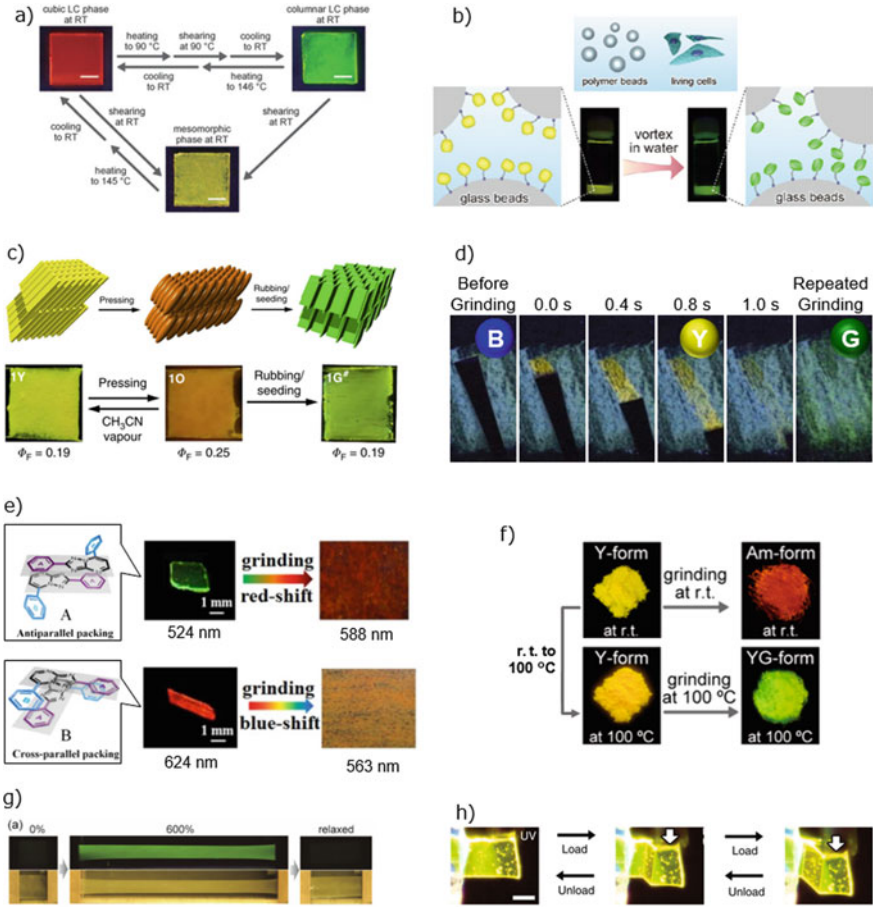

Fig. 5.2 Photographs and schematic representations of selected mechanochromic molecules which exhibited unique characteristics. Part a is adapted with permission from ref. [26] Copyright 2011 Wiley-VCH, All Rights Reserved. Part b is adapted with permission from ref. [31] Copyright 2014 American Chemical Society, All Rights Reserved. Part c is adapted with permission from ref. [27] Copyright 2014 Springer Nature Limited, All Rights Reserved. Part d is adapted with permission from ref. [36] Copyright 2016 American Chemical Society, All Rights Reserved. Part e is adapted with permission from ref. [38] Copyright 2016 American Chemical Society, All Rights Reserved. Part f is adapted with permission from ref. [39] Copyright 2017 American Chemical Society, All Rights Reserved. Part g is adapted with permission from ref. [41] Copyright 2018 Springer Nature Limited, All Rights Reserved. Part h is adapted with permission from ref. [45] Copyright 2020 Springer Nature Limited, All Rights Reserved

5.2 Luminescent Mechanochromism of Gold(I) Isocyanide Complexes

5.2.1 Luminescent Mechanochromism of Complex 4 and Its Subsequent Development

During the course of our investigations on catalytic reactions, the luminescent mechanochromism of gold(I) isocyanide complex **4** (Fig. 5.1 and 5.3) was accidentally discovered, which was reported in 2008 [16]. Pristine sample of complex **4** was a white powder and showed weak blue luminescence when irradiated with ultraviolet (UV) light (Fig. 5.3a). When a mechanical stimulus was applied to the complex, the emission of the powder changed to yellow and the maximum emission wavelength ($\lambda_{em,max}$) shifted from 415 to 533 nm (Fig. 5.3c). The single-crystal and powder X-ray diffraction structural analyses revealed that the mechanical stimulation caused a phase transition from the crystalline phase to the amorphous phase. This transformation in the crystal structure is thought to have induced a modification in the pattern of intermolecular interactions exerted on the molecules in the crystal, thereby resulting in a change in luminescence. The luminescence of gold(I) complexes has been reported to shift to longer wavelengths owing to the formation of aurophilic interactions [11, 46–52]. Therefore, the luminescence of complex **4** was also expected to be shifted by the formation of aurophilic interactions in the amorphous phase [16]. However, no definitive experimental data on the formation of aurophilic interactions have been reported thus far.

Complex **4** was the first luminescent mechanochromic molecule reported by our research group. Isocyanide is a relatively soft ligand with a C≡N–R structure and a lone pair of electrons at the terminal carbon. Furthermore, isocyanide is known to form end-on type stable coordination complexes with various transition metals [53–55]. Isocyanides have a particularly high affinity for gold(I) atoms. Consequently,

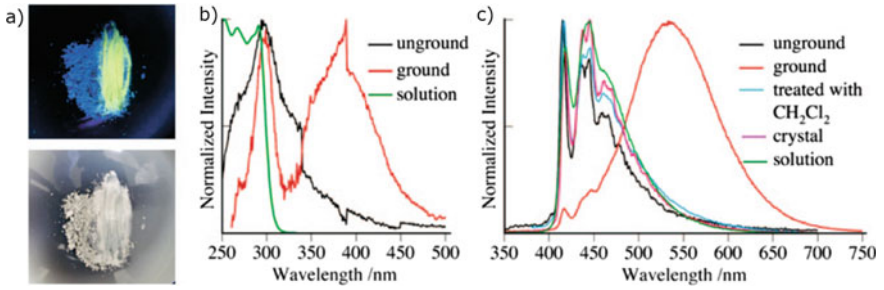

Fig. 5.3 **a** Photographs (taken under UV illumination) and emission spectra of the solids of **4** before and after applying mechanical stimulation. **b** absorption/excitation and **c** emission spectra of **4** at various conditions. Adapted with permission from ref. [16] Copyright 2008 American Chemical Society, All Rights Reserved

a variety of gold(I) isocyanide complexes have been synthesized and their physical properties have been investigated in detail [56–62]. Most of these gold(I) complexes form two-coordinate linear complexes. Although halogen [56], alkynyl [57–60], and cyano groups [61] have been extensively investigated as substituents on the gold(I) atom in these gold(I) isocyanide complexes, only a few examples of complexes with aryl groups as substituents on the gold(I) atom of these complexes have been reported thus far [62]. Therefore, we synthesized analogues of aryl gold(I) isocyanide complexes and successfully produced various unique mechanochromic properties, which will be discussed in the subsequent sections.

5.2.2 Mechanochromic Gold(I) Complexes with Tetrachromatic Luminescence

The solid sample of the diisocyanide-bridged tetrafluoropyridyl gold(I) complex **7** reversibly switches between four different color luminescences upon solvent addition and mechanical stimulation [29] (Fig. 5.4). The pristine solid sample of complex **7Y** shows yellow luminescence. When **7Y** was suspended in acetone, the blue luminescent phase **7B** was obtained. Subsequently, the evaporation of acetone resulted in the transformation of **7B** into the green luminescent phase **7G**. When a mechanical stimulus was applied to **7G**, the yellow luminescent **7Y** was regenerated, and the application of further force resulted in its transformation to the luminescent orange powder **7O**. Notably, the changes in complex **7** were found to be reversible.

Complexes **7B**, **7G**, and **7Y** form different crystal structures, whereas **7O** was found to be amorphous. The single crystal corresponding to **7B** was obtained by recrystallization in the presence of acetone. The single crystal of **7G** was obtained by the slowest possible phase transition from **7B** by removing the crystallizing solvent. As for complex **7Y**, it was difficult to prepare a single crystal of this complex. Therefore, the crystal structure was elucidated from powder diffraction data and Rietveld refinement. Complex **7Y** is the first example of a successful ab initio structural analysis of the ground phase of mechanochromic compounds. The crystal structures of **7B**, **7G**, and **7Y** are shown in Fig. 5.5a. In complex **7B**, the intermolecular interactions between the molecules are weakened by the position of acetone (two equivalents per **7**) between the molecules. In contrast, in complex **7G**, the amount of solvent inclusion (acetone or water) is sufficiently small (assuming acetone, 0.5 equivalents per **7**) compared with complex **7B**, which allows for stronger interactions between the complex molecules (Fig. 5.5b). However, the distances between the gold(I) atoms of **7B** and **7G** are 3.5452(7) Å and 3.571(2) Å, respectively, which suggests that these complexes do not form aurophilic interactions. Conversely, there is no solvent inclusion in the complex **7Y** crystals. The interatomic distance between gold(I) atoms is 3.428(2) Å, which confirms the formation of aurophilic interactions (Fig. 5.5c). This is thought to be the reason for the occurrence of the spectral band in the longer

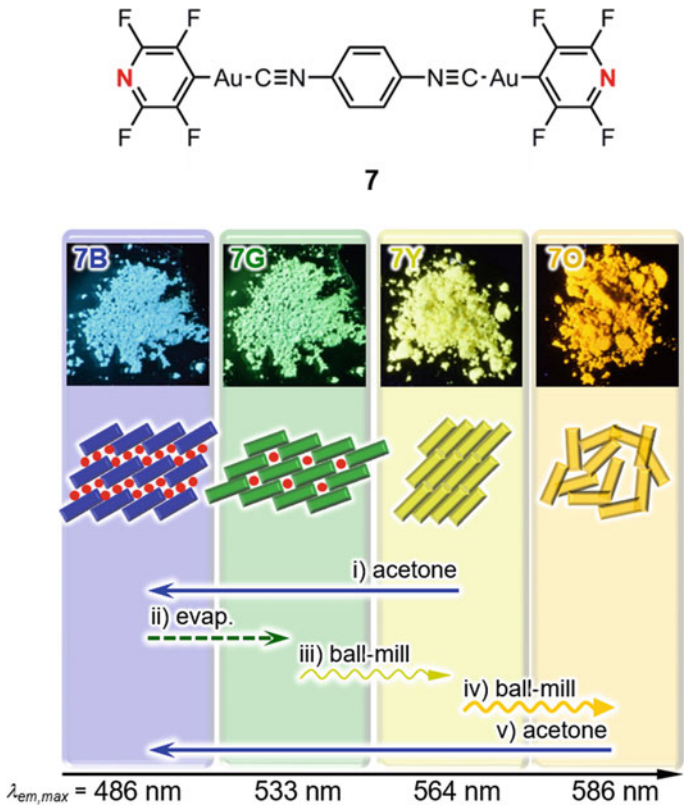

Fig. 5.4 Molecular structure of complex **7**, photographs of the luminescent powders, and a schematic of the solid structures of each luminescent phase (indicated by rectangles and red circles for the inclusion of the solvent, acetone) and the experimental operations used to switch between luminescent phases. Adapted with permission from ref. [29] Copyright 2015 Royal Society of Chemistry, All Rights Reserved

wavelength region compared with those of **7B** and **7G**. Complex **7O** was identified as amorphous because no clear peaks were observed by powder X-ray diffraction.

5.2.3 Screening of 48 Complex Species for Mechanochromic Properties

A series of complexes with various substituents were systematically synthesized with the aim of controlling the emission wavelength of mechanochromic gold(I) isocyanide complexes. A total of 48 **R^1–R^2** complexes were synthesized by introducing various substituents into the para positions of the two benzene rings, R^1 and R^2, using phenyl gold(I) phenyl isocyanide complex as the scaffold (Fig. 5.6).

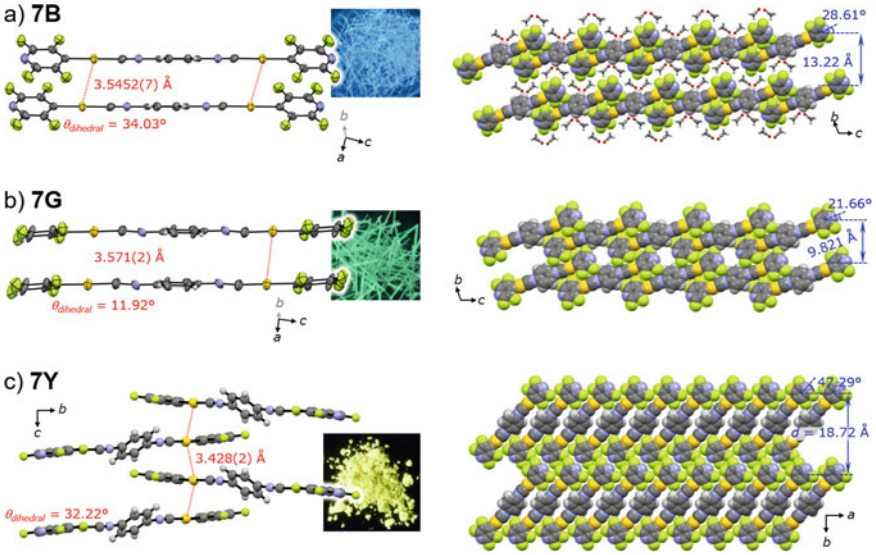

Fig. 5.5 Crystal structures of **a 7B**, **b 7G**, and **c 7Y** and corresponding single crystals photographed under UV irradiation. Adapted with permission from ref. [29] Copyright 2015 Royal Society of Chemistry, All Rights Reserved

Photographs of the powdered forms of the 48 $\mathbf{R^1–R^2}$ complex species were taken under UV light irradiation, as shown in Fig. 5.6. Each panel corresponds to an $\mathbf{R^1–R^2}$ complex with a specific R^1 substituent (vertical column) and R^2 substituent (horizontal column). The substituents are arranged in order, from top to bottom and left to right, from electron-donating to electron-withdrawing groups, respectively. The pictures (taken under UV light) on the left and right of each panel correspond to the powders before and after the application of a mechanical stimulus, respectively.

After synthesizing the 48 $\mathbf{R^1–R^2}$ complexes, the $\mathbf{CF_3–CN}$ complexes were found to exhibit mechanochromism based on the crystal-to-crystal phase transition using the "screening approach" [63]. By controlling the crystallization conditions, different single crystals were successfully obtained before and after the application of a mechanical stimulus. Consequently, a clear decrease in the interatomic distance between gold(I) atoms was observed from 3.706 to 3.119 Å, which was found to be the cause of the luminescence change (Fig. 5.7). The crystal-to-crystal phase transition is relatively rare, since less than 10% of all mechanochromic molecules exhibit this phenomenon. In terms of the color of the luminescence of the $\mathbf{R^1–R^2}$ complexes, it is found that the wavelength of luminescence color became longer as the electron-withdrawing property of the R^2-position increased (from left to right in Fig. 5.6), and the luminescence color was observed to be yellow or orange instead of blue or green. Figure 5.6 shows various patterns of emission color change, and we propose that this information contained in Fig. 5.6 can serve as a library of mechanochromic molecules that can select a desired emission color change. Recently, Wu et al. reported

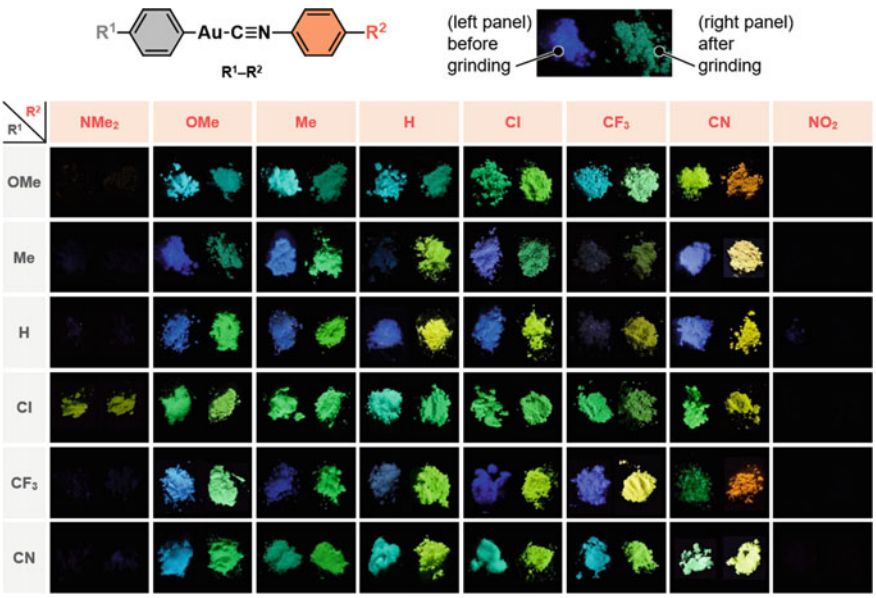

Fig. 5.6 Structure of R^1-R^2. Photographs (under UV light) of R^1-R^2 complexes before (left) and after (right) grinding. Adapted with permission from ref. [63] Copyright 2016 American Chemical Society, All Rights Reserved

the systematic synthesis of a variety of mechanochromic molecules by applying the C-H activation reaction to realize various luminescent colors [38].

5.2.4 Infrared Luminescent Mechanochromic Gold(I) Complexes

Extension of the π-conjugated system: Subsequently, we attempted to extend the π-conjugated system to develop a new mechanochromic molecule that emits light at longer wavelengths. The molecular structure depicted in the upper left of Fig. 5.8 corresponds to the **H–H** complex, as shown in the Fig. 5.6, which will be called "complex **8**" hereafter. A new complex **9** was then synthesized, in which the phenyl group that binds to the gold(I) atom was extended to a naphthyl group. The emission spectrum of **9a** exhibited three peaks and the $\lambda_{em,max}$ was observed at 523 nm (Fig. 5.8). **9b** was obtained by grinding **9a**. Orange-emitting **9b** had a broad emission spectrum and the $\lambda_{em,max}$ was observed at 599 nm. This wavelength is longer than that of the **Me-CN** complex (592 nm), which exhibited the longest $\lambda_{em,max}$ among the 48 **R^1-R^2** complexes. These results indicate that the extension of the aromatic

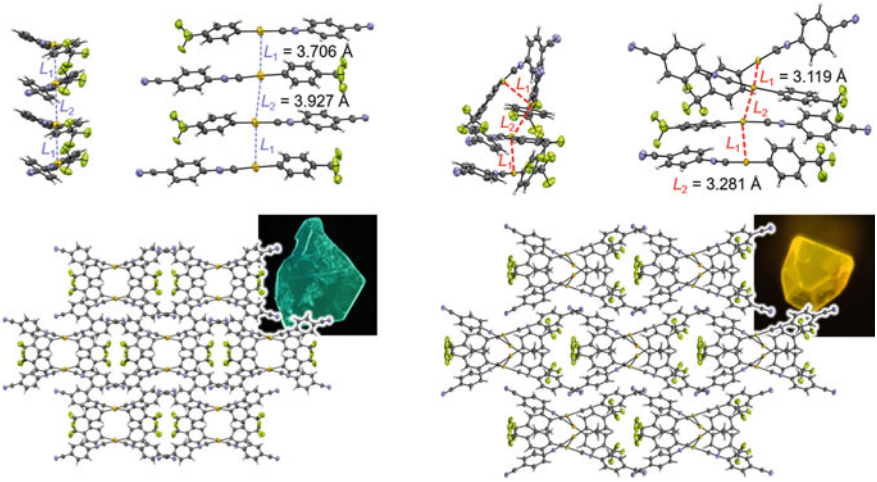

Fig. 5.7 Single crystal structure of **CF_3–CN** species, corresponding to the molecular arrangement before (left) and after (right) **CF_3–CN** exhibits luminescent mechanochromism. Adapted with permission from ref. [63] Copyright 2016 American Chemical Society, All Rights Reserved

ring attached to the gold(I) atom is an effective strategy to extend the emission wavelength. Indeed, complex **10** was observed to have a $\lambda_{em,max}$ in the infrared region [64].

A novel gold(I) isocyanide complex **10**, which consists of a gold(I) atom and an anthracene group, was synthesized. A pristine microcrystal of **10a** exhibited blue emission. Complex **10a** had a relatively sharp emission spectrum with $\lambda_{em,max}$ at 448 nm (Fig. 5.8), and the absolute emission quantum yield Φ_{em} was 0.5%. The conjugated system was extended, but the emission was observed in the shorter wavelength region compared with that of **8** and **9**. Notably, the average lifetime τ_{av} [$= \Sigma({}_nA\tau)_n{}^2/\Sigma({}_nA\tau_n)$] was found to be 0.11 ns, which was attributed to fluorescence. This result is in contrast to previously reported results of the luminescence lifetimes of aryl gold(I) isocyanide complexes, of which the majority are of microsecond phosphorescence origin.

Mechanical stimulation of complex **10a** resulted in the powdered form of **10b**. However, complex **10b** exhibited almost no visible luminescence (Fig. 5.8). However, when the emission spectrum of **10b** was measured, a broad emission was observed with a $\lambda_{em,max}$ of 900 nm (Fig. 5.8) This is the longest wavelength emission observed for a mechanochromic molecule to date. Although the Φ_{em} of **10b** is low (0.09%), it is reasonable to consider that the Φ_{em} values [65] of infrared-emitting solid-state organic compounds and transition-metal complexes are generally extremely low. Furthermore, the luminescence lifetime was measured to be 0.69 μs, which is typical for gold(I) complexes. The mechanochromism observed for the transformation of complex **10a** to **10b** shows a significant shift of luminescence to relatively

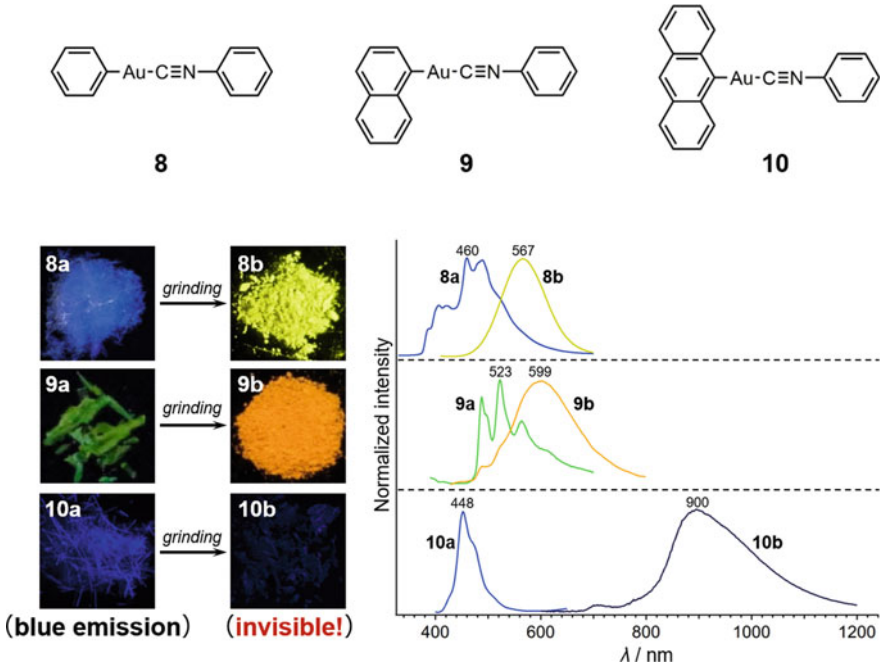

Fig. 5.8 Structures, photographs (taken under UV light), and emission spectra of complex **8**, **9**, and **10**. Adapted with permission from ref. [64] Copyright 2017 American Chemical Society, All Rights Reserved

longer wavelengths and a clear change in the luminescence process from fluorescence to phosphorescence. There are only a few examples [66] of this phenomenon in literature.

X-ray diffraction was performed to investigate the mechanism of mechanochromism in complex **10**. Initially, a single crystal of **10a** was prepared and the space group was found to be $P2_1/n$. As shown in Fig. 5.9, the anthracene and benzene rings in the molecular structure of **10a** were almost orthogonal (dihedral angle = 86.17°). Furthermore, they were stacked in a head-to-tail configuration with neighboring molecules, forming dimers via two CH-π interactions (H···π distance = 2.778 Å). There were no visible intermolecular interactions between dimers, and the individual dimers did not form strong intermolecular interactions.

Quantum chemical calculations were then performed based on the single crystal structure of **10a** to investigate the mechanism of luminescence. The molecular coordinates for **10a** were extracted from the single crystal data and the electronic transitions in the singlet were calculated by time-dependent density functional theory (TD-DFT) [RI-B3LYP/def-SV(P)]. It is noteworthy that the transition to the first excited state of **10a** is forbidden. This transition corresponds to the highest occupied molecular orbital/lowest unoccupied molecular orbital (HOMO–LUMO) transition, and can be attributed to the electronic transition from the anthracene moiety to the isocyanide

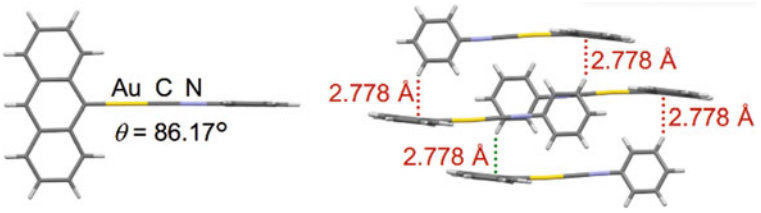

Fig. 5.9 Single crystal structure of complex **10a**. Adapted with permission from ref. [64] Copyright 2017 American Chemical Society, All Rights Reserved

ligand. The reason this transition is forbidden is thought to be because of the nearly orthogonal configuration of the anthracene and benzene rings. Conversely, the transition to the second excited state is allowed, and was attributed to the delocalized π–π^* transition on the anthracene group. These results suggest that the luminescence of complex **10a** is caused by the second excited state (π–π^* excited state), which is consistent with the occurrence of luminescence in the short wavelength region and the short sub-nanosecond luminescence lifetime observed for complex **10a**.

Powder X-ray diffraction was performed to investigate the mechanism of the luminescence of complex **10** after the application of mechanical stimulation. Complex **10a** exhibited several strong diffraction peaks indicating its crystalline nature (Fig. 5.10), which is consistent with the simulation pattern obtained from the single crystal structure. Conversely, almost no diffraction peaks were observed for complex **10b** after mechanical stimulation (Fig. 5.10), which indicates its amorphous nature. These results indicate that the luminescent mechanochromism of **10a** → **10b** originates from the phase transition from the crystalline phase to the amorphous phase. The crystalline-amorphous phase transition is a most typical pattern found in luminescent mechanochromic phenomena [63].

In the case of an amorphous phase **10b**, the methods available to investigate the intermolecular interactions formed by the constituent molecules are limited. In this study, the infrared absorption (IR) spectra of **10a** and **10b** were measured. The isocyanide stretching vibration of **10a** was observed at 2200 cm^{-1}, whereas that of **10b** was observed at 2193 cm^{-1}. This result indicates that a shift of 7 cm^{-1} occurred

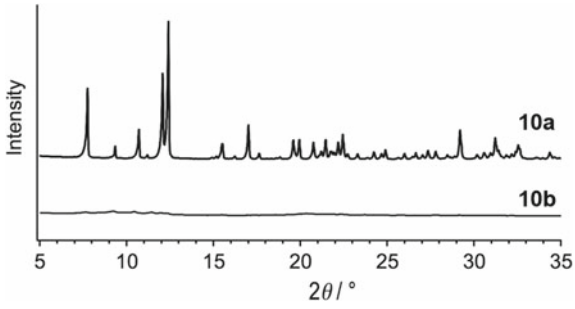

Fig. 5.10 Powder X-ray diffraction patterns of complex **10a** and **10b**. Adapted with permission from ref. [64] Copyright 2017 American Chemical Society, All Rights Reserved

upon mechanical stimulation, which supports the formation of aurophilic interactions. Generally, it is known that the formation of aurophilic interactions significantly affects the luminescence properties of gold(I) complexes, and results in a red shift of the luminescence [46]. This is also consistent with the change in the luminescence lifetime of **10b** to 0.69 μs after mechanical stimulation. In addition, the luminescent mechanochromism of anthracene, which is known to form π-π stacking when amorphized, also results in a long-wavelength shift of the luminescence [67]. In the case of **10b**, the interactions and intermolecular interactions formed by the anthracene ring can be caused to produce an unprecedented infrared emission for mechanochromic materials. According to previous reports of gold(I) isocyanide complexes, the absorption bands associated with the stretching vibrations of the isocyanide ligand shifts to a lower wavenumber when aurophilic interactions occur [16, 65]. Indeed, the gold(I) isocyanide complexes that we have reported so far are consistent with this result [63, 64, 68].

5.2.5 Switching Chirality

With regard to the molecular arrangement of mechanochromic molecules, the majority of these molecules are either crystalline or amorphous with inversion centers before and after mechanical stimulation. However, in case of complex **11** (Fig. 5.11), luminescent mechanochromism occurred based on the change in crystal structure, which switched between the presence and absence of an inversion center [69]. Complex **11** can be prepared as a microcrystalline material (**11**$_{ch}$) that strongly emits a yellow-green color. When a mechanical stimulus is applied to **11**$_{ch}$, it changes to **11**$_{\text{ground}}$, which exhibits green luminescence with a weak emission intensity. Powder X-ray diffraction measurements revealed that **11**$_{ch}$ and **11**$_{\text{ground}}$ are composed of different crystal phases. The space group of **11**$_{ch}$ was found to be $P2_12_12_1$, and the complex formed one dimensional column structure via aurophilic interactions (Au–Au distance = 3.1089(9) Å). In contrast, the space group of **11**$_{\text{ground}}$ was found to be *P*-1, and complex **11**$_{\text{ground}}$ formed a dimer via aurophilic interactions (Au–Au distance = 3.343(1) Å). Moreover, complex **11**$_{\text{ground}}$ had an inversion center relative to the adjacent dimer. Therefore, mechanical stimulation altered the space group without an inversion center to a space group with an inversion center. When a single molecule yields crystal systems with both chiral and non-chiral space groups, it is known that the non-chiral crystal system is thermodynamically more stable and favored [70]. Therefore, the luminescent mechanochromism of complex **11** can be attributed to the phase transition to a thermodynamically stable phase. To date, there has been no example of a system that shows luminescent mechanochromism by switching the chirality of the crystal (that is, the presence or absence of an inversion center) by changing the molecular arrangement [69]. Moreover, based on unreported experimental results, it was found that the signal in the circular dichroism spectrum had a clear intensity for complex **11**$_{ch}$ that changed to a silent signal for **11**$_{\text{ground}}$ upon the phase transition induced by mechanical stimulation. This indicates that the

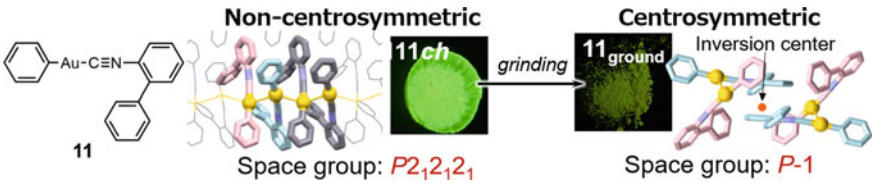

Fig. 5.11 Molecular structure of complex **11**. Photographs (taken under UV light) of the solids and crystal structures before and after mechanical stimulation. Adapted with permission from ref. [69] Copyright 2017 American Chemical Society, All Rights Reserved

chiral optical properties can be controlled by switching the presence or absence of the inversion center in crystal structures under mechanical stimulation.

5.3 Single-Crystal-To-Single-Crystal Phase Transition Induced by Mechanical Stimulation

5.3.1 Introduction

In molecules exhibiting luminescent mechanochromism, the phase transition from the crystalline to the amorphous material proceeds upon the application of mechanical stimuli, and the luminescence properties were found to change in numerous cases [71]. As mentioned earlier, for amorphous materials, it is difficult to identify the intermolecular interactions formed as a result of mechanical stimulation because of a limitation for detailed structural analysis using characterization techniques such as X-ray diffraction. Therefore, many luminescent mechanochromism systems exist, in which it is not possible to clearly elucidate how the intermolecular interactions are altered before and after the mechanical stimulation and how the luminescence properties are changed. Contrary, we have systematically discovered luminescent mechanochromic complexes that show a single-crystal-to-single-crystal phase transition upon the application of a mechanical stimulus, in which the change in intermolecular interactions can be clearly elucidated.

After the mechanochromism of complex **4** was reported in 2008, we synthesized various gold(I) isocyanide complexes, and reported their mechanochromic properties [29, 72, 73] and the control of their luminescence properties based on polymorphic properties [74]. In this study, we found that complex **8** and **12** exhibited a very unique phenomenon (Fig. 5.12) [75, 76]. In complex **8**, a single-crystal-to-single-crystal phase transition was induced by the application of a mechanical stimulus, and the luminescence color changed as a result. The peculiarity of this phenomenon is that the phase transition proceeds between two different single crystals of the same molecule. In most cases, mechanical stimulation of a crystal disturbs the molecular arrangement in the crystal, which complicates the single-crystal structural analysis

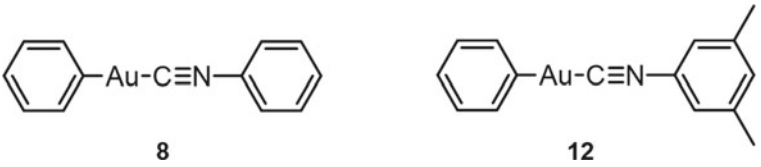

Fig. 5.12 Structures of complex **8** and **12**

of the ground phase. However, since these complexes were mechanically stimulated to single crystals, it was possible to elucidate how the crystal structure and pattern of intermolecular interactions were transformed before and after the phase transition. Based on the detailed information derived from the crystal structure analysis, the change in the luminescence property owing to the phase transition could be rationally explained. More details are described in the subsequent section.

5.3.2 Single-Crystal-To-Single-Crystal Phase Transition with Formation of the Aurophilic Interaction

The gold(I) isocyanide complex **8** forms a single crystal **8b**, which emits blue light, when it is rapidly recrystallized in a dichloromethane/hexane mixture [75]. One of the **8b** crystals were isolated and scratched with a fine needle, as indicated by an arrow in Fig. 5.13. The emission color of the scratched area changed to yellow. Interestingly, when the crystal was left in air at room temperature, the crystal area with the changed luminescence color gradually expanded. The changed luminescence color propagated to the entire crystal in approximately 9 h for the crystal shown in Fig. 5.13, and the **8y** crystal was obtained finally (Fig. 5.13 right). X-ray structural analysis of the single crystals, before and after the application of a mechanical stimulus, showed that the single crystal-single crystal phase transition was correlated with the change in luminescence color.

Single crystal **8b** (blue luminescence) had a space group of *P*-1 before the application of mechanical stimulation (Fig. 5.14a) [75]. The molecules were stacked in a head-to-tail configuration via CH/π interactions (indicated by the red line in Fig. 5.14a), and one-dimensionally elongated substructures were observed. The shortest distance between gold(I) atoms was 5.733 Å. Typically, the interaction between gold(I) atoms occurs at a distance of approximately <3.5 Å; therefore, the interaction between gold(I) atoms does not occur in single crystal **8b**. Conversely, the yellow-emitting single crystal **8y**, obtained by mechanical stimulation of the single crystal **8b**, showed a change in the space group to *I*-42*d* (Fig. 5.14b). **8y** also showed stacking and one-dimensional elongation of molecules. However, in the case of complex **8y**, the stacking between adjacent molecules is twisted rather than face-to-face. The distance between the gold(I) atoms in the single crystal **8y** is 3.1773(4) Å, which indicates that aurophilic interactions were induced by the phase transition.

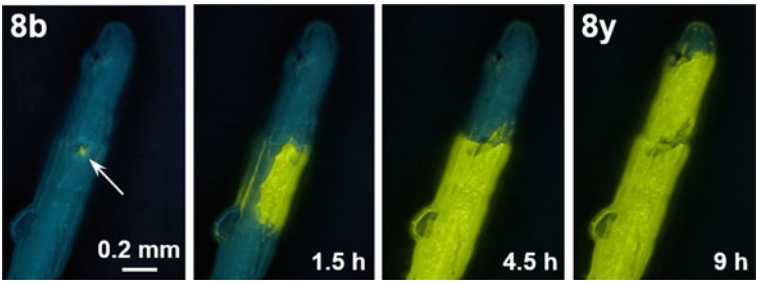

Fig. 5.13 Single-crystal-to-single-crystal phase transition of complex **8** induced by the application of a mechanical stimulus that caused an emission change of the crystal under UV irradiation. The arrow indicates the location where the mechanical stimulus was applied. Adapted with permission from ref. [75] Copyright 2013 Springer Nature Limited, All Rights Reserved

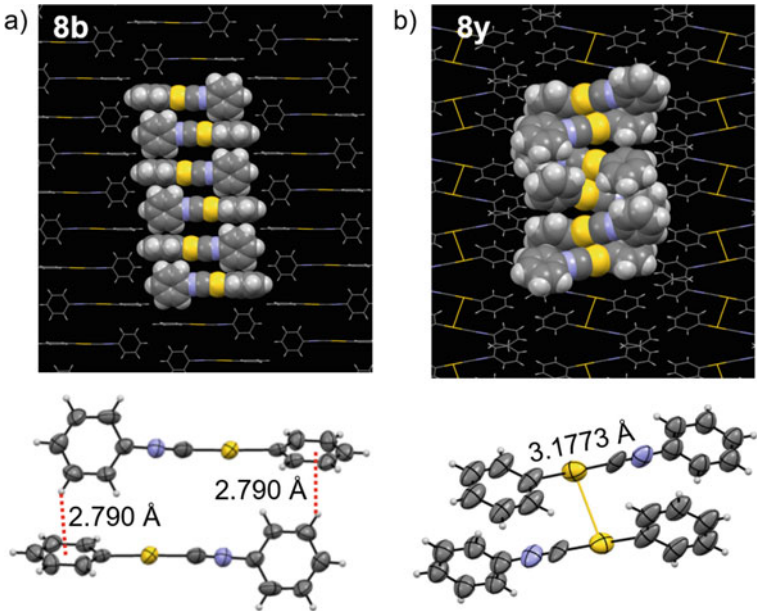

Fig. 5.14 Single crystal structure of **a 8b** and **b 8y**. Adapted with permission from ref. [75] Copyright 2013 Springer Nature Limited, All Rights Reserved

Generally, the luminescence properties of gold(I) complexes are strongly affected by the formation of aurophilic interactions [11, 46–52]. Figure 5.15a shows a schematic representation of the formation of aurophilic interactions and corresponding energy levels. The aurophilic interaction is a type of dispersion force. When the distance between two gold(I) atoms is less than approximately 3.5 Å the formation of an aurophilic interaction is generally recognized. Owing to the pronounced relativistic effects on the gold(I) atom, the strength of the aurophilic interactions

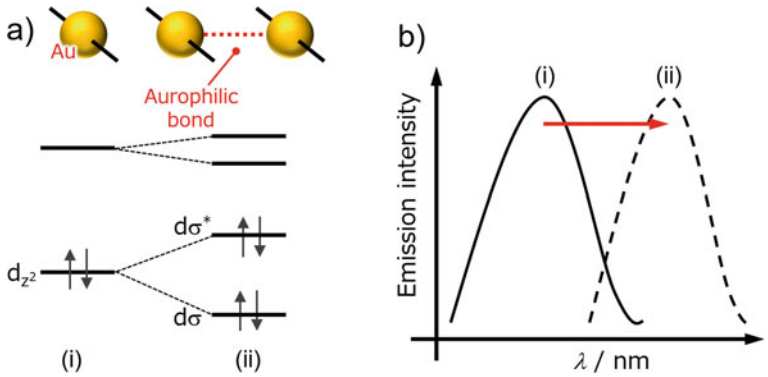

Fig. 5.15 **a** Schematic representation of the orbital levels and the effect of the aurophilic interaction on the orbital levels. Typically, the formation of an aurophilic interaction results in the splitting of the HOMO orbital to form a bonding orbital dσ and an antibonding orbital dσ* (ii). **b** Schematic representation of the change in the emission spectrum of the gold(I) complex owing to the formation of aurophilic interactions

is stronger than the conventional *van der* Waals force, and reaches the same level as that of a hydrogen bond. Generally, the d_z^2 of the gold(I) atom is thought to be essential for the HOMO of gold(I) complexes [Fig. 5.15a, (i)] [47, 77]. The formation of an aurophilic interaction within a gold(I) complex in solution or a crystal lattice results in the splitting of the HOMO and the formation of new orbitals dσ and dσ* [Fig. 5.15a, (ii)]. These newly formed orbitals have bonding and antibonding properties, respectively. Consequently, the HOMO becomes an antibonding dσ* [Fig. 5.15a, (ii)], and is energetically destabilized compared to before the formation of aurophilic interactions, which results in a smaller band gap. Therefore, when gold(I) complexes form aurophilic interactions, the absorption and emission wavelengths typically red shifted (Fig. 5.15b) [11, 46–52].

Complex **8** undergoes a phase transition upon mechanical stimulation, and a red shift was observed in the emission spectrum owing to the formation of aurophilic interactions (Fig. 5.16). **8b** has a maximum emission wavelength at 490 nm, while that of complex **8y** after mechanical stimulation showed a broad spectrum peak at 567 nm. This was equivalent to a red shift of 77 nm. Furthermore, the luminescence lifetime was shortened by more than an order of magnitude, and an increase in the luminescence quantum yield (from 15 to 43%) was observed. These changes in the optical properties of gold(I) complexes were caused by the crystalline phase transition along with the onset of aurophilic interaction.

By differential scanning calorimetry (DSC) measurements and the observation of the change in luminescence with increasing temperature, **8y** was found to be the thermodynamically more stable phase, whereas **8b** is the thermodynamically more unstable metastable phase. The luminescence of **8b** was also changed by intensely applying a manual force using a mortar and, and the mechanochromism was observed to change to yellow luminescence similar to that of **8y**. XRD patterns of the obtained

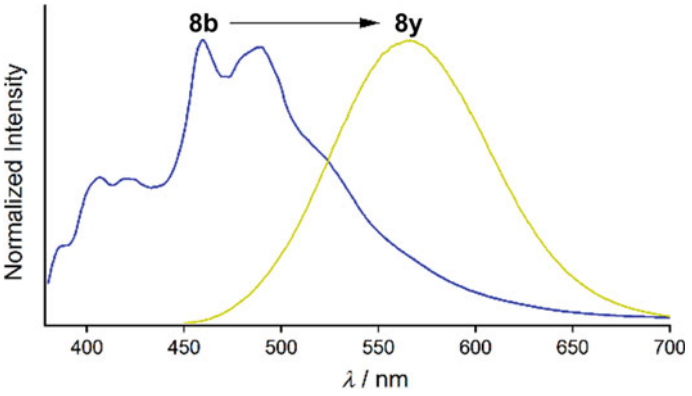

Fig. 5.16 Normalized emission spectra depicting the changes before and after the single crystal-single crystal phase transition of complex **8**. Adapted with permission from ref. [75] Copyright 2013 Springer Nature Limited, All Rights Reserved

powders were almost consistent with that of the simulated patterns for single crystal **8y**. Based on these results, the mechanism of the phase transition was deduced. As shown in Fig. 5.17, the application of a local mechanical stimulus to metastable **8b** (a) results in the formation of a stable molecular arrangement **8y** at the application region (b). This can be thought of as localized mechanochromism. The crystalline domain serves as the "nucleus" for subsequent spontaneous phase transitions. Molecules of the metastable phase **8b** located around the nucleus rearrange themselves for a phase transition to the more stable phase **8y** (c). Subsequently, a domain **8y** with a different emission color expands around the nucleus (d). Lastly, the rearrangement of molecules proceeds from the nucleus to the entire crystal, and the crystal transitions to the crystalline phase **8y**. This phenomenon was named the "molecular domino" effect because the initial local change resulted in a gradual change in the molecular arrangement of the entire crystal. Moreover, it is noteworthy that when crystals of **8b** and **8y** are gently brought into contact with each other, the point of contact becomes a nucleus from which molecular rearrangement proceeds, and a single-crystal-to-single-crystal phase transition from **8b** to **8y** is observed.

5.3.3 Single-Crystal-To-Single-Crystal Phase Transition with Disappearance of the Aurophilic Interaction

In addition, complex **12** (Fig. 5.12) was also found to exhibit a single-crystal-to-single-crystal phase transition upon local mechanical stimulation (Fig. 5.18) [76]. In contrast to complex **8**, the phase transition is accompanied by a blue shift of the emission peak owing to the disappearance of aurophilic interactions. A single crystal of **12g** before mechanical stimulation (space group: $P2_1/n$) consists of six

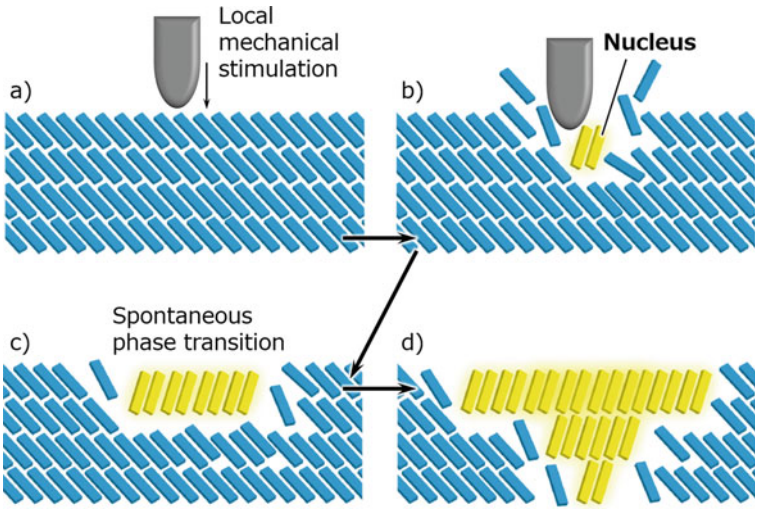

Fig. 5.17 Schematic representation of the mechanically stimulated single-crystal-to-single-crystal phase transition of the complex **8**. The blue and yellow rectangles represent the molecules **8** in the **8b** and **8y** phases, respectively. Adapted with permission from ref. [75] Copyright 2013 Springer Nature Limited, All Rights Reserved

molecules are packed in a helical configuration via aurophilic interactions (average Au–Au distance: 3.206 Å). Conversely, mechanical stimulation of **12g** yields a single crystal of **12b** (space group: *Ima*2), which shows weak blue luminescence. However, no aurophilic interactions are observed for **12b** (average Au–Au distance: 4.784 Å), which indicates that the loss of intermolecular aurophilic interactions was caused by the crystal phase transition induced by mechanical stimulation. Alternatively, in **12b**, all the molecules exhibit one CH/π interaction, which is thought to compensate for the enthalpy loss that is caused by the loss of the aurophilic interactions. The disappearance of the aurophilic interaction induces the shift in emission bands to the shorter wavelength region compared with the maximum emission wavelength (emission shift: 535 → 423, 445 nm). This trend of the shift in emission wavelength was expected to occur as a result of the disappearance of the aurophilic interactions. Complex **8** and **12** exhibited contrasting results in terms of the change pattern of intermolecular interactions and the shift in emission wavelengths.

In the mechanically stimulated single-crystal-to-single-crystal phase transition reported by Tao et al., single-crystal X-ray structure analysis of the elongated crystal found that the layers slide laterally while maintaining the molecular-level layered arrangement, and that the crystal outline changes dramatically in a specific direction [78]. Moreover, Takamizawa's group at Yokohama City University reported the first superelastic phenomenon in organic crystals [79, 80]. When a force was applied to a particular face of an organic crystal, the crystal deformed easily without breaking, and when the applied force was removed, the original crystal shape was restored. Takamizawa and co-workers performed single-crystal X-ray structural analysis on

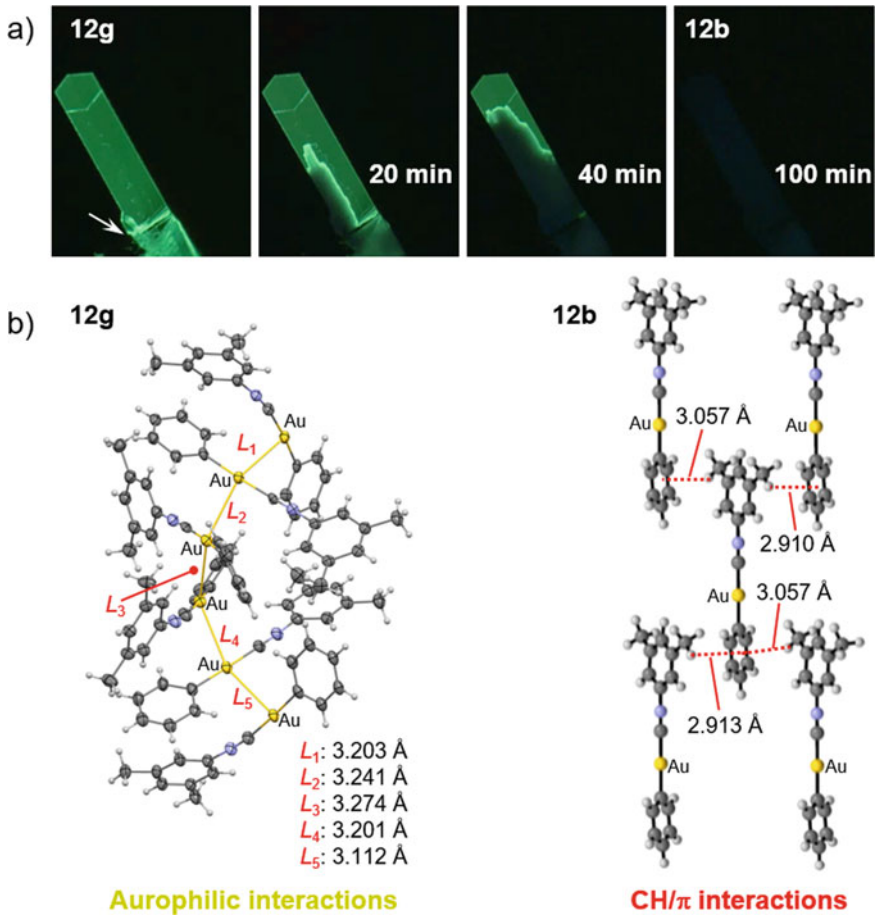

Fig. 5.18 Single-crystal-to-single-crystal phase transition of complex **12** induced by mechanical stimulation. **a** Photograph of a crystal under UV irradiation. The arrow indicates the location of the application of mechanical stimulation. **b** The corresponding changes in single-crystal structures. Adapted with permission from ref. [76] Copyright 2013 Wiley-VCH, All Rights Reserved

the deformed crystal under mechanical stimulation, and found that a single-crystal-to-single-crystal phase transition occurred at the bent section of the crystal. The organic crystals and complexes (**8** and **12**) introduced in this section are rare systems, in which the structural factors that influence the macroscopic changes in the crystal properties were elucidated based on crystal structure analysis before and after mechanical stimulation. Based on the improved performance of recent X-ray diffractometers, in terms of both software and hardware, reports of single-crystal-to-single-crystal phase transitions induced by mechanical stimulation are expected to increase in the future.

5.3.4 *Reversible Single-Crystal-To-Single-Crystal Phase Transition*

Although we have reported a number of single-crystal-to-single-crystal phase transitions, in which luminescence changes with a red or blue shift, we have not been able to reverse the single-crystal **β** obtained after mechanical stimulation to the original single-crystal **α**. However, complex **13** was reported to exhibit a single-crystal-to-single-crystal phase transition (**α** → **β**) upon mechanical stimulation, followed by a reverse phase transition to the original crystalline phase (**β** → **α**) upon exposing the crystal to a solvent vapor [81]. The recrystallization of this gold(I) complex yielded a green-emitting single crystal **α** (Fig. 5.19, left). The application of mechanical stimulation by cutting the single crystal under MeOH vapor gradually changed the emission color to orange and yielded a single crystal **β** (Fig. 5.19, center). The single-crystal X-ray structural analysis of **α** and **β** revealed that the single-crystal-to-single-crystal phase transition (**α** → **β**) was induced by mechanical stimulation. X-ray structural analysis revealed that the obtained crystal has the same single-crystal structure as that of **α**, which confirmed that the reversible phase transition (**β** → **α**) including mechanical stimulation-induced single-crystal-to-single-crystal phase transitions was achieved for the first time [81]. The key to achieving reversible single-crystal-to-single-crystal phase transitions is that the **α** phase encapsulates MeOH, and in the MeOH atmosphere, an equilibrium between the uptake and desorption of MeOH. When mechanical stimulation was applied, the equilibrium shifted towards MeOH desorption, which resulted in the transition to the MeOH-free **β** phase.

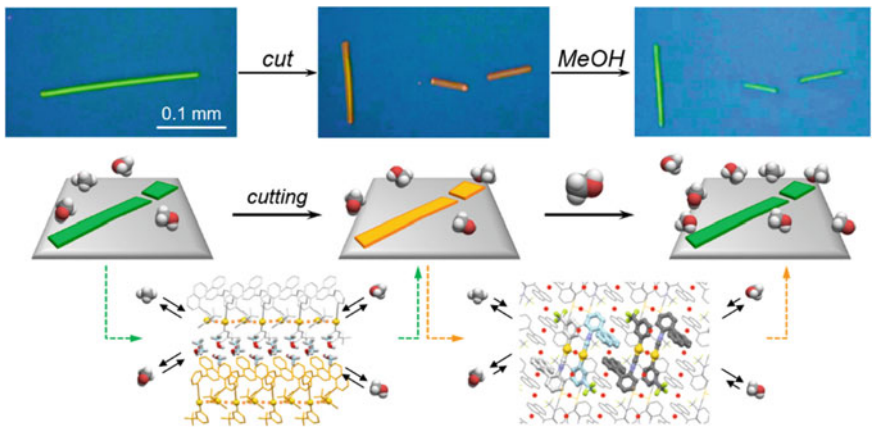

Fig. 5.19 Photograph of a crystal of complex **13** (taken under UV light). The luminescence color changes upon mechanical stimulation and exposure to MeOH. Schematic representation of the corresponding crystal structures and molecular arrangements. Adapted with permission from Ref. [81] Copyright 2018 American Chemical Society, All Rights Reserved

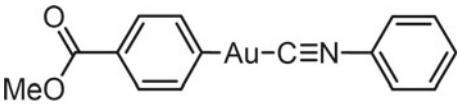

14

Fig. 5.20 Structure of complex **14**

5.4 Optical Phase Transition and the Photosalient Effect

5.4.1 Introduction

The investigation of stimuli-responsivity of various gold(I) isocyanide complexes revealed that complex **14** (Fig. 5.20) has a unique photo-responsive property. Complex **14** exhibits a typical luminescent mechanochromism, in which mechanical stimulation induces a crystal phase transition that results in a change in the luminescence color from blue to yellow. While monitoring the change in luminescence of the complex **14** under UV irradiation, it was accidentally discovered that the same change in luminescence (blue → yellow) also occurs under irradiation with UV light. Moreover, when the complex was irradiated with intense UV light, a single-crystal-to-single-crystal phase transition was observed in the entire crystal [82]. Furthermore, single-crystal X-ray structural analysis and quantum chemical calculations revealed that the unique property of the aurophilic interaction is important for the photoresponsive structural change of complex **14** in the presence of UV light irradiation. Subsequently, the phenomenon of crystal jumping (that is, the photosalient effect) upon the application of an external stimulus will be discussed.

5.4.2 Gold(I) Complexes Exhibiting Optical Phase Transitions and the Photosalient Effects

Gold(I) complexes that form aurophilic interactions exhibit interesting behavior in the excited state, as shown in Fig. 5.21. As presented in Fig. 5.15, when the aurophilic interaction occurs in a pair of gold(I) complexes, the electron in the HOMO of the gold(I) complex has an antibonding character. Upon photoexcitation, the electron in the HOMO is electronically excited [Fig. 5.21(iii)]. The electrons that originally occupied the antibonding orbitals are then transferred to higher energy level orbitals, and the antibonding character between gold(I) atoms are reduced (that is, the bonding character increased). Therefore, the distance between gold(I) atoms is shorter in the excited state. This phenomenon has been investigated in detail using theoretical calculations, which has been reported [83, 84].

Although few experimental observations of enhanced aurophilic interactions upon photoexcitation have been reported thus far, Iwamura and Tahara reported results of time-resolved emission spectroscopy of a gold(I) complex [77]. The behavior of

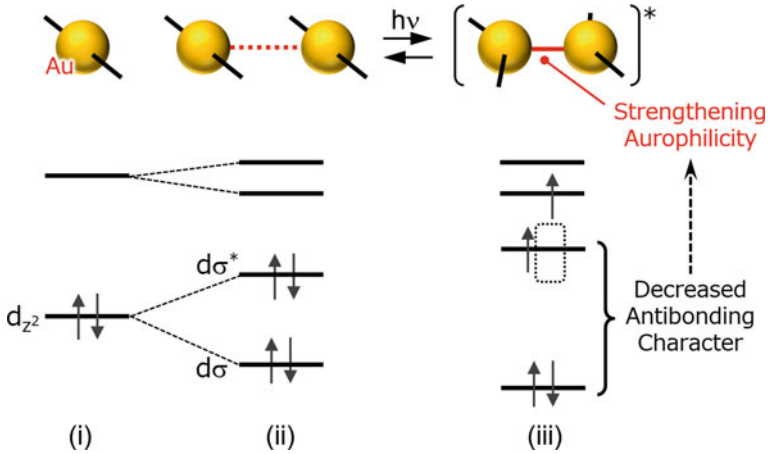

Fig. 5.21 Schematic representation of the orbital level and the effect of the formation of the aurophilic interaction on the orbital level. Photoexcitation of a gold(I) complex that forms an aurophilic interaction typically results in an electronic transition from the antibonding $d\sigma^*$ orbital (HOMO) that enhances the aurophilic interaction (iii)

$[Au(CN)_2^-]_3$ complexes in aqueous solution was investigated, and the emission of an excited species was observed at 420 nm with a lifetime of 2.0 ns. This excited species was reported to be a transient species in which the aurophilic interactions are enhanced. Furthermore, Adachi and Nozawa investigated the excited state of a gold(I) complex in aqueous solution using synchrotron radiation and reported the detailed dynamics of the formation and enhancement processes of aurophilic interactions [85]. Moreover, it is known that the intermetallic interaction of organometallic complexes with metals other than gold(I), such as platinum, rhodium, and iridium, is transiently enhanced by photoexcitation [86–88]. These reports confirm the enhancement of the intermetallic interaction as a transient species in solution or by measurements under UV irradiation. In contrast, we focused on the phase transition phenomenon in the crystal, and found that the gold(I) isocyanide complex **14** (Fig. 5.20) undergoes a phase transition to form a new crystal structure owing to the enhancement of the aurophilic interaction by light irradiation.

Rapid recrystallization of complex **14** in a dichloromethane-hexane solution under dark conditions yields a single crystal **14B** with weak blue luminescence (Fig. 5.22, left). The absolute quantum yield Φ_{em} of the luminescence of **14B** was 2.2%, and the average lifetime τ_{av} $[= (\Sigma A_i \tau_i)/(\Sigma A_i)]$ was 34.2 μs. As shown in Fig. 5.23, the emission spectrum of **14B** (solid blue line) exhibits a maximum emission wavelength ($\lambda_{em,max}$) at 448 nm. The excitation spectrum of **14B** monitored at 590 nm is indicated by the dotted blue line in Fig. 5.23, which had a maximum at 371 nm and showed almost no optical absorption in the visible region above 400 nm.

The crystal structure of a blue-emitting single crystal **14B** was analyzed by X-ray diffraction method. The space group and crystal system were determined to be *P*-1 and triclinic, respectively (Fig. 5.22). No residual electron density indicating

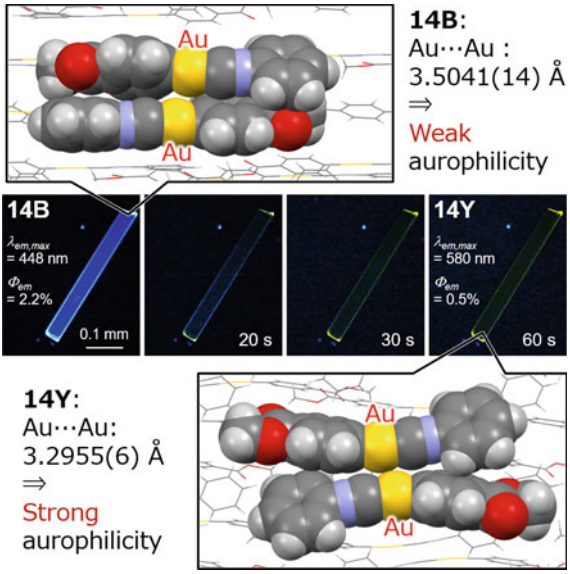

Fig. 5.22 Single crystal structures and photomicrographs of the crystals **14B** and **14Y**. Excitation light used to induce the phase transition: wavelength of 367 nm, intensity of ~ 100 mW cm^{-2}, irradiation time is indicated in the lower right corner of each photomicrograph. Excitation light for photographing: wavelength of 365 nm, intensity of < 1 mW cm^{-2}. Adapted with permission from ref. [82] Copyright 2015 Royal Society of Chemistry, All Rights Reserved

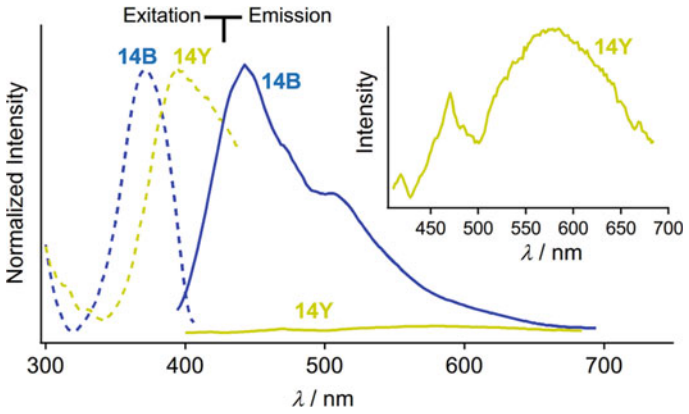

Fig. 5.23 Excitation and emission spectra of **14B** and **14Y**. Blue-yellow dotted lines: excitation spectra normalized to the excitation maxima of **14B** (monitoring wavelength: 450 nm) and **14Y** (monitoring wavelength: 590 nm). Blue-yellow solid line: emission spectra of **14B** (excitation wavelength: 370 nm) and **14Y** (excitation wavelength: 390 nm), which was normalized based on the intensity of the absorption spectrum. Inset: magnified view of the emission spectrum of **14Y**. Adapted with permission from ref. [82] Copyright 2015 Royal Society of Chemistry, All Rights Reserved

solvent inclusion was observed, which was confirmed by the results of elemental analysis, thermal analysis, and ^{1}H NMR measurements. A pair of complex **14** molecules formed a head-to-tail dimer unit. The intermolecular Au–Au distance between the molecules in the dimer was determined to be 3.5041(14) Å, which indicated that the aurophilic interactions formed were relatively weak. The dimer is then stacked to form a one-dimensional column structure, which is aligned in a sheet-like configuration with adjacent columns.

When **14B** was irradiated with intense UV light, the luminescence color gradually changed, and a crystal **14Y** with weak yellow luminescence was obtained (Fig. 5.22, right), after 60 s of UV irradiation. The luminescence of **14Y** was very weak ($\Phi_{em} = 0.5\%$), with an $\lambda_{em,max}$ of 580 nm (indicated by the solid yellow line in Fig. 5.23), which is 132 nm longer compared with that of **14B**. The maximum emission wavelength of the excitation spectrum (indicated by the dotted yellow line in Fig. 5.23) also shifted by 23 nm upon light irradiation, and τ_{av} was determined to be 0.685 μs, which was approximately 50 times shorter than that of **14B**.

X-ray diffraction measurements of **14Y** revealed that **14B** undergoes a single-crystal-to-single-crystal phase transition upon light irradiation. Several crystals of **14B** were then prepared, which was successfully analyzed by single-crystal structure analysis, and irradiated using UV light under the same conditions presented above to form **14Y**. Subsequently, X-ray diffraction measurement was performed. Consequently, it was reproducibly confirmed that both **14B** and **14Y** retained their single-crystalline nature before and after UV irradiation, even when a single piece of crystal was used. The space group of the single crystal **14Y** was *P*-1 (Fig. 5.22). The intensity of the residual electron density was sufficiently low, which indicated that no solvent inclusion was present. Furthermore, the results of elemental, thermal and ^{1}H NMR analyses supported this finding, which indicates that **14Y** forms a head-to-tail dimer configuration with a sheet structure composed of an array of stacked column structures. These features of the crystal structure are similar to those of **14B**, but differ in the following two aspects. Firstly, the **14Y** molecule is significantly bent. Whereas, the gold(I) isocyanide moiety connecting the two benzene rings in the **14B** molecule is nearly linear. Secondly, the interatomic distance between gold(I) atoms in **14Y** was 3.2955(6) Å, which is approximately 0.21 Å shorter than that in **14B**. Therefore, the aurophilic interaction was enhanced by the crystal phase transition, and caused the red shift of the emission spectrum.

DFT calculations based on single-crystal structure data revealed that the photo-induced crystalline phase transition from **14B** to **14Y** was induced by enhancement of aurophilic interactions in the excited state. The dimer was extracted from the single-crystal structure data of **14B** and DFT calculations (PBEPBE/SDD) of this model structure were performed under various conditions. Firstly, the molecular orbitals of the **14B** dimer were obtained by a single-point calculation using the crystal structure of **14B**. As shown in Fig. 5.24 (i) the HOMO of the dimer has a distribution of nodes between the gold(I) atoms, which indicates that the dimer has an antibonding character. This indicates that **14B** also possesses the molecular orbital features typically observed during the formation of aurophilic interactions, as

shown in Figs. 5.15 and 5.21(ii). The same **14B** dimer was used as the initial structure, which was optimized by assigning the overall spin as a triplet under vacuum conditions to obtain a model $\mathbf{14T_{Opt}}$ to represents the optimized structure of the triplet excited state of the **14B** dimer [Fig. 5.24(ii)]. Although the head-to-tail dimer configuration was maintained, the gold(I) isocyanide unit that links benzene rings in the molecule was significantly bent. Additionally, the interatomic distance between gold(I) atoms were reduced to 2.8611 Å. These results indicate that the interatomic distance between the gold(I) atoms of the **14B** dimer unit was reduced when the **14B** dimer unit transitions to the triplet state upon photoexcitation. This is owing to the enhancement of aurophilic interactions by the excitation of the electron occupying the antibonding HOMO to the higher energy level orbital, as discussed earlier. Moreover, the structure of $\mathbf{14T_{Opt}}$ is similar to that of the dimer extracted from the crystal structure of **14Y** [Fig. 5.24(iii), top]. These results demonstrate that photoexcitation can enhance the interaction between the gold(I) atoms in the **14B** dimer, which induces the structural change to a similar structure compared with that of the **14Y** dimer. These results suggest that the photoinduced crystal phase transition of complex **14B** to **14Y** proceeds via the rearrangement of the entire **14B** molecule, owing to the attractive interactions between gold(I) atoms. To date, the photoinduced single-crystal-to-single-crystal phase transition via the enhancement of metal–metal interactions has not been reported.

Furthermore, it was found that complex **14** exhibits an interesting phenomenon called the photosalient effect, in which the crystal structure changes owing to variations in the external environment, causing the crystal to "jump" (Fig. 5.25) [89]. The reason this effect is that the molecular arrangement in the crystal changes upon the application of a specific external stimulus, and strain is generated in the crystal structure. The release of this strain at a certain moment instantaneously generates a mechanical force and the crystal moves ("jumps") into the air. The "jumping" of a crystal in response to a change in temperature is called the thermosalient effect, while that in response to light irradiation is called the photosalient effect [90]. Notably, there are fewer reports of crystals showing the photosalient effect [91–94], compared to thermosalient crystals.

Complex **14** exhibited the photosalient effect when irradiated with intense UV light. When the **14B** crystal was irradiated with UV light with an intensity of approximately 400 mW cm^{-2}, the color of the luminescence changed from blue to yellow in approximately 5 s, as shown in Fig. 5.26, which indicates that the crystal phase transition from **14B** to **14Y** occurred. After further irradiation, small cracks appeared in the crystal, and the crystal "jumped" out of the photographic frame after 21 s (Fig. 5.26). Unfortunately, not all **14B** crystals exhibited the photosalient effect under the investigated conditions (only 1% of the **14B** crystals exhibited this effect). However, out of the total number of crystals tested, 80% of the crystals were cracked by UV irradiation, and 20% of the crystals were broken into two or more small pieces. In addition to the crystal "jumping" effect, a previously reported salient-active molecule also showed mechanical responses, such as cracking or breaking of the crystal surface [90]. The photosalient effect of this molecule was induced by the enhancement of

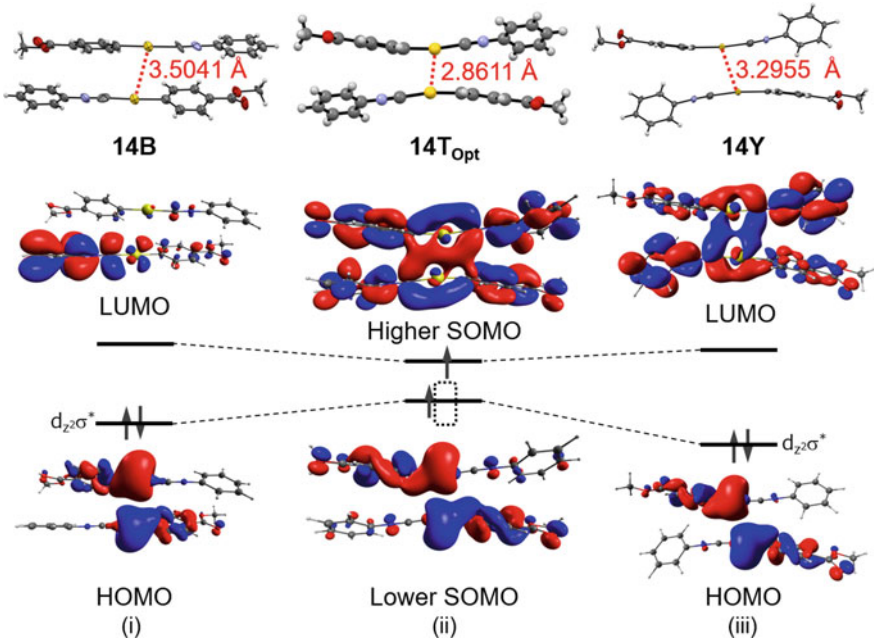

Fig. 5.24 Structures of the **14B, 14T$_{Opt}$,** and**14Y** dimers with diagrams of the frontier orbital energy levels and corresponding molecular orbitals. Calculation conditions: PBEPBE/SDD. Adapted with permission from ref. [82] Copyright 2015 Royal Society of Chemistry, All Rights Reserved

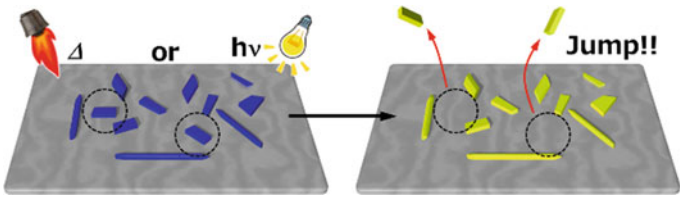

Fig. 5.25 Schematic of the thermosalient and photosalient effects

aurophilic interactions by photoexcitation. In the previously reported photosalient-active molecule, the photocyclization of diarylethene and olefins recombines the covalent bonds of the molecules in the crystal, which results in a phase transition of the entire crystal, and the photosalient effect is observed [91–94]. However, the system that exhibits the salient effect without the formation or degradation of covalent bonds has not been reported thus far [82].

Figure 5.26 shows a phase transition from **14B** to **14Y** before and after the photosalient effect. The features of these crystal structures are in good agreement with the typical crystal structures of previously reported salient-active molecules. Naumov and co-workers recently conducted a very intensive study on the salient effect [90].

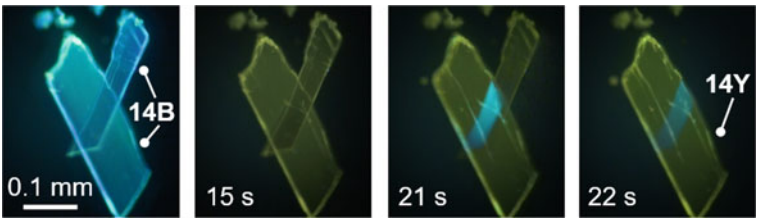

Fig. 5.26 Photographs of the photosalient effect of complex **14**. Adapted with permission from ref. [82] Copyright 2015 Royal Society of Chemistry, All Rights Reserved

To comprehensively discuss the mechanism of the salient effect and its relationship to molecular-level arrangements and interactions, we have thoroughly reexamined the previously reported thermosalient active molecules as well as detailed observations of the "jumping" phenomenon using single-crystal X-ray structural analysis, thermal analysis, and a high-speed camera. Based on these results, we summarize the characteristics of the crystal structures common to salient-active molecules as follows: the crystal phase transitions occurred before and after the salient effect. However, the crystal structures before and after the salient effect were very similar to each other, and the relative spatial positions of the molecules were only slightly altered. For salient-active molecules, the degree of change in the crystal structure before and after the "jump" was minimal, the space group remained the same, and the change in the *V/Z* values of the crystal parameters was very small (< 25 Å in all reported cases). Additionally, anisotropic changes in the crystal lattice size occurred, with a slight elongation of particular lattice lengths in certain directions and slight contraction of the other lattice lengths. Therefore, we propose that the salient effect is owing to small local strains generated by the molecular rearrangement that are released from the crystal without canceling each other as a whole. Moreover, complex **14** also satisfies many of the characteristic features of the crystal structure common to salient-active molecules, as discussed by Naumov et al. In complex **14**, the space group is invariant at *P*-1 and the *V*/*Z* value is very small ($V/Z = 6.8$ Å^3). Complex **14** also shows anisotropic lattice axis length variation. Therefore, complex **14** is the first case in which intermolecular interactions are essential to phase transitions in a photosalient-active molecule, and as mentioned above, it also satisfies many of the conditions for a crystal to exhibit the salient effect.

5.5 Conclusion

The aryl gold(I) isocyanide complexes described in detail in this paper are responsive to specific external environmental stimuli, which induce changes in luminescent color and mechanical motion. We successfully developed a mechanochromic

molecule with unique features, such as multicolor and infrared luminescence properties, with the potential for various applications. Although many studies on luminescent mechanochromism have been reported thus far, the mechanochromic molecule we developed has a great advantage in terms of the characteristic features that set it apart from other studies. Furthermore, we reported a number of complexes that exhibit phase transitions between different crystals before and after mechanical stimulation or light irradiation, without loss of crystallinity, and successfully controlled the induction of luminescence changes and motions. Based on this feature, X-ray structural analysis has enabled us to elucidate the detailed molecular arrangement before and after the response, and clarify the importance of changes in the atomic interactions between gold(I) atoms. Particularly, it is noteworthy that the contrast between the type of stimulus and molecular response induced by the stimulus in the complex **8**, **12**, and **14**. In complex **8** (and **12**), mechanical stimulation induces a crystalline phase transition that strengthens (weakens) the aurophilic interactions, which resulted in a change in the luminescence properties. In contrast, in the complex **14**, light irradiation induced a mechanical response in which the crystal phase transition proceeded by strengthening the aurophilic interactions, which resulted in a crystal "jump." It can be concluded that these complexes showed stimuli-responsive properties that reflect the characteristics of the interactions formed between the gold(I) atoms. More recently, we have successfully developed a unique crystalline material that strictly deforms by the mechanical stimulation of the transition between single crystals.

References

1. Beharry AA, Woolley GA (2011) Chem Soc Rev 40:4422
2. Garcia-Amoros J, Velasco D (2012) Beilstein J Org Chem 8:1003
3. Bandara HM, Burdette SC (2012) Chem Soc Rev 41:1809
4. Irie M, Fukaminato T, Matsuda K, Kobatake S (2014) Chem Rev 114:12174
5. Irie M (2000) Chem Rev 100:1685
6. Ube T, Ikeda T (2014) Angew Chem Int Ed 53:10290
7. Panda MK, El Azhary N, Alzaabi MA, Wahba BM, Jacob J, Naumov P (2014) Croat Chem Acta 87:475
8. Chi Z, Zhang X, Xu B, Zhou X, Ma C, Zhang Y, Liu S, Xu J (2012) Chem Soc Rev 41:3878
9. Zhang X, Chi Z, Zhang Y, Liu S, Xu J (2013) J Mater Chem C 1:3376
10. Sagara Y, Kato T (2009) Nat Chem 1:605
11. Balch AL (2009) Angew Chem Int Ed 48:2641
12. Jobbágy C, Deák A (2014) Eur J Inorg Chem 2014:4434
13. Mataka S, Moriyama H, Sawada T, Takahashi K, Sakashita H, Tashiro M (1996) Chem Lett 25:363
14. Lee YA, Eisenberg R (2003) J Am Chem Soc 125:7778
15. Sagara Y, Mutai T, Yoshikawa I, Araki K (2007) J Am Chem Soc 129:1520
16. Ito H, Saito T, Oshima N, Kitamura N, Ishizaka S, Hinatsu Y, Wakeshima M, Kato M, Tsuge K, Sawamura M (2008) J Am Chem Soc 130:10044
17. Kunzelman J, Kinami M, Crenshaw BR, Protasiewicz JD, Weder C (2008) Adv Mater 20:119
18. Zhang G, Lu J, Sabat M, Fraser CL (2010) J Am Chem Soc 132:2160

19. Mizukami S, Houjou H, Sugaya K, Koyama E, Tokuhisa H, Sasaki T, Kanesato M (2005) Chem Mater 17:50
20. Ooyama Y, Kagawa Y, Fukuoka H, Ito G, Harima Y (2009) Eur J Org Chem 2009:5321
21. Abe T, Itakura T, Ikeda N, Shinozaki K (2009) Dalton Trans 711
22. Sagara Y, Yamane S, Mutai T, Araki K, Kato T (2009) Adv Funct Mater 19:1869
23. Yoon S-J, Chung JW, Gierschner J, Kim KS, Choi M-G, Kim D, Park SY (2010) J Am Chem Soc 132:13675
24. Tsukuda T, Kawase M, Dairiki A, Matsumoto K, Tsubomura T (2010) Chem Commun 46:1905
25. Osawa M, Kawata I, Igawa S, Hoshino M, Fukunaga T, Hashizume D (2010) Chem Eur J 16:12114
26. Sagara Y, Kato T (2011) Angew Chem Int Ed 50:9128
27. Yagai S, Okamura S, Nakano Y, Yamauchi M, Kishikawa K, Karatsu T, Kitamura A, Ueno A, Kuzuhara D, Yamada H, Seki T, Ito H (2014) Nat Commun 5:4013
28. Lin Z, Mei X, Yang E, Li X, Yao H, Wen G, Chien C-T, Chow TJ, Ling Q (2014) CrystEngComm 16:11018
29. Seki T, Ozaki T, Okura T, Asakura K, Sakon A, Uekusa H, Ito H (2015) Chem Sci 6:2187
30. Nagura K, Saito S, Yusa H, Yamawaki H, Fujihisa H, Sato H, Shimoikeda Y, Yamaguchi S (2013) J Am Chem Soc 135:10322
31. Sagara Y, Komatsu T, Ueno T, Hanaoka K, Kato T, Nagano T (2014) J Am Chem Soc 136:4273
32. Barcenilla M, Folcia CL, Ortega J, Etxebarria J, Coco S, Espinet P (2022) J. Mater. Chem. C 10:941–946
33. Krishna GR, Kiran MSRN, Fraser CL, Ramamurty U, Reddy CM (2013) Adv Funct Mater 23:1422
34. Bu L, Sun M, Zhang D, Liu W, Wang Y, Zheng M, Xue S, Yang W (2013) J. Mater. Chem. C 1:2028
35. Hariharan PS, Venkataramanan NS, Moon D, Anthony SP (2015) J Phys Chem C 119:9460
36. Yagai S, Seki T, Aonuma H, Kawaguchi K, Karatsu T, Okura T, Sakon A, Uekusa H, Ito H (2016) Chem Mater 28:234
37. Ito S, Taguchi T, Yamada T, Ubukata T, Yamaguchi Y, Asami M (2017) RSC Adv 7:16953
38. Wu J, Cheng Y, Lan J, Wu D, Qian S, Yan L, He Z, Li X, Wang K, Zou B, You J (2016) J Am Chem Soc 138:12803
39. Sagara Y, Kubo K, Nakamura T, Tamaoki N, Weder C (2017) Chem Mater 29:1273
40. Seki T, Kobayashi K, Ito H (2017) Chem Commun 53:6700
41. Sagara Y, Karman M, Verde-Sesto E, Matsuo K, Kim Y, Tamaoki N, Weder C (2018) J Am Chem Soc 140:1584
42. Sagara Y, Karman M, Seki A, Pannipara M, Tamaoki N, Weder C (2019) ACS Cent Sci 5:874
43. Hayashi S, Yamamoto SY, Takeuchi D, Ie Y, Takagi K (2018) Angew Chem Int Ed 57:17002
44. Hayashi S, Ishiwari F, Fukushima T, Mikage S, Imamura Y, Tashiro M, Katouda M (2020) Angew Chem Int Ed Engl 59:16195
45. Mutai T, Sasaki T, Sakamoto S, Yoshikawa I, Houjou H, Takamizawa S (2020) Nat Commun 11:1824
46. Balch AL (2004) Gold Bull 37:45
47. Pyykko P (2004) Angew Chem Int Ed 43:4412
48. Yam VW, Cheng EC (2008) Chem Soc Rev 37:1806
49. Katz MJ, Sakai K, Leznoff DB (2008) Chem Soc Rev 37:1884
50. Schmidbaur H, Schier A (2008) Chem Soc Rev 37:1931
51. He X, Yam VW-W (2011) Coord Chem Rev 255:2111
52. Schmidbaur H, Schier A (2012) Chem Soc Rev 41:370
53. Daws CA, Exstrom CL, Sowa JR, Mann KR (1997) Chem Mater 9:363
54. Chen Y, Lu W, Che C-M (2013) Organometallics 32:350
55. Sluch IM, Miranda AJ, Elbjeirami O, Omary MA, Slaughter LM (2012) Inorg Chem 51:10728
56. White-Morris RL, Olmstead MM, Balch AL, Elbjeirami O, Omary MA (2003) Inorg Chem 42:6741
57. Meng X, Moriuchi T, Kawahata M, Yamaguchi K, Hirao T (2011) Chem Commun 47:4682

58. Hau FK, He X, Lam WH, Yam VW (2011) Chem Commun 47:8778
59. Fujisawa K, Kawakami N, Onishi Y, Izumi Y, Tamai S, Sugimoto N, Tsutsumi O (2013) J Mater Chem C (in press)
60. White-Morris RL, Stender M, Tinti DS, Balch AL, Rios D, Attar S (2003) Inorg Chem 42:3237
61. Lefebvre J, Batchelor RJ, Leznoff DB (2004) J Am Chem Soc 126:16117
62. Bayon R, Coco S, Espinet P, Fernandez-Mayordomo C, Martin-Alvarez JM (1997) Inorg Chem 36:2329
63. Seki T, Takamatsu Y, Ito H (2016) J Am Chem Soc 138:6252
64. Seki T, Tokodai N, Omagari S, Nakanishi T, Hasegawa Y, Iwasa T, Taketsugu T, Ito H (2017) J Am Chem Soc 139:6514
65. White-Morris RL, Olmstead MM, Balch AL (2003) J Am Chem Soc 125:1033
66. Xiao Q, Zheng J, Li M, Zhan SZ, Wang JH, Li D (2014) Inorg Chem 53:11604
67. Teng M, Wang Z, Ma Z, Chen X, Jia X (2014) RSC Adv 4:20239
68. T. Seki, H. Ito, *Chem. Eur. J.*, **22**, z (2016).
69. Jin M, Seki T, Ito H (2017) J Am Chem Soc 139:7452
70. Wallach O (1895) Liebigs Ann Chem 286:90–143
71. According to our investigation, more than 80% of solid-state mechanochromic molecules (excluding liquid crystal molecules) change their luminescence by the phase transition from crystal to amorphous. On the other hand, less than 10% of the mechanochromic molecules change their luminescence by the phase transition from crystal to new crystal.
72. Kawaguchi K, Seki T, Karatsu T, Kitamura A, Ito H, Yagai S (2013) Chem Commun 49:11391
73. Seki T, Sakurada K, Ito H (2015) Chem Commun 51:13933
74. Seki T, Kurenuma S, Ito H (2013) Chem Eur J 19:16214
75. Ito H, Muromoto M, Kurenuma S, Ishizaka S, Kitamura N, Sato H, Seki T (2013) Nat Commun 4:2009
76. Seki T, Sakurada K, Ito H (2013) Angew Chem Int Ed 52:12828
77. Iwamura M, Nozaki K, Takeuchi S, Tahara T (2013) J Am Chem Soc 135:538
78. Liu G, Liu J, Liu Y, Tao X (2014) J Am Chem Soc 136:590
79. Takamizawa S, Miyamoto Y (2014) Angew Chem Int Ed 53:6970
80. Takamizawa S, Takasaki Y (2015) Angew Chem Int Ed 54:4815
81. Jin M, Sumitani T, Sato H, Seki T, Ito H (2018) J Am Chem Soc 140:2875–2879
82. Seki T, Sakurada K, Muromoto M, Ito H (2015) Chem Sci 6:1491
83. Pan QJ, Zhang HX (2004) Inorg Chem 43:593
84. Cui G, Cao XY, Fang WH, Dolg M, Thiel W (2013) Angew Chem Int Ed 52:10281
85. Kim KH, Kim JG, Nozawa S, Sato T, Oang KY, Kim TW, Ki H, Jo J, Park S, Song C, Sato T, Ogawa K, Togashi T, Tono K, Yabashi M, Ishikawa T, Kim J, Ryoo R, Kim J, Ihee H, Adachi S (2015) Nature 518:385
86. van der Veen RM, Milne CJ, El Nahhas A, Lima FA, Pham VT, Best J, Weinstein JA, Borca CN, Abela R, Bressler C, Chergui M (2009) Angew Chem Int Ed 48:2711
87. Christensen M, Haldrup K, Bechgaard K, Feidenhans'l R, Kong Q, Cammarata M, Lo Russo M, Wulff M, Harrit N, Nielsen MM (2009) J Am Chem Soc 131:502
88. Haldrup K, Harlang T, Christensen M, Dohn A, van Driel TB, Kjaer KS, Harrit N, Vibenholt J, Guerin L, Wulff M, Nielsen MM (2011) Inorg Chem 50:9329
89. Nath NK, Panda MK, Sahoo SC, Naumov P (2014) CrystEngComm 16:1850
90. Sahoo SC, Panda MK, Nath NK, Naumov P (2013) J Am Chem Soc 135:12241
91. Colombier I, Spagnoli S, Corval A, Baldeck P, Giraud M, Léaustic A, Yu P (2005) Mol Cryst Liq Cryst 431:495
92. Natarajan A, Tsai C, Khan SI, McCarren P, Houk K, Garcia-Garibay MA (2007) J Am Chem Soc 129:9846
93. Naumov P, Sahoo SC, Zakharov BA, Boldyreva EV (2013) Angew Chem Int Ed 52:9990
94. Medishetty R, Sahoo SC, Mulijanto CE, Naumov P, Vittal JJ (2015) Chem Mater 27:1821

Open Access This chapter is licensed under the terms of the Creative Commons Attribution 4.0 International License (http://creativecommons.org/licenses/by/4.0/), which permits use, sharing, adaptation, distribution and reproduction in any medium or format, as long as you give appropriate credit to the original author(s) and the source, provide a link to the Creative Commons license and indicate if changes were made.

The images or other third party material in this chapter are included in the chapter's Creative Commons license, unless indicated otherwise in a credit line to the material. If material is not included in the chapter's Creative Commons license and your intended use is not permitted by statutory regulation or exceeds the permitted use, you will need to obtain permission directly from the copyright holder.

Chapter 6
Elastic and Plastic Soft Crystals with Superelasticity, Ferroelasticity, and Superplasticity

Satoshi Takamizawa and Masako Kato

Abstract Superelasticity is the ability of a plastically deformed solid to spontaneously recover its shape upon unloading due to stress loading. From its discovery in Au–Cd alloys in 1932, superelasticity had been believed to be limited to certain alloys until the discovery of "organic superelasticity" in 2014, which revealed it to be a general phenomenon observed in organic crystals along with ferroelasticity—reversible plastic deformability that is not accompanied by spontaneous shape recovery. In this chapter, we will introduce the discovery of organic superelasticity and the shape-memory effect, discuss superelasticity and ferroelasticity, and explain the properties and characteristics of various molecular crystals, including metal complexes. Furthermore, "organic superplasticity"—irreversible plastic deformation of several hundred percent or more, accompanied by the retention of crystallinity—has also been described.

Keywords Organic crystal · Superelasticity · Shape-memory effect · Ferroelasticity · Superplasticity

6.1 Introduction

In this chapter, we will focus on mechanically soft crystals, in which the crystal-outline change is induced by very weak mechanical stimuli. Crystal deformation is well known in atomic solids, such as gold. However, unlike atomic solids and polycrystals, single crystals—especially molecular single crystals composed of strongly anisotropic organic molecules—exhibit anisotropic deformability. Although the optical, electric, and magnetic functionalities of molecular crystals, which are

S. Takamizawa
Yokohama City University, 22-2 Seto, Yokohama 236-0027, Japan
e-mail: staka@yokohama-cu.ac.jp

M. Kato (✉)
Department of Applied Chemistry for Environment, Kwansei Gakuin University, 1 Gakuen Uegahara, Sanda 669-1330, Japan
e-mail: katom@kwansei.ac.jp

© The Author(s) 2023

M. Kato and K. Ishii (eds.), *Soft Crystals*, The Materials Research Society Series,
https://doi.org/10.1007/978-981-99-0260-6_6

related to their electronic states, have been actively studied, their mechanical properties have not received much attention because molecular crystals are generally low in their solid-state stabilities and they are fragile and easily collapsible [1].

Recently, many examples of mechanical responses to external stimuli, such as bending and twisting in response to mechanical force, heat, or light, have been reported [2]; however, they have not been fully understood. In contrast, "strict deformability", whereby single crystals retain their nature before and after deformation, seems to be advantageous for a rapid and rigorous understanding of solid deformation and its mechanism. Therefore, we will also review the developments in "strictly deformable" superelasticity, ferroelasticity, and superplasticity in organic single crystals.

6.2 Organic Superelasticity and Shape-Memory Effects

In general, when an external force is applied to a solid, it undergoes elastic deformation with spontaneous reversibility, and at a certain threshold, reaches irreversible deformation such as a permanent strain or fracture due to plastic deformation (Fig. 6.1a). The strain due to elastic deformation is usually 0.1–0.2% for metals and alloys. The ability of a deformed solid to spontaneously and elastically return to its original shape is called superelasticity. Specifically, superelasticity emerges based on plastic deformation without the diffusion of atoms and molecules in a crystal lattice and significant reversible deformation beyond the elastic limit. Superelasticity was discovered in Au–Cd alloys in 1932 [3] and later observed in Cu–Zn alloys (brass) in 1938 [4]. The stress–strain curves for superelasticity are characterized by a unique hysteresis and a nearly constant stress value in the plastic-deformation region (Fig. 6.1b). In contrast, a non-diffusive plastic deformation that exhibits a spontaneous strain for a spontaneous shape recovery is called "ferroelasticity"—a ferric property [5]. In ferroelastic materials, a large deformation equivalent to that in superelastic materials is possible; however, shape recovery requires loading in a direction opposite to that of deformation (Fig. 6.1c). Shape recovery, if induced by temperature, appears as a shape-memory phenomenon (temperature-induced phase transition) with respect to the initial shape (Fig. 6.1d). In 1951, the shape-memory effect was first observed in a Au–Cd alloy [6], and its applications were extensively studied, until a TiNi alloy with a good shape-memory effect was discovered [7]. The reversible strain in TiNi alloys is approximately 11% and that in copper-based shape-memory alloys is approximately 20%. Shape-memory alloys have been used in a wide range of applications such as temperature sensors, actuators, eyeglass frames, and orthodontic wires [8]. The increasing prominence of shape-memory alloys has popularized the shape-memory effect.

Superelasticity and shape-memory effects had been believed to be unique to certain alloys until 2014, when superelasticity was observed in a single crystal of terephthalamide (TPA)—a simple aromatic organic compound—and named "organic superelasticity" [9]. As shown in Fig. 6.2, the TPA crystal was sheared and deformed

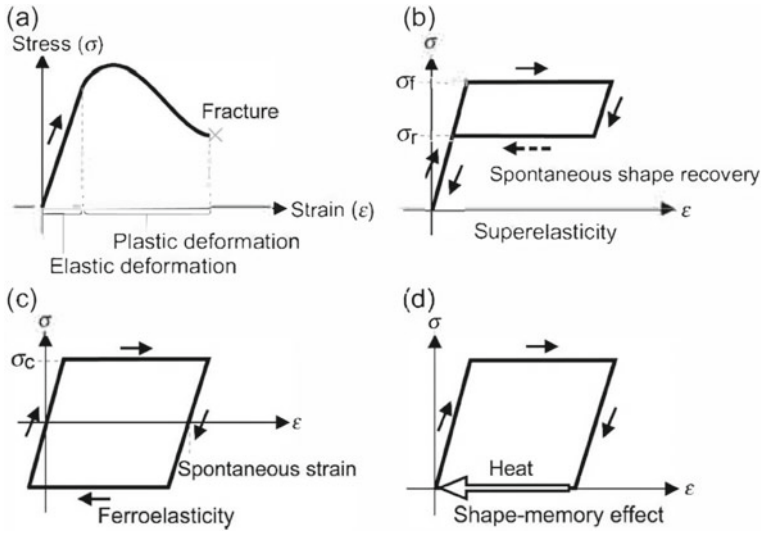

Fig. 6.1 Stress–strain curves of **a** common, **b** superelastic, **c** ferroelastic, and **d** shape-memory materials. σ_f and σ_r represent the forward- and reverse-deformation stresses in superelasticity, while σ_c indicates coercive stress in ferroelasticity

and, upon unloading, spontaneously returned to its original shape. The phenomenon was a non-diffusive solid-state deformation accompanied by a single-crystal-to-single-crystal structural transition, whereby the relative positions of molecules were maintained during the formation and disappearance of new crystal domains, and the molecular-arrangement transformation and crystal deformation were strictly coordinated. Subsequent active searches for organic superelastic crystals led to the discovery of a series of organic crystals exhibiting superelasticity, including fatty acids, bulky cyclic molecules, urea derivatives, fluorescent molecules, organic salts, and even single crystals of one-dimensional coordination polymer complexes, in addition to simple aromatic organic compounds such as TPA (Fig. 6.3). As of 2022, organic superelastic crystals are no longer rare. Incidentally, the shape-memory effect of polymers is known to be similar to that of alloys in terms of shape recovery with temperature change; however, it employs glass transition and has a different mechanism from the shape-memory effect of alloys, which is based on crystal-structure transformation [10]. Therefore, shape-memory alloys and polymers have different temperature dependence of the shape-recovery force and speed, besides functional differences such as biocompatibility and conductivity.

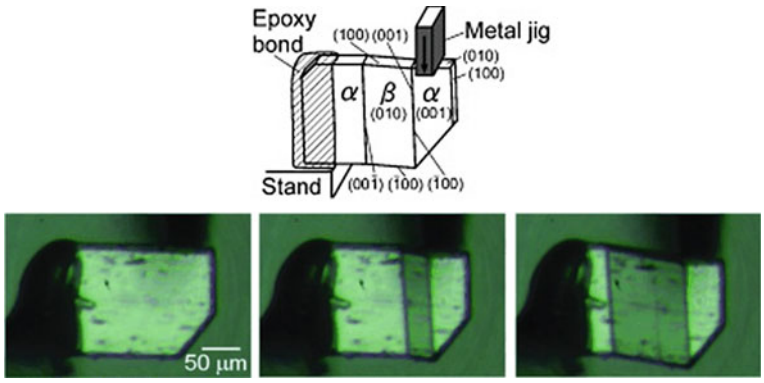

Fig. 6.2 A schematic representation of the experimental setup with face indices and snap shots of the superelastic behavior of a tetraphthalamine (TPA) crystal. Reprinted with permission from ref. [9]

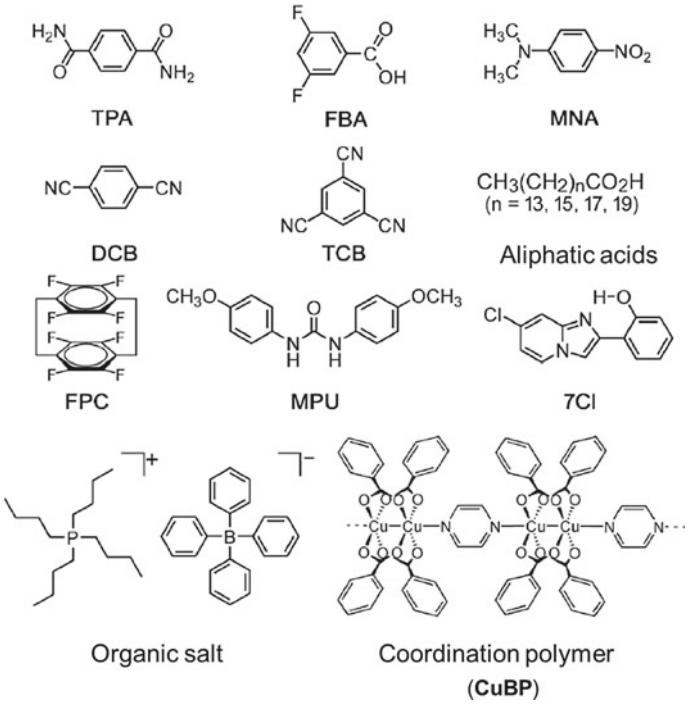

Fig. 6.3 Molecular structures of organosuperelastic crystals

6.2.1 Phase-Transition-Type Organic Superelasticity

As described in the previous section, TPA crystals were the first organic crystals found to exhibit superelasticity. When thin plate-like crystals with thicknesses <100 μm were sheared, they were observed to bend and spontaneously recover with the unloading of the shear force (Fig. 6.4). The stress–strain curves during deformation showed typical superelastic hysteresis curves, and the deformation and reverse-deformation stresses during shape recovery were 0.496 and 0.456 MPa, respectively. Surprisingly, the superelasticity of the TPA single crystal was almost unchanged in the first and hundredth cycles, indicating high stability (Fig. 6.4a). Incidentally, for superelastic materials such as TiNi alloys, pre-use mechanical training is essential, because the superelastic properties change significantly over the first few tens of cycles.

To clarify the detailed mechanism of superelastic deformation, X-ray crystal structural analysis was performed using a crystal in the bent state (two-phase coexisting state) as a twin crystal. The phase transition is believed to have been caused by mechanical forces as well as superelasticity, based on the martensitic transformation known for alloys, and the Gibbs-energy difference between the α and β phases is believed to have driven the spontaneous shape recovery. Essentially, the stress-induced phase β is unstable at room temperature and spontaneously transitions to the stable α phase by eliminating stress. The difference in the crystal structures of the α and β phases suggests a molecular orientation change during the stress-induced phase transition (Fig. 6.4b). In superelastic crystals, the cooperative motion of molecules in restricted molecular motion induces the bulk shape change. Such molecular motion in soft crystals is interesting (although difficult to define objectively).

Not only have aromatic-compound crystals been found to be superelastic but also fatty-acid crystals with long-chain alkyl groups (Fig. 6.5), and detailed deformation properties of pentadecanoic acid (PDA) have revealed that superelasticity is based on a stress-induced phase transition from the high-temperature (A′) to the low-temperature (B′) phase [11]. As the Gibbs-energy difference is the driving force for the spontaneous shape recovery corresponding to superelasticity during deformation at a certain temperature, the material exhibits superelasticity above that temperature. In contrast, near the phase-transition temperature, no reverse deformation occurred and the A'_h and B′ phases stably coexisted, indicating a ferroelastic deformation. Heating the crystals increased the Gibbs-energy difference, and the B′ phase transitioned to the A'_h phase, resulting in the shape-memory effect. Fatty acids are biocompatible and are also found in foods, and may lead to the development of materials that solve the existing problems of shape-memory alloys, such as the toxicity of Ni.

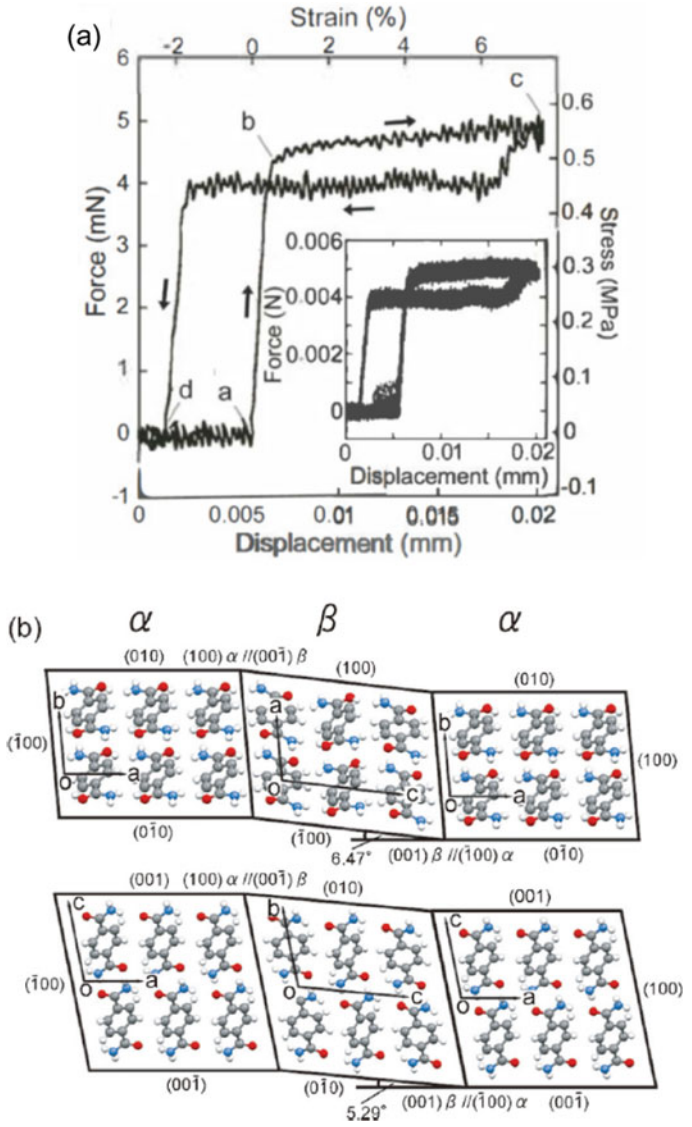

Fig. 6.4 **a** Single-cycle and 100-cycle (inset) results of the stress–strain curves for superelasticity; **b** $[001\text{-}]_\alpha$ and $[010]_\alpha$ projection views. C: Gray; H: white; N: blue; O: red. Reprinted with permission from ref. [9]

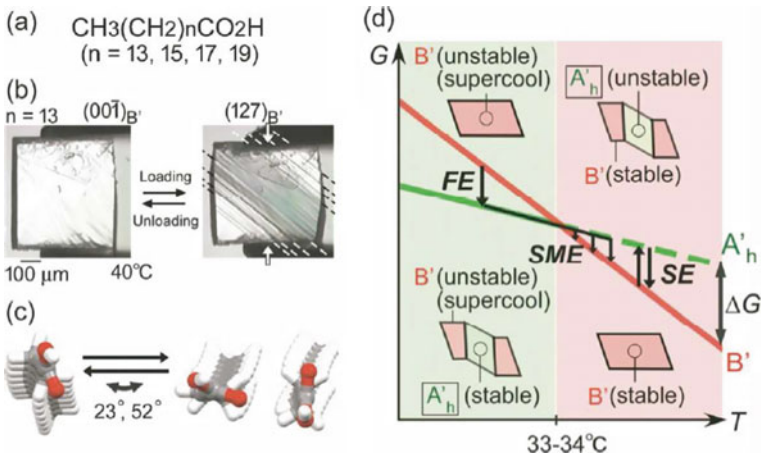

Fig. 6.5 **a** Chemical formula of aliphatic acids: n = 13; pentadecanoic acid (PDA). **b** Superelastic behavior of a PDA crystal, **c** estimated movement of PDA during superelastic behavior, and **d** Gibbs-energy diagram explaining the interchange between A'_h and B′ phases with classifications of ferroelasticity (FE), shape-memory effect (SME), and superelasticity (SE). Reprinted with permission from ref. [11]

6.2.2 *Twin-Crystal-Type Organic Superelasticity*

The next superelastic example is 3,5-difluorobenzoic acid (FBA) crystals [12]. FBA is a derivative of benzoic acid with fluorine atoms substituted at the 3 and 5 positions, and its crystal structure belongs to the $2_1/c$ space group. Columnar FBA crystals obtained via sublimation, when sheared, bent at approximately 27°, producing a stress-induced daughter (α_1) phase from the parent (α_0) phase, and spontaneously recovered their shape upon stress relief (Fig. 6.6). The stress–strain curve at the time showed a typical hysteresis curve of superelasticity, as in the case of shape-memory alloys and TPA crystals (Fig. 6.6). The deformation and reverse-deformation stresses during shape recovery were 0.07 and 0.02 MPa, respectively, which were significantly low, ranging from 1/7 to 1/23 times those of the TPA crystal.

The deformation of the FBA crystals was investigated in detail via X-ray crystallography and was found to be attributable to mechanical twinning, unlike that of TPA crystals, which was based on stress-induced phase transition. This difference in the deformation-stress mechanisms is considered to be responsible for the large difference in the deformation stresses. In twins with identical crystal structures, the Gibbs energies are equal under similar conditions. Therefore, in the superelastic spontaneous shape recovery, the reverse transformation from the α_1 phase to the α_0 phase is expected to have a driving force other than the Gibbs-energy difference. Currently, the driving force is believed to be the strain accumulated by the twin-interface distortion and elastic deformation, but further investigation is necessary to elucidate the mechanism.

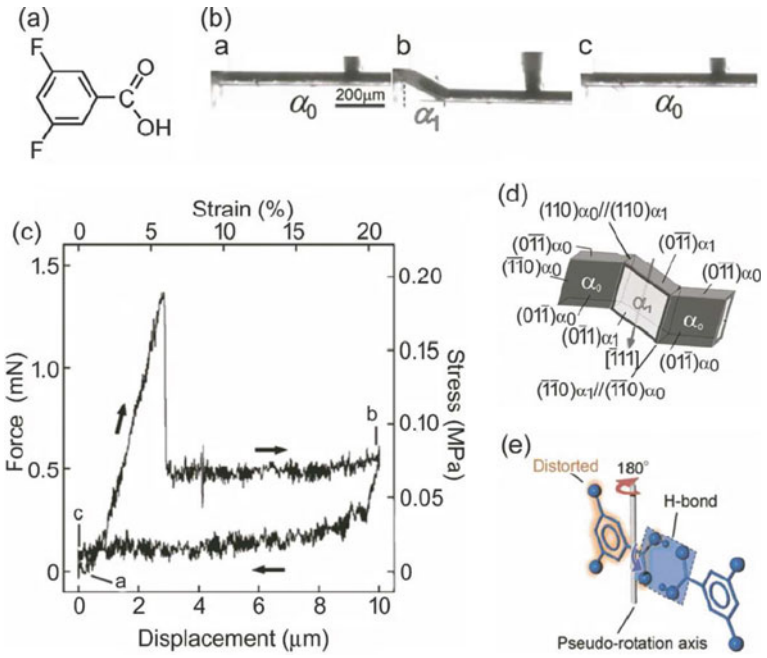

Fig. 6.6 **a** Chemical structure of 3,5-difluorobenzoic acid (FBA), **b** superelastic deformation of FBA, **c** stress–strain curve of deformation, **d** face indices of a mechanically twinned FBA crystal, and **e** possible molecular movement during twinning. Reproduced with permission from ref. [12]

6.2.3 Organosuperelastic Crystals Exhibiting Luminescent Chromism

2-(2′-Hydroxyphenyl)imidazo[1,2-a]pyridine (HPIP) shows a large Stokes-shift emission (ESIPT emission) due to photoirradiation-induced intramolecular charge separation caused by an excited-state proton transfer. Mutai et al. have previously reported crystal-polymorph-dependent ESIPT luminescence in HPIP and its derivatives [13]. Superelasticity was discovered in the luminiscent 7-chloro-2-(2′-hydroxyphpenyl)imidazo[1,2-*a*]pyridine (**7Cl**) (Fig. 6.3) crystals with intramolecular hydrogen bonding. The yellow-green luminescent crystal phase (α_{YG}) of **7Cl** exhibited superelasticity [14]. A yellow-orange luminescent crystal phase (α_{YO}) was generated via phase transition induced by mechanical loading and spontaneously recovered to the original α_{YG} phase after unloading (Figs. 6.7a and 7b). The appearance of each crystalline phase was revealed via X-ray structural analysis, and the face index of the crystalline-phase interface was (120)YG//(120)YO (or (120)YG//(120)YO). The calculated value of the bending angle (42.1°) was consistent with the value measured microscopically (42°). The bending angles of the crystalline phases during the transition from Y to YO, the 68-degree (or 61-degree and 16-degree) rotation of

the 7Cl molecules, and their further mutation by 2.0 and 1.9 Å suggested an optimized herringbone-type arrangement (Fig. 6.7c). This mechanochromic luminescence mechanism is based on superelasticity (plastic deformation without diffusion and spontaneous shape recovery), which allows reversible, stepless, and instantaneous control over the two-color emission ratio via a single-crystal-to-single-crystal phase transition by controlling a single stimulus: stress [14].

6.2.4 Superelasticity in Metal-Complex Crystals

Metal complexes combine the excellent designability of organic molecules with the excellent electronic properties of metal atoms. In particular, coordination polymers with porous structures are expected to be useful for gas adsorption and other applications, based on the uptake of guest molecules. Mechanical twinning-based superelasticity was observed in one such type of porous coordination polymer, the $\{Cu_2(bza)_4(pyz)\}_n$ (bza = benzoate, pyz = pyradine; CuBP) crystal (Fig. 6.3) [15], which exhibits gas permeability along the channel direction. Interestingly, they succeeded in reversibly converting the channel direction into a nearly orthogonal direction via mechanical twinning followed by superplasticity (Fig. 6.8). Such a single-crystal–gas-permeable film, with a controllable channel structure achieved via mechanical force, is a good example of the effective use of structural changes accompanied by superelasticity.

6.2.5 Shape-Memory Effect

Next, we focus on the shape-memory effect in organic crystals. In the search for organic superelastic materials, tetrabutyl-n-phosphonium tetraphenylborate (BPPB) crystals were found to exhibit strong elastic, superelastic, and shape-memory effects (Fig. 6.9) [16]. When columnar BPPB crystals, obtained via recrystallization from acetone, were sheared at room temperature, they bent at approximately 12°, while generating a daughter (α^-) phase from the mother (α^+) phase, and maintained this shape after stress relieving. Upon heating, the crystals transitioned to the high-temperature (β) phase at approximately 125 °C, yielding a linearly layered phase. When cooled to approximately 122 °C, the crystalline phase became linear—containing only the α^+ phase—via a bending state, wherein it coexisted with the α^- phase. Essentially, it exhibited the shape-memory effect (Fig. 6.9b). The crystals exhibited superelasticity due to stress-induced phase transition at approximately 125 °C, where the high-temperature phase was stable and the deformation and reverse-deformation stresses increased with the temperature (Fig. 6.9c), which was similar to the temperature dependence of the superelasticity of alloys. Although organic crystals are recognized to be brittle and fragile, these shape-memory effects and the increase in the shape recovery with temperature proved that even a small crystal,

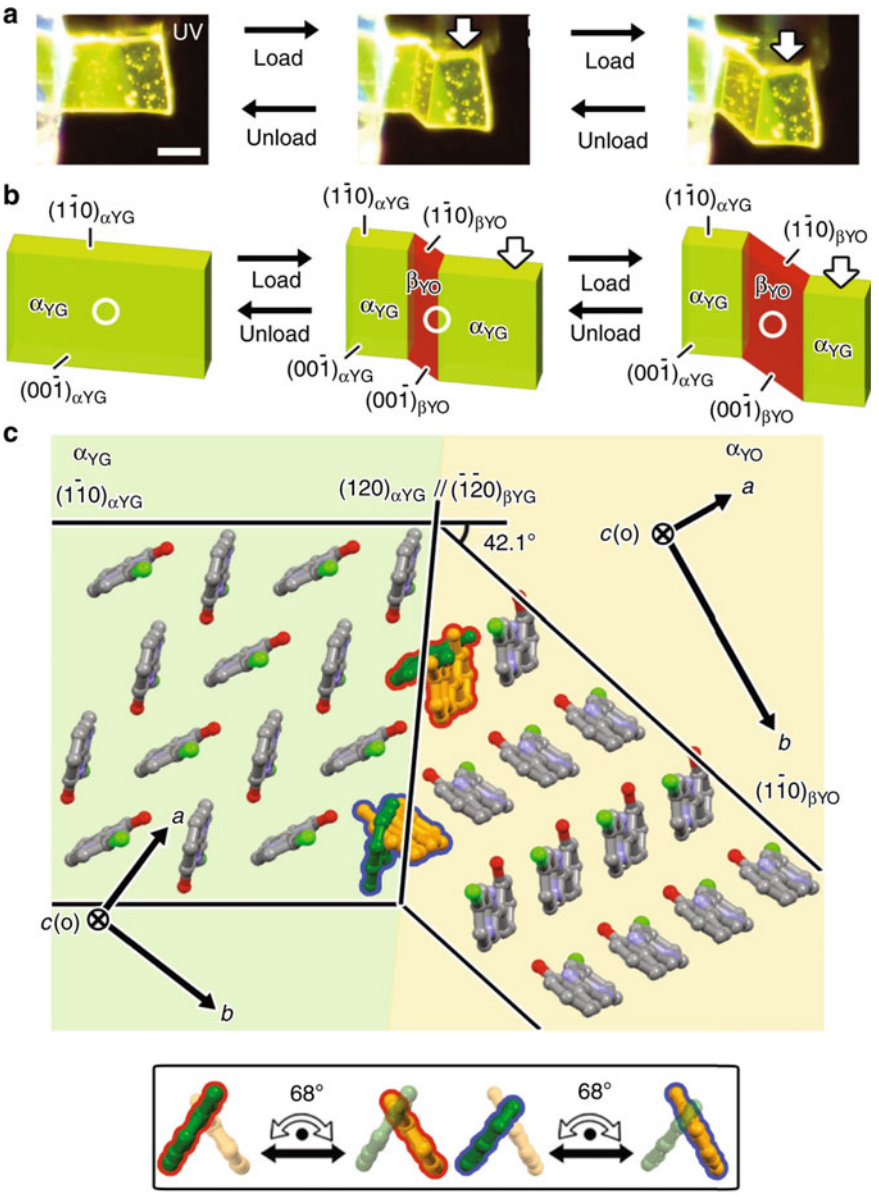

Fig. 6.7 **a** Snapshots of superelastic deformation of a YG crystal under UV light (365 nm) (scale bar: 100 μm). **b** Schematic representation of superelastic deformation and **c** estimated molecular correspondence at the αYG//βYO interface in a deformed YG crystal based on X-ray results. Reprinted with permission from ref. [14]

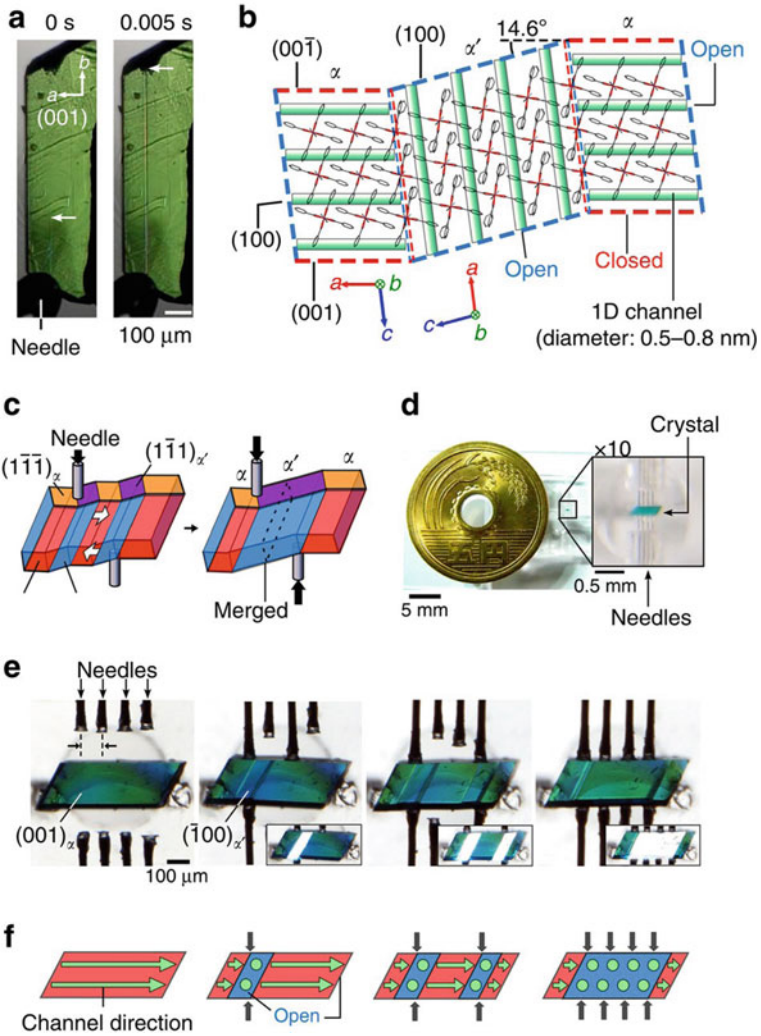

Fig. 6.8 **a** Growth of a 5-μm-wide band from the pushed edge of the (1–1-1) crystal surface at room temperature. **b** Connection of the mother (α) and daughter (α′) crystal phases at 298 K accompanied by the rotation of the channel direction (green bands) under the twinned state at a bending angle of 14.6° along the projected direction of [010]α and [010]α′, based on crystallography. **c** The regulation of the α′ crystal domains sandwiched by the pushing positions as a shear on {1–1-1}α. **d** The experimental system. **e** Active generation/degeneration of the daughter-crystal domains by shearing the microcrystal of 1 ($0.48 \times 0.17 \times 0.10$ mm^3) with movable needles and **f** the directions of the penetrating channels. Reprinted with permission from ref. [15]

with a width and thickness of 0.6 and 0.3 cm, respectively, can bear >100 g of weight (Fig. 6.9d). The BPPB crystals also proved that superelasticity can be achieved in multicomponent organic crystals such as organic salts, co-crystals, and inclusion compounds, indicating the possibility of tuning superelastic properties by changing the combinations of molecules.

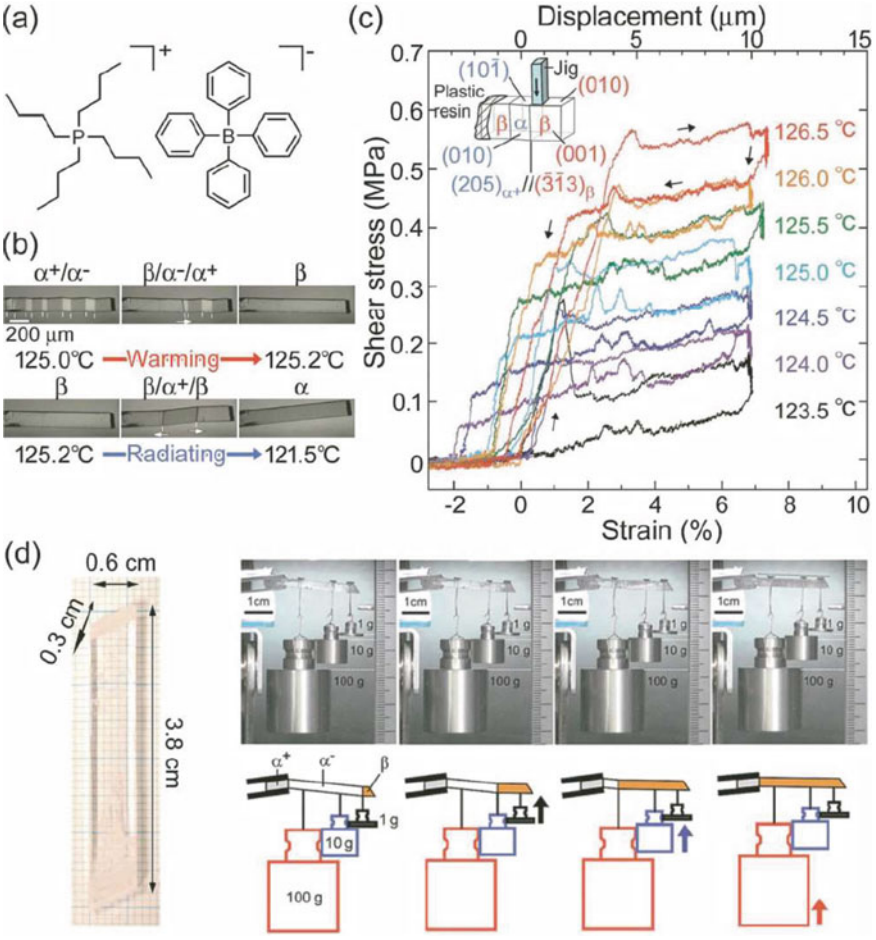

Fig. 6.9 **a** The chemical structure of tetrabutyl-n-phosphonium tetraphenylborate (BPPB), **b** shape-memory effect in BPPB, **c** temperature-dependent stress–strain curves, and **d** mechanical work using the shape-memory effect of a BPPB crystal. Reproduced with permission from ref. [16]

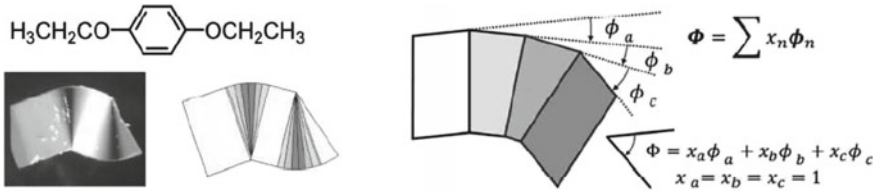

Fig. 6.10 Ferroelastically deformed 1,4-diethoxybenzene (EB). Reprinted with permission from ref. [19]

6.3 Organic Ferroelasticity

Ferroelasticity is a non-diffusive plastic deformation that shows spontaneous strain and is characterized by hysteresis of symmetric stress–strain curves. Despite being extensively studied in inorganic crystals, owing to its tractability and functionality, ferroelasticity was first reported in the organic squaric acid crystals [17]. In 2017, ferroelastic deformation and the corresponding hysteresis curves were observed for 5-chloro-2-nitoroaniline (CNA) crystals, and the molecular deformation mechanism was elucidated via X-ray crystallography [18]. Systematic investigation revealed ferroelasticity to be a relatively common phenomenon even in organic crystals, which are considered to be brittle and fragile. X-ray crystallographic analyses also revealed ring rotation, conformational change of alkyl chains, and flipping of cyclohexane rings, which reflect the molecular structure of crystals. 1,4-Diethoxybenzene (EB) crystals exhibited deformation due to zone-multiple twinning, which constituted continuous mechanical twinning around the zone axis [19]. Thus, strains many times higher than those attainable via single mechanical twinning deformation were achieved (Fig. 6.10). Such free deformability, accompanied by the retention of the crystalline nature of single crystals, is unique. As described previously, ferroelasticity is an attractive property in the formation of organic crystals, because it allows permanent strain beyond the elastic limit while maintaining crystallinity. The energy-dissipation property of ferroelasticity is also expected to be useful in vibration absorption.

6.4 Coexistence of Organic Superelasticity and Ferroelasticity

Superelasticity shows spontaneous shape recovery, whereas ferroelasticity shows spontaneous strain (permanent strain). Therefore, they are regarded as properties with opposing mechanical responses. The shape-memory effect can be achieved by switching these two properties via thermal phase transition. If these two properties can be made to coexist under identical conditions, organic crystals can be made to exhibit superelasticity in multiple directions, depending on the shape deformed by

a ferroelastic forming process. Multidirectional superelasticity can create organic crystalline materials with free-deformation superelasticity, such as shape-memory alloys. Here, as examples of coexistence of organic superelasticity and ferroelasticity, we will describe a superelastic–ferroelastic transformation process and a shear-direction-selective expression of superelasticity and ferroelasticity.

6.4.1 Shape Remembrance and Antiferroelasticity of Organic Crystals Via Superelastic–Ferroelastic Conversion

1,4-Dicyanobenzene (DCB) crystals show superelasticity due to mechanical twinning (Fig. 6.11) [20], even though they do not have a conformationally changeable site like FBA, as described in Sect. 6–2-2. The superelasticity of DCB is attributable to rotational twinning at 180°, as in FBA crystals, but the actual motion during the deformation was elucidated to be an orientational change of only 5–7°, rather than the rotation of the entire molecule by 180°. Interestingly, by holding the DCB crystal in the bent shape for a long time, the mechanical properties of the bent region were found to gradually change as superelastic → ferroelastic → superelastic, and the crystal became uniaxially superelastic in two directions, positive and negative (Fig. 6.11). The shape of the stress–strain hysteresis curve of such uniaxial bidirectional superelasticity resembles that of the electric-field-polarization hysteresis curve of antiferroelectric materials, indicating antiferroelasticity proposed by Aizu in 1969 [21]. In the case of shape remembrance (rewriting) from a straight shape to a bent shape via memory processing, a processing time $\geq$300 h was required before antiferroelasticity was exhibited. At a higher temperature of 50 °C, the processing time was shortened, and antiferroelasticity was observed after approximately 200 h. While returning the flexural shape to the original linear system, shape remembrance progressed 60–200 times faster than the flexural shape memory. In contrast to the shape-memory treatment of shape-memory alloys, which requires heating to several hundred degrees Celsius or higher, DCB crystals can be treated at <100 °C. Although DCB crystals have a low thermal stability and sublimate at high temperatures, the thermally stable organic superelastic crystals can be processed in seconds to minutes at temperatures >100 °C. Shape remembrance has not yet been achieved in DCB crystals because of their low thermal stability. Further investigations into shape-remembrance properties and low-temperature and high-speed shape-memory processing could lead to the discovery of practical applications of organic superelastic materials.

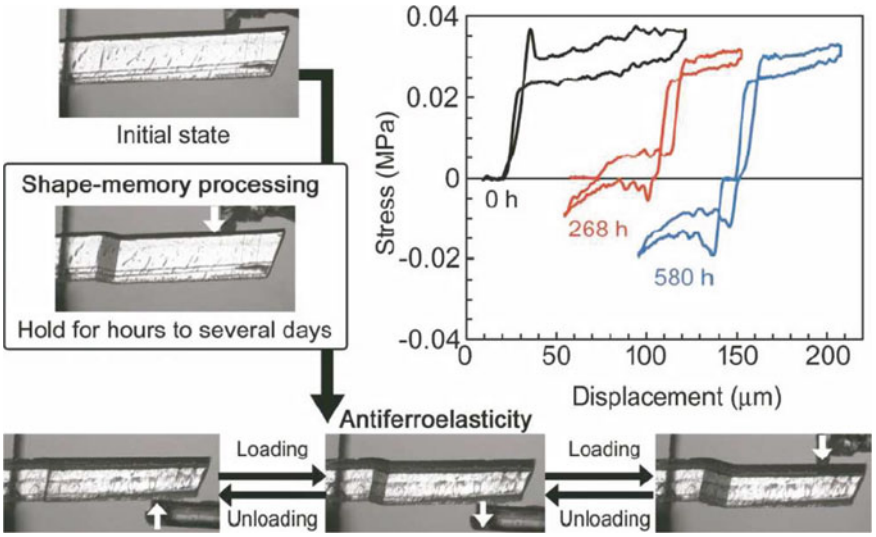

Fig. 6.11 Shape-memory processing and superelastic behavior of a DCB crystal in opposing directions (antiferroelasticity) with stress–strain curves after shape-memory processing for 0 h (black), 268 h (red), and 580 h (blue). Reprinted with permission from ref. [20]

6.4.2 Shear-Direction Selectivity of Superelasticity-Ferroelasticity and Multidirectional Superelastic Crystals

Metallic crystals, which are aggregates of spherical atoms, have multiple crystallographically equivalent directions and show identical responses in these directions. In contrast, organic crystals exhibit strongly anisotropic structures and functions due to the shape of their constituent molecules. Organic hyperelasticity and ferroelasticity are also caused by the anisotropic molecular motion induced by the application of shear stress to organic crystals from a specific direction, indicating the possibility of selective expression of superelasticity and ferroelasticity in single crystals depending on the loading direction.

Recently, shear-direction-dependent manifestations of superelasticity and ferroelasticity were observed in 1,3-bis(4-methoxyphenyl)urea (MPU) crystals (Fig. 6.3) [22]. Furthermore, zigzag, crankshaft, S-shaped, and U-shaped MPU crystals exhibiting multidirectional superelasticity were fabricated by subjecting MPU crystals to permanent strain via ferroelastic deformation and exploiting the coexistence of superelasticity and ferroelasticity in the unified crystals (Fig. 6.12). Each deformation was a mechanical twinning that maintained its single-crystalline and superelastic properties. Thus, each of the differently oriented single-crystalline domains was a multidirectional superelastic crystal.

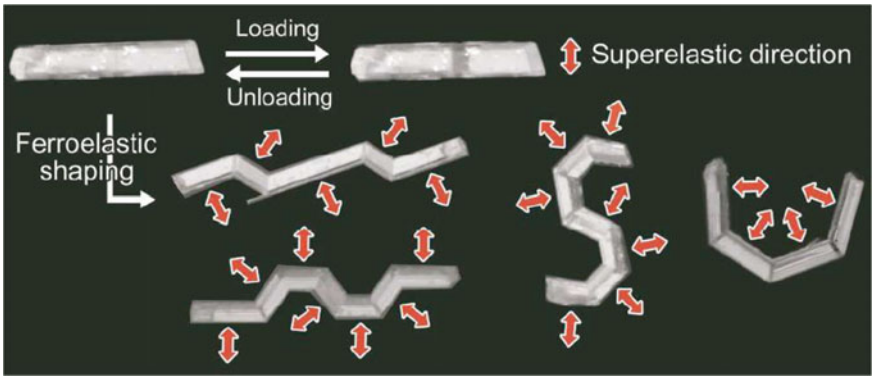

Fig. 6.12 Directions of superelasticity before and after ferroelastic shaping of MPU crystals. Reprinted with permission from ref. [22]

6.5 Organic Superplasticity

Superplasticity, originally known as a processing and forming method for metallic materials, enables the deformation of solids by more than several hundred percent via grain-boundary slip of polycrystalline bands under heating. Organic crystals, which are considered to be brittle and fragile, can also exhibit deformations of several hundred percent or more without losing their crystallinity, a phenomenon we call "organic superplasticity" [23].

The chiral and polar N,N-dimethyl-4-nitoroanilinie (MNA) crystals—having electron-withdrawing nitro groups in the para position of the electron-donating dimethylamino groups, a large dipole moment, and an achiral molecular structure despite belonging to the $P2_1$ space group—were investigated. Plate-like MNA crystals, obtained using acetone, showed superelasticity, whereby they bent at approximately 23° due to mechanical twinning via shear and spontaneously recovered their shape when the force was removed. X-ray crystallographic analysis of the bent crystals suggested that the mechanical twinning caused a change in the dihedral angle of <3° between the dimethylamino and nitro groups with respect to the benzene ring. Due to such miniscule changes, the mother (α_0) and daughter (α_1) phases of the twins had a crystallographic relationship of rotational symmetry at 180°. Interestingly, when a shear force was applied to the plate-like MNA crystal parallel to the (001) plane in the [100] direction, the crystal exhibited multiple slip planes and finally a shear strain of >500% (Fig. 6.13). Thus, a superplastic deformation mechanism different from that of metallic materials was found. After deformation, the crystals also showed superelasticity, indicating that the single-crystalline nature was maintained even after slip deformation. Organic superplasticity, which enables large deformation of organic crystals while maintaining their crystalline properties, can provide new formability to organic crystals and has basic and applied research prospects.

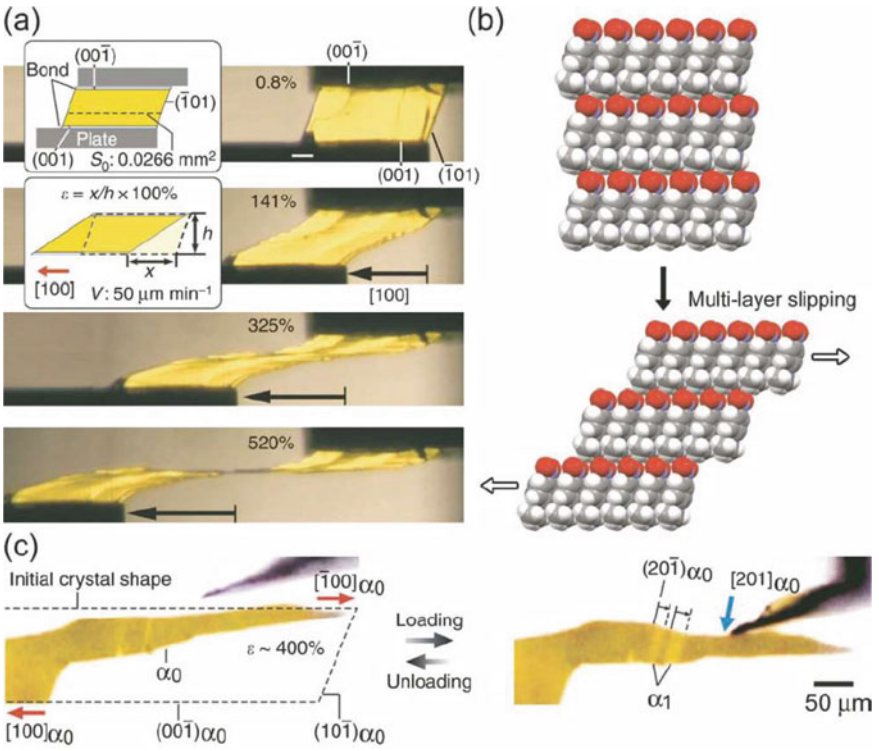

Fig. 6.13 **a** Superelastic behavior of an MNA crystal via multilayer slipping and **b** the estimated molecular movement in the crystalline state. **c** Superelastic behavior after superplastic deformation ($\varepsilon = 400\%$) of an MNA-crystal deformation. Reprinted with permission from ref. [23]

6.6 Conclusion

In this chapter, we discussed the rigorous deformability of molecular crystals via hyperelasticity, ferroelasticity, and superplasticity. Previously, organic crystals were considered to be fragile, and their mechanical properties had been largely ignored. However, intensive research has significantly advanced organic superelasticity and related theories. Recently, organic superelastic crystals have been actively developed [24]. Organic superelasticity is expected to create a variety of functional elastic materials with higher-order properties and functions than those of conventional alloys and polymers. The addition of superelasticity to the fundamental properties of materials, such as elasticity and plasticity, could lead to new developments in materials chemistry.

References

1. Kitaigorodskii AI (1973) Molecular crystals and molecules. Academic Press, London
2. (a) Naumov P, Chizhik S, Panda MK, Nath NK, Boldyreva E (2015) Chem Rev 115:12440; (b) Saha S, Mishra MK, Reddy CM, Desiraju GR (2018) Acc Chem Res 51:2957–2967; (c) Karothu DP, Mahmoud J Halabi, Ahmed E, Ferreira R, Spackman PR, Spackman MA, Naumov P (2022) Angew Chem Int Ed Engl **61**:e202113988; (d) Spackman PR, Grosjean A, Thomas SP, Karothu DP, Naumov P, Spackma MA (2022) Angew Chem Int Ed Engl 61:e202110716; Koshima H, Hasebe S, Hagiwara Y, Asahi T (2021) Isr J Chem 61:683–696; Yu Q, Aguila B, Gao J, Xu P, Chen Q, Yan J, Xing D, Chen Y, Cheng P, Zhang Z, Ma S (2019) Chem Eur J 25:5611–5622
3. Ölander A (1932) J Am Chem Soc 4:3819
4. Greninger AB, Mooradian VG (1938) Trans. Metallurg. Soc. AIME 128:337
5. (a) Aizu K (1970) Phys Rev B 2:754
6. Chang C, Read TA (1951) Transactions of the AIME 189:47
7. Buehler WJ, Gilfrich JV, Wiley RC (1963) J Appl Phys 34:1475
8. (a) Otsuka K, Ren X (1999) Intermetallics 7:511; (b) Jani JM, Leary M, Subic A, Gibson MA (2014) Mater Des 56:1078
9. Takamizawa S, Miyamoto Y (2014) Angew Chem Int Ed 53:6970
10. (a) Sokolowski WM, Chmielewski AB, Hayashi A, Yamada T (1999) Proceedings of Society of Photooptical Instrucmentation Engineers (SPIE), vol 3669, p 179; (b) Lendlein A, Kelch S (2002) Angew Chmie Int Ed 41:2034; (c) Behl M, Lendlein A (2007) Mater Today 10:20
11. Takamizawa S, Takasaki Y (1912) Cryst Growth & Des 2019:19
12. Takamizawa S, Takasaki Y (2015) Angew Chem Int Ed 54:4815
13. (a) Mutai T, Tomoda H, Ohkawa T, Yabe Y, Araki K (2008) Angew Chem Int Ed 47:9522–9524; (b) Mutai T, Shoni H, Shigemitsu Y, Araki K (2014) CrystEngCom 16:3890–3895
14. Mutai T, Sasaki T, Sakamoto S, Yoshikawa I, Houjou H, Takamizawa S (1824) Nat Commun 2020:11
15. Takasaki Y, Takamizawa S (2015) Nat Comm 6:1–5
16. Takamizawa S, Takasaki Y (2016) Chem Sci 7:1527
17. Suzuki I, Okada K (1979) Solid State Commun 29:759–762
18. Mir SH, Takasaki Y, Engel ER, Takamizawa S (2017) Angew Chem Int Ed 56:15882–15885
19. Engel ER, Takamizawa S (2018) Angew Chem Int Ed 57:11888–11892
20. Sakamoto S, Sasaki T, Sato-Tomita A, Takamizawa S (2019) Angew Chem Int Ed 58:13722
21. Aizu K (1969) J Phys Soc Jpn 27:1171–1178
22. Sasaki T, Sakamoto S, Takamizawa S (2020) Angew Chem Int Ed 59:4340–4343
23. Takamizawa S, Takasaki Y, Sasaki T, Ozaki N (2018) Nat Comm 9:3984
24. Ahmed E, Karothu DP, Naumov P (2018) Angew Chem Int Ed Engl 57:8837–8846

Open Access This chapter is licensed under the terms of the Creative Commons Attribution 4.0 International License (http://creativecommons.org/licenses/by/4.0/), which permits use, sharing, adaptation, distribution and reproduction in any medium or format, as long as you give appropriate credit to the original author(s) and the source, provide a link to the Creative Commons license and indicate if changes were made.

The images or other third party material in this chapter are included in the chapter's Creative Commons license, unless indicated otherwise in a credit line to the material. If material is not included in the chapter's Creative Commons license and your intended use is not permitted by statutory regulation or exceeds the permitted use, you will need to obtain permission directly from the copyright holder.

Chapter 7
Triboluminescence of Lanthanide Complexes

Miki Hasegawa and Yasuchika Hasegawa

Abstract The photoluminescence of lanthanide complexes originating from f–f transitions is generally sensitized through energy transfer from the ligand to the lanthanide ion in the excited state under UV irradiation. This phenomenon is known as the photo-antenna effect. Luminescence driven by mechanical stimuli, such as tapping or rubbing, is called mechanoluminescence or triboluminescence (TL). In recent years, reports on TL in rare-earth complexes, which have attracted attention as novel luminescent materials that do not require an electrical excitation source, have steadily increased. In this chapter, we focus on triboluminescent lanthanide complexes. Specifically, we introduce the history and detection methods of TL and cite recent examples of materials demonstrating this phenomenon, particularly coordination polymer-like and discrete molecular crystalline lanthanide complexes. Finally, we summarize the application prospects of these complexes as soft crystals.

Keywords Triboluminescence · Lanthanide complexes · Crystal structure · Coordination polymer · Mechanical luminescence

7.1 Introduction

Changes in state from solid to liquid to gas occur as energy is absorbed and released. The single crystal–single crystal and crystal–amorphous phase transitions of molecular systems, such as soft crystals, as well as their chromic behavior, have recently been observed [1]. Mechanical stimulation can induce chemical changes by providing pressure-induced stimuli [2, 3] and changes in energy between excited states during electronic transition [4–8]. Especially in the case of molecular crystals, electronic absorption and emission bands are induced by changes in the distortion

M. Hasegawa (✉)
Department of Science and Engineering, College of Science and Engineering, Aoyama Gakuin University, 5-10-1 Fuchinobe, Chuo-Ku, Sagamihara-Shi, Kanagawa 252-5258, Japan
e-mail: hasemiki@chem.aoyama.ac.jp

Y. Hasegawa
Division of Applied Chemistry, Faculty of Engineering, Hokkaido University, Kita 13, Nishi 8, Kita-Ku, Sapporo 060-8628, Hokkaido, Japan

© The Author(s) 2023

M. Kato and K. Ishii (eds.), *Soft Crystals*, The Materials Research Society Series,
https://doi.org/10.1007/978-981-99-0260-6_7

or co-planarity of π-electronic systems depending on the flexibility of the bonds of functional groups under high pressure.

In this chapter, we introduce the concept of triboluminescence (TL) in lanthanide complexes; TL is a mechanoluminescence (ML) property and refers to the luminescence phenomenon observed when crystals are fractured. Mechanochromic luminescence has been reported in polymorphic systems, and ML could be observed in not only inorganic compounds but also organic crystals and complexes [9–13]. ML systems can be roughly classified into two groups: systems that show photoluminescence (PL) changes under UV excitation and those that show PL without the need for photoexcitation. In this chapter, we focus on the TL of lanthanide complexes, which manifests as luminescence during crystal fracturing under a driving force, such as a shock wave or shearing (Fig. 7.1).

TL can be observed by crushing sucrose crystals or striking quartz rocks against each other with force [14]. While it is a phenomenon that is widely observed in both organic or inorganic compounds, the TL phenomenon is incompletely understood. This problem is attributed to three main reasons: (1) the principle behind TL remains a matter of speculation, (2) the stimulus cannot be quantified at the time of collision, and (3) the available methods and means to observe luminescence and structural phase transitions are insufficient.

Xu et al. [15] observed TL in systems in which Eu and Dy were loaded on Sr alumina. This phenomenon was thus believed to be related to thermally excited states via the defect levels of the alumina. Several hypotheses have been offered to explain the principle of TL in organic molecules and complexes. For example, the excitation of atmospheric N_2 is believed to be promoted by the frictional energy during rubbing, which results in emission [16]. A recent report indicated that X-rays are generated when Scotch tape is rubbed at high speed [17]. Knowledge of the activation principle, manipulation, and material design of the TL phenomenon can lead to the development of new energy-conversion materials.

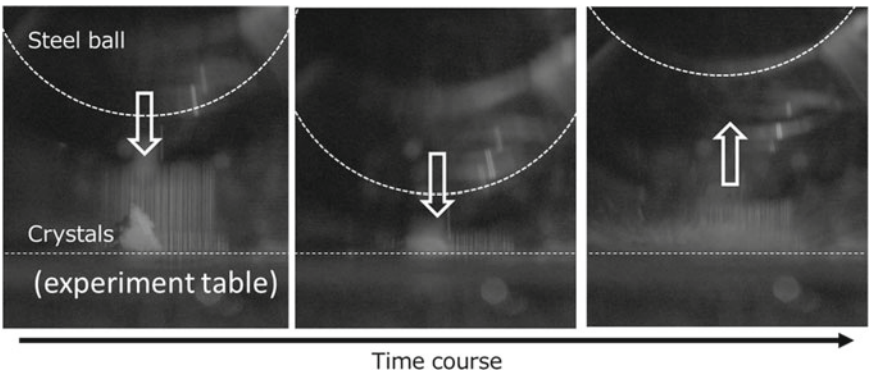

Fig. 7.1 Snapshots of Eu-complex crystals crushed by a drop-tower system and recorded by a high-speed camera (Photoron Co., Ltd.). The ball size diameter is ca. 170 mm (Private data: M. Hasegawa, AGU). See also Fig. 7.8

PL is enhanced or quenched under different atmospheres, such as N_2 or O_2, because the spin multiplicity of orbitals involved in energy relaxation varies depending on the central metal species. In particular, lanthanide complexes are suitable candidates for understanding the photophysical principle of TL because their PL phenomena are based on lanthanide-specific f–f transitions arising from the spin multiplicity of excited organic ligands.

7.2 Aim of This Chapter

In this chapter, we discuss the history and measurement methods of TL, the quantification of stimuli, and various theories of the principle of TL expression, focusing on lanthanide complexes as examples of TL soft crystals. The f-electron configurations of lanthanides are $[Xe]4f^{n+1}$ ($n = 3, 5, 6, 9, 12, 13$; Ln = Nd, Sm, Eu, Dy, Tm, Yb) and $[Xe]4f^n$ 5d ($n = 0, 1, 2, 7, 8, 10, 11, 14$; Ln = La, Ce, Pr, Gd, Tb, Ho, Er, Lu). The luminescence bands can be classified into two main types: f–f transitions localized in f orbitals, which are inherently forbidden, and d–f transitions [18]. In this chapter, we mainly discuss the f–f transitions (or f–f luminescence) of lanthanide complexes with organic molecular ligands.

In general, the PL of lanthanide complexes is due to the highly efficient photoexcitation of π-electronic ligands under UV light irradiation. Energy transfer from the excited ligand to the lanthanide ion promotes f–f luminescence from the latter [19]. In the 1960s, the crystal-field splitting levels of the f orbitals of a series of trivalent lanthanide ions were attributed to the photoemission spectra of He (see Sect. 7.4.1 [20]). The crystal-field splitting levels are not drastically influenced by the surrounding media. Eu^{III} and Tb^{III} show red and green emissions, respectively, when energy transfer is established, regardless of the ligand type. As the absorption coefficient of the f–f transition is very small and the Stokes shift is almost zero, the luminescence obtained from the direct excitation of f–f absorption has weak efficiency. The emergence of f–f luminescence observed via the photoexcitation of the ligand is called the photo-antenna effect, which is used to increase in the efficiency of PL. The luminescence lifetime and quantum yield of PL have been experimentally evaluated in both organic and inorganic luminescent materials.

In contrast to PL, not much about the principle of TL and its possible manifestation is known. The earliest surviving document on this topic dates back 400 years (see Sect. 7.3, [21]). However, the methods for TL evaluation remain in the developmental stage, and various TL molecular designs and principles have been proposed.

Here, we introduce some methods to measure the TL of lanthanide complexes and discuss the effects of soft-crystalline structural changes on this phenomenon.

7.3 History of Triboluminescence Derived from Weak Stimuli

A fundamental issue in chemistry is the relationship between the effects of macroscopic mechanical stress on bulk materials and the molecular-level changes in the structure and properties of these materials [22]. Various mechanochemical effects have been studied to determine this relationship, among which stress and macroscopic distortion were observed to induce changes in microscopic properties, such as mechanochromic, piezoelectric, and photomechanical properties [23]. TL is also an interesting phenomenon of mechanical stress [24]. In the seventeenth century, Francis Bacon observed light emission from sugar cubes during crushing [24]. Different types of materials exhibiting TL, such as organic crystals, polymers, and metal complexes, have been studied [25–27]. The origin of TL has been discussed, and some recent studies have demonstrated the contribution of the piezoelectric effect to this phenomenon during the breakage of non-centrosymmetric bulk crystals [27]. The structure of sugar crystals, which are chiral and, thus, have a non-centrosymmetric structure, is expected to contribute significantly to their obvious TL [28]. The hydrogen-bonding networks in sugar crystals also seem to contribute to their relatively large resistivity against mechanical stress prior to their breakdown and, thus, their intense TL.

The publication trend of studies on TL was determined using the information retrieval system Web of Science (research date: January 20, 2022). The trend of publications on TL and ML is shown in Fig. 7.2.

TL can be induced by crushing the crystals of minerals, sugars, etc. In 1903, Armstrong and Lowry speculated that a two-state transformation based on the structural change of N atoms is induced when crystals of saccharine, a type of sugar, are crushed [29]. In 1910, Andrews reported that yellow TL was produced by crushing a mixture of 70% zinc carbonate, 30% fluorinated sulfur, and a small amount of manganese sulfide [30]. In 1911, Alfred described the TL of U metal in the scientific journal *Nature* [31]. Publications on TL research began to increase in 1967, but only a

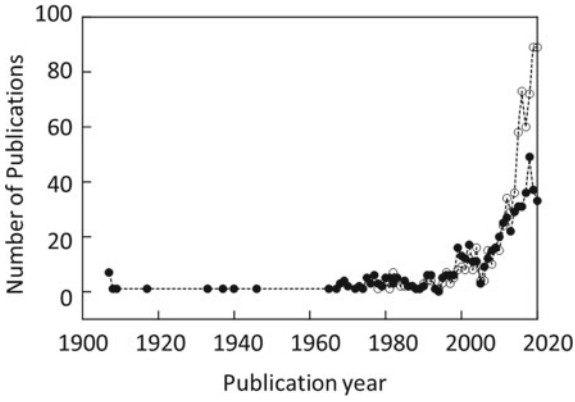

Fig. 7.2 Number of publications on triboluminescence (black dot) and mechanoluminescence (circle) from 1900 to January 2021 in Web of Science®

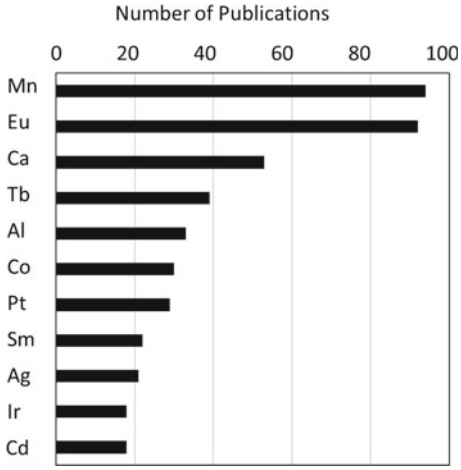

Fig. 7.3 Element-classified statistics of published papers on triboluminescence

few papers on the origins of TL were published annually until the year 2000. Reports on ML began to be increase in 1980. In 2010, the number of papers describing TL and ML were almost equal. In 2020, the number of papers describing ML was four times greater than that describing TL.

Various TL materials and their luminescence phenomena have been reported and investigated worldwide. Figure 7.3 shows the statistics of published papers on TL according to element.

The data show that many reports on TL materials containing Mn and Eu have been published. The TL of both inorganic manganese-compounds and Mn(II) complexes has been reported. The TL of inorganic Eu(II)-ion containing compounds and Eu(III) complexes has also been described. Ca and Al have been reported to be host media for TL materials. TL materials containing Pt and Ir have also been reported.

7.4 Luminescent Lanthanide Complexes

7.4.1 Evaluation of Photoluminescence by the Photo-Antenna Effect

PL provides a large amount of information that could be used to evaluate the TL of lanthanide complexes. Because the experimental method of photoexcitation has previously been established and the apparatus is commercially available, the measurement of PL is relatively easy. Such measurements allow us to determine the position of the luminescence band and quantitatively determine the luminescence lifetime and quantum yield. Here, we describe the principle of the PL of lanthanides and its evaluation.

The f–f transition of lanthanide ions involves a transition between electronic levels due to the splitting of the f orbital. This level is not susceptible to the so-called ligand field, unlike d-group metal ions, because lanthanides are inner-shell transition-metal ions, and the f orbital, which controls the properties, is in the inner shell, while the d or s orbitals, which are involved in bonding, are in the outer shell. Given this electronic structure, the half-width of the absorption or emission band due to the f–f transition is narrower and less affected by the coordination field compared with those of d-meal complexes. In other words, the splitting energy levels of the f orbitals are constant for any coordination atom or ligand, which can be attributed to a series of He photoemission spectra of lanthanide chlorides [20]. A diagram of these energy levels is called a Dieke diagram (Fig. 7.4).

Because f–f transitions are inherently forbidden and the Stokes shift is small, deriving the f–f emission from the excitation of the absorption bands of f–f transitions is challenging. The optical antenna effect can overcome this difficulty. The photo-antenna effect can enhance the f–f emission of lanthanide ions via the excitation energy of a π-electronic ligand with a large absorption coefficient complexed with a lanthanide ion [33].

In general, many complexes of Eu and Tb have been synthesized because they show red and green luminescence, respectively. Establishing a good relationship between the excited state energy of the ligand and acceptor level of Eu and Tb is important for more efficient luminescence. The concepts of Dexter- [34] or Förster [35]-type energy transfer can be applied to the optical antenna effect of lanthanide complexes, which is based on (1) energy level resonance between the energy donor (EnD) and acceptor (EnA), (2) energy transfer between the EnD and conservation of spin multiplicity before and after energy transfer at the EnA level, and (3) the distance between the EnD and EnA (Fig. 7.5).

The Dieke diagram (Fig. 7.4) shows that the EnA level depends on the type of metal ion. Therefore, the EnD level can be designed as necessary to promote highly efficient energy transfer and luminescence. In fact, the singlet energy level of Pr functions as EnA and a molecule tailored to this level can promote f–f luminescence at the selected level [32]. The EnD levels of the ligands of lanthanide complexes can be determined by coordinating them with Gd, which does not have an EnA level, and measuring its fluorescence and phosphorescence to determine the position of the excited singlet and triplet, respectively [36].

7.4.2 Evaluation Methods of Triboluminescence

TL could be manifested by directly applying mechanical stimuli, such as pressure [37], rubbing [38], laser ablation [39], and direct impact [40], to crystals, for example, by (Fig. 7.6). Video recording followed by image analysis and spectral detection by connecting optical fibers to a small spectrometer, for instance, have been reported. Quantifying stimuli and quantitative TL analysis are still under development. In this section, we introduce the evaluation methods of TL materials.

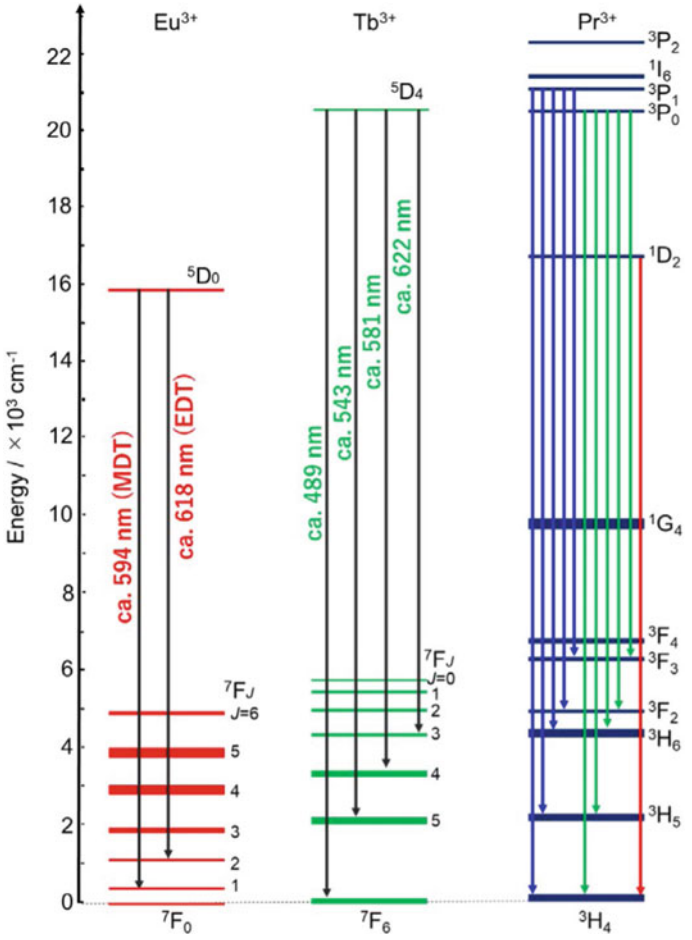

Fig. 7.4 Dieke diagram of trivalent Eu, Tb, and Pr ions for different luminescence band wavelengths. MDT = magnetic dipole transition; EDT = electric dipole transition. Ref. [32] Copyright (2020) Chemical Society of Japan

Many reports of the use of digital cameras to capture the exact moment when crystals are crushed or rubbed with a metal spatula or glass rod have been published [41]. Such recordings are important to the observation of TL in the visible region.

Xu et al. developed a method in which an inorganic oxide exhibiting mechanical luminescence is mixed with a polymer and solidified into a disc; the disc is then stimulated by rubbing at different rotational speeds [38].

Xu et al. combined the method of constant pressure and observation in a photo cell to measure the spatial distribution of luminescence in situ (Fig. 7.7) [37]. They also reported a method in which a sample is applied to a stainless-steel plate with crack-inducing slits and the plate is pulled at opposite sides to observe the resulting

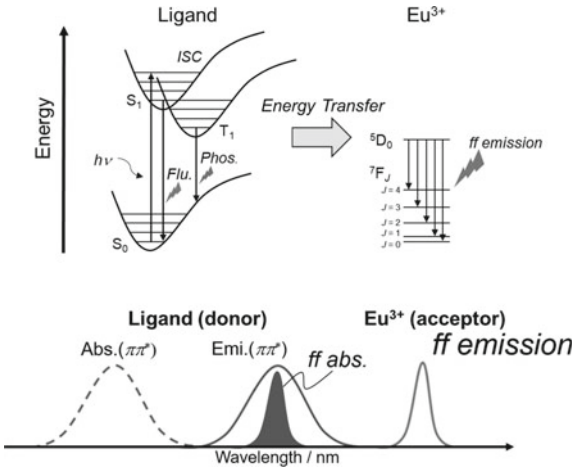

Fig. 7.5 Energy diagram of the f–f emissions induced by the photo-antenna effect (top). Principle of the acceleration of energy transfer by the superimposition of ligand-centered emission (π–π* transition) and lanthanide-centered absorption (f–f transition) (bottom)

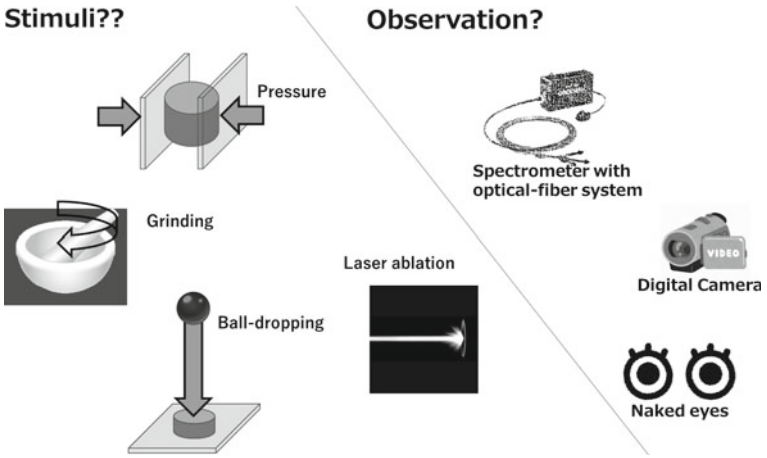

Fig. 7.6 Various stimuli used to enhance triboluminescence and its observation methods

TL. This approach could be used as a diagnostic method to visualize the correlation between cracks in the stainless-steel plate and the distorted portions of the plate, not just single crystals.

Tsuboi et al. reported the quantitative measurement of the TL of sucrose using laser ablation [39]. Suslick et al. successfully induced TL with ultrasound and measured its spectrum [39]. Ilatovskii et al. reported a method to achieve the quantitative stimulation of membraned TL materials using a texturometer [39].

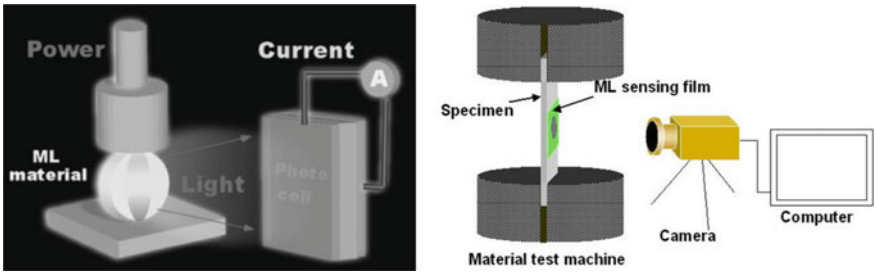

Fig. 7.7 Image of the mechano-luminescence sensing system. Ref. [37] Copyright (2007) The Japan Society of Applied Physics and (2008) The Visualization Society of Japan, respectively

Fontenot et al. [40] and İncel et al. [41] related the free-dropping energy of a metal ball dropped from various heights to the TL intensity (Fig. 7.8). Based on this system, M. Hasegawa et al. developed a drop-tower system (DTS) that used a pipe made of methyl polymethacrylate, attached a starter at an arbitrary height, and freely dropped a stainless-steel ball [42]. The edge of the optical fiber was attached to a plate, which served as a falling point, and TL was observed through the polycarbonate plate; the wavelength and relative emission intensity of this luminescence were then recorded by a small spectrometer. Placing the entire device in a glove bag allowed for the measurement of TL spectra in atmospheres of Ar and N_2. In addition, the potential energy due to free fall can be estimated from the height and the mass of the stainless-steel ball.

Sage et al. developed a detection method for measuring the TL of a series of organic crystals [43]. Longchambon et al. devised another measurement method in which the crystals were entrained in an airstream and impinged on a quartz substrate placed in front of a detector (Fig. 7.9) [44]. Unfortunately, this method was not suitable for fine particles. Meyer et al. applied the leverage principle and reported an impact method in which a needle was dropped onto a crystal [45]. In this system,

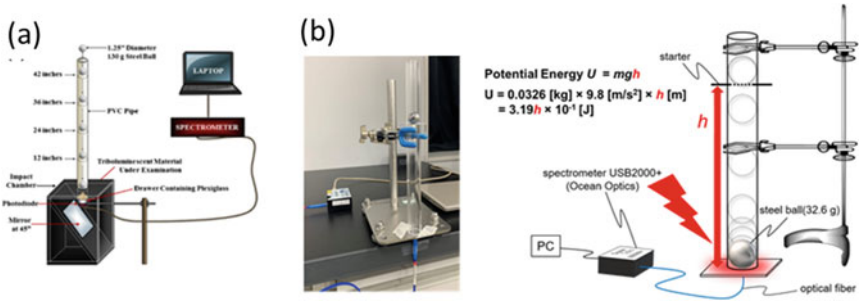

Fig. 7.8 Drop-tower system developed by İncel et al. (**a**) and its modified version using a transparent tube (**b**). Refs. [41, 42] Copyright (2017) American Chemical Society, and (2020) The Imaging Society of Japan

changing the number of weights allowed for variations in the magnitude of the impact, and the apparatus itself could be placed in a box to allow experiments in different environments. Nowak et al. developed an apparatus in which a crystal was placed between a gear and plate and the force of the gear turning with the weights crushed the crystal [46]. Based on these trial-and-error methods, the methods of crushing by a piston using compressed air (Fig. 7.10) [47], placing a crystal on a detector and impacting it with a plastic plug in free fall [48], and suspending a weight on a pulley and letting it fall freely [49] were also devised.

Hasegawa et al. evaluated the TL performance of pulverized crystals under magnetic stirring in an atmosphere-controlled flask by detecting the resulting TL spectrum and analyzing the images captured by a charge-coupled device (CCD) camera (Fig. 7.11). Using this method, the authors found that the polymer chain arrangement of Eu(III) coordination polymers in the crystals affected their TL intensity [50].

Time-dependent TL multiplied by an instantaneous impact has been reported. Hasegawa et al. analyzed the emission lifetime of Eu(III) coordination polymers using a nanosecond pulsed laser (Fig. 7.12) [51]. The TL emission spectra and emission lifetime analyses of 4f–4f transitions in this Eu(III) coordination polymer indicated that the nonradiative rate in the TL process is approximately five times higher

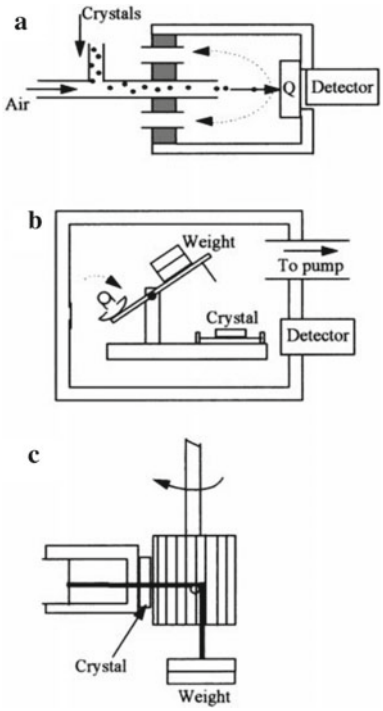

Fig. 7.9 Methods for inducing triboluminescence. **a** The air-driven technique, **b** the impacting-needle technique, and **c** the crystal-milling technique. Ref. [43] Copyright (2001) Royal Society of Chemistry

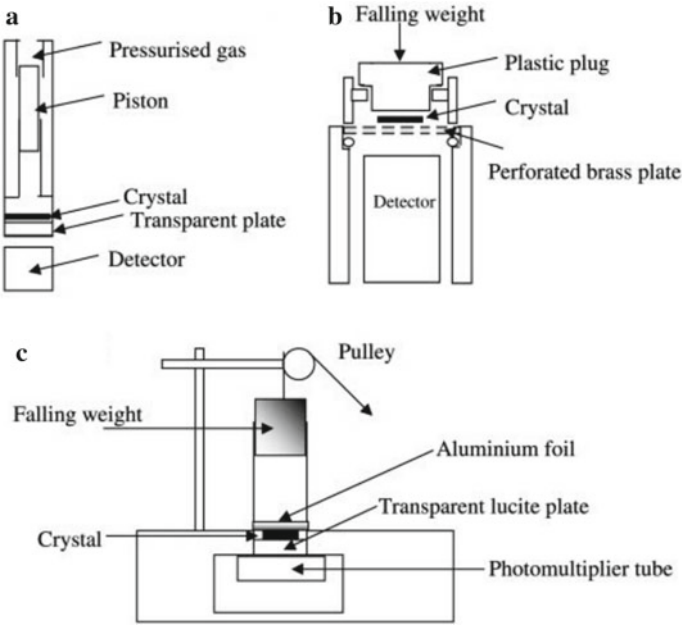

Fig. 7.10 Modern techniques for inducing triboluminescence. **a** The air-driven piston technique, **b** the falling-weight technique, and **c** a variant of the falling-weight technique. Ref. [47] Copyright (1980) American Physical Society

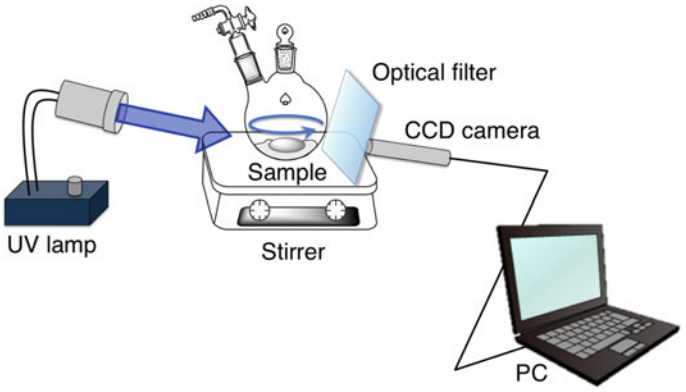

Fig. 7.11 Method for triboluminescence observation. Magnetic stirring is conducted in an atmosphere-controlled flask, the resulting spectrum is detected, and the images captured using a CCD camera are analyzed. Ref. [50] Copyright (2017) Wiley–VCH Verlag GmbH & Co. KGaA, Weinheim

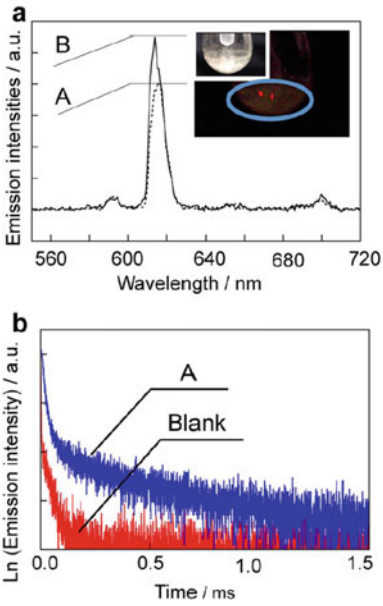

Fig. 7.12 **a** Triboluminescence (TL; A:a) and photoluminescence (PL; B:c) spectra. The PL spectrum is observed by excitation at 355 nm. Inset: TL image of $[Eu_3(hfa)_9(tppb)_2]_n$. **b** Emission decay profiles of the TL of $[Eu_3(hfa)_9(tppb)_2]_n$ (A: blue line) and $BaSO_4$ powders (blank: red line) under shockwave irradiation. Ref. [51]. Copyright (2017) Wiley–VCH Verlag GmbH & Co. KGaA, Weinheim

than that in the photo-excited luminescence process. In other words, TL involves a larger nonradiative process compared with photoexcited luminescence.

Time-resolved TL analysis has been performed using shock waves in which the air pressure can be controlled (Fig. 7.13) [52]. In this system, the TL of Tb(III) and Eu(III) coordination polymers was measured under air shock wave (ASW) pressures ranging from 100 to 400 kPa. The photophysical data obtained from the time-resolved TL analysis indicated that the TL intensity of the Tb(III) coordination polymer depended on the air pressure, which was related to the energy transfer process (Fig. 7.13). Thermal effects on TL were hardly observed under the experimental conditions employed, but oxygen pressure affected the TL performance. TL experiments using Tb(III)/Eu(III) mixed coordination polymers demonstrated that the energy transfer process from Tb(III) to Eu(III) is not as effective as the photoexcitation process (Fig. 7.14).

7.4.3 Discrete Complex Systems with Lanthanide Ions

In this section, we describe the TL phenomena and molecular structures and arrangements of lanthanide complexes, in which discrete molecules are packed into a crystal lattice. Various combinations of molecular structures and compositions have been reported to control the conditions for TL manifestation. For example, a series of tetrakis(β-diketonate)Ln derivatives have been used to discuss the symmetry of crystal systems [53–55]. Chandra et al. [53] reported that they produced TL only

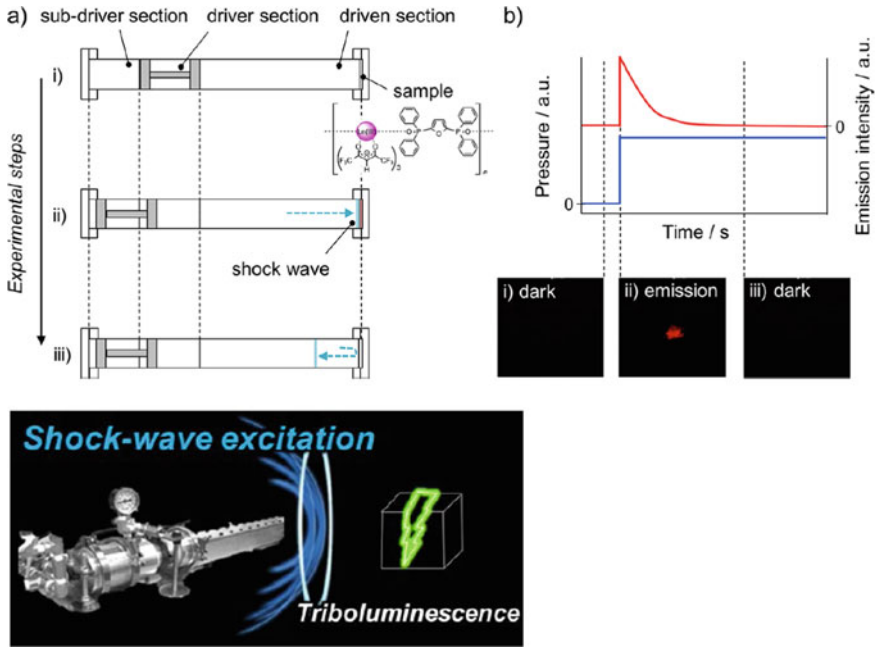

Fig. 7.13 **a** Schematic of aerodynamic shock wave experiments and **b** the corresponding profiles and images (red line, emission profile; blue line, pressure profile). Ref. [52]. Copyright (2019) American Chemical Society

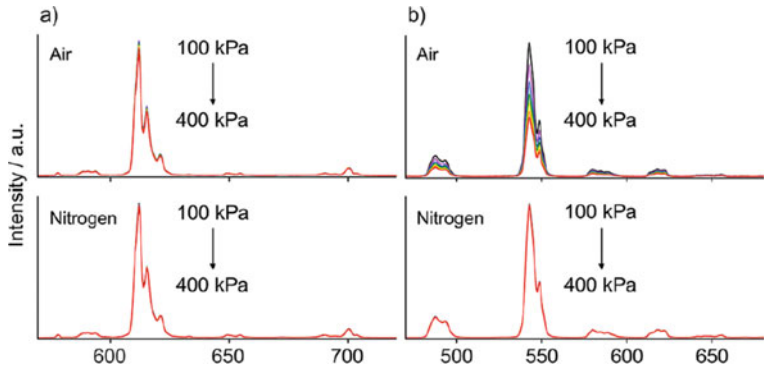

Fig. 7.14 Pressure-dependent emission spectra of **a** $[Eu(hfa)_3(dpf)]_n$ and **b** $[Tb(hfa)_3(dpf)]_n$ under air and N_2 gas ($\lambda_{ex} = 380$ nm, P = 100–400 kPa, solid state). Ref. [52]. Copyright (2019) American Chemical Society

in pyroelectric crystals with non-centrosymmetric symmetry. By contrast, Cotton [54] and Wong [56] found that TL also occurs in crystalline systems with central symmetry. The relationship between central symmetry and TL has been discussed for ternary complexes of Eu and Tb with bipyridine or 1,10-phenanthroline coordinated to tetrakis(β-diketonate)Ln; the findings of some related studies are summarized in Fig. 7.15 and Table 7.1 [26, 56–59].

The compound $(dbm)_3bpy$ shows TL even as centrosymmetric crystals, while the non-centrosymmetric crystal $Eu(dbm)_4TMP$ is pyroelectric and shows strong TL properties under pressure (Fig. 7.16) [56]. Similar considerations have been reported

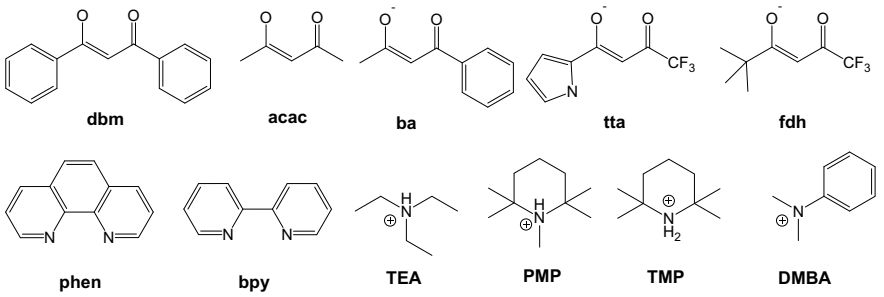

Fig. 7.15 Examples of organic ligands to induce TL of lanthanide in their complexes

Table 7.1 Summary of the TL activities and crystal structural properties of Ln(III) complexes

Compound	TL activity	Space group	Crystal symmetry	References
$Eu(dbm)_3phen$	**Inactive**	**P21/c**	**Centrosymmetric**	[56]
$Eu(dbm)_3bpy$	**Active**	**P-1**	**Centrosymmetric**	[56]
$Eu(tta)_3phen$	**Active**	**$Pca2_1$**	**Non-centrosymmetric**	[56]
$Eu(tta)_3bpy$	**Active**	**$P2_1/n$**	**Centrosymmetric**	[56]
$Eu(fdh)_3phen$	**Inactive**	**$P4_12_12$**	**Non-centrosymmetric**	[56]
$Eu(fdh)_3bpy$	**Active**	**P-1**	**Centrosymmetric**	[56]
$Eu(dbm)_4TEA$	**Active**	***Cc***	**Non-centrosymmetric**	[56]
$Eu(dbm)_4PMP$	**Inactive**	**P-1**	**Centrosymmetric**	[56]
$Eu(dbm)_4TMP$	**Active**	**Pca21**	**Non-centrosymmetric**	[56]
$Eu(tta)_3PMP$	**Active**	**$P\text{-}42_1c$**	**Non-centrosymmetric**	[56]
$Eu(tta)_3TMP$	**Active**	**$P\text{-}42_1c$**	**Non-centrosymmetric**	[56]
$Eu(dbm)_4TEA$	**Active**	***I 2/a***	**Centrosymmetric**	[26]
$Eu(dbm)_4DCM$	**Inactive**	***I 2/a***	**Centrosymmetric**	[26]
$Tb(ba)_4PP$	**Active**	**$P2_1/n$**	**Centrosymmetric**	[26]
$Eu(dbm)_4DMBA$	**Active**	**$Pca2_1$**	**Non-centrosymmetric**	[60]
$Tb(acac)(phen)_2$	**Active**	***P2/n***	**Centrosymmetric**	[61]
$Tb(acac)_3phen$	**Active**	**$P2_1/n$**	**Centrosymmetric**	[58]

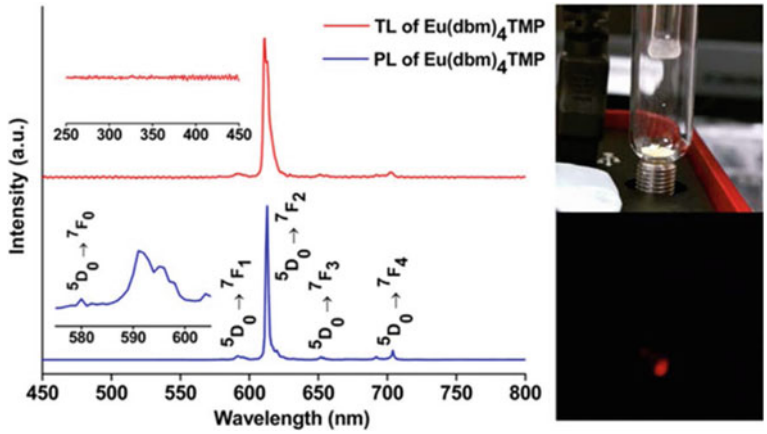

Fig. 7.16 TL and solid-state PL spectra of $Eu(dbm)_4TMP$ at room temperature. The images on the right show the CCD spectrometer captureing light emission induced by fracture of the crystals. Ref. [62] Copyright (2004) Elsevier B. V

for other systems [57–61, 63, 64]. Sweeting et al. found that triethylammonium tetrakis(benzoylethanate)Eu exhibited TL when recrystallized in methanol but not in dichloromethane (DCM) (Fig. 7.17) [26]. The former involves TEA coordination to the Eu ion and the latter involves a solvent for crystallization [5]. Li et al. observed TL and dielectric properties from the polymorphs of Eu complexes of tetrakis(β-diketonate)Ln coordinated with a terpyridyl derivative with chiral moieties [57]. They experimentally showed that crystals in the space group $P2_1$ (monoclinic) exhibited a TL band that could be attributed to the f–f transition of Eu ($^5D_0 \rightarrow {}^7F_2$) as well as good dielectric properties. By contrast, the polymorphic crystals of space group $P2_12_12_1$ (orthorombic) showed no TL or dielectric properties. These results indicate that TL depends on the polarity of the crystals (Fig. 7.18).

The research groups of Kalinovskaya and Bukvetskii used a ternary complex with quinalidic acid mixed with $Eu/Tb(acac)_4$ or phen as a matrix and argued that the piezoelectric effect affects the TL expression of this complex (Fig. 7.19) [58, 59, 61, 63]. Crystal structural analysis showed the formation of a layered structure and importance of the concepts of "destruction zone" and "destruction zone width" due to mechanical impact to TL expression. Based on a similar consideration of the crystal system, Bukavetskii et al. reported the TL expression of Sm complexes [59].

Structural or chemical driving forces, for example, charge separation during crystal fracturing and dielectric properties, are believed to be involved in the manifestation of TL upon stimulation. However, owing to the difficulty of instantaneous measurement, whether this belief is accurate remains a matter of speculation (Figs. 7.19 and 7.20) [65]. Hasegawa et al. recently applied nitric acid as a reductive counter anion and performed TL experiments using a DTS on the chiral crystals of lanthanide complexes with amino acid derivated-bipyridine derivative (Fig. 7.21) [37]. This complex also forms racemic crystals [66], but they did not

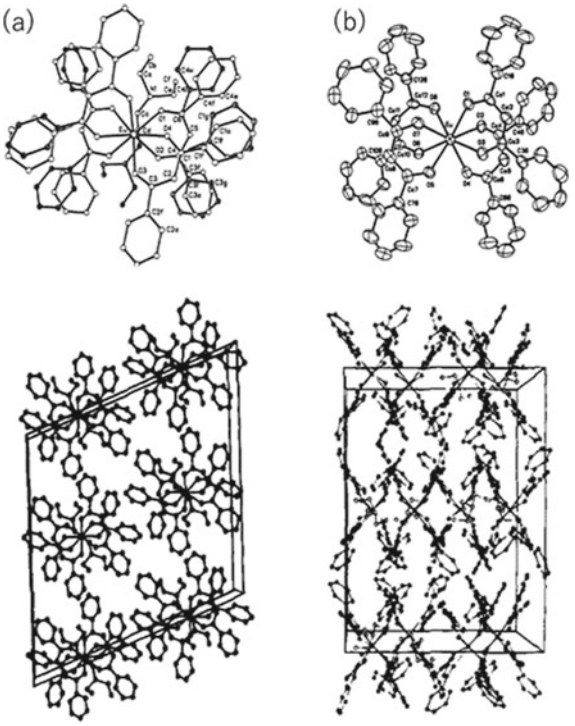

Fig. 7.17 Molecular structures and unit cell packing diagrams for **a** triboluminescent Eu complex and **b** non-triboluminescent one containing solvent of crystallization. Ref. [26] Copyright (1987) American Chemical Society

show TL. This finding suggests the possibility of a system associated with chemical reactions. Kubota and Ito et al. suggested that the presence of electrons is useful in promoting coupling reactions with hammering stimuli [65]. Such findings indicate a novel mechanism for the driving force of TL.

7.4.4 Coordination Polymer Complexes

Coordination polymers composed of metal complexes and organic ligands have been studied extensively in recent years. One-, two-, and three-dimensional organic–inorganic hybrid polymers have been reported. In 2004, Yuan reported the TL phenomenon of $[Eu(TPA)_3(HTPA)_2]_n$ (TPA: α-thiophene carboxylate, HTPA: α-thiophenecarboxylic acid) without emission spectra (Fig. 7.22) [67]. Eliseeva described the TL spectra of red-luminescent Eu(III) ($[Eu(hfa)_3(dmtph)]_n$ and green luminescent Tb(III) $[Eu(hfa)_3(dmtph))]_n$ (dmtph: 1,4-dimethyltherephtalate) coordination polymers for the first time (Fig. 7.23). [62] In 2011, Hasegawa reported the TL phenomenon of $[Eu(hfa)_3(bipypo)]_n$ (bipypo: 3,3-bis(diphenylphosphoryl)-2,2-bipyridine) with a high emission quantum efficiency (71% at 465 nm excitation) (Fig. 7.24) [68]. Hasegawa also reported the ratiometric TL spectra and

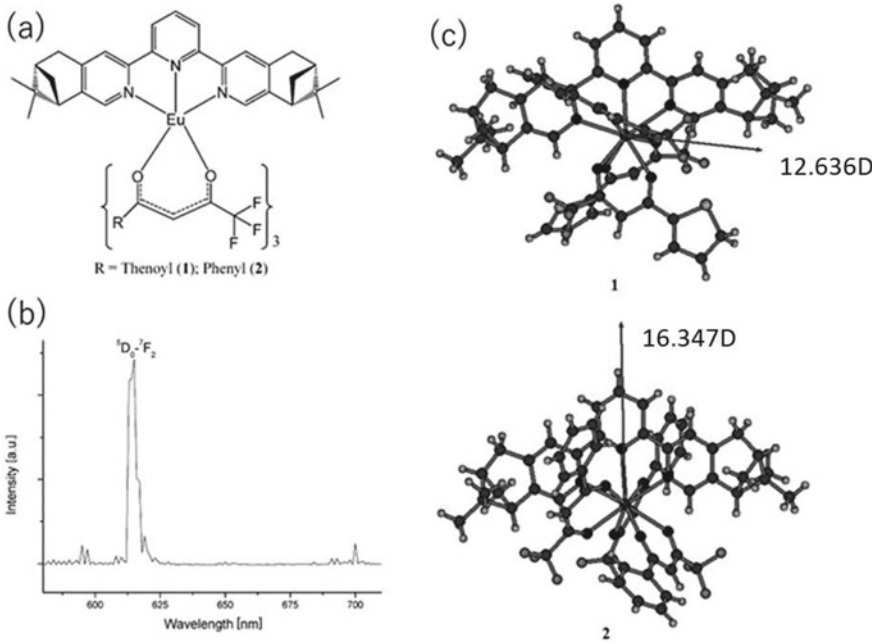

Fig. 7.18 Chiral terpyridyl Eu Complex (**a**), triboluminescence spectrum of the complex (**b**) and the dipolemoments of TL active (1) /inactive (**b**) species (**c**). Ref. [57] Copyright (2009) Wiley–VCH Verlag GmbH & Co. KGaA, Weinheim

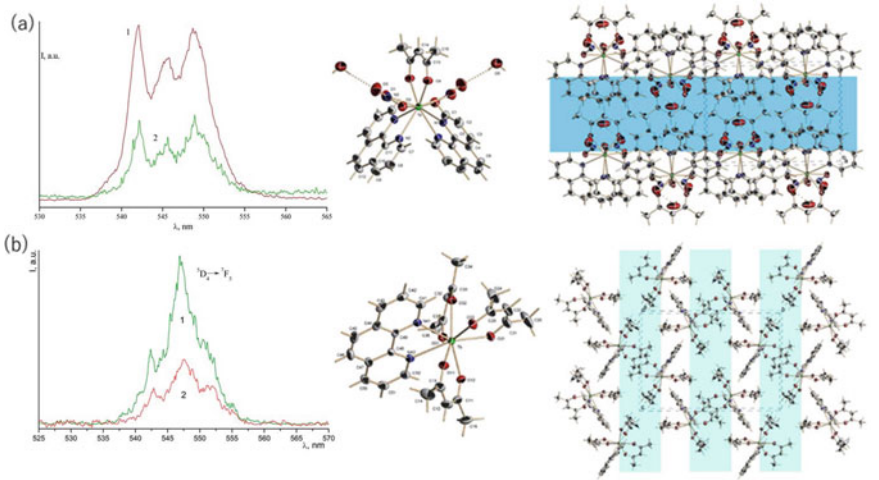

Fig. 7.19 TL (red) and PL (green) spectra and observed molecular structure and packings of $Tb(NO_3)(acac)(phen)_2$ (**a**) and $Tb(acac)_3phen$ (**b**). Refs. [58, 61] Copyright (2016) John Wiley & Sons, Ltd. and (2018) Elsevier B. V

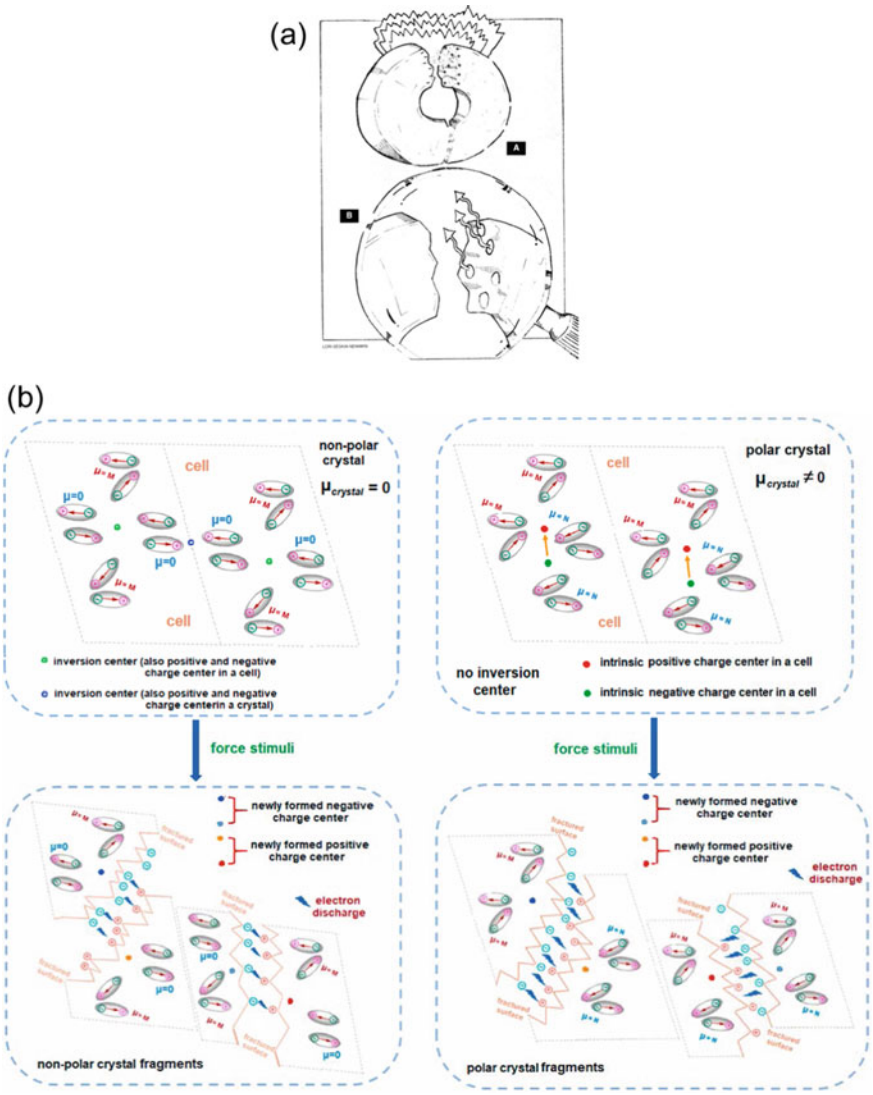

Fig. 7.20 **a** When a candy is cracked open resulting the TL. **b** Schematic diagrams of mechanoluminescence on crystals with non-and centrosymmetric space group. Ref. [64] Copyright (1990) American Chemical Society and (2020) Elsevier Ltd, respectively

images of mixed green- and red-luminescent Eu(III)/Tb(III) coordination polymers $[Eu,Tb(hfa)_3(dpt)]_n$ (dpt: 2,5-bis(diphenylphosphoryl)thiophene). The spectral intensity ratio of the green and red emission bands of the TL of these polymers under crystal milling were different from that of their PL (Fig. 7.25) [50, 69]. This difference in spectral intensity ratio is due to population differences

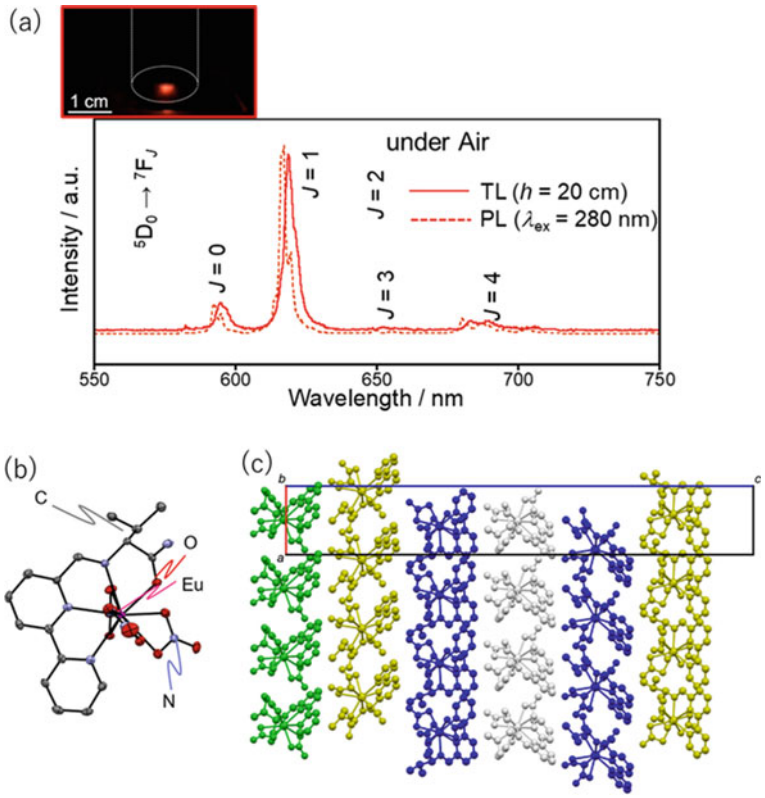

Fig. 7.21 TL of a chiral Eu complex with tetradentate ligand observed by modified dorop-tower system (**a**) and the molecular structure (**b**) and packing (**c**) of the complex

between PL and TL. Analysis of the TL of $[Eu_3(hfa)_9(tppb)_2]_n$ (dppb: tris(4-diphenylphosphorylphenyl)benzene (tppb)) induced by laser shock wave has been performed [51]. This analysis revealed that the radioluminescence-free deactivation rate during the luminescence process is enhanced in TL. The TL analysis of Eu(III) coordination polymers under laser shock wave has also been conducted. [52] Wu reported the TL phenomena of helical Sm(III) and Eu(III) coordination polymers $[Ln_2(L)_3(H_2O)_5]\infty$-$3H_2O$ (L: 2-(2-hydroxy-3,5-dinitrophenyl) (Fig. 7.26) [70]. Photochemical reactions using the TL phenomena of Eu(III) coordination polymers were recently observed (Fig. 7.27) [71].

The TL of Mn coordination polymers has been reported. In 2020, Artem'ev reported that a Mn coordination polymer $[MnX_2(L)]_n$, with phosphine oxide and carborane units showed blue TL (Fig. 7.28) [72]. Although the TL of tetrahedral Mn compounds had been reported in 1961, this report was the first to present a polymeric Mn system with a tetrahedral structure [73].

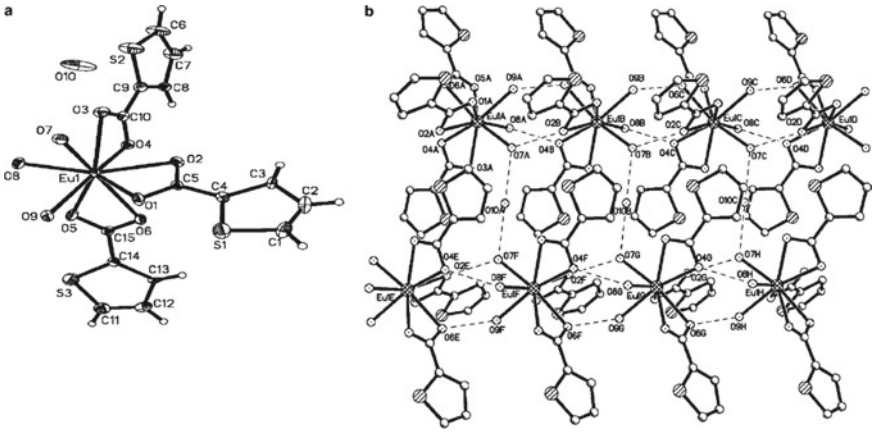

Fig. 7.22 Coordination structures of a) $[Eu(TPA)_3(HTPA)_2]_n$. Ref. [67] copyright (2004) Elsevier B. V

At present, reports on the TL of coordination polymers are scarce. The TL analysis of coordination polymers containing several types of luminescent metal ions will greatly contribute to the understanding of TL phenomena.

7.5 Conclusions

In this chapter, the TL of lanthanide complexes, including its historical background, observation methods, and recent examples of discrete molecular arrangements and coordination polymer systems, were described.

In systems containing lanthanides in oxides and other materials, ML or TL materials based on SrAlO:Dy,Eu [74], which is widely known as a phosphorescent agent, have been the subject of intensive research and are expected to be useful as a diagnostic technology for structures such as bridges [75]. The mechanism of the PL phenomenon of this type of compounds is believed to involve thermoluminescence, which has yet to be reported for lanthanide complexes.

Lanthanide complexes contain significantly fewer lanthanide ions than inorganic ML materials. Moreover, the electronic state unique to lanthanides does not only involve energy conversion, such as PL; the TL phenomenon itself is the visualization of the force. The TL of lanthanide complexes may be related to the thermoluminescence mechanism described above. A system in which lanthanide complexes were mixed with polymers demonstrated a chemical reaction upon stretching, and chemiluminescence was considered the driving force behind this luminescence [76]. Research on the TL of lanthanide complexes remains in its infancy and should be expanded to promote the applications of soft crystals as future energy-conversion devices.

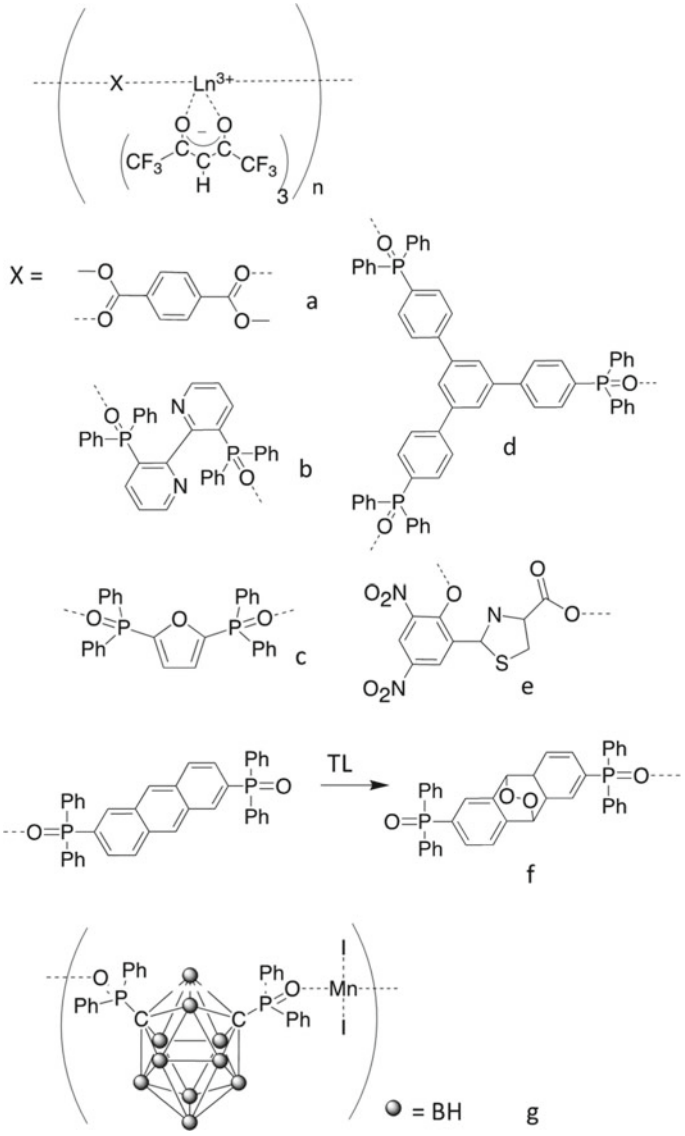

Fig. 7.23 Chemical structures of **a** $[Eu(hfa)_3(dmtph))]_n$ [62], **b** $[Eu(hfa)_3(bipypo)]_n$ [68], **c** $[Eu,Tb(hfa)_3(dpt)]_n$ [51], **d** $[Eu_3(hfa)_9(tppb)_2]_n$ [52], and **e** $[Ln_2(L)_3(H_2O)_5]\infty\text{-}3H_2O$ [70], **f** Photochemical reactions using the TL phenomena of Eu(III) coordination polymers [71], and **g** $[MnX_2(L)]_n$ [72]

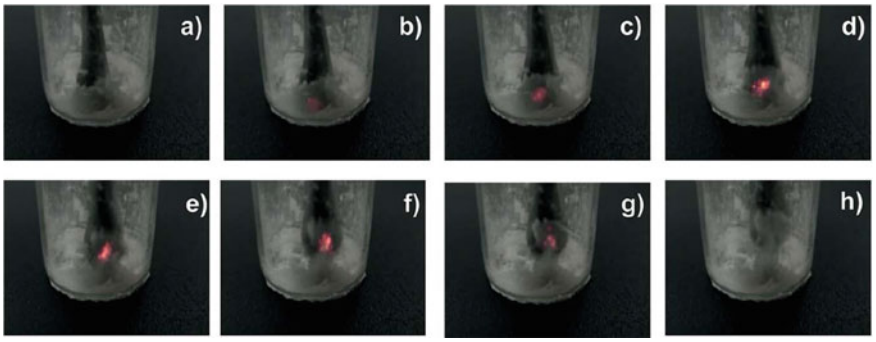

Fig. 7.24 Observed sequence-picture images of triboluminescence $[Eu(hfa)_3(bipypo)]_n$ powder upon pushing with a black stick at ambient temperature and in daylight. Ref. [50]. Copyright (2017) Wiley–VCH Verlag GmbH & Co. KGaA, Weinheim

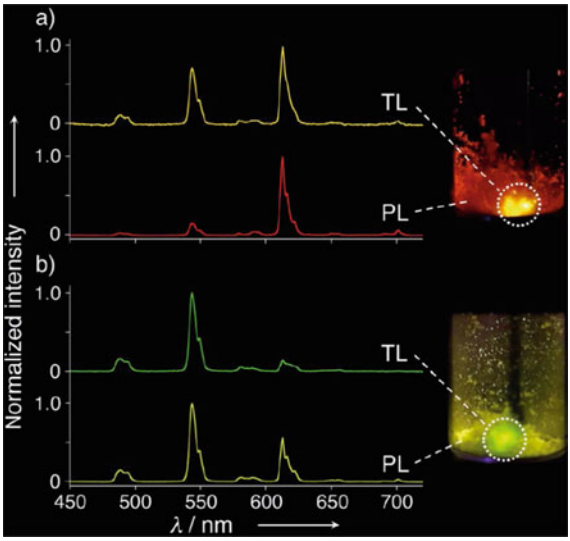

Fig. 7.25 Normalized TL and PL spectra and images of **a** $[Tb,Eu(hfa)_3(dpf)]_n$ (Tb/Eu = 1) and **b** $[Tb,Eu(hfa)_3(dpf)]_n$ (Tb/Eu = 10) Ref. [51]. Copyright (2017) Wiley–VCH Verlag GmbH & Co. KGaA, Weinheim

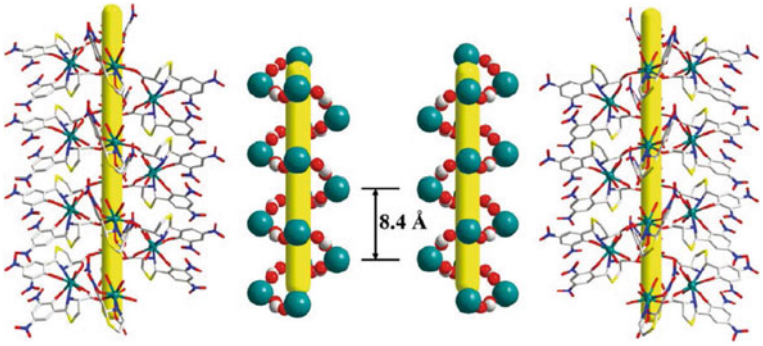

Fig. 7.26 Chiral coordination polymer of Eu complexes with helical structure of Δ-(left) and Λ-form (right). Ref. [70]. Copyright (2022) Royal Society of Chemistry

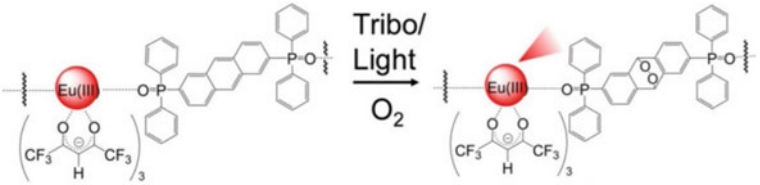

Fig. 7.27 Chemical reaction under the stimuli by tribo or light of the coordination polymer of Eu complexes. Ref. [71]. Copyright (2021) Wiley–VCH Verlag GmbH & Co. KGaA, Weinheim

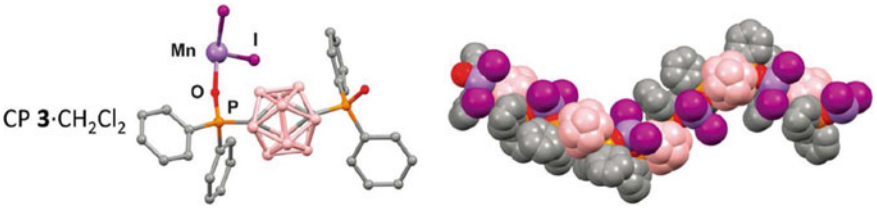

Fig. 7.28 Coordination polymer of Mn complex showing green TL. Ref. [72]. Copyright (2021) Royal Society of Chemistry

References

1. Kato M, Ito H, Hasegawa M, Ishii K (2019) Chem Euro J 25:5105
2. Traylor TG, Luo J, Simon JA, Ford PC (1992) J Am Chem Soc 114:4340
3. Liu H, Dai Y, Wang K, Zhang S, Chen G, Zou B, Yang B (2020) J Am Chem Soc 142:1153
4. Crane DR, Ford PC (1991) J Am Chem Soc 113:8510
5. Tran D, Bourassa JL, Ford PC (1997) Inorg Chem 36:439–442
6. Lechner A, Gliemann G (1989) J Am Chem Soc 111:7969
7. Gu Y, Wang K, Dai Y, Xiao G, Ma Y, Qiao Y, Zou B (2017) J Phys Chem Lett 8:4191
8. Ma Z, Liu Z, Lu S, Feng X, Yang D, Wang K, Xiao G, Zhang L, Redfern SAT, Zou B (2018) Nature Commun 9:4506

9. Bünzli JCG, Wong K-L (2018) J Rare Earths 36:1
10. Nakayama H, Nishida J, Takeda N, Sato H, Yamashita Y (2012) Chem Mater 24:671
11. Nowak R, Krajewska A, Samoć M (1983) Chem Phys Lett 94:270–271
12. Tsuboi Y, Seto T, Kitamura N (2008) J Phys Chem 112:6517
13. Shuang Y, Xie R-J (2021) Adv Mater 33:2205925
14. (a) Zink JI (1978) Acc Chem Res 11:289; (b) ChampmanGN, Walton AJ (1983) J Appl Phys 54:5961; (c) Walton AJ (1997) Adv Phys 26:887
15. Akiyama M, Xu C-N, Nonaka K, Watanabe T (1998) Appl Phys Lett 73:3046
16. (a) Zink JI (1981) Naturwissenschaften 68:507; (b) Sharipov FL, Tukhbatullin AA, Abdrakhmanov AM (2001) Prot Metals Phys Chem Surf 47:13
17. Camara CG et al (2008) Nature 455:1089
18. Bünzli J-CG (2015) Coord Chem Rev 293–294:19
19. Bünzli J-CG (2005) C Piguet 34:1048
20. (a) Dieke GH (1961) Adv Quantum Electron. In: Singer JR (ed). Columbia University Press, New York; (b) Dieke GD, Crosswhite HM (1963) Appl Opt 2:675; (c) Dieke GH, Crosswhite HM, Dunn B (1961) J Opt Soc Am 51:820
21. Bacon FThe advancement of learning, vol 1605. Macmillan, Novem Organum, London, p 209. Book IV, Ch. III
22. Piepenbrock M-OM, Lloyd GO, Clarke N, Steed JW (2010) Chem Rev 110:1960
23. (a) Marsella MJ, Reid RJ, Estassi S, Wang L-S (2002) J Am Chem Soc 124:12507; (b) Lee Y-A, Eisenberg R (2003) J Am Chem Soc 125:7778; (c) Beyer MK, Clausen-Schaumann H (2005) Chem Rev 105:2921; (d) Ahir SV, Terentjev EM (2005) Nat Mater 4:491; (e) Zanuy D, Aleman C (2007) Chem Eur J 13:2695; (f) Kobatake S, Takami S, Muto H, Ishikawa T, Irie M (2007) Nature 446:778
24. (a) Wiedemann G, Schmidt F (1895) Ann Phys (Leipzig) 54:604; (b) Walton AJ (1977) Adv Phys 26:887; (c) Zink JI (1978) Acc Chem Res 11:289
25. (a) Verezub NV, Krauya UÉ, Kalnin PP, Lavrinenko SN (1991) Mech Compos Mater 27:207; (b) Sage I, Badcock R, Humberstone L, Geddes N, Kemp M, Bourhill G (1999) Smart Mater Struct 8:504; (c) Sage I, Bourhill G (2001) J Mater Chem 11:231; (d) Bourhill G, Palsson LO, Samuel IDW, Sage IC, Oswald IDH, Duignan JP (2001) Chem Phys Lett 336:234–241
26. (a) Hardy GE, Kaska WC, Chandra BP, Zink JI (1981) J Am Chem Soc 103:1074; (b) Sweeting LM, Rheingold AL (1987) J Am Chem Soc 109:2652; (c) Rheingold AL, King W (1989) Inorg Chem 28:1715; (d) Antipin VA, Voloshin AI, Ostakhov SS, Kazakov VP (1996) Russ Chem Bull 45:1099; (e) Reynolds GT (1997) J Lumin 75:295; (f) Takada N, Sugiyama J, Minami N, Hieda S (1997) Mol Cryst Liq Cryst 295:71; (g) Akiyama M, Xu C-N, Nonaka K, Watanabe T (1998) Appl Phys Lett 73:3046; (h) Xu C-N, Watanabe T, Akiyama M, Zheng XG (1999) Appl Phys Lett 74:2414; (i) Chen X-F, Zhu X-H, Xu Y-H, Shanmuga Sundara Raj S, Öztürk S, Fun H-K, Ma J, You X-Z (1999) J Mater Chem 9:2919; (j) Liu Y, Xu C-N, Matsui H, Imamura T, Watanabe T (2000) J Lumin 87–89:1297; (k) Zeng X-R, Xiong R-G, You X-Z, Cheung K-K (2000) Inorg Commun 3:341; (l) Chen X-F, Duan C-Y, Zhu X-H, You X-Z (2001) Mater Chem Phys 72:11; (m) Zarkhin LS (2002) Polymer Sci Sri A 44:992; (n) Soares-Santos PCR, Nogueira HIS, Almeida Paz FA, Sá Ferreira RA, Carlos LD, Klinowski J, Trindade T (2003) Eur J Inorg Chem 3609; (o) Ronfard-Haret JC (2003) J Lumin 104:103; (p) Bulgakov RG, Kuleshov SP, Zuzlov AN, Vafin RR (2004) Russ Chem Bull Int Ed53:2712; (q) Jia Y, Yei M, Jia W (2006) Opt Mater 28:974; (r) Bukvetskii BV, Mirochnik AG, Zhikhareva PA, Karasev VE (2006) J Struct Chem 47:575; (s) Li X-L, Zheng Y, Zuo J-L, Song Y, You X-Z (2007) Polyhedron 26:5257; (t) Chandra BP (2008) J Lumin 128:1217; (u) Bergeron NP, Hollerman WA, Goedeke SM, Moore RJ (2008) Int J Impact Eng 35:1587
27. Chen X-F, Zhu X-H, Xu Y-H, Shanmuga Sundararaj S, Öztürk S, Fun H-K, Ma J, You X-Z (1999) J Mater Chem 9:2919
28. Feffrey GA (1973) Carbohyfrate Res 28:233
29. Armstrong HE, Lowry M (1903) Proc R Soc Lond 72:258
30. Andrews TWS (1910) J Ind Eng Chem 478.
31. Egerton ACG, Woolwich RMA (1911) Nature 85:308

32. (a) Hasegawa M, Ishii A, Kishi S (2006) J Photochem Photobiol 178:220;(b) Hasegawa M, Ohmagari H (2020) Chem Lett 49:845; (c) Hasegawa M (2022) Lanthanide luminescence enhancement in nanostructures by coordination chemistry. In: Ntwaeaborwa OM (ed) Luminescent nanomaterials. E-book, Jenny Stanford Publishing Pte. Ltd. ISBN: 9789814968119
33. (a) Bünzli J-C (2006) Acc Chem Res 39:51; (b) Binnemans K (2015) Coord Chem Rev 295:1; (c) Hasegawa Y, Wada Y, Yanagida S (2004) J Photochem Photobiol C 5:183
34. Dexter DL (1953) J Chem Phys 21:836
35. Förster T (1948) Ann Phys 437:55
36. Chow CY, Eliseeva SV, Trivedi ER, Nguyen TN, Kampf JW, Petoud S, Pecoraro VL (2016) J Am Chem Soc 138:5100
37. (a) Terasaki N, Xu C-N, Imai Y, Yamada H (2007) Jpn J Appl Phys 46:2385; (b) Li C, Xu CN, Zhang L, Yamada H, Imai Y (2008) J Visualization 11:329
38. (a) Xu CN, Zheng XG, Watanabe T, Akiyama M, Usui I (1999) Thin Solid Films 352:273; (b) Palumbo DT, Brown JJ, Jr (1970) J Electrochem Soc 117:1184; (c) Zhang Y, Ma L, Wang K, Xu X, Gao Y, Wen S, Luo J (2017) J Lumin 182:22
39. (a) Tsuboi Y, Seto T, Kitamura N (2008) J Phys Chem 112:6517; (b) Eddingsaas NC, Suslick KS (2006) Nature 444:163; (c) Ilatovskii DA, Tyutkov NA, Vinogradov VV, Vinogradov AV (2018) ACS Omega 3:18803
40. Fontenot ES, Hollerman WA, Aggarwal MD, Bhat KN, Goedeke SM (2012) Measurement 45:431
41. (a) Sage I, Badcock R, Humberstone L, Geddes N, Kemp M, Bourhill G (1999) Smart Mater Struct 8:504; (b) Sage I, Badcock R, Humberstone L, Geddes N, Kemp M, Bishop S, Bourhill G (1999) Proc SPIE-Int Soc Opt Eng 3675:169; (c) İncel A, Emirdag-Eanes M, McMillen CD, Demir MM (2017) ACS Appl Mater Interfaces 9:6488
42. (a) Hasegawa M, Ohmagari H (2020) J Imaging Soc Jpn 59:325; (b) Hasegawa M, Saso A, Yamamoto Y, Ohmagari H, Saito D, Hattori S, Karasawa M, Ito S, Kato M,. Ishii K (2022) (in preparation)
43. Sage I, Bourhill G (2001) J Mater Chem 11:231–245
44. (a) Longchambon H (1925) Bull Soc Fr Miner 48:130; (b) Sodomka L (1971) Phys Status Solidi A 7:K65
45. (a) Meyer K, Polly F (1965) Phys Status Solidi 8:441; (b) Meyer K, Obrikat D, Rossberg M (1970) Krist Tech 5:181
46. (a) Nowak R, Krajewska A, SamocÂ M (1983) Chem Phys Lett 94:270; (b) Tokhmetov AT, Vettegren VI (1989) Sov Phys Sol State 31:2125
47. Chandra BP, Zink JI (1980) Phys Rev B: Solid State 21:816
48. Reynolds GT (1997) J Lumin 75:295
49. Shikha ST, Tiwari S, Sahu BK, Chandra BP (1995) Bull Mater Sci 18:503
50. Hirai Y, Nakanishi T, Kitagawa Y, Fushimi K, Seki T, Ito H, Hasegawa Y (2017) Angew Chem Int Ed 56:7171
51. Hasegawa Y, Tateno S, Yamamoto M, Nakanishi T, Kitagawa Y, Seki T, Ito H, Fushimi K (2017) Chem Eur J 23:2666
52. Hirai Y, Kotani A, Sakaue H, Kitagawa Y, Hasegawa Y (2019) J Phys Chem C 123:27251
53. (a) Chandra BP, Deshmukh NG, Jaiswal AK (1987) Mol Cryst Liq Cryst 142:157; (b) Wolff G, Gross G, Stranski IN (1952) Z Electrochem 56:420.
54. Cotton FA, Daniels LM (2001) Inorg Chem Commun 4:319
55. Chandra BP, Zink JI (1981) J Phys Chem Solids 42:529–532
56. Wong H-Y, Lo W-S, Chan WTK, Law G-L (2017) Inorg Chem 56:5153–5140
57. Li D-P, Li C-H, Wang J, Kang L-C, Wu T, Li Y-Z, You X-Z (2009) Eur. J. Inorg. Chem 4844
58. Bukvetskii BV, Mirochnik AG, Shishov AS (2018) J Lumines 195:44
59. Bukvetskii BV, Mirochnik AG, Zhikhareva PA (2018) Inorg Chim Acta 483:565
60. Xiong R-G, You X-Z (2002) Inorg Chem Commun 5:677–681
61. Mirochnik AG, Shishov AS, Bukvetskii BV (2016) Lumines 31:1329
62. Eliseeva SV, Pleshkov DN, Lyssenko KA, Lepnev LS, Bünzli J-CG, Kuzmina NP (2010) Inorg Chem 49:9300–9311

63. Bukvetskii BV, Kalinovskaya IV (2017) J Fluorec 27:773
64. (a) Sweeting LM (1990) Chem Matt 10–11; (b) Gao G-L, Jia Y-R, Jiang H, Xia M (2021) Dye Pigment 186:109030
65. Kubota K, Pang Y, Miura A, Ito H (2019) Science 366:1500–1504
66. Hasegawa M, Iwasawa D, Kawaguchi T, Koike H, Saso A, Ogata S, Ishii A, Ohmagari H, Iwamura M, Nozaki K (2020) ChemPlusChem 85:294–300
67. Yuan L, Yin M, Yuan E, Sun J, Zhang K (2004) Inorg Chim Acta 357:89
68. Hasegawa Y, Hieda R, Miyata K, Nakagawa T, Kawai T (2011) Eur J Inorg Chem 4978–4984
69. Hirai Y, Paulo Ferreira da Rosa P, Nakanishi T, Kitagawa Y, Fushimi K, Seki T, Ito H, Hasegawa Y (2018) Inorg Chem 57:14653–14659
70. Wu M-Y, Xu J-X, Chen Y-H, Lu I-C, Han J-L, Lin P-H (2022) Dalton Trans 51:69–73
71. Kitagawa Y, Naito A, Fushimi K, Hasegawa Y (2021) Chem Eur J 27:2279–2283
72. Artem'ev AV, Davydova MP, Berezin AS, Sukhikh TS, Samsonenko DG (2021) Inorg Chem Front 8:2261–2270
73. Goodgame DML, Cotton FA, 726 (1961). Phosphine oxide complexes Part V. Tetrahedral complexes of manganese (II) containing triphenylphosphine oxide, and triphenylarsine oxide as ligands. J Chem Soc 3735–3741
74. (a) Matsuzawa T, Aoki Y, Takeuchi N, Murayama Y (1996) J Electrochemical Soc 143:2670–2673; (b) Akiyama M, Xu C-N, Nonaka K, Watanabe T (1998) Appl Phys Lett 73:3046–3048
75. Zhang J-C, Wang X, Marriott G, Xu C-N (2019) Prog Mater Sci 103:678–742
76. Yang F, Yuan Y, Sijbesma RP, Chen Y (2020) Macromoleclues 53:905–912

Open Access This chapter is licensed under the terms of the Creative Commons Attribution 4.0 International License (http://creativecommons.org/licenses/by/4.0/), which permits use, sharing, adaptation, distribution and reproduction in any medium or format, as long as you give appropriate credit to the original author(s) and the source, provide a link to the Creative Commons license and indicate if changes were made.

The images or other third party material in this chapter are included in the chapter's Creative Commons license, unless indicated otherwise in a credit line to the material. If material is not included in the chapter's Creative Commons license and your intended use is not permitted by statutory regulation or exceeds the permitted use, you will need to obtain permission directly from the copyright holder.

Chapter 8
Thermosalient Phenomena in Molecular Crystals: A Case Study of Representative Molecules

Yoshinori Yamanoi, Kenichiro Omoto, Toyotaka Nakae, and Masaki Nishio

Abstract Molecular crystals have a regularly packed structure, and their physical properties often depend on intramolecular and intermolecular interactions. Here, we review the crystal jumping phenomena under a thermal stimulus (thermosalient phenomenon). Thermosalient phenomena are characterized by thermal phase transitions and anisotropic lattice expansion/contraction at a microscopic scale and jumping behavior through bending/deformation/rotation/cleavage of crystals at a macroscopic scale. The absence of strong intermolecular interaction in the crystal and the misalignment of the crystal plane associated with the phase transition are explained as factors causing the thermosalient phenomena. In this chapter, various case studies with representative molecular crystals that exhibit the thermosalient phenomenon are explained in detail.

Keywords Thermosalient phenomena · Jumping crystals · Phase transitions · Polymorphism

8.1 Introduction

Some molecular crystals are known to change their physical properties on mechanical stimulation or exposure to solvent vapor. Such crystals, whose packing arrangement and physical properties change in conjunction with weak external stimuli, are called "soft crystals," and they have attracted considerable attention recently [1]. When a crystal is heated, it generally melts and becomes a liquid. However, some crystals

Y. Yamanoi (✉) · K. Omoto · T. Nakae · M. Nishio
Department of Chemistry, The University of Tokyo, Bunkyo-Ku, Tokyo 113-0033, Japan
e-mail: yamanoi@chem.s.u-tokyo.ac.jp

K. Omoto
Division of Materials Science, Nara Institute of Science and Technology (NAIST), Ikoma, Nara 630-0101, Japan

T. Nakae
Department of Applied Chemistry, Tokyo Metropolitan University, Hachioji, Tokyo 192-0397, Japan

© The Author(s) 2023

M. Kato and K. Ishii (eds.), *Soft Crystals*, The Materials Research Society Series,
https://doi.org/10.1007/978-981-99-0260-6_8

exhibit jumping phenomena through distortion, deformation, and cleavage of crystals with phase transition. These were referred to as terms such as “jumping crystals” or “hopping crystals”. Gigg et al. named these crystals that convert thermal stimuli into mechanical motion “thermosalient crystals” (salient: meaning “jumping”), and the term is now well established [2]. Approximately 60 “thermosalient crystals” have been reported by 2021. The characteristics of thermosalient crystals are as follows: they exhibit (1) first-order phase transition, (2) similar crystal packing before and after the phenomenon, (3) no change in space group and a little change in lattice parameters, (4) anisotropic lattice size change, and (5) negative coefficient of thermal expansion in one axis direction at least. Some reviews related to the thermosalient phenomenon have been reported so far [3, 4]. However, this research is a new field and there are many unknown aspects. The definition is not unified, and there are some exceptions which do not observe the characteristics ((1)–(5)) mentioned above.

Although the mechanism of the thermosalient phenomenon is still unclear, it has been pointed out the relation with the martensitic dislocation (transformation) observed in shape memory alloys [5, 6]. The shape memory alloy forms a square lattice in the high-temperature phase. At low temperatures, the crystal packing changes to a folding screen shape due to shear deformation, in which the rhombic lattice shifts maintaining the linkage with adjacent atoms through the slip plane (Fig. 8.1). Molecular crystals showing thermosalient phenomenon exhibit a similar response to martensitic dislocations and have displacement motion against the slip plane without strong interaction in the crystal. When volume and/or shape changes occur in the original crystal structure through a phase transition, the accumulated stress (strain) is rapidly released near the lattice defect, and the crystal exhibits a mechanical response with deformation or cleavage along the slip plane. In an ordinary crystal, the deformation and cleavage proceed slowly, and the external shape gradually changes. On the other hand, the crystals exhibiting thermosalient phenomenon are characterized by the generation of instantaneous mechanical power that causes the crystals to jump.

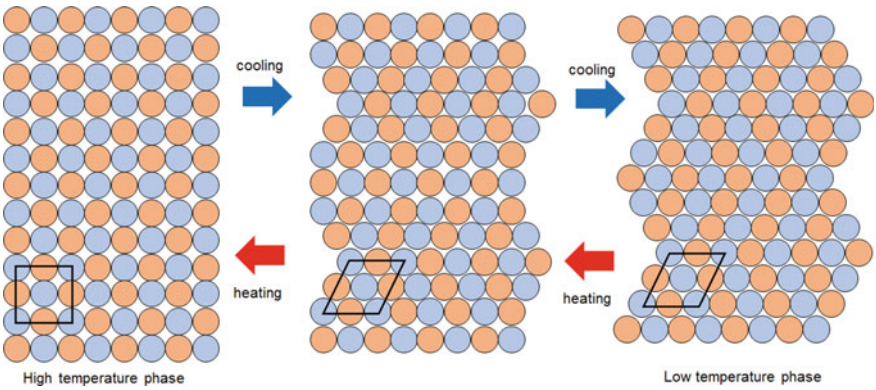

Fig. 8.1 Schematic diagram of a martensitic dislocation

8.2 Analytical Methods for Thermosalient Phenomena

The thermosalient phenomenon is generally mainly observed visually on a temperature variable plate. The phenomenon is considered to be caused by an accidental rapid structural change from the metastable phase to the stable phase of the crystal with changes in temperature, and often requires observation time in the range of several milliseconds to several seconds. Therefore, observation with a high-speed camera on a temperature-controlled stage is a useful method for instantaneously capturing crystal deformation and jumping behavior and linking microscopic phenomena to macroscopic shape changes. The phenomenon is confirmed by analytical chemistry methods such as temperature-variable X-ray diffraction and thermal analysis. Basically, the temperature of the phase transition and the temperature showing the thermosalient phenomenon are almost the same. The differential scanning calorimetry (DSC) of the molecules that exhibit thermosalient phenomenon results in the saw-toothed or jagged peaks. One of the reasons for this phenomenon is that the timing of the accidental structural change from the metastable to stable crystal packing is affected by the crystal size and/or shape.

8.3 Thermosalient Phenomena in Crystals Classified Based on Crystal Characteristics and Mechanism of the Thermosalient Phenomena

The thermosalient phenomena depend on molecular structure, and the visually observed phenomena can be classified into jumping, rotation, fragmentation, explosion, cracking, and splitting. In fact, the mechanical response is caused by a mixture of these phenomena, and the jumping distance is several mm to several cm, which is larger than the crystal size. The thermosalient phenomenon is often exhibited by organic crystals or complex crystals with weak intramolecular interaction, intermolecular interaction, steric hindrance, and high flexibility.

In 2013, Naumov conducted a systematic analysis of the thermal analysis, kinetic properties, and crystal structures of ca. 10 compounds that exhibited thermosalient phenomena at that time. They classified the compounds into three classes: crystals of flat rigid molecules aggregated in sheets (class I crystals), Crystals of molecules with bulky substituents attached to a cyclic core group (class II crystals), and crystals of molecules with extended intermolecular hydrogen bonds (class III crystals) [7–10]. During the last decade, many other crystals exhibiting thermosalient behaviors have been found. Although it is not easy to classify them clearly into Naumov's three categories, we will explain representative molecules as case studies referring to the classification.

8.3.1 *Crystals of Flat Rigid Molecules Aggregated in Sheets (Class I Crystals)*

The characteristic of this type molecules is the formation of layered structure through π–π stacking and dipole interaction in the crystalline state. Crystals are anisotropically slid and released as mechanical motion when strains that exceed the interlayer interaction are accumulated by thermal stimulation. Typical molecules of class I crystals are shown in Fig. 8.2.

1, 2, 4, 5-Tetrabromobenzene **1** forms a layered packing structure through the interaction between Br···Br and Br···H; however, it shows a tendency to form contact

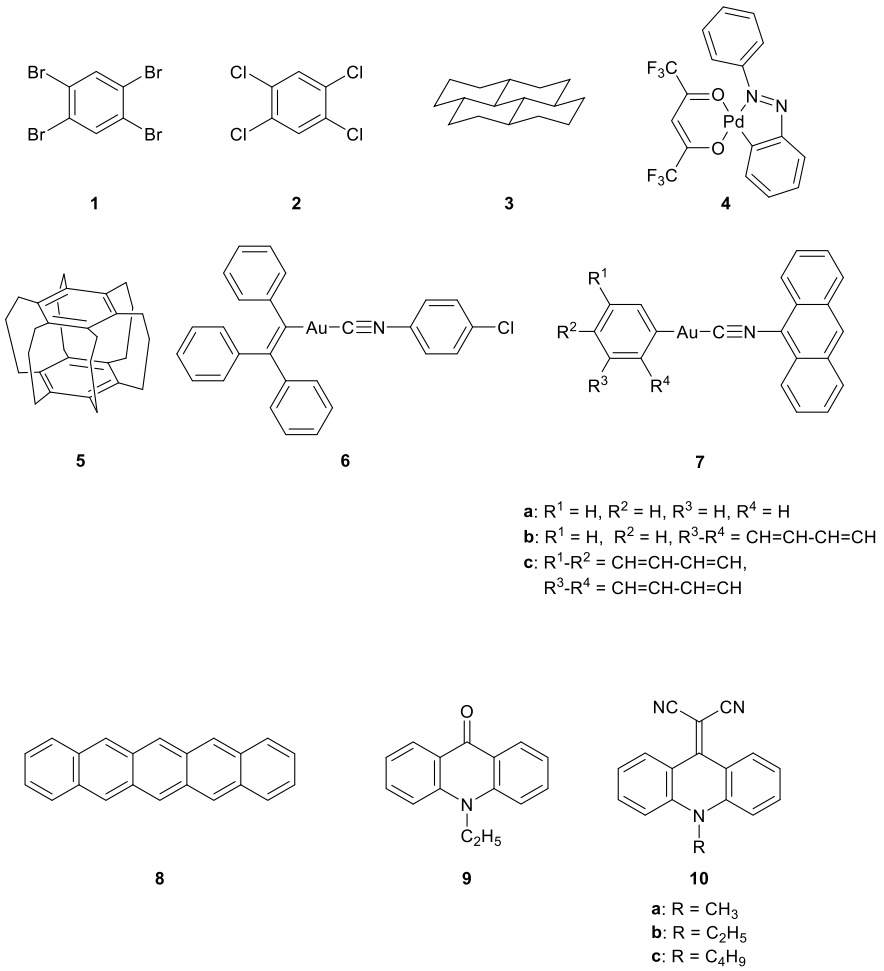

Fig. 8.2 Representative examples of molecules that create class I crystals

twins with respect to the (110) crystalline plane. Crystals of compound **1** have a stable β phase at room temperature and a stable γ phase at > 46 °C. Naumov et al. studied the direction and motion for more than 150 crystals with heating [11, 12]. They observed that the crystals are cleaved along the twin plane when heated parallel to the twin plane, and are crushed when heated perpendicular to the twin plane. Both β and γ phases have a layered structure, and the crystal jumping phenomenon is governed by the interaction between Br…Br and CH…Br. Comparing the two structures, the crystal lattice stretches anisotropically during the phase-to-phase transition. The angle between adjacent aromatic rings changes from 22.6° in β phase to 13.7° in γ phase. This slight change in inclination causes the flattening of the entire sheet-like structure, and the strain is finally accumulated and converted into mechanical behavior through cleavage and rupture [13]. Similarly, crystals of 1,2,4,5-tetrachlorobenzene **2** exhibit a thermosalient phenomenon by the mechanism as **1**, but it shows thermosalient phenomenon at a lower temperature (around 200 K) [14].

Crystals of hexadecahydropyrene **3** exhibit a crystal jump phenomenon when heated above 71.5 °C and when cooled below 65.5 °C, respectively [15]. Hexadecahydropyrene **3** has a chair-shaped conformation and is layered and packed parallel via van der Waals interactions. Because the crystals after the phase transition sublimate, X-ray structure analysis has not been successful. Although we cannot discuss the mechanism in detail, the molecule slides in the layer and strain is accumulated due to the displacement of the crystal plane under heating. The internal stress is relaxed at the transition point (e.g., lattice defect), and crystal cleavage is induced from the slip plane, resulting in a crystal jumping.

Crystals of palladium complex **4** were already known to exhibit thermosalient phenomenon in 1983 [16], but was investigated in detail by Naumov et al. [17]. This molecule has five polymorphs. A reversible phase transition occurs between the α and β phases. The stacked sheet-like structures separate from each other, as the layers between the molecules slide against each other and the molecular arrangements decline. At this time, a crystal jumping phenomenon is observed. The γ crystal undergoes a phase transition to the β crystal at 369 K. In this case, the alternating layers slide in opposite directions to form a head-to-tail stacking structure, which is transformed into a thermodynamically stable β crystal.

[3.3.3.3.3.3](1,2,3,4,5,6)-Cyclophane (superphane, **5**) are hexa-bridged cyclophanes in which all aromatic carbons of the benzene dimer are linked by propylene spacers. This compound was first synthesized by Virgil Boekelheide in 1979 as a model compound for the investigation of physical properties including aromaticity. This compound shows a crystal jumping phenomenon when heated [18]. Although the single-crystal structure at low temperature has been reported [19], the structural analysis at high temperature and the mechanism of the crystal jumping phenomenon are not well understood.

Seki and Ito et al. analyzed the crystal jumping phenomenon associated with the phase transition of triphenylethynyl 4-chlorophenyl isocyanide gold(I) complex **6** at around −40 °C with a high-speed camera (Fig. 8.3) [20]. In this crystal, a sheet-like structure is formed through π–π stacking structure. A phase transition is observed in the crystal lattice upon cooling, and the crystal lattice expands and contracts

anisotropically. The misalignment of the π–π stacking and Au–Au bonds in the packing induces deformation and cleavage of the crystal, which leads to thermosalient phenomena before and after the phase transition.

Further developing this study, crystals of (9-isocyanoanthracene)gold(I) complex **7** exhibit thermosalient and photosalient (crystal jumps due to light irradiation) phenomena in response to two different external stimuli (UV irradiation and cooling) [21]. On cooling, the crystal contracts anisotropically without changing the chemical structure. The X-ray structure analysis at 20 °C and −140 °C shows that the distance between Au…Au in the stacked dimer changes from 3.6714−3.6124 Å. Correspondingly, the crystal lattice anisotropically expanded and contacted. In contrast, the anthracene moiety is photodimerized and the structure changes significantly under UV irradiation. These changes are the reason for the salient phenomenon. The crystal shows a continuous mechanical response by alternating cooling and UV irradiation.

Pentacene **8** has four polymorphs in single crystal and thin film [22]. In the single-crystal state, pentacene **8** has a herringbone packing with an interplanar distance d_{001} = 1.41 nm in the low-temperature phase. A phase transition occurs around 486 K (high-temperature phase, Campbell phase) with a change in the interplanar distance to d_{001} = 1.44 nm [23, 24]. The angle between the molecular long axis and the normal to the *ab*-plane is 24.2° and 24.6° in the low-temperature phase changes to 21.0° and 22.5° in the high-temperature phase. Cracking and jumping of the crystal during the crystalline phase transition are reported, but no detailed analysis has been performed.

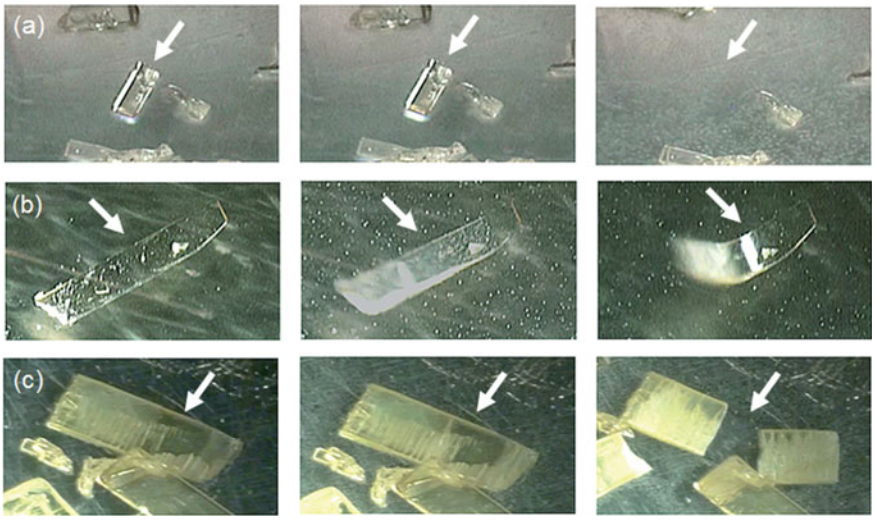

Fig. 8.3 High-speed camera observation of crystals of molecule **6** in a cooling process. The arrows indicate the points of change, **a** jumping, **b** bending, and **c** cleavage. From reference [20]. Copy right © 2019 Royal Society of Chemistry

Takeda and Akutagawa reported that crystals of ethylacridone **9** and dicyanomethylenated acridones **10** show thermosalient phenomena [25]. Especially for **10**, they investigated the molecules with different lengths of alkyl groups introduced on the nitrogen. Among them, only **10a**, **10b**, and **10c** showed the thermosalient phenomenon. Although these molecules have a bent structure, they have intermolecular interactions between C≡N···H–C(sp^2) and C≡N···H–C(sp^3). Hence, they adopt a stacked layered structure. They are considered to exhibit molecular inversion and thermosalient phenomena. When the alkyl chain becomes long, the thermosalient phenomenon is not exhibited. It is considered to be because the fluctuation of the alkyl chain becomes larger than the inversion of the ring structure under heating.

8.3.2 Crystals of Molecules with Bulky Substituents Attached to a Cyclic Core Group (Class II Crystals)

Crystals classified as class II are composed of molecules with bulky and flexible substituents attached to a cyclic core. Conformational changes of flexible substituents in crystals result in crystal-to-crystal thermal phase transition with anisotropic change in the unit cell. Accumulated strain energy is converted into mechanical motion. In some cases, crystal structures of class II thermosalient crystals have not been clarified, making it difficult to explain the mechanism of their mechanical behaviors. Representative examples of molecules that provide class II thermosaliant crystals are shown in Fig. 8.4.

Oxitropium **11** bromide is an anticholinergic drug used in the treatment of bronchial asthma and chronic obstructive pulmonary disease [26]. Block-like crystals prepared from methanol and methylene chloride show crystal jumping phenomenon upon heating up to 45 °C and cooling down to 27 °C, respectively. When this crystal is heated, the rigid aza-tricyclic moiety shows little conformational change, whereas the conformations of the ester moiety and phenyl ring are altered, causing a crystal-to-crystal phase transition. The resulting anisotropic cell expansion and packing switches induce cleavage and jumping of crystals [27].

Crystals of the sugar alcohol derivative (±)-3,4-di-*O*-acetyl-1,2,5,6-tetra-*O*-benzyl-*myo*-inositol **12** have long been known to exhibit a thermosalient phenomenon. Crystal structural analysis at variable temperature revealed **12** has three polymorphic forms (I, II, and III), which exhibit thermal phase transition at 30 °C (I → II)、70 °C (II → III), 40 °C (III → II), and 11 °C (II → I) respectively. In the case of phase transition between II and III, the occupied volume of a molecule in the crystals changes by approximately 2% resulting in a thermosalient phenomenon [28]. Whereas in the case of transition between I ⇄ II, the change of occupied volume of a molecule is smaller (approximately 1.4%). Although the molecular packing in each crystal is similar, the drastic change in the torsion of the flexible C–O–CH_2–C_6H_4 moiety (especially positions 1 and 5) work as a key

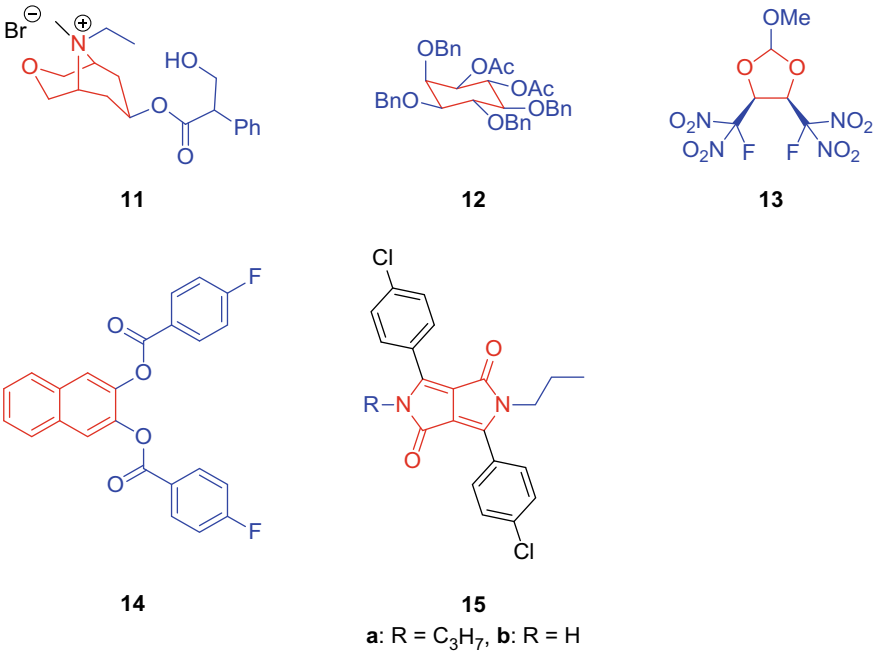

11 **12** **13**

14 **15**

a: R = C_3H_7, **b**: R = H

Fig. 8.4 Representative examples of molecules which create class II crystals. The cyclic cores are shown in red, and the bulky and flexible substituents are shown in blue

role to realize crystal-to-crystal phase transition with the thermosalient phenomenon (Fig. 8.5).

Crystals of 4,5−bis(fluorodinitromethyl)−2−methoxy−1,3−dioxolane **13** have been reported to crack and jump up to approximately 1 cm upon heating to 40 °C on a glass plate [29]. Single crystal X-ray structure analysis revealed that in crystal,

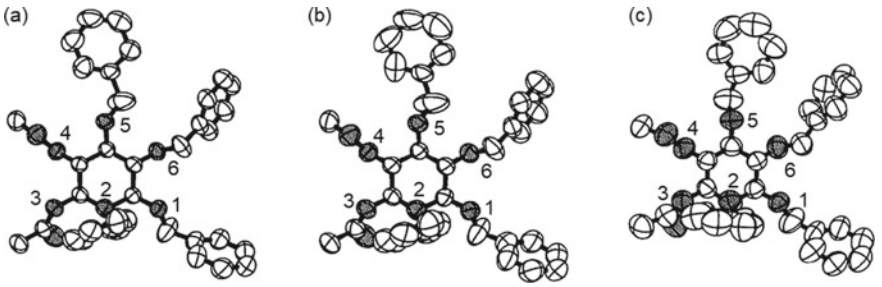

Fig. 8.5 Conformational changes of the molecule **12** before and after the phase transition. Numbers from 1 to 6 represent the position of the benzyloxy and the acetyl groups. **a** Form II, 18 °C. **b** Form II, 60 °C. **c** Form III, 80 °C. From reference [28]. Copy right © 1993 International Union of Crystallography

(1) the 1,3-dioxolane ring of the core of **13** is slightly twisted, (2) **13** constructs a layered structure parallel to the *bc* plane, and (3) the distance between the nitro group O···O is as short as 2.9 Å within layers. No detailed discussion about the correlation between structure and the thermosalient phenomenon was provided.

The diester molecule **14** with a naphthalene moiety as a core has five polymorphic forms (I–V). Among them, a reversible crystalline phase transition accompanied with a thermosalient phenomenon is observed in the transition between crystals I and IV. Crystal structures of these two polymorphs revealed that the reversible tweezering motion of the flexible diester arms of **14** induces crystal-to-crystal thermal phase transition accompanying with the thermosalient phenomenon [30].

Matsumoto et al. reported that diketopyrrolopyrrole **15a** has two polymorphic forms which exhibit a thermal phase transition with a thermosalient phenomenon. [31, 32] In the crystal of phase I, **15a** forms a one-dimensional chain packing (space group: *P*-1) through Cl···Cl interactions and π-stacking. On the other hand, upon heating of the crystals up to around 440 K, crystals transit to phase II in which **15a** forms a herringbone-type packing (space group $P2_1/c$) without any specific intermolecular interaction. Significant conformational changes of propyl and *p*-chlorophenyl groups are observed before and after thermal phase transition, which may have an important role to realize the thermosalient phenomenon. Moreover, crystals of **15b** also exhibit a thermosalient phenomenon which accompanies conformational change of the flexible propyl group during phase transition [33].

8.3.3 Crystals of Molecules with Extended Intermolecular Hydrogen Bonds (Class III Crystals)

Molecules classified in this group have hydrogen bonding sites, such as carboxyl, amide, and hydroxyl groups, etc. on their backbones, which create hydrogen bonding networks in crystals. For crystals to exhibit thermosalient phenomena, these hydrogen-bonded networks must have a two-dimensional or one-dimensional structure, and these assemblies must be packed with weak intermolecular interactions. Upon temperature change, thermal phase transition accompanying cooperative sliding of hydrogen-bonded assemblies proceeds in crystals, and the resulting strain energy converts into mechanical motion. Representative examples of molecules that provide class III crystals are shown in Fig. 8.6.

In crystal, terephthalic acid **16** forms intermolecular hydrogen-bonded carboxyl dimers at both carboxyl groups on its phenyl ring to develop two-dimensional infinite sheet-like structures which stack along [001] direction. As shown in Fig. 8.7, **16** forms two polymorphic forms: Form I, in which hydrogen-bonded carboxyl dimer in one layer locate just above that in the adjacent layer, and Form II, in which hydrogen-bonded carboxyl dimer in one layer locate above phenyl ring of **16** in the adjacent layer. Upon heating crystals, Form II crystals exhibit phase transition at around 90–95 °C and convert into Form I. The stress applied during this thermal phase transition

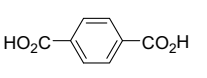

16

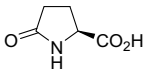

17

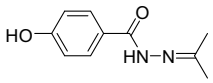

18

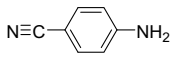

19

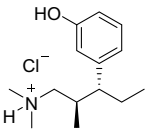

20

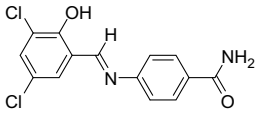

21

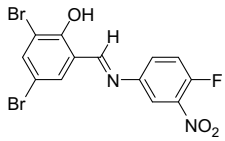

22

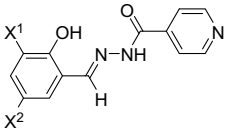

23

a: X^1 = Cl, X^2 =Cl
b: X^1 = Cl, X^2 =Br
c: X^1 = Br, X^2 = Br
d: X^1 = I, X^2 = I

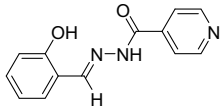

24

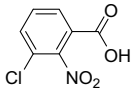

25

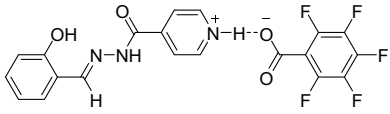

26

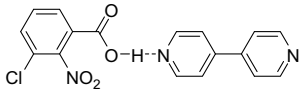

27

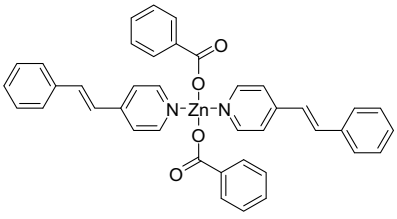

28

Fig. 8.6 Representative examples of molecules that create class III crystals

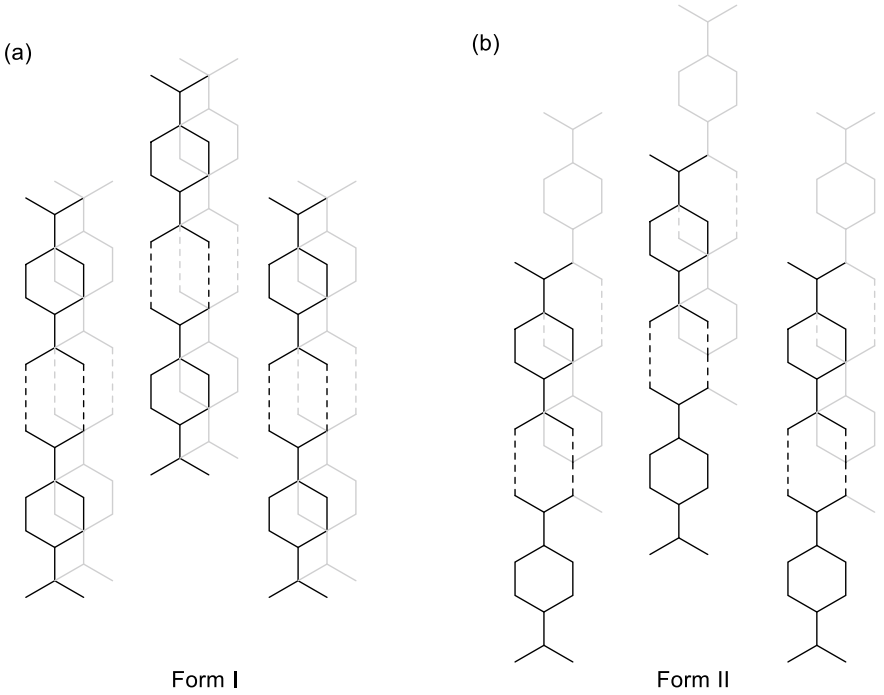

Fig. 8.7 Schematic presentation of the crystal packing of terephthalic acid **16**. The dotted lines indicate hydrogen bond, and the gray lines indicate the underlying sheet-like structure

is converted into mechanical energy to realize crystal jumping behavior. This thermal phase transition is reversible and has been observed upon cooling of Form I crystals down to 30 °C to revert to Form II [34].

L-pyroglutamic acid **17** forms a low-dimensional (one) hydrogen bonding network in crystals, which exhibit a thermosalient phenomenon associated with phase transitions [11, 35]. Large changes in hydrogen bonding (N–H···O) distances and angles have been observed before and after the phase transition. The crystals of enantiomeric D-pyroglutamic acid also shows a thermosalient phenomenon, while the racemic crystal is inert and does not exhibit crystal-to-crystal thermal phase transition.

Single crystals of *N*-2-propylidene-4-hydroxybenzohydrazide **18** exhibit single-crystal-to-single-crystal thermal phase transition among three different phases (Phase I–III) of the same space group ($Pna2_1$). Phase I is a metastable state and undergoes a phase transition via Phase II to a more stable Phase III. The phase transition from Phase I to Phase II is irreversible and proceeds at 147 °C. During this phase transition, the *c*-axis shows drastic contraction (15%), and the single crystals fragment and scatter violently [36]. Notably, the crystal fragments jump up to 1 m from their initial position. The transition between Phase II and III is reversible and does not

involve crystal jumping. The molecule exhibits second harmonic generation (SHG), the intensity of which changes before and after the phase transition.

Crystals of 4-aminobenzonitrile **19** show a thermosalient phenomenon around 180 K. This molecule forms a one-dimensional strand in a head-to-tail fashion via hydrogen bonding between N–H···N≡C in crystals. Each strand interacts with only one adjacent layer via NH…π interactions [37]. In addition, this double layer forms a crystal packing via CH···π(C≡N) interactions. Comparison of single crystal structures of **19** at 180 K and 160 K revealed a significant difference in unit cell angle (β) and the orientation of the CH···π(C≡N) interaction between two phases, indicating shearing translation of adjacent layer parallel to (100) during thermal phase transition.

Gaztañaga et al. reported that crystals of tapentadol hydrochloride **20** show a reversible first-order phase transition with the remarkable movement of samples upon heating up to 318 K and cooling down to 300 K [38]. Single-crystal structural analysis of phases I and II revealed that **20** develops hydrogen bonding parallel to the *a*-axis in crystals. Notably, there is a significant difference in the orientation of the methyl group at the end of the main alkyl chain of **20** between phases I and II, which induces a significant change in the length of the *b*- and *c*-axes and the angle of β during thermal phase transition.

Nangia et al. reported the thermosalient phenomenon of crystals of 4-((3,5-dichloro-2-hydroxybenzylidene)amino)benzamide **21** involving the C–Cl···O (halogen bond) and N–H···O (hydrogen bonds) [39]. The crystal polymorphs, Form I, Form III, and Form IV are layered, and Form II is packed in a wave-like structure. In the case of Form I and Form III, when the crystal is heated, the heat is transferred uniformly from the plane, and as a result, the thermal stress is transferred mainly in one direction, and the thermosalient phenomenon manifests as a crystal jump. On the other hand, in the case of Form II, heat transfer becomes non-uniform due to the wave-like arrangement, and it is seen that the crystal suddenly bursts.

Mishra and Ghosh et al. reported that 2-hydroxy-3,5-dibromobenzylidine-4-fluoro-3-nitroaniline **22** has two crystal polymorphic forms, one exhibiting jumping and the other exhibiting bending upon heating [40]. The differences in mechanical behaviors associated with these crystal phase transitions can be explained by the difference in conformation, packing, and intermolecular interactions of **22** in these two crystals. Crystal exhibiting jumping has a layered molecular packing via π-stacking and undergoes a phase transition with an anisotropic expansion of the cell upon heating. On the other hand, crystal exhibiting bending has an interlocked molecular packing with multiple weak and dispersive interactions and can absorb strain gradually, so that instantaneous mechanical behavior does not appear and bending behavior like bimetallic strips is realized.

Nangia et al. examined the thermosalient phenomena of crystals of halogenated salinazide derivatives **23** [41]. They discussed the effects of halogen-halogen interactions, as well as NH…N(pyridine) hydrogen bonds, on the packing structure of these molecules in crystals. Among them, crystals of **23a** exhibit a particularly pronounced thermosalient phenomenon. In this system, the weakness of the Cl···Cl interaction

is a key factor for the highly reversible phase transition accompanied by thermosalient phenomena. **23a** has three crystal polymorphic forms, Form I, II, and III; Form I and III belong to the $P2_1/c$ and Form II to the $Pca2_1$ space groups, respectively. The reversible phase transition between Form I and III shows a thermosalient phenomenon accompanied by crystal rupture. On the other hand, the phase transition from Form II to III did not involve any thermosalient phenomena.

Reddy et al. found that crystals of salinazide **24** and 3-chloro-2-nitrobenzoic acid **25** exhibit thermosalient phenomena at 130–140 °C and 210–220 °C, respectively. Moreover, co-crystals of these compounds with specific organics molecules (coformers), **26** and **27**, exhibit thermosalient phenomena at lower temperatures (at 100 °C and 100–110 °C respectively) [42]. Pentafluorobenzoic acid and 4,4'-bipyridine, which co-crystallize with **24** and **25**, do not exhibit thermosalient phenomena. The approach to developing multicomponent systems rather than single component would be promising for the preparation of libraries of thermosalient crystals to study various factors that alter the response time and temperature of thermosalient phenomenon. Moreover, proper choice of the conformer would realize additional functions such as luminescence and conductivity.

Dinnerbier, Ji and Vittal et al. reported that crystals of zinc complex **28** exhibit various properties, including thermosalient, photosalient, and SHG [43]. Single-crystal X-ray structure analysis revealed the formation of head-to-tail molecular packing structure through hydrogen bonding (C–O···H) in crystal. Upon heating, the crystals undergo a phase transition at around 140 °C without changing the space group of the crystal (C_2/c). The significant positive thermal expansion occurring along the *b*-axis of the unit lattice is due to the weakening of the π–π, CH–π, C–O···H interactions between benzoate and SPY ligands upon increasing temperature.

8.3.4 Thermosalient Phenomena Based on the Conformational Change of Flexible and Deformable Ring Structures

As examples that are difficult to classify into the above-mentioned classes (Class I–III), herein, we will discuss recently reported examples of thermosalient phenomena exhibited by crystals of cyclic molecules. Cyclic molecules have been widely studied for their potential applications in molecular recognition, catalysis, and optical materials [44, 45]. Although, conformational flexibility of cyclic compounds has been studied mainly in solution, recently there are some reports which revealed that conformational change of the cyclic molecules in crystal plays an important role in the crystal-to-crystal thermal phase transition. Designing cyclic molecules that have high crystallinity and conformational flexibility provides a clue to developing thermosalient crystals. Representative molecules are shown in Fig. 8.8.

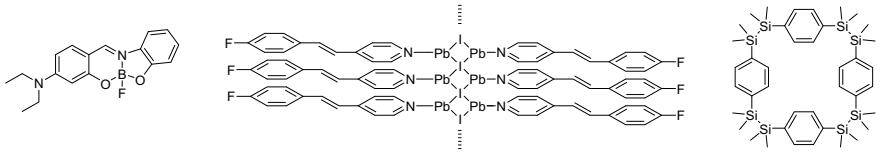

29 30 31

Fig. 8.8 Flexible and deformable cyclic molecules of crystals exhibiting thermosalient phenomena

Gon and Chujo et al. reported that a boron-fused azomethine derivative **29** has two crystal polymorphic forms (α, β) which exhibit thermosalient phenomena. In the low-temperature phase (α-type), the molecule has a nearly planar conformation, whereas in the high-temperature phase (β-type), it has a bent conformation [46, 47]. In the phase transition from α to β phase accompanied with a thermosalient phenomenon, the crystal lattice stretches anisotropically (*a*-axis ca. +10%, *b*-axis ca. +20%, and *c*-axis ca. −20%). Notably, the luminescence behavior of these crystals changes before and after the thermosalient phenomenon, and α crystal has a higher luminescence quantum yield.

Dinnebier and Vittal et al. reported that crystals of a linear 1D coordination polymer **30** composed of Pb(II) and 4-fluoro-4'-sterylpyridine exhibit a thermosalient phenomenon accompanied by structural changes in the rhombic framework of Pb(μ−I)$_2$ [48]. During the phase transition from crystalline phase I (low-temperature phase) to crystalline phase II (high-temperature phase), the aspect ratio of Pb(μ−I)$_2$ the diagonal of the rhombic skeleton changes.

The authors have synthesized a variety of disilane-bridged aromatic molecules and studied their structures and properties in crystals [49–53]. Disilane-bridged aromatic molecules have attracted much attention as building blocks of stimuli-responsive materials, because of their structural flexibility unique to σ bond and electron conjugation between σ orbital of Si–Si and π-orbitals of aromatic moiety (σ–π conjugation). So far, there are several reports about disilane-bridged aromatic molecules that exhibit stimuli-responsive polymorphism and solid-state physical properties specific to their molecular packing structures [54–56].

Recently, the authors have synthesized a rhombic disilanyl macrocycle **31** possessing four *p*-phenylenes linked by Si–Si bonds which exhibits thermal phase transition with crystal jumping and cracking [57]. Crystal structure analysis at variable temperature revealed that the disilanyl macrocycle has a rhombic structure with the disilane moiety at the apexes in both the α-form (high-temperature phase) and β-form (low-temperature phase). In the transition between α-form and β-form, the disilanyl macrocycle shows conformational transformation accompanied with a concerted parallel crank motion to change the aspect ratio of its rhombic structure. The anisotropic stretching/shrinking of the crystal lattice in the thermal phase transition induces mechanical stress resulting in crystal jumping and cracking. The bulky tetramethyldisilane structure, which suppresses π-stacking in the crystal,

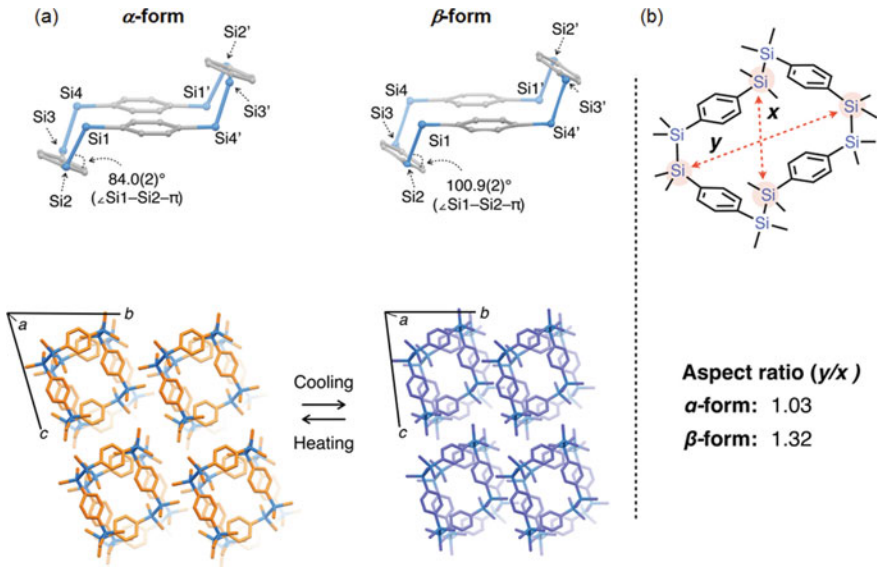

Fig. 8.9 **a** Change in the crystal structure and packing structure of the molecule **31** before and after the phase transition. **b** Change in aspect ratio of the ring structure (rhombic structure) before and after the phase transition. From ref. [57]. Copy right © 2020 American Chemical Society

seems to realize a conformational change of the disilane-based flexible skeleton of the macrocycle in the crystal (Fig. 8.9).

Garcia-Garibay, Naumov, and Rodríguez-Molina et al. [58] have reported that amphidynamic crystals of **32** composed of carbazole and DABCO (crystals with high crystallinity and fast rotation in some parts of the molecular structure) exhibit a thermosalient phenomenon (Fig. 8.10). In this crystal, four adjacent carbazole molecules create a rhombic cavity via CH···π interaction, which encapsulates DABCO via CH···N interaction. At around 320 K, a phase transition occurs from Form I to Form II as shown in Fig. 8.10, during which the rhombic cavity was deformed. From visual observation, a crystal jump phenomenon was observed from the (100) plane, which was consistent with the direction of the crystal lattice change.

8.3.5 Miscellaneous Crystals Exhibiting Thermosalient Phenomena Due to a Phase Transition

Figure 8.11 shows the molecules showing thermosalient phenomena due to the phase transition that cannot be classified in 8.3.1−8.3.4.

Xu and Raing et al. have reported that crystals of 2,7-di([1,1'-biphenyl]-4-yl)fluorenone **33** exhibit a thermosalient phenomenon [59]. In this case, it is explained

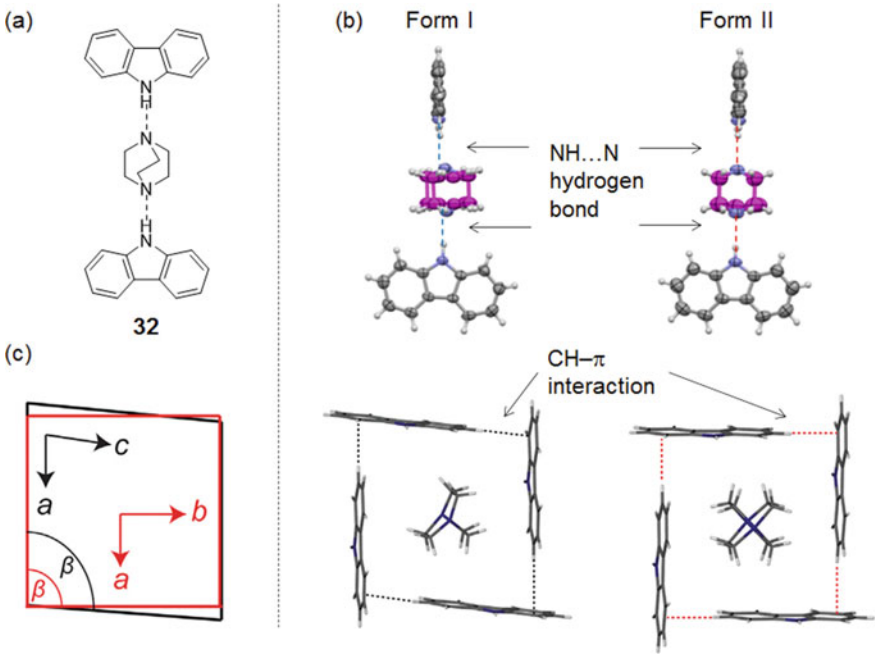

Fig. 8.10 **a** Structure of the amphidynamic crystal of **32** composed of DABCO incorporated into the rhombic structure of carbazole. **b** Phase transition of the amphidynamic crystal with DABCO incorporated into a four carbazole molecules between Form I and Form II. (c) Changes in the rhombic framework before and after the phase transition. Black: Form I. Red: Form II. From reference [58]. Copy right © 2019 Elsevier

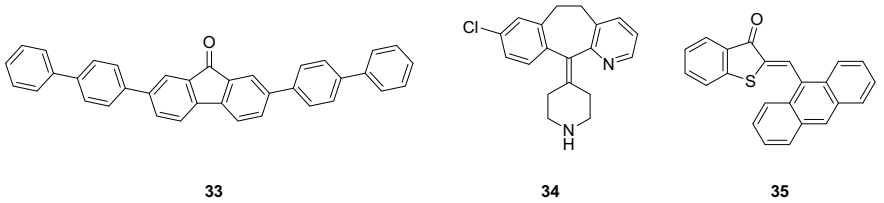

33 34 35

Fig. 8.11 Molecules of miscellaneous crystals which undergo phase transitions to exhibit thermosalient phenomena

in their report that the thermosalient phenomenon does not originate from the conformational change caused by the hindered rotation as explained in class II. The crystal phase transition and the deformation of the whole crystal are induced by the changes in the little dihedral angles among the aromatic rings located at the terminal. Anisotropic expansion and contraction of crystal lattice result in this process in crystal jumping phenomenon.

Desloratadine **34** is a common antihistamine used in the treatment of allergic reactions [60]. In the crystal, the piperidine ring in this molecule shows a ring-flipping motion resulting in phase transitions. The phase transitions of Phase I to Phase II and Phase II to Phase III occur at around 330 K and 350 K, respectively [61]. The X-ray structure analysis did not reveal any hydrogen bonding between NH···N or the formation of a two-dimensional packing structure in the crystal.

Wolf et al. studied the molecule **35** consisting of thioindiogo and anthracene [62]. When the crystals of the *Z*-form molecule are heated to 130 °C, an irreversible phase transition occurs with crystal jumping. Upon the transition, the dihedral angle between thioindigo and anthracene changes to form a *Z*'-isomer. The crystals also exhibit a photosalient phenomenon, i.e., a crystal jumping phenomenon based on the *Z-E* isomerization under UV irradiation.

Gaudon et al. reported the thermosalient phenomenon in the crystals of the inorganic compound $CuMo_{0.9}W_{0.1}O_4$ **36** [63]. With this molecule, the γ-crystal at the low-temperature forms octahedral sites with six Mo–O (W–O) bonds, whereas the α-crystal at the high-temperature forms tetrahedral sites with four Mo–O (W–O) (Fig. 8.12) [64]. A reversible thermosalient phenomenon is shown at 360 K from γ-crystal to α-crystal and at 275 K from α-crystal to γ-crystal, respectively. The γ-crystal has weak Mo–O (W–O) bonds forming molecules, while the α-crystal has higher rigidity and stronger Mo–O (W–O) bonds that crystallize with low-density packing. Thermosalient phenomenon is not observed in crystals of $CuMoO_4$, which does not contain any W. When the ratio of W to Mo is more than 0.1, it becomes a wolframite-type crystal with an octahedral structure and does not show the thermosalient phenomenon.

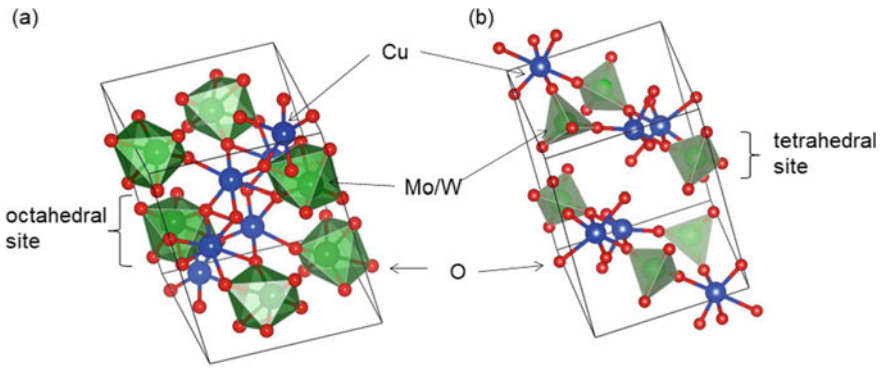

Fig. 8.12 Crystal structure of $CuMo_{0.9}W_{0.1}O_4$ **36**. **a** γ-crystal. **b** α-crystal. From reference [64]. Copy right © 2021 Elsevier

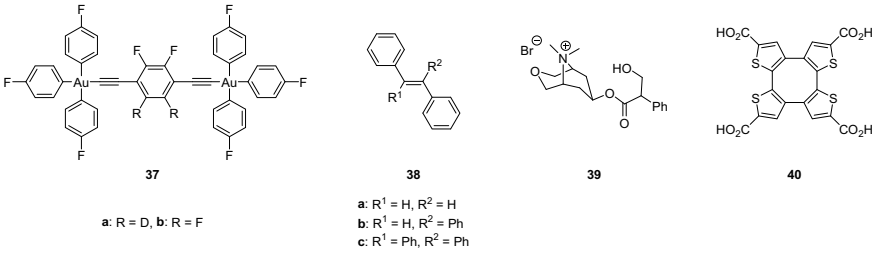

Fig. 8.13 Molecules exhibiting thermosalient phenomena without a crystal phase transition

8.3.6 Thermosalient Phenomena without Crystal Phase Transition

In this section, we introduce the thermosalient phenomenon which does not involve the crystal phase transition unlike the earlier sections. Typical compounds are shown in Fig. 8.13.

Ito and Garcia-Garibay et al. reported that crystals of dumbbell-shaped gold complexes **37** exhibit thermosalient phenomena without crystal phase transitions [65]. In this case, crystal migration and jumping phenomena are observed due to large and reversible thermal expansion with anisotropy. The luminescence behavior of these materials changes during the thermosalient phenomenon.

Seki and Ito et al. reported that crystals of a group **38** of simple hydrocarbon compounds with tetraphenylethene as a matrix skeleton exhibit a thermosalient phenomenon upon cooling to approximately −80 °C [66]. Unlike other groups of crystals, these are different crystals in which no phase transition occurs during the crystal jump phenomenon, as shown by single-crystal X-ray diffraction and differential thermal analysis. Anisotropy of thermal expansion leads to anisotropic size change of lattice parameter. Although the cause of the thermosalient phenomenon is not well understood, the approach of molecules along the direction perpendicular to the olefin plane upon cooling can be considered.

Skoko et al. have reported that crystals of methscopolamine bromide **39**, an analogue of compound **11** described in Sect. 8.3.2, exhibits a reversible thermosalient phenomenon when heated to 323–340 K and cooled to 313–303 K [67]. Although this crystal does not undergo a phase transition, it has anisotropic thermal expansion coefficients of the crystal lattice, which is the cause of the thermosalient phenomenon. Unlike the thermosalience of **11** which is derived from crystal phase transition, the crystal jumps over a wide temperature range (>10 K).

Takeda and Akutagawa reported a crystal jump phenomenon based on the adsorption and desorption of tetrahydrofuran (THF) in the channel of the hydrogen-bonded three-dimensional framework (HOF) [68] of tetra[2.3]thienylenetetracarboxylic acid **40** and the torsional motion of the ring-conjugated chain [69, 70]. The molecules of **40** form a diamond-shaped HOF. The size of the channels (vacancies) in this structure is 22.1× 23.6 Å, enclosing two THF molecules per unit. As THF is released

under heating, the core site of the tetra[2.3]thiophene skeleton undergoes a flipping motion, and the crystal lattice expands and contracts anisotropically [71]. After THF is removed, the vacancies were occupied by H_2O. This structure is transformed into the original THF-incorporated structure on exposure to THF vapor. The changes in the crystal composition and structural transformation due to the desorption of THF by heating are the causes of the thermosalient phenomenon. Although HOF is a weak structure compared to porous materials utilizing other interactions, the weak structure of HOF interestingly enables it to develop into heat-responsive materials.

Gong et al. reported the jumping behavior of crystals of a charge-transfer complex **41** that is a 1:1 co-crystal of coronene (COR; donor) and tetrafluoro-1,4-benzoquinone (TFBQ; acceptor) (Fig. 8.14) [72]. COR and TFBQ form alternating stacked crystals. The characteristic feature of this system is the utilization of TFBQ as a component, which readily volatilizes when thermally stimulated. As the temperature is gradually increased, the mechanical motion of the crystals that repeatedly flip, jump, rotate, shift, and swing is observed due to the change in crystal packing.

Shi et al. have studied the mechanical behavior of crystals of helical supramolecular metal complexes **42a** and **42b** composed of $UO_2(NO_3)_2$, dicarboxylic acid and phenanthroline (Fig. 8.15) [73]. Although no clear phase transition was observed from the temperature-variable PXRD observations, they reported that the crystals jump due to the anisotropic thermal expansion and the change in the π-stacking of the inner phenanthroline. Since the $–SO_2–$ unit in the dicarboxylic acid backbone is less sterically hindered than the $–C(CF_3)_2–$ unit, the crystal of **42b** exhibits a thermosalient phenomenon at lower temperatures.

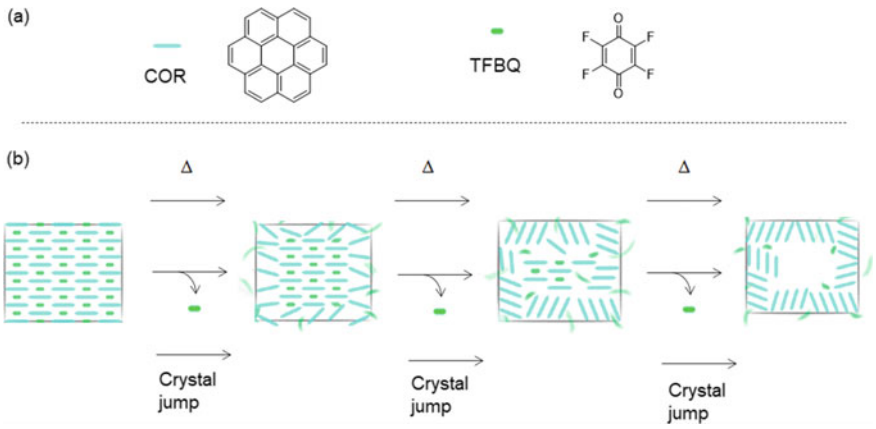

Fig. 8.14 Thermosalient phenomena utilizing components that readily volatilize upon thermal stimulation. **a** Structure of COR and TFBQ. **b** Thermally induced jumping behavior of the charge-transfer complex **41**, a 1:1 co-crystal of COR and TFBQ. From reference [72]. Copy right © 2021 American Chemical Society

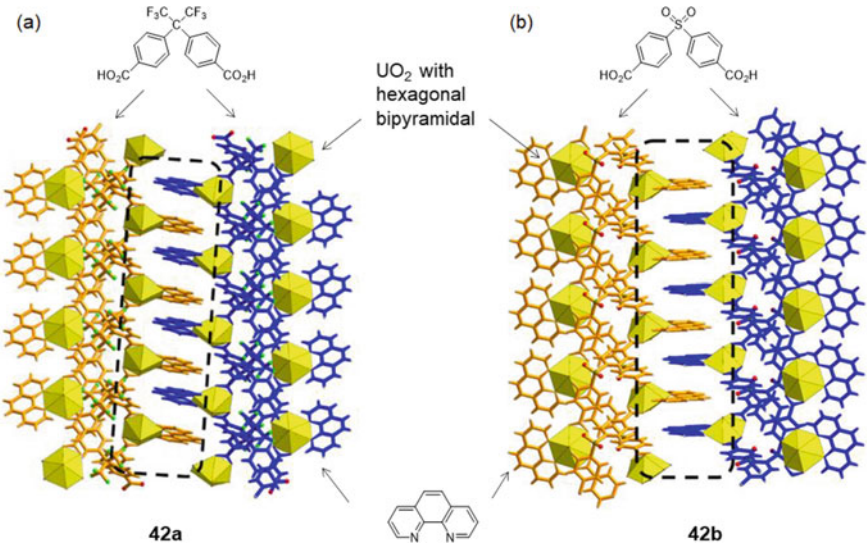

Fig. 8.15 Packing structures of supramolecular complexes **42a** and **42b** exhibiting thermosalient phenomena. From reference [73]. Copy right © 2021 Wiley–VCH

8.4 Summary

Thermosalient phenomena are caused by small changes in the arrangement of molecules in crystals in response to thermal stimuli, and manifested as fragmentation/explosion/cracking/splitting caused by changes in the crystal lattice. The constituent units of organic crystals are very simple, and it is surprising that small changes at the molecular level can be converted into macroscopic mechanical responses such as crystal jumping. The crystals exhibiting thermosalient phenomena may be used in micro-(or nano-) scale molecular machines, artificial muscles, and so on [74]. In particular, the crystal cleaves when thermosalient phenomenon occurs, which can be applied as a molecular fuse to prevent overcurrent in an electric circuit [75].

A detailed review of different type of crystals and the mechanism of the thermosalient phenomenon exhibited by them under external stimuli was provided. It is difficult to predict the crystal phase transition, the crystal polymorphism and the design of a molecule which shows the thermosalient phenomenon. Therefore, we have not yet clarified the whole picture of the thermosalient phenomenon, and various interpretations and possibilities are assumed. At present, the basic data are insufficient, and it is necessary to clarify the principle for many compounds to enable design of compounds with such properties. In this review, we introduced the salient phenomenon by thermal stimulation, and a similar phenomenon by optical stimulation (photosalient phenomenon) is also developing. For further details, another review is referred for additional information [76].

References

1. Kato M, Ito H, Hasegawa M, Ishii K (2019) Chem Eur J 25:5105–5112
2. Gigg J, Gigg R, Payne S, Conan R (1987) J Chem Soc Perkin Trans I:2411–2414
3. Seki T (2015) Kagaku to Kogyo 68:254–255
4. Takeda T (2019) Mol Sci 13:A0102
5. Porter DA, Eastering K, Sherif M (2009) Phase transformations in metals and alloys, 3rd edn. CRC Press
6. Lexcellent C (2013) Shape-memory alloys handbook. Wiley
7. Nath NK, Panda MK, Sahoo SC, Naumov P (2014) CrystEngComm 16:1850–1858
8. Commins P, Desta IT, Karothu DP, Panda MK, Naumov P (2016) Chem Commun 52:13941–13954
9. Sahoo SC, Panda MK, Nath NK, Naumov P (2013) J Am Chem Soc 135:12241–12251
10. Naumov P, Chizhik S, Panda MK, Boldyreva E (2015) Chem Rev 115:12440–12490
11. Panda MK, Runcevski T, Husain A, Dinnebier RE, Naumov P (2015) J Am Chem Soc 137:1895–1902
12. Sahoo SC, Sinha SB, Kiran MSRN, Ramamurty U, Dericioglu AF, Reddy CM, Naumov P (2013) J Am Chem Soc 135:13843–13850
13. Lieberman HF, Davey RJ, Newsham DMT (2000) Chem Mater 12:490–494
14. Karothu DP, Naumov P (2021) Isr J Chem 61:557–562
15. Ding J, Herbst R, Praefcke K, Kohne B, Saenger W (1991) Acta Cryst B47:739–742
16. Etter MC, Siedle AR (1983) J Am Chem Soc 105:641–643
17. Panda MK, Runcevski T, Sahoo SC, Belik AA, Nath NK, Dinnebier RE, Naumov P (2014) Nat Commun 5:4811
18. Takemura H (2005) Kagaku 60:46–49
19. Yasutake M, Sakamoto Y, Onaka S, Sako K, Tatemitsu H, Shinmyozu T (2000) Tetrahedron Lett 41:7933–7938
20. Seki T, Mashimo T, Ito H (2019) Chem Sci 10:4185–4191
21. Kato K, Seki T, Ito H (2021) Inorg Chem 60:10849–10856
22. Siegrist T, Besnard C, Haas S, Schiltz M, Pattison P, Chernyshov D, Batlogg B, Kloc C (2007) Adv Mater 19:2079–2082
23. Campbell RB, Robertson JM, Trotter J (1961) Acta Crystallogr 14:705
24. Campbell RB, Robertson JM, Trotter J (1962) Acta Crystallogr 15:289
25. Takeda T, Akutagawa T (2016) Chem Eur J 22:7763–7770
26. Restrepo RD (2007) Respir Care 52:833–851
27. Skoko Z, Zamir S, Naumov P, Bernstein J (2010) J Am Chem Soc 132:14191–14202
28. Steiner T, Hinrichs W, Saenger W, Gigg R (1993) Acta Cryst B49:708–718
29. Corbett JM, Dickman MH (1996) Acta Crystallogr. Sect C: Cryst Struct Commun 52:1851–1853
30. Tamboli MI, Karothu DP, Shashidhar MS, Gonnade RG, Naumov P (2018) Chem Eur J 24:4133–4139
31. So H-S, Minami T, Jindo T, Matsumoto S (2018) CrystEngComm 20:5317–5320
32. So H-S, Matsumoto S (2019) Acta Cryst B75:414–422
33. Kikuchi Y, Matsumoto S (2021) CrystEngComm 23:5882–5890
34. Davey RJ, Maginn SJ, Andrews SJ, Black SN, Buckley AM, Cottier D, Dempsey P, Plowman R, Rout JE, Stanley DR, Taylor A (1994) Mol Cryst Liq Cryst 242:79–90
35. Wu H, Reeves-McLaren N, Pokorny J, Yarwood J, West AR (2010) Cryst Growth Des 10:3141–3148
36. Centore R, Jazbinsek M, Tuzi A, Roviello A, Capobianco A, Peluso A (2012) CrystEngComm 14:2645–2653
37. Alimi LO, van Heerden DP, Lama P, Smith VJ, Barbour LJ (2018) Chem Commun 54:6208–6211
38. Gaztañaga P, Baggio R, Halaca E, Vega DR (2019) Acta Cryst B75:183–191

39. Mittapalli S, Perumall DS, Nangia A (2017) IUCrJ 4:243–250
40. Chinnasamy R, Munjal B, Suryanarayanan R, Peedikakkal AMP, Mishra MK, Ghosh S (2022) Cryst Growth Des 22:615–624
41. Mittapalli S, Perumall DS, Nanubolu JB, Nangia A (2017) IUCrJ 4:812–823
42. Rawat H, Samanta R, Bhattacharya B, Deolka S, Dutta A, Dey S, Raju KB, Reddy CM (2018) Cryst Growth Des 18:2918–2923
43. Bolla G, Chen Q, Gallo G, Park I-H, Kwon KC, Wu X, Xu Q-H, Loh KP, Chen S, Dinnebier RE, Ji W, Vittal JJ (2021) Cryst Growth Des 21:3401–3408
44. Davis F, Higson S (2011) Macrocycles: Construction, Chemistry and Nanotechnology Applications. John Wiley & Sons, Chichester
45. Liu Z, Nalluri SKM, Stoddart JF (2017) Chem Soc Rev 46:2459–2478
46. Gon M, Tanaka K, Chujo Y (2021) Chem Rec 21:1358–1373
47. Ohtani S, Gon M, Tanaka K, Chujo Y (2017) Chem Eur J 23:11827–11833
48. Rath BB, Gallo G, Dinnebier RE, Vittal JJ (2021) J Am Chem Soc 143:2088–2096
49. Nakae T, Nishio M, Yamanoi Y (2020) Bull Jpn Soc Coord Chem 76:31–39
50. Shimada M, Yamanoi Y, Nishihara H (2016) Yuki Gosei Kagaku Kyokaishi 74:1098–1107
51. Yamanoi Y (2019) Kagaku Kogyo 70:260–266
52. Yamanoi Y, Nishihara H (2009) Yuki Gosei Kagaku Kyokaishi 67:778–786
53. Yamanoi Y (2018) Keiso Kagaku Kyokaishi 35:11–17
54. Nakae T, Nishio M, Usuki T, Ikeya M, Nishimoto C, Ito S, Nishihara H, Hattori M, Hayashi S, Yamada T, Yamanoi Y (2021) Angew Chem Int Ed 60:22871–22878
55. Nishio M, Shimada M, Omoto K, Nakae T, Maeda H, Miyachi M, Yamanoi Y, Nishibori E, Nakayama N, Goto H, Matsushita T, Kondo T, Hattori M, Jimura K, Hayashi S, Nishihara H (2020) J Phys Chem C 124:17450–17458
56. Nakae T, Nishio M, Yamada T, Yamanoi Y (2021) Molecules 26:6852
57. Omoto K, Nakae T, Nishio M, Yamanoi Y, Kasai H, Nishibori E, Mashimo T, Seki T, Ito H, Nakamura K, Kobayashi N, Nakayama N, Goto H, Nishihara H (2020) J Am Chem Soc 142:12651–12657
58. Colin-Molina A, Karothu DK, Jellen MJ, Toscano RA, Garcia-Garibay MA, Naumov P, Rodríguez-Molina B (2019) Matter 1:1033–1046
59. Duan Y, Semin S, Tinnemans P, Cuppen H, Xu J, Rasing T (2019) Nat Commun 10:4573
60. DuBuske LM (2005) Expert Opin Pharmacother 6:2511–2523
61. Srirambhatla VK, Guo R, Dawson DM, Price SL, Florence AJ (2020) Cryst Growth Des 20: 1800–1810
62. Hean D, Alde LG, Wolf MOJ (2021) Mater Chem C 9:6789–6795
63. Robertson L, Penin N, Blanco-Gutierrez V, Sheptyakov D, Demourgues A, Gaudon MJ (2015) Mater Chem C 3:2918–2924
64. Pudza I, Kalinko A, Cintins A, Kuzmin A (2021) Acta Mater 205:116581
65. Jin M, Yamamoto S, Seki T, Ito H, Garcia-Garibay MA (2019) Angew Chem Int Ed 58:18003–18010
66. Seki T, Mashimo T, Ito H (2020) Chem Lett 49:174–177
67. Klaser T, Popović J, Fernandes JA, Tarantino SC, Zema M, Skoko Ž (2018) Curr Comput-Aided Drug Des 8:301
68. Lin R-B, He Y, Li P, Wang H, Xhao W, Chen B (2019) Chem Soc Rev 48:1362–1389
69. Takeda T, Ozawa M, Akutagawa T (2019) Angew Chem Int Ed 58:10345–10352
70. Takeda T, Akutagawa T (2020) Kagaku 75:66–67
71. Takeda T, Ozawa M, Akutagawa T (2019) Cryst Growth Des 19:4784–4792
72. Chen Y, Li J, Gong J (2021) ACS Materials Lett. 3:275–281
73. Mei L, An S-W, Hu K-Q, Wang L, Yu J-P, Huang Z-W, Kong X-H, Xia C-Q, Chai Z-F, Shi W-Q (2020) Angew Chem Int Ed 59:16061–16068
74. Karothu DP, Halabi JM, Li L, Colin-Molina A, Rodríguez-Molina B, Naumov P (2020) Adv Mater 32:1906216
75. Khalil A, Ahmed E, Naumouv P (2017) Chem Commun 53:8470–8473
76. Koshima H, Hasebe S, Hagiwara Y, Asahi T (2021) Isr J Chem 61:1–15

Open Access This chapter is licensed under the terms of the Creative Commons Attribution 4.0 International License (http://creativecommons.org/licenses/by/4.0/), which permits use, sharing, adaptation, distribution and reproduction in any medium or format, as long as you give appropriate credit to the original author(s) and the source, provide a link to the Creative Commons license and indicate if changes were made.

The images or other third party material in this chapter are included in the chapter's Creative Commons license, unless indicated otherwise in a credit line to the material. If material is not included in the chapter's Creative Commons license and your intended use is not permitted by statutory regulation or exceeds the permitted use, you will need to obtain permission directly from the copyright holder.

Chapter 9
Soft Crystal Chemiluminescence Systems Using Organic Peroxides

Takashi Hirano and Chihiro Matsuhashi

Abstract Chemiluminescence (CL) is a phenomenon in which a chemical reaction produces an excited-state product that emits light. Taking advantage of this property, several analytical methods to study the CL reactions by photon detection have been developed in the literature. By applying this methodology to molecular crystals, soft crystal CL systems have been constructed to analyze the intracrystalline reactions of chemiluminescent compounds. In this chapter, the fundamental concept and applications of CL are presented. Using the example of the CL reactions involving organic peroxides, important characteristics of CL such as chemiexcitation, quantum yield and emission wavelengths are discussed. Furthermore, CL in solid state and in molecular crystals are described. Finally, the application of organic peroxides as a soft crystal CL system and the characteristics of their intracrystalline reactions such as crystal structure-dependencies, reaction kinetics and inductions of phase transitions are elucidated. This chapter concludes with a brief outlook towards the future of soft crystal CL systems.

Keywords Chemiluminescence · Organic peroxide · 1,2-Dioxetane · Crystalline-state reaction · Real-time analysis

9.1 Introduction: Research Significance of Soft Crystal Chemiluminescence Systems

Chemiluminescence (CL) is a phenomenon in which light is emitted during a chemical reaction that yields an electronically excited product [1–3]. Soft crystal CL systems are a group of crystalline materials that demonstrate CL during chemical reactions in crystals with soft properties. A "soft property of a crystal" means that the crystal has a property to undergo its facile structural transformation and phase transition in response to weak but specific stimuli. Basic and applied research studies

T. Hirano (✉) · C. Matsuhashi
Department of Fundamental Science and Engineering, Graduate School of Information Science and Engineering, The University of Electro-Communications, Chofu, Tokyo 182-8585, Japan
e-mail: thirano@uec.ac.jp

© The Author(s) 2023

M. Kato and K. Ishii (eds.), *Soft Crystals*, The Materials Research Society Series,
https://doi.org/10.1007/978-981-99-0260-6_9

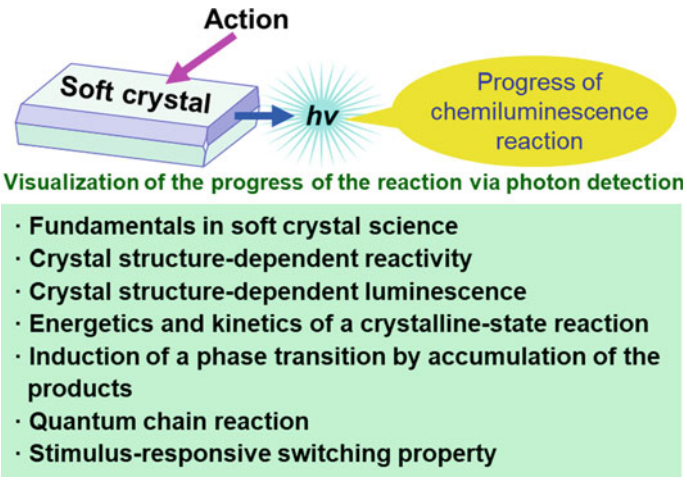

Fig. 9.1 Application of chemiluminescence in soft crystal science

on CL have been conducted as CL is a useful analytical technique when used along with photon detection, especially in the crystalline state chemistry (Fig. 9.1). For instance, if CL is induced by a mechanical force, as seen in the mechanochemistry of polymers described below, the applied stress can be optically detected. In this way, the chemical reaction in the crystal can be visualized.

A crystalline-state reaction has the advantage of yielding a selective product that reflects the crystal structure of the reactant. In fact, crystalline-state photochemical reactions of organic compounds and photochemical and thermal polymerizations of alkynes in crystals have been studied for a long time [4–6], which provided important reaction modes. Recently, mechanochemical methods, which involve mixing crystals mechanically, have been developed for organic synthesis [7, 8], to pioneer environmentally friendly reactions. In the field of pharmaceutical sciences, drugs are often dosed in the crystalline state; therefore, it is necessary to understand the reactivity of these drugs, especially the kinetics, in the crystalline state to understand their stability [9, 10]. Because of all of these current and potential applications, studying the basic theory of the chemical reactions that occur in crystals is important. In particular, the "soft property of crystals", i.e., a property of the crystal that changes the molecular and crystal structures during chemical reactions, is an important research topic (Fig. 9.1) [11]. However, several unresolved problems must be addressed in crystalline-state chemical reactions which require an understanding of the relationships between crystal structures and reactivities, the energetics and kinetics of reactions, the mechanism of tuning the luminescence properties within crystals, and the mechanism of "action" responsiveness based on the fundamental theories. Soft crystal CL systems are a valuable tool to address these problems and to visualize and track the progress of intracrystalline reaction. In this context, in recent years, efforts to elucidate the reaction mechanisms of crystalline-state CL reactions and to

construct a fundamental theory of intracrystalline reactions have been underway. In this chapter, first, we will discuss the fundamentals and general usefulness of the CL reactions of organic peroxides, followed by the features of peroxide CL in the solid state and condensed state and those in molecular crystals. In particular, characteristics of intracrystalline reactions that have recently been revealed by soft crystal CL systems will be described, followed by a future perspective.

9.2 Characteristics of the Chemiluminescence Reactions of Organic Peroxides

9.2.1 Real-Time Analysis by Photon Detection

As described above, CL is luminescence caused by a chemical reaction, which includes bioluminescence (BL) seen in a firefly or a sea firefly. In analytical chemistry, we exert an "action" on a "sample" and detect its "response" to obtain the necessary information, such as the concentration, mass, or physical properties, on the target material in the sample. Because a CL reaction generates photons, we can recognize that "a chemical reaction has occurred" by photon detection (Fig. 9.2). Therefore, CL is widely used as an analytical method because the "response" to the "action" of the CL during the reaction can be detected optically [12]. It is well known that the CL of luminol is used for bloodstain detection and the firefly BL reaction is used for ATP detection; these reactions are based on the fact that the analyte is an essential factor in the reaction progression. For instance, hemoglobin in the blood catalyzes the acceleration of the CL reaction of luminol, and ATP is the reagent responsible for the activation (adenylation) of firefly luciferin (Fig. 9.3). Because the presence or absence of an analyte and its abundance can be confirmed by photon detection, information on the production, consumption, and transfer of the analyte can be traced by relying on the luminescence.

A representative example of this is the firefly BL reaction. Firefly BL is based on the luciferin-luciferase (L-L) reaction involving the substrate, firefly luciferin and the enzyme, luciferase; this reaction requires ATP and oxygen to react with luciferin and Mg^{2+} to activate the enzyme [13, 14]. All the above substrates and reagents are essential to produce photons in the L-L reaction; hence, all of them can be marked as analytes whose presence can be confirmed by luminescence. Luciferase is created through gene expression in a cell and is lost due to degradation. Since ATP, oxygen, and Mg^{2+} are normally present in the cell, gene expression and migration of luciferase in the cell can be tracked by photon detection by injecting luciferin into the cell (Fig. 9.2e). The same analysis can be performed in vivo in a mammal, such as a mouse, enabling us to "watch" (analyze) the reaction in a living organism in real time via BL imaging [15–17]. This ability of "real-time analysis" by photon detection is the most attractive aspect of CL [18, 19].

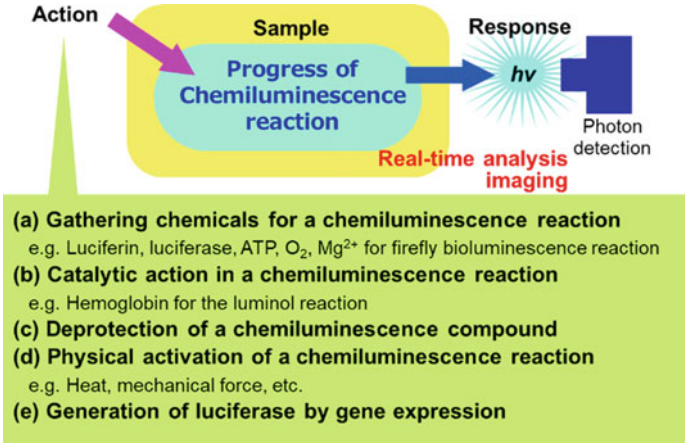

Fig. 9.2 Chemical analyses of chemiluminescence reactions

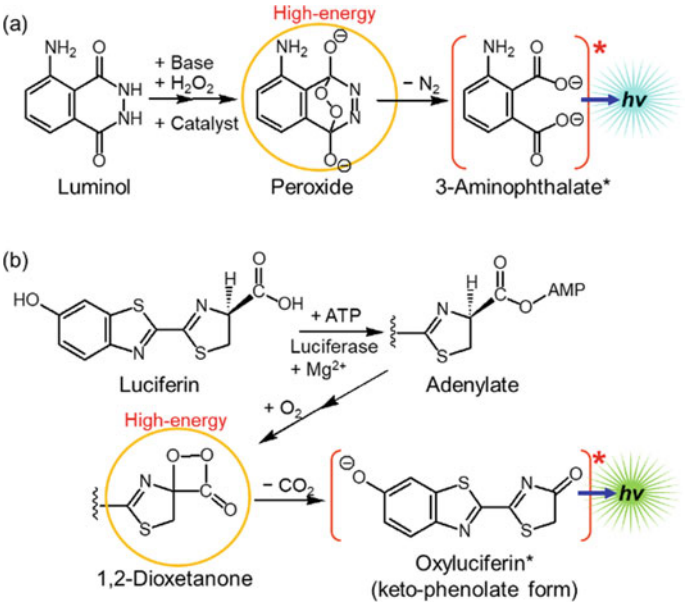

Fig. 9.3 **a** Chemiluminescence reaction of luminol and **b** bioluminescence reaction of firefly luciferin

9.2.2 *Chemiexcitation, Quantum Yield and Emission-Wavelength Regulation*

For a chemical reaction to produce photons, in most cases, the reaction must be exothermic, in which the energy emitted must be equivalent to that required for the production of photons. The CL reaction of luminol proceeds with O_2 or hydrogen peroxide under basic conditions via a cyclic peroxide intermediate, whose thermal decomposition gives the excited-state product, which emits light (Fig. 9.3a). In the firefly BL reaction, the adenylated form of luciferin gives a cyclic peroxide intermediate via oxygen addition and its thermal decomposition gives the excited-state product (Fig. 9.3b). Many chemiluminescent compounds involve such peroxide intermediates in their reactions. Thus, the essence of CL lies in the fact that a peroxide intermediate acts as a high-energy compound, which yields the essential emissive excited-state product by thermal decomposition (Fig. 9.4). This process is called "chemiexcitation". For chemiexcitation to occur, the process must be an exothermic reaction and the energy difference between the transition state of the high-energy compound and the ground-state products must be sufficient to emit light. The peroxide intermediates described above satisfy the chemiexcitation conditions.

Notably, the peroxide intermediate in the firefly reaction is a 1,2-dioxetanone, which is a derivative of the 1,2-dioxetane and a historically key structure involved in the BL reactions [2, 3]. 1,2-Dioxetanes have a strained four-membered ring structure with an O–O bond, which easily undergoes a ring-opening reaction to yield two carbonyl products by the cleavage of O–O and C–C bonds. Among the 1,2-dioxetane derivatives, 3,3,4,4-tetramethyl-1,2-dioxetane (TMD) has been studied the most, as a representative derivative, to develop the energy diagram for the thermal decomposition reaction to yield the excited singlet (S_1) or excited triplet (T_1) states of the product acetone (Fig. 9.5) [20, 21]. The activation energies of the thermolytic reactions and the efficiencies for generating excited-state products of 1,2-dioxetane derivatives have been widely studied [22, 23].

The efficiency with which the excited-state product is generated by the thermal decomposition of a 1,2-dioxetane derivative is termed as chemiexcitation efficiency, which is an important CL property. For instance, the L-L reaction using firefly

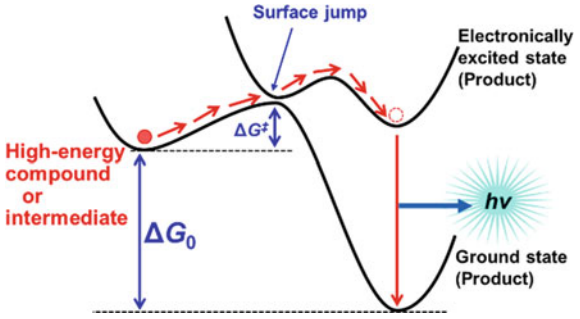

Fig. 9.4 Chemiexcitation process of a high-energy compound or intermediate

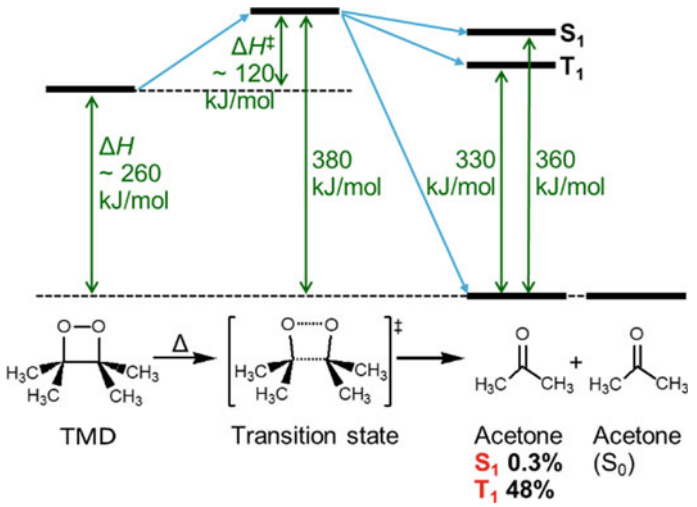

Fig. 9.5 Chemiluminescence reaction of TMD

luciferin and North American firefly luciferase produces photons with an efficiency of 41% [24], which means that 41 photons are produced from 100 molecules of luciferin. This efficiency is otherwise known as the BL quantum yield (Φ_{BL}). The light-emitter in the L-L reaction is oxyluciferin, which is the oxidation product of luciferin, and this oxyluciferin emits photons in the S_1 state. Because the chemiexcitation from the 1,2-dioxetanone intermediate to give the S_1-state oxyluciferin is part of the multistep process in the L-L reaction, the chemiexcitation efficiency will be more than 41%. The contents of Φ_{BL} is similar to those of the CL quantum yield (Φ_{CL}) as explained later.

It is expected that 1,2-dioxetanes undergo efficient chemiexcitations; however, in practice, efficient chemiexcitations are limited to a few cases such as the firefly BL reaction. An example of an inefficient chemiexcitation is the thermolysis of TMD in benzene, in which the S_1 and T_1 states of acetone molecules were produced with 0.3 and 48% efficiencies, respectively (Fig. 9.5) [21]. Similar to TMD, several alkyl-substituted 1,2-dioxetanes mainly yield T_1-state products by chemiexcitation processes, however, with different chemiexcitation efficiencies from that of the firefly BL reaction. The differences in the chemiexcitation efficiencies are attributed to the substituent effects on 1,2-dioxetanes [2]. The methyl groups in TMD do not exert strong electronic substituent effects on the homolytic bond cleavages of the 1,2-dioxetane ring. Theoretical calculations indicate that the O–O bond cleavage starts first as a rate-limiting step, followed by the C–C bond cleavage [25, 26]. The homolytic progression of the O–O bond cleavage gives the 1,4-dioxy biradical, in which the energies of the singlet and triplet states are close to each other, leading to the efficient formation of a T_1-state product. In contrast, in the firefly BL reaction, the 1,2-dioxetanone ring in the intermediate is spiro-linked to the π-conjugated moiety of luciferin (Fig. 9.3b). The π-conjugated moiety containing the phenolate anion

is electron-donating (D) and the 1,2-dioxetanone is electron-accepting (A), which leads to an intramolecular electron transfer and subsequent decomposition of 1,2-dioxetanone generates the oxyluciferin radical and the CO_2 radical anion. When the CO_2 radical anion transfers an electron to the oxyluciferin radical, oxyluciferin in the S_1 state (phenolate anion) will be generated with high efficiency [27]. This mechanism is called the CIEEL (chemically initiated electron exchange luminescence) mechanism.

Subsequent theoretical calculations lead to a modification of the CIEEL mechanism to the CTIL (charge transfer induced luminescence) mechanism, in which the reaction proceeds by intramolecular charge transfer instead of electron transfer [28]. In the CTIL mechanism, unlike the homolytic bond cleavage mechanism described above, the chemiexcitation proceeds through the transition state in the S_1 state which has a high charge-transfer ability and a reduced biradical character. The CTIL mechanism of the 1,2-dioxetanone intermediate of the firefly BL reaction proceeds so rapidly that the intermediate has not been directly observed to date; however, its existence has been confirmed by isotope experiments. In general, CL reactions via the CTIL mechanism proceed rapidly. On the other hand, stable 1,2-dioxetane derivatives have been found, including TMD, whose thermolytic reactions proceed by the homolytic bond cleavage mechanism. Three groups of compounds with the adamantane moiety are representative examples of stable 1,2-dioxetanes (Fig. 9.6: Adox, Ad-OSi, and Ad-Acr) [29–31]. Among them, adamantylideneadamantane 1,2-dioxetane (Adox) has the highest thermal stability [3, 32]. The stability of these derivatives is attributed to the inhibition of the elongation of the O–O bond to give a trapezoidal shape to the 1,2-dioxetane ring before the homolytic bond cleavage. This deformation results in a spatial proximity between the substituents attached to C3 and C4 of the 1,2-dioxetane ring. In the case of the thermal decomposition of Adox, the two adamantane moieties must be brought spatially closer, which requires a relatively high activation energy. Then, Adox has a thermal stability. Other 1,2-dioxetanes with the adamantane moiety also have a thermal stability in the similar manner to Adox. Among the three compounds Adox, Ad-OSi, and Ad-Acr, Ad-OSi demonstrates a reactivity change by silyl-deprotection [30]. Ad-OSi is easily converted to unstable Ad-O^- by a reagent for silyl-deprotection. The 1,2-dioxetane ring in Ad-O^- is connected to the electron-donating moiety and activates the CTIL mechanism, leading to a fast reaction rate and generation of the S_1-state product with high efficiency. Thus, the stability of a 1,2-dioxetane derivative can be manipulated by deprotection. Moreover, this technique is useful for analyzing a deprotection reagent. For example, by replacing the silyl group of Ad-OSi with the acetyl group, the enzymatic action of an esterase for ester hydrolysis can be analyzed by photon detection (Fig. 9.2c) [33].

As the important characteristics of CL reactions, the regulation of the efficiency and reaction rate of the chemiexcitation have been discussed. The chemiexcitation efficiency is an important component of the CL quantum yield (Φ_{CL}). That is, for a CL reaction that emits photons from the S_1 state products, the Φ_{CL} value is described as follows:

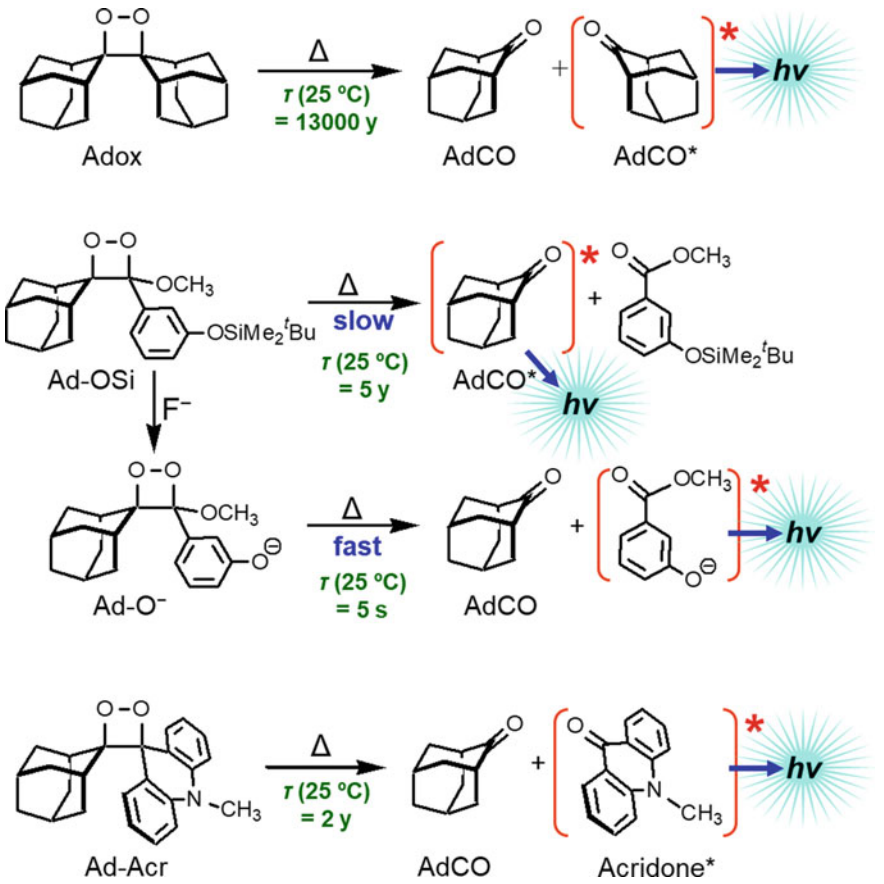

Fig. 9.6 Chemiluminescence reactions of stable 1,2-dioxetanes

$$\Phi_{CL} = \Phi_R \times \Phi_S \times \Phi_F \tag{9.1}$$

where Φ_R is the reaction efficiency to afford the main products in the ground and excited states, Φ_S is the chemiexcitation efficiency to yield the product in the S_1 state by decomposition of the high-energy intermediate, and Φ_F is the fluorescence emission efficiency of the product in the S_1 state. Eq. (9.1) is applicable to the analysis of a Φ_{BL} value. In the case of the thermolytic reaction of a 1,2-dioxetane, two carbonyl products are obtained quantitatively, indicating $\Phi_R = 1$. Thus, the equation becomes

$$\Phi_{CL} = \Phi_S \times \Phi_F \tag{9.2}$$

Another important characteristic of the CL reactions is the emission wavelength, which is determined by the nature of the excited-state product of the reaction. Most of the CL reactions including BL reactions produce light from the S_1-state products.

For instance, in the CL reaction of luminol, blue emission occurs from the S_1 state of 3-aminophthalate (Fig. 9.3a). In the firefly BL reaction, the phenolate anion of oxyluciferin, which is in the S_1 excited state, emits green to red light (Fig. 9.3b) [34]. The visible light emission wavelength (i.e., color) can be varied by adjusting the stability of the S_1 state of oxyluciferin in the active site of luciferase. The thermolytic reaction of TMD shows violet emission from the S_1 state of acetone, while its Φ_{CL} value is low, owing to the low Φ_S value to generate the S_1-state acetone and the low Φ_F value of acetone Eq. (9.2).

To analyze CL, a desired emission wavelength must be obtained. To achieve this, one method is to adjust the π-electronic system of the excited state product. In the case of the CL reaction of a 1,2-dioxetane derivative, the fluorescence emission wavelength of either of the two carbonyl products can be adjusted. The thermolytic reaction of the stable 1,2-dioxetane derivative Ad-Acr, for instance, yields 2-adamantanone (AdCO) and acridone as the products. Because acridone has a wider π-electronic system than AdCO, the S_1 state of acridone is preferentially generated by chemiexcitation and shows blue-light emission (Fig. 9.6) [31].

Chemiluminescence resonance energy transfer (CRET) is another method to achieve a desired emission wavelength. When a fluorophore is linked to a chemiluminescent moiety in a non-conjugated manner, intramolecular Förster-type resonance energy transfer can take place from the S_1-state product of the chemiluminescent moiety to the fluorophore moiety [35], thus achieving emission from the fluorophore moiety. This mechanism is named CRET, similar to fluorescence resonance energy transfer (FRET), which is the resonance energy transfer between two fluorescent dyes. If the product generated from the chemiluminescent moiety has a low Φ_F value, CRET can be applied to improve Φ_{CL}. When the intermolecular distance between the chemiluminescent and fluorophore moieties is shortened, CRET aids in modulating the emission wavelength. Several living organisms, such as the jellyfish *Aequorea,* have also utilized CRET in their BL reactions [36]. This jellyfish has a photoprotein, aequorin, which has the chemiluminescent compound in the apoprotein, and a green fluorescent protein (GFP), which has a fluorophore within a β-barrel structure. The S_1-state product generated within the apoprotein of aequorin usually emits blue light. However, aequorin and GFP, which are in close proximity to each other, experience energy transfer from the S_1-state product of aequorin to GFP, resulting in the emission of green luminescence. This mechanism is called bioluminescence resonance energy transfer (BRET), which is a BL version of CRET. On a related note, aequorin has a Ca^{2+}-chelating site (EF hand), and this Ca^{2+}-binding triggers the BL reaction in aequorin. Therefore, aequorin has been used as a BL indicator for Ca^{2+} (Fig. 9.2a).

In this section, we reviewed the chief characteristics and reaction mechanisms of CL, including BL. For the explanations, we described the thermolytic reactions of 1,2-dioxetanes, which are the representative high-energy compounds. The bicyclic peroxide intermediate derived from luminol was also an example of a high-energy compound for chemiexcitation (Fig. 9.3a). As other peroxides for CL reactions, two examples will be introduced here. One is diphenoyl peroxide (Fig. 9.7), which shows CL when in combination with an electron-donating aromatic compound. This

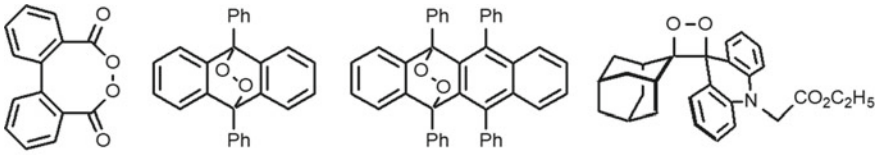

Fig. 9.7 Organic peroxides capable of chemiluminescence

peroxide was used to elucidate the CIEEL mechanism [37]. Another is an endoperoxide of an aromatic hydrocarbon. Interestingly, endothermic thermolytic reactions of endoperoxides of naphthalenes and anthracenes show CL [38]. For example, the endoperoxide of 9,10-diphenylanthracene (DPA) (Fig. 9.7) thermally decomposes to give DPA and a singlet oxygen [39]. The singlet oxygen is converted to the triplet state accompanied by near-infrared light emission (1270 nm), demonstrating that it is a CL reaction. Although this reaction is endothermic and not exothermic, CL is achieved because the singlet oxygen is generated according to the spin conservation law. Thus, the CL reactions of the endoperoxides of aromatic hydrocarbons have different chemiexcitation character from those of other peroxides including 1,2-dioxetanes.

9.3 Chemiluminescence in the Solid State and Condensed State

CL is a useful analytical tool for photon detection; therefore, studies have focused mainly on its application in solution. Although CL in the solid state has been known for a long time, there have only been a few systematic studies. In 1926, Moureau et al. reported that heated crystals of rubrene endoperoxide (Fig. 9.7) emitted red light; the reaction mechanism remains unresolved to date [40, 41]. Crystals of Adox were also known to glow during thermal analysis [42]. In addition, studies of CL were conducted by heating the solid samples to analyze the subsequent reaction and to access the condensed state. A condensed state including the crystalline state is a state of high concentration, in which intermolecular interactions and energy transfer are expected to be favored.

In a condensed state, the photoreactivity of 1,2-dioxetane is related to the CL reaction, to make a quantum chain reaction [43]. In the photoreaction reaction of 1,2-dioxetane, the carbonyl products are formed in the S_1 and T_1 states similar to the thermolytic reaction. When the photoreaction of the 1,2-dioxetane derivative is conducted in a condensed state, the excited-state product enables energy transfer to the unreacted 1,2-dioxetane derivative, resulting in its decomposition. This process triggers a quantum chain reaction with a high quantum yield. For example, the quantum chain

photoreaction of TMD in a solution has a quantum yield that exceeds 200 [44]. A similar reaction was reported using solid-state Adox where a condensed state was obtained by concentrating a mixed solution of Adox and a lanthanide ion complex such as $Eu(fod)_3$ [45]. A lanthanide ion complex catalyzes the thermal decomposition of 1,2-dioxetane, in addition to acting as an energy acceptor for light emission. Therefore, this combination of Adox and a lanthanide ion complex in the condensed state demonstrates a successful synergistic CL with the quantum chain reaction. Another example of CL in condensed state was demonstrated with a stable 1,2-dioxetane derivative with the acridane moiety, Ad-Acr(ester) (Fig. 9.7) [46]. Ad-Acr(ester) derivatives, which are used for the surface modification of silica nanoparticles, were employed to design an analytical technique for the CL analysis of a biomolecule in a condensed state on the surface of nanoparticles.

Furthermore, the mechanochemical applications of CL have recently been reported in the field of polymer chemistry [47, 48]. Adox, a stable chemiluminescent moiety, was introduced into polymers to synthesize various chemically modified derivatives. The mechanochemical CL properties of these modified polymers were then investigated. When the two ends of a polymer film were pulled in opposite directions, the applied stress induces bond cleavage of the 1,2-dioxetane rings of the Adox moieties, resulting in CL. The bond cleavage can be observed by photon detection in real time (Fig. 9.2d). This idea was realized by a rubber-like network polymer with an Adox structure inserted into poly(methyl acrylate) [49]. When the polymer film was cleaved mechanically by applying sufficient stress until the stretching force exceeded a certain threshold, CL was observed. By using this methodology, the molecular mechanism of the damage in the polymer chains depending on the magnitude of applied stress has been elucidated. Similar experiments on the mechanochemical damages were conducted on various polymers such as polyamides and polyesters [47, 48]. Moreover, the use of fluorescent dyes in Adox-bearing polymers to effectively modulate CL via CRET has also been reported [47, 48].

9.4 Chemiluminescence in Molecular Crystals

9.4.1 Mechanistic Studies of Chemiluminescence Reactions in Crystals

Studies on the reaction mechanisms of the crystalline-state CL have been reported recently [50, 51]. A single-step reaction such as the thermolytic reaction of 1,2-dioxetane can be applied to the study of crystalline-state CL; therefore, CL reactions of organic peroxides have been investigated using their molecular crystals.

The first studies to correlate the crystal structures with luminescence properties in crystals were the CL reactions of the stable 1,2-dioxetane derivative Ad-OH and the bicyclic dioxetane derivatives Dx-AOH, Dx-BOH and $Dx\text{-}AOCH_3$ (Fig. 9.8a)

[50]. The bicyclic dioxetane structure has been precisely designed by taking advantage of the stabilizing factors in the molecular structure of Ad-OH as explained in Sect. 9.2.2 [52]. The stability of these compounds is advantageous for preparing crystal samples with a purity to study. In Dx-AOCH$_3$, the phenolic hydroxy group is protected by the methyl group. Ad-OH, Dx-AOH and Dx-BOH yielded the corresponding phenolate anions by the action of a base in solution. The anions promptly decomposed to exhibit CL via the CTIL mechanism. The phenolate anions of the 3-hydroxybenzoate moieties (the CL reaction of Ad-O$^-$ in Fig. 9.6), which are the light-emitters, showed emission with the maxima at 460–500 nm. Crystal samples of the four dioxetanes were heated at temperatures below their melting points to initiate their CL reactions. While the methoxy derivative Dx-AOCH$_3$ showed only weak CL, the CL emission spectra for the hydroxy derivatives were measurable. The CL of Ad-OH and Dx-AOH was emitted from the excited states of the phenolate anions of their 3-hydroxybenzoate moieties, whereas that of Dx-BOH was emitted from the excited state of the neutral 3-hydroxybenzoate moiety. The crystal structures of Dx-AOH and Dx-BOH indicated that the hydroxy groups of the 3-hydroxyphenyl moieties form hydrogen bonds with the oxygen atoms of the 1,2-dioxetane rings (Fig. 9.8b). When the crystal samples were heated, the oxygen atom of the 1,2-dioxetane ring assisted the deprotonation of the phenolic hydroxy group via hydrogen bonding, which promoted the decomposition of the 1,2-dioxetane ring via the CTIL mechanism. Because the donor–acceptor distance in the hydrogen bonding in Dx-AOH is relatively short (1.93 Å), the phenolate anion of the 3-hydroxybenzoate moiety is effectively generated as the excited-state product for light emission (Fig. 9.8b). In the case of Dx-BOH, the hydrogen bonding donor–acceptor distance is relatively long (2.02 Å); therefore, the deprotonation does not occur and the excited state of the neutral 3-hydroxybenzoate moiety is responsible for light emission (Fig. 9.8b). These results confirmed that the crystal structures determine the CL behavior. Moreover, the CL reaction of the crystalline-state Dx-AOH which is heated to 100 °C demonstrated first-order reaction kinetics. This relationship between the reaction kinetics and the crystallinity is a significant issue to consider because a reaction in the crystalline state destroys the crystal structure.

Crystalline-state CL reactions of lophine hydroperoxide (LHP) were also studied by photon detection [51]. Lophine is the first artificially synthesized CL compound, which reacts with O_2 under basic conditions to demonstrate CL via the hydroperoxide anion of LHP [53]. A plausible reaction mechanism is the formation of a 1,2-dioxetane intermediate from the LHP anion, which undergoes chemiexcitation upon thermal decomposition to yield the S_1-state benzoylamidine anion for light emission (Fig. 9.9) [54]. LHP was prepared by the ene reaction of lophine with a singlet oxygen. In solution, the CL reaction of LHP can be initiated by the action of a base via the abovementioned pathway. Recrystallization of LHP yielded cm-size crystals, which were used for crystalline-state CL reactions. The thermolytic reaction of crystalline LHP produced the major products lophine and O_2 along with the minor products benzoylamidine and an unidentified product in less than 5% yield. During this reaction, the bubbling of oxygen from the heated crystals was observed. The CL emission maximum observed at 530 nm suggests the emission of phosphorescence

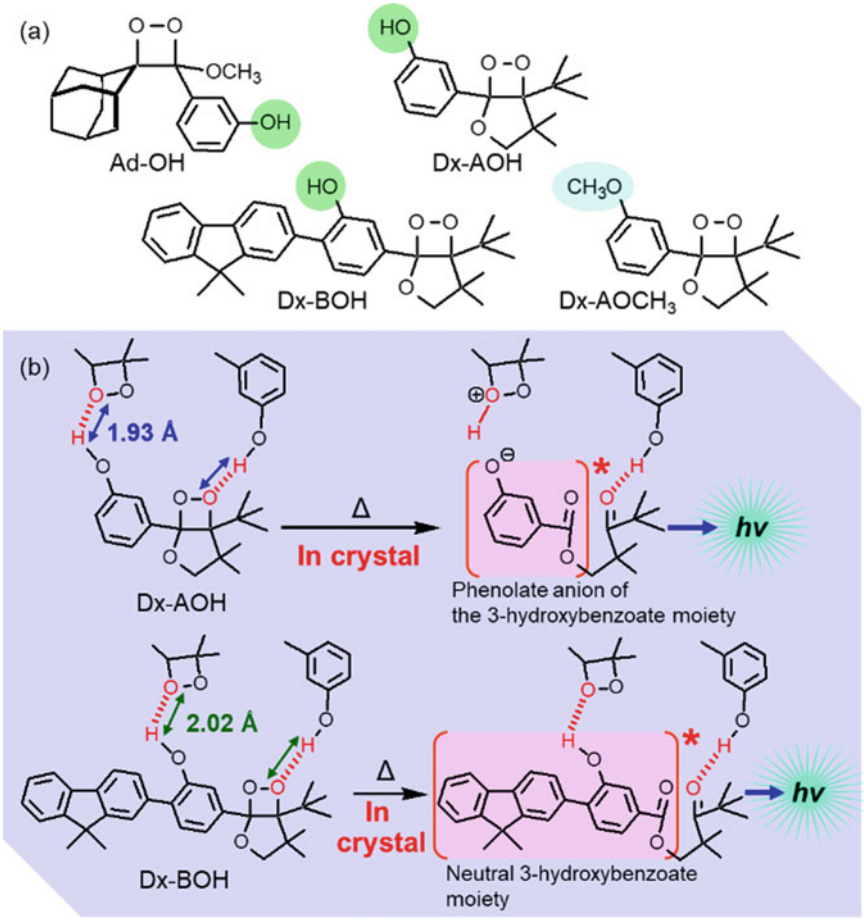

Fig. 9.8 **a** 1,2-Dioxetane derivatives for crystalline-state chemiluminescence and **b** CL reactions of crystalline-state Dx-AOH and Dx-BOH

from the T_1 state of the lophine anion (Fig. 9.9). Furthermore, the study reported the CL emission spectra of the heated crystal samples of Adox, rubrene endoperoxide, and benzoyl peroxide. This study by Schramm et al., like the study reported by Watanabe et al. on the crystalline-state 1,2-dioxetane derivatives, also raises an important question regarding the dynamic relationship between the reaction progress and the structural change in crystals.

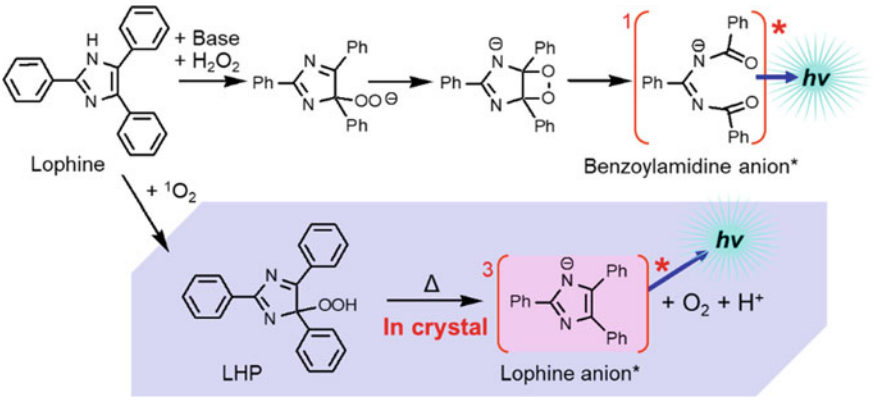

Fig. 9.9 Chemiluminescence reactions of lophine and lophine hydroperoxide (LHP)

9.4.2 *Exploring the Science of Intracrystalline Reactions with Soft Crystal Chemiluminescence Systems*

Mechanistic studies on the progress of crystalline-state reactions and the corresponding dynamic changes in the crystal structures owing to the accumulation of reaction products were conducted based on the concept of soft crystal science [11]. That is, a "soft property of a crystal" is expected to allow the structural change and phase transition of the crystal in response to the accumulation of reaction products. In this section, the relationships between the crystal structures, the luminescence properties and reactivity were elucidated with soft crystal CL systems.

Matsuhashi et al. adopted Adox derivatives as the CL substrates for their soft crystal CL system to study intracrystalline reactions. Adox derivatives were synthesized by linking fluorophore moieties to tune the CL properties of the crystals (Fig. 9.10) [55, 56]. Adox derivative **1** with a fluorophore side chain (FL1: *N*-(4-trifluoromethylphenyl)phthalimide) has two stereoisomers (*syn*-**1** and *anti*-**1**). In the case of di-substituted derivative **2**, there are three stereoisomers (*cis-syn*-**2**, *cis-anti*-**2**, and *trans*-**2**) and 5-(4-methoxyphenyl)-*N*-(4-trifluoromethylphenyl)phthalimide was used as a fluorophore moiety FL2. Utilization of the stereoisomers is advantageous in the evaluation of a reactivity change caused by the difference in the crystal structures, because the isomers have similar reactivity in solution. In addition, the fluorophore moieties in **1** and **2** will accept energy from the excited state of a neighboring AdCO moiety via the CRET mechanism as previously explained in Sect. 9.2.2. Because AdCO has a low Φ_F of approximately 0.001 in solution, the Φ_{CL} value was expected to improve after the energy transfer. Furthermore, the fluorophore moiety was expected to tune emission wavelength, control crystallinity and form an excited dimer or complex. For the design of di-substituted derivative **2**, the fluorophore FL2 was adopted in place of FL1, because FL2 showed stronger fluorescence than FL1.

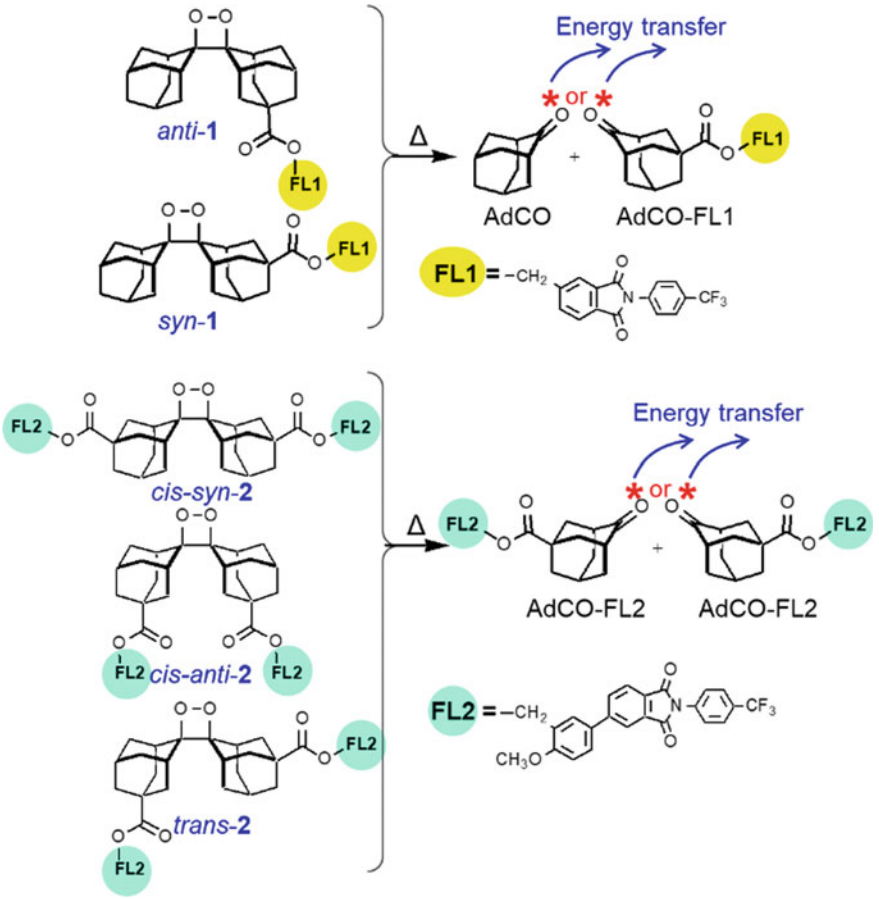

Fig. 9.10 Chemiluminescence reactions of the isomers of fluorophore-linked Adox derivatives **1** and **2**

Mono-substituted derivatives *syn*-**1** and *anti*-**1** showed clear differences in crystal structures, CL emission properties and reactivities [55]. When the crystal samples of *syn*-**1**, *anti*-**1**, and Adox were heated to 160 °C, they all showed CL with the emission maxima of 465 nm, 440 nm, and 430 nm, respectively. Interestingly, the CL of *syn*-**1** is caused by distinct energy transfer. Upon heating, the CL intensity for *syn*-**1** was stronger than that for Adox, while the CL intensity for *anti*-**1** was weaker than that for Adox. This is because the CL intensity depends on both the CL quantum yield Φ_{CL} and the reaction rate ($-$d[R]/dt, where [R] is the reactant concentration). Because the reaction rate in crystals for *syn*-**1** was faster than that for *anti*-**1**, *syn*-**1** had the higher CL intensity. Morphological observations of the heated crystals also showed a characteristic difference. The crystals of *syn*-**1** started melting at approximately 3 min after the heating had begun, whereas *anti*-**1** maintained its crystalline state for approximately 15 min after the heating had begun. It is evident

that the differences in the luminescence properties, reaction rates, and the abilities to maintain the crystalline state upon heating reflect the differences in the crystal structures. In fact, *syn*-**1** has a crystal structure in which Adox and FL1 moieties are stacked alternately along the *b*-axis, whereas *anti*-**1** has a crystal structure in which Adox and FL1 moieties are in separate aggregated layers (Fig. 9.11). The thermolytic reactions of *syn*-**1** and *anti*-**1** generated the excited states of either AdCO or the AdCO moiety in AdCO-FL1 (Fig. 9.10). In the crystal of *syn*-**1**, the energy transfer from the excited state of either AdCO or the AdCO moiety to the FL1 moiety in a neighboring molecule is efficient because of the alternated layer structure of the crystal in which both the species are in close proximity to each other. On the other hand, in the crystal of *anti*-**1**, the excited-state of either AdCO or the AdCO moiety in AdCO-FL1 and a FL1 moiety are farther apart owing to the separately layered structure, rendering the efficiency of the energy transfer lower than that of *syn*-**1**. In addition, in the crystal of *anti*-**1**, there are more CO●●●HC interactions between the neighboring FL1 moieties than that in the crystal of *syn*-**1**. Thus, the softness of *anti*-**1** crystal structure is lower than that of *syn*-**1**. As a result, the intracrystalline CL reaction of *anti*-**1** is slower and the crystal of *anti*-**1** is more resistant to collapse of the crystalline state during the progress of the reaction.

Because the CL intensity corresponds to the amount of decomposition of the reactant per unit time, the duration of the CL emission and the magnitude of CL intensity indicate the continuity and rate of the reaction, respectively. Figure 9.12 shows the plot of CL intensities as a function of time for the reactions of *syn*-**1** and *anti*-**1** crystals heated to 140 and 160 °C, respectively. In contrast to the first-order reaction kinetics of the CL reaction of *syn*-**1** in solution, the crystalline-state kinetics data showed a nearly constant CL intensity for 10 min, followed by decay. In the case of *anti*-**1**, a gradual increase in the CL intensity was observed for 15 min, followed

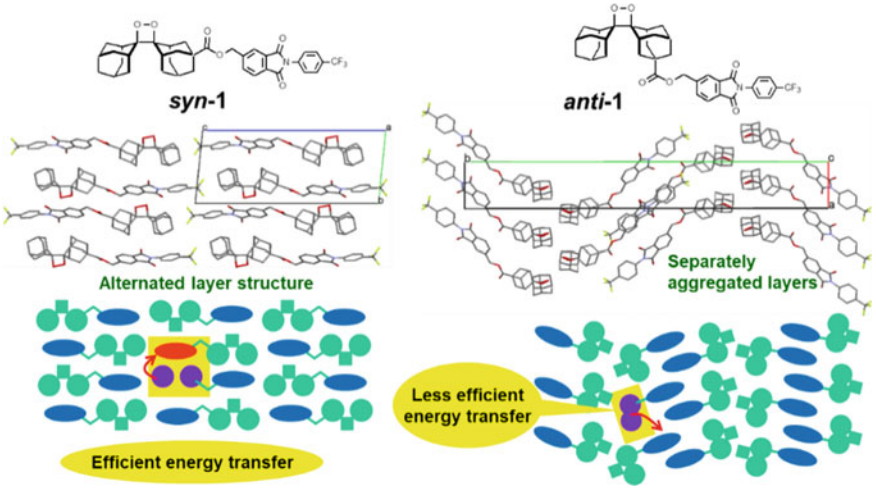

Fig. 9.11 Crystal structures of *syn*-**1** and *anti*-**1**

by rapid decay. In large crystals such as the LHP crystals, the CL reaction will begin from the heating surface where the crystal is in contact with the heater. Because the *syn*-**1** and *anti*-**1** crystals are in the size range of 1−300 μm, it is expected that the entire crystal will reach the desired temperature immediately after the heating has begun, resulting in instant CL reactions. However, a nearly constant CL intensity for *syn*-**1** and the gradual increase in the CL intensity for *anti*-**1** were observed during the time range t_c. These data indicate that the CL reaction exhibits zero-order kinetics, in which the reaction rate is independent of the concentration of the reactant; a constant number of the reactant molecules per unit time and per unit volume undergo the CL reaction (Fig. 9.13). The gradual increase in the CL intensity observed for *anti*-**1** suggests that in addition to exhibiting zero-order kinetics, the reaction is accelerated owing to the generated products. Therefore, the crystal structure of the reactant is maintained until the product accumulation reaches a certain threshold, beyond which a phase transition to the molten state occurs in both *syn*-**1** and *anti*-**1** (Fig. 9.14).

To confirm the zero-order kinetics of the CL reaction in crystals, it is necessary to analyze the reaction kinetics in a single crystal. Matsuhashi et al. investigated the CL reactions of a single crystal of Adox, which has a crystal size of 10−1000 μm [57]. When a single crystal of Adox was heated to 140 °C, the CL intensity remained constant for 20 s to 10 min after the heating had begun and then decayed with time. Morphological observations of the heated crystals indicate that during the time interval of constant CL intensity, the crystalline state was maintained and the decay of the CL intensity correlated with the crystals being finely crushed. Because the values of the constant CL intensities are proportional to the volumes of the crystals used, it was concluded that the reaction rate depended on the number of molecules in the crystal. The constant CL intensity indicates that the CL reaction exhibits zero-order reaction kinetics.

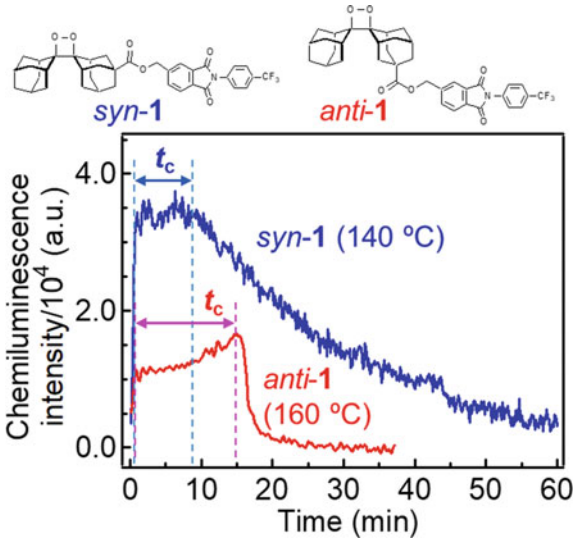

Fig. 9.12 CL intensity as a function of time (min) for the reaction of *syn*-**1** crystals heated to 140 °C and *anti*-**1** crystals heated to 160 °C

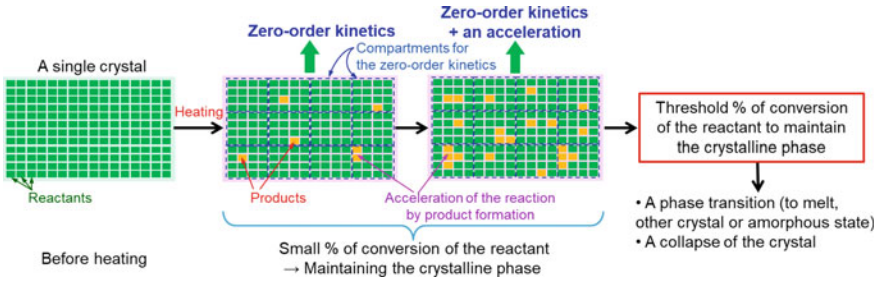

Fig. 9.13 Schematic diagram of the changes in a single crystal of the reactant during the course of a thermal reaction

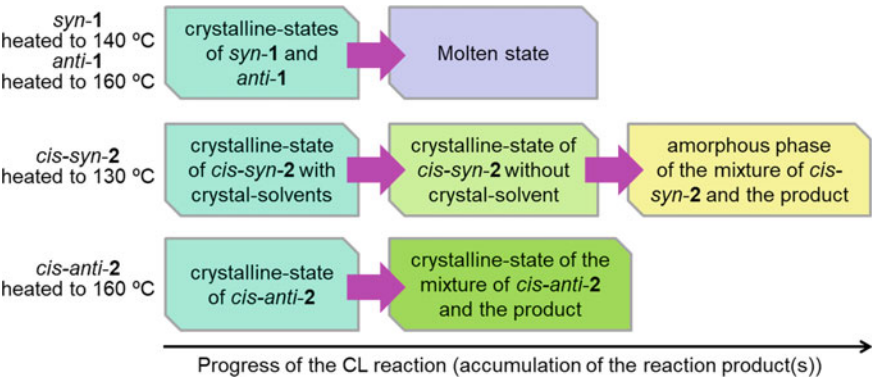

Fig. 9.14 Phase transitions induced by the accumulation of the products for the crystalline-state chemiluminescence reactions of *syn*-**1**, *anti*-**1**, *cis-syn*-**2**, and *cis-anti*-**2**

The Johnson–Mehl–Avrami-Kolmogorov (JMAK) model, which was proposed for the kinetics of crystalline phase transitions, was used to analyze the CL reaction in a single crystal of Adox. The zero-order reaction kinetics were confirmed by the analysis with the Sharp-Hancock equation for the JMAK model. After that, the first-order-like kinetics of the reaction were observed when the crystal was finely crushed. The CL reaction of Adox with a powder sample obtained by grinding bulk crystals also showed a first-order-like kinetic decay of the CL intensity, indicating that the reaction exhibits zero-order kinetics only with crystals of a certain size. The minimum compartment size of a reactant cluster in a crystal to exhibit zero-order kinetics will depend on the properties of the crystal (Fig. 9.13). Thermophysical measurements confirmed that a constant thermal diffusivity was maintained in the inside of a single Adox crystal during the zero-order reaction kinetics, indicating that the reaction field in the crystal was homogeneous and has become a thermal steady state. The accumulation of AdCO during the progress of the CL reaction causes crystal fracturing, which induces a change in the reaction kinetics.

The heated crystals of *syn*-**1** and *anti*-**1** showed a phase transition to the molten state induced by the accumulation of the products (Fig. 9.14). In the case of the di-substituted derivative **2,** which has two FL2 side chains, only one type of the product, AdCO-FL2 was produced by the CL reaction. Thus, the crystalline-state CL reactions of **2** were expected to show a change in the phase transition behavior. Solid-to-solid phase transitions were observed in the CL reactions of *cis-syn*-**2** and *cis-anti*-**2** in the crystalline state [56]. The crystals of *cis-syn*-**2** contain methylene chloride and *n*-hexane as crystalline solvents. When the crystals of *cis-syn*-**2** were heated to 130 °C, desorption of crystalline solvent molecules occurred during the first 15 min accompanied by a significant increase in the CL intensity. Thus, heating the crystals induced a transition from the crystalline phase containing crystalline solvents to the crystalline phase without the crystalline solvents (Fig. 9.14). Desorption of the crystalline solvents caused a change in the crystalline environment resulting in bent crystals and caused the acceleration of the CL reaction. In the subsequent 3 h, the accumulation of the product induced a transition from the crystalline phase without the crystalline solvents to the amorphous phase (Fig. 9.14) which correlated with a gradual increase in the CL intensity. The CL emission also showed a spectral change accompanied by these phase transitions, indicating that the molecular environment in the crystal was continuously changed by the phase transitions. The solvatochromic fluorescence property of the FL2 moiety in **2** and that of AdCO-FL2 were utilized to monitor the change in the intracrystalline environment. In contrast, the crystal of *cis-anti*-**2** heated to 160 °C maintained its crystal structure until 4 h of heating while the CL reaction progressed. The schematic diagram of the progress of the crystalline-to-crystalline phase transition from the phase of *cis-anti*-**2** to the phase of the mixture of *cis-anti*-**2** and AdCO-FL2 is shown in Fig. 9.14. During this phase transition, the intensity and the maximum wavelength of CL showed a characteristic change with time.

The relationship between the progress of an intracrystalline reaction and a phase transition has been first reported in the denitrogenation reaction of triazoline derivatives in crystals [58, 59], but more information is required to establish a general theory to explain the phase transition mechanisms. The data of phase transitions obtained by the crystalline-state CL reactions of **1** and **2** provide a basis for analyzing the relationship between the accumulation of the products and the lattice energy, as the accumulation of the products leads to the destruction of the crystal lattice. The relationships between the phase transitions and the kinetics of the CL reactions of *cis-syn*-**2** and *cis-anti*-**2** remain unclear. They are next challenging problems.

The CL reactions of Adox and its derivatives **1** and **2** proceed within a temperature range in which the crystalline states were maintained. Thus, they are soft crystal CL systems. However, if a crystal has a low melting point, its intracrystalline reactions cannot be studied by heating at a temperature above its melting point. Furthermore, a crystal lattice may reduce the reactivity of a CL substrate. For example, the thermolytic reaction of DPA endoperoxide (Fig. 9.7) does not proceed in the crystalline state when heated to 160 °C for 1 min, while its lifetime in solution is estimated to be only a few seconds at 160–200 °C. Interestingly, a crystal sample of DPA endoperoxide heated to 200 °C resulted in a singlet oxygen emission and the melting of

the crystal, indicating that the CL reaction proceeds with breaking the crystal lattice [60]. Thus, the crystal lattice structure has an important role to govern the reactivity by restricting the molecular motion for the reaction.

In this section, it was confirmed that the crystals of Adox and its derivatives **1** and **2** are soft crystals, which can undergo thermolytic reactions within the crystals. Hence, they are soft crystal CL systems, in which ongoing CL reactions can be tracked in real time by photon detection. The real-time analyses of their CL reactions provided valuable information on the intracrystalline reaction kinetics and the phase-transition inductions by the reaction progress, while there are still many unsolved problems described above. To establish the reaction theory to explain the relationships between crystal structures and reactivities, the energetics and kinetics of reactions, it is necessary to accumulate more data of intracrystalline reactions. For this purpose, the crystals of Adox and its derivatives **1** and **2** will be useful as role models to design novel soft crystal CL systems. Furthermore, it is expected that soft crystal CL systems exhibit molecular functions such as a stimulus-responsive property based on the unique CL reaction properties within the crystals. We expect further development of the chemistry of soft crystal CL systems learned from this text.

References

1. Garcia-Campana AM, Roman-Ceba M, Baeyens WRG (2001) Historical evolution of chemiluminescence. In: Garcia-Campana AM, Baeyens WRG (eds) Chemiluminescence in Analytical Chemistry. Marcel Dekker, New York, pp 1–39
2. Vacher M, Fdez Galv an I, Ding B-W, Schramm S, Berraud-Pache R, Naumov P, Ferre N, Liu Y-J, Navizet I, Roca-Sanjuan D, Baader WJ, Lindh R (2018) Chemi-and bioluminescence of cyclic peroxides. Chem Rev 118:6927–6974
3. Hirano T, Matsuhashi C (2022) A stable chemiluminophore, adamantylideneadamantane 1,2-dioxetane: from fundamental properties to utilities in mechanochemistry and soft crystal science. J Photochem Photobiol C 51:100483
4. Tanaka K, Toda F (2000) Solvent-free organic synthesis. Chem Rev 100:1025–1074
5. Kaupp G (2003) Solid-state molecular syntheses: complete reactions without auxiliaries based on a new solid-state mechanism. CrystEngComm 5:117–133
6. Kaupp G (2005) Organic solid state reactions with 100% yield. Top Curr Chem 254:95–183
7. James SL, Adams CJ, Bolm C, Braga D, Collier P, Friscic T, Grepioni F, Harris KDM, Hyett G, Jones W, Krebs A, Mack J, Maini L, Orpen AG, Parkin IP, Shearouse WC, Steed JW, Waddell DC (2012) Mechanochemistry: opportunities for new and cleaner synthesis. Chem Soc Rev 41:413–447
8. Wang GW (2013) Mechanochemical organic synthesis. Chem Soc Rev 42:7668–7700
9. Byrn SR, Xu W, Newman AW (2001) Chemical reactivity in solid-state pharmaceuticals: formulation implications. Adv Drug Delivery Rev 48:115–136
10. Glass BD, Novak C, Brown ME (2004) The thermal and photostability of solid pharmaceuticals - a review. J Therm Anal Calorim 77:1013–1036
11. Kato M, Ito H, Hasegawa M, Ishii K (2019) Soft crystals: flexible response systems with high structural order. Chem Eur J 25:5105–5112
12. Garcia-Campana AM, Baeyens WRG, Zhang X (2001) Chemiluminescence-based analysis: an introduction to principles, instrumentation, and applications. In: Garcia-Campana AM, Baeyens WRG (eds) Chemiluminescence in Analytical Chemistry. Marcel Dekker, New York, pp 41–65

13. McElroy WD, DeLuca M (1978) Chemistry of firefly luminescence. In: Herring PJ (ed) Bioluminescence in Action. Academic Press, London, pp 109–127
14. Shimomura O (2012) The fireflies and luminous insects, in *Bioluminescence: Chemical Principles and Methods*, rev. World Scientific Publishing, Singapore, pp 1–30
15. Contag CH, Bachmann MH (2002) Advances in in vivo bioluminescence imaging of gene expression. Annu Rev Biomed Eng 4:235–260
16. Greer III LF, Szalay AA (2002) Imaging of light emission from the expression of luciferases in living cells and organisms: a review. Luminescence 17:43–74
17. Iwano S, Sugiyama M, Hama H, Watakabe A, Hasegawa N, Kuchimaru T, Tanaka KZ, Takahashi M, Ishida Y, Hata J, Shimozono S, Namiki K, Fukano T, Kiyama M, Okano H, Kizaka-Kondoh S, McHugh TJ, Yamamori T, Hioki H, Maki S, Miyawaki A (2018) Single-cell bioluminescence imaging of deep tissue in freely moving animals. Science 359:935–939
18. Roda A, Guardigli M, Pasini P, Mirasoli M, Michelini E, Musiani M (2005) Bio- and chemiluminescence imaging in analytical chemistry. Anal Chim Acta 541:25–35
19. Yan Y, Shi P, Song W, Bi S (2019) Chemiluminescence and bioluminescence imaging for biosensing and therapy: in vitro and in vivo perspectives. Theranostics 9:4047–4065
20. Turro NJ, Lechtken P (1973) Thermal and photochemical generation of electronically excited organic molecules: tetramethyl-1,2-dioxetane and naphthvalene. Pure Appl Chem 33:363–388
21. Turro NJ, Lechtken P, Schore NE, Schuster G, Steinmetzer HC, Yekta A (1974) Tetramethyl-1,2-dioxetane. experiments in chemiexcitation, chemiluminescence, photochemistry, chemical dynamics, and spectroscopy. Acc Chem Res 7:97–105
22. Adam W (1982) Determination of chemiexcitation yields in the thermal generation of electronic excitation from 1,2-dioxetane. In: Adam W, Cilento G (ed), In *Chemical and Biological Generation of Excited States*. Academic Press, New York, pp. 115–152
23. Adam W, Beinhauer A, Hauer H (1989) Chapter 12 Activation parameters and excitation yields of 1,2-dioxetane chemiluminescence. In: Scaiano JC (ed) In *Handbook of Organic Photochemistry*, vol 2. CRC Press, Boca Raton, pp. 271–327
24. Ando Y, Niwa K, Yamada N, Enomoto T, Irie T, Kubota H, Ohmiya Y, Akiyama H (2008) Firefly bioluminescence quantum yield and color change by pH-sensitive green emission. Nat Photonics 2:44–47
25. Reguero M, Bernardi F, Bottoni A, Olivucci M, Robb MA (1991) Chemiluminescent decomposition of 1,2-dioxetanes: an MC-SCF/MP2 study with VB analysis. J Am Chem Soc 113:1566–1572
26. Vacher M, Farahani P, Valentini A, Frutos LM, Karlsson HO, Galvan IF, Lindh R (2017) How do methyl groups enhance the triplet chemiexcitation yield of dioxetane?". J Phys Chem Lett 8:3790–3794
27. Schuster GB (1979) Chemiluminescence of organic peroxides. Conversion of ground-state reactants to excited-state products by the chemically initiated electron-exchange luminescence mechanism. Acc Chem Res 12:366–373
28. Isobe H, Takano Y, Okumura M, Kuramitsu S, Yamaguchi K (2005) Mechanistic insights in charge-transfer-induced luminescence of 1,2-dioxetanones with a substituent of low oxidation potential. J Am Chem Soc 127:8667–8679
29. Wieringa JH, Strating J, Wynberg H, Adam W (1972) Adamantylideneadamantane peroxide: a stable 1,2-dioxetane. Tetrahedron Lett. 169–172
30. Schaap AP, Chen TS, Handley RS, DeSilva R, Giri BP (1987) Chemical and enzymatic triggering of 1,2-dioxetanes. 2. chemiluminescence from (tert-butyldimethylsilyl)oxy-substituted dioxetanes. Tetrahedron Lett 28:1155–1158
31. McCapra F, Beheshti I, Burford A, Hann RA, Zaklika KA (1977) Singlet excited states from dioxetane *decomposition.* J Chem Soc. 944–946
32. Hummelen JC, Luider TM, Wynberg H (1987) Functionalized adamantylideneadamantane 1,2-dioxetanes: investigations on stable and inherently chemiluminescent compounds as a tool for clinical analysis. Pure Appl Chem 59:639–650
33. Schaap AP, Handley RS, Giri BP (1987) Chemical and enzymatic triggering of 1,2-dioxetanes. 1: Aryl esterase-catalyzed chemiluminescence from a naphthyl acetate-substituted dioxetane, Tetrahedron Lett 28:935–938

34. Hirano T (2016) Molecular origin of color variation in firefly (beetle) bioluminescence: a chemical basis for biological imaging. Curr Top Med Chem 16:2638–2647
35. Turro TJ, Ramamurthy V, Scaiano J (2010) Modern molecular photochemistry of organic molecules. University Science Books, Sausalito
36. Shimomura O (2012) The jellyfish *Aequorea* and other luminous coelenterates, in *Bioluminescence: Chemical Principles and Methods*, rev. Scientific Publishing, Singapore, pp 91–165
37. Koo JY, Schuster GB (1978) Chemiluminescence of diphenoyl peroxide-chemically-initiated electron exchange luminescence-new general mechanism for chemical production of electronically excited-states. J Am Chem Soc 100:4496–4503
38. Adam W, Kazakov DV, Kazakov VP (2005) Singlet-oxygen chemiluminescence in peroxide reactions. Chem Rev 105:3371–3387
39. Turro NJ, Chow MF, Rigaudy J (1981) Mechanism of thermolysis of endoperoxides of aromatic compounds: activation parameters, magnetic field, and magnetic isotope effects. J Am Chem Soc 103:7218–7224
40. Moureau C, Dufraise C, Butler CL (1926) Peroxyde de rubrene: nouvelles experiences. Compt Rend Acad Sci 183:101–105
41. Frankevich EL, Rumyantsev BM, Lesin VI (1975) Magnetic field effect on thermostimulated chemiluminescence of photoperoxidized rubrene. J Lumin 11:91–106
42. Höhne G, Schmidt AH, Lechtken P (1979) High energy molecules. part 4. Thermoanalysis of crystalline adamantylideneadamantone-1, 2-dioxetane. Tetrahedron Lett. 3587–3590
43. Lechtken P, Yekta A, Turro NJ (1973) Tetramethyl-1, 2-dioxetane: mechanism for an autocatalytic decomposition. Evidence for a quantum chain reaction. J Am Chem Soc 95: 3027–3028
44. Turro NJ, Waddell WH (1975) Quantum chain processes: direct observation of high quantum yields in the direct and photosensitized excitation of tetramethyl-1,2-dioxetane. Tetrahedron Lett. 2069–2072
45. Kazakov VP, Voloshin AI, Ostakhov SS (1999) Quantum chain reactions with energetic branching: catalytic decomposition of dioxetanes. Kinet Catal 40:180–193
46. Roda A, Di Fusco M, Quintavalla A, Guardigli M, Mirasoli M, Lombardo M, Trombini C (2012) Dioxetane-doped silica nanoparticles as ultrasensitive reagentless thermochemiluminescent labels for bioanalytics. Anal Chem 84:9913–9919
47. Chen YJ, Mellot G, van Luijk D, Creton C, Sijbesma RP (2021) Mechanochemical tools for polymer materials. Chem Soc Rev 50:4100–4140
48. Yuan Y, Chen Yl (2017) Visualized bond scission in mechanically activated polymers. Chin J Polym Sci 35:1315–1327
49. Chen Y, Spiering AJH, Karthikeyan S, Peters GWM, Meijer EW, Sijbesma RP (2012) Mechanically induced chemiluminescence from polymers incorporating a 1,2-dioxetane unit in the main chain. Nat Chem 4:559–562
50. Watanabe N, Takatsuka H, Ijuin HK, Wakatsuki A, Matsumoto M (2016) Hydrogen bonding network-assisted chemiluminescent thermal decomposition of 3-hydroxyphenyl-substituted dioxetanes in crystal. Tetrahedron Lett 57:2558–2562
51. Schramm S, Karothu DP, Lui NM, Commins P, Ahmed E, Catalano L, Li L, Weston J, Moriwaki T, Solntsev KM, Naumov P (2019) Thermochemiluminescent peroxide crystals. Nat Commun 10:1–8
52. Matsumoto M (2004) Advanced chemistry of dioxetane-based chemiluminescent substrates originating from bioluminescence. J Photochem Photobiol C 5:27–53
53. White EH, Harding MJC (1965) Chemiluminescence in liquid solutions. Chemiluminescence of lophine and its derivatives. Photochem. Photobiol 4:1129–1155
54. Boaro A, Reis RA, Silva CS, Melo DU, Pinto AGGC, Bartoloni FH (2021) Evidence for the formation of 1,2-dioxetane as a high-energy Intermediate and possible chemiexcitation pathways in the chemiluminescence of lophine peroxides. J Org Chem 86:6633–6647
55. Matsuhashi C, Ueno T, Uekusa H, Sato-Tomita A, Ichiyanagi K, Maki S, Hirano T (2020) Isomeric difference in the crystalline-state chemiluminescence property of an adamantylideneadamantane 1,2-dioxetane with a phthalimide chromophore. Chem Commun 56:3369–3372

56. Matsuhashi C, Oyama H, Uekusa H, Sato-Tomita A, Ichiyanagi K, Maki S, Hirano T (2022) Crystalline-state chemiluminescence reactions of two-fluorophore-linked adamantylideneadamantane 1,2-dioxetane isomers accompanied by solid-to-solid phase transitions. CrystEngComm 24:3332–3337
57. Matsuhashi C, Fujisawa H, Ryu M, Tsujii T, Morikawa J, Oyama H, Uekusa H, Maki S, Hirano T (2022) Intracrystalline kinetics analyzed by real-time monitoring of 1,2-dioxetane chemiluminescence reaction in a single crystal. Bull Chem Soc Jpn 95:413–420
58. de Loera D, Garcia-Garibay MA (2012) Efficient aziridine synthesis in metastable crystalline phases by photoinduced denitrogenation of crystalline triazolines. Org Lett 14:3874–3877
59. de Loera D, Stopin A, Garcia-Garibay MA (2013) Photoinduced and thermal denitrogenation of bulky triazoline crystals: Insights into solid-to-solid transformation. J Am Chem Soc 135:6626–6632
60. Yamasaki N, Matsuhashi C, Maki S, Hirano T (2021) Singlet-oxygen chemiluminescence from heated crystal samples of 9,10-diphenylanthracene endoperoxides. Chem Lett 50:1681–1683

Open Access This chapter is licensed under the terms of the Creative Commons Attribution 4.0 International License (http://creativecommons.org/licenses/by/4.0/), which permits use, sharing, adaptation, distribution and reproduction in any medium or format, as long as you give appropriate credit to the original author(s) and the source, provide a link to the Creative Commons license and indicate if changes were made.

The images or other third party material in this chapter are included in the chapter's Creative Commons license, unless indicated otherwise in a credit line to the material. If material is not included in the chapter's Creative Commons license and your intended use is not permitted by statutory regulation or exceeds the permitted use, you will need to obtain permission directly from the copyright holder.

Chapter 10
Molecular Crystal Calculation Prospects for Structural Phase Transitions

Naofumi Nakayama and Hitoshi Goto

Abstract To establish the theory of soft crystals, computational chemistry must be applied to analyze the structural phase transitions of molecular crystals and develop new methodologies. The accuracy of first-principles calculations for molecular crystals has rapidly improved over the last decade with the contribution of the Cambridge Crystallographic Data Centre blind test, which predicts the crystal structure from the structural formula. However, it is often difficult to apply first-principles calculations to large molecular crystals, such as typical soft crystals, because of the computational cost. In this chapter, we review the applicability of crystal force field calculations as an alternative method for theoretically analyzing molecular crystals. We also introduce some examples of our previous collaborations and discuss the promising methodologies to elucidate the soft crystal phenomena.

Keywords Computational chemistry · Crystal structure prediction · Crystal force field · Metallic complex · Crystal dynamics simulation

10.1 Introduction

Soft crystals are a group of molecular materials that exhibit structural phase transitions from one stable single crystal to another single crystal (or amorphous state) upon weak external stimuli [1]. They are typically metallic complexes with photochemical changes of vapochromism and mechanochromism [2, 3] or organic compounds that exhibit unique properties of superelasticity [4, 5]. Many soft crystals can return to their original crystalline phase when the external stimuli is removed, or a different stimulus is added. These soft crystals are expected to develop into new functional materials and thus, it is important to understand the properties and

N. Nakayama
CONFLEX Corporation, 3-23-17 Takanawa, Tokyo, Japan
e-mail: nakayama@conflex.co.jp

H. Goto (✉)
Toyohashi University of Technology, 1-1 Hibarigaoka, Toyohashi 441-8122, Japan
e-mail: gotoh@tut.jp

© The Author(s) 2023

M. Kato and K. Ishii (eds.), *Soft Crystals*, The Materials Research Society Series,
https://doi.org/10.1007/978-981-99-0260-6_10

phenomena observed in experiments and to elucidate the principles of their physical properties. This can be accomplished by applying computational chemistry and performing detailed analyses. Thus, how should we approach each of the various phenomena exhibited by these rare soft crystals using computational chemistry? Before we discuss our methodology and examples of our work, we will provide some information about computational chemistry for molecular crystals, including soft crystals.

10.1.1 Contribution of Crystal Structure Prediction to the Computational Chemistry of Molecular Crystals

Computational approaches to soft crystals present several major challenges that arise from the fact that soft crystals are molecular crystals, which have several characteristics that make them unsuited to computational analysis approaches. First, molecules composed of rigid covalent bonds have complex three-dimensional structures. Second, molecules can flexibly adopt multiple conformations by intramolecular interactions. In other words, the molecules as the crystalline fillings are not spherical like atoms but have complex three-dimensional structures and can be deformed. Third, the three-dimensional order is maintained by various types of intermolecular interactions that are much weaker than covalent interactions, such as isotropic interactions like van der Waals forces and electrostatic forces, strongly anisotropic interactions like hydrogen bonds, and coordination bonds in the case of metallic complexes. These factors cause a property called polymorphism, which is the formation of multiple metastable crystal structures with different molecular orientations and conformations. This property has made computational chemical approaches to molecular crystals difficult.

Computational chemistry methods for the analysis of molecular crystals have been rapidly developed in the last decade. In particular, the crystal structure prediction (CSP) blind tests [6–11] organized by the Cambridge Crystallographic Data Centre (CCDC) have undoubtedly made significant contributions to this development [12]. Through the blind tests, the accuracy of the dispersion force corrected density functional theory (DFT-D) method, which combines first-principles calculations of DFT with dispersion force correction by two-body potentials, has been considerably improved.

In the CSP blind test, only the structural formula and crystallization conditions of a molecule whose crystal structure has not yet been published are provided as questions, and participants predict the crystal structure using their prediction techniques. There are two major prediction techniques that participants must develop. One is the search for crystal polymorphs by generating a large number of possible crystal structures of the target molecule and ensuring that the crystal structure generated is the same as the experimentally observed crystal structure. Another is to rank the generated polymorphs and provide the highest evaluation of the crystal structure

that can be regarded as one corresponding to the experimentally observed crystal structure. Ideally, the polymorphic structure with the lowest crystal energy should be the most thermodynamically stable. In the fourth blind test reported in 2009, the Neumann group was the first to use the DFT-D method with periodic boundary conditions [9]. In the sixth blind test reported in 2016, which included five different molecules, such as co-crystals, salt hydrates, and molecules with high conformational flexibility, eight of the nine crystal structures were correctly obtained using the improved DFT-D method [11]. Although the evaluation by the improved DFT-D method agrees with the experimental structure within or below the experimental error for the crystal structure, room for improvement in the crystal polymorph ranking by crystal energy has been identified.

10.1.2 Challenges of Molecular Crystal Calculations Using the Force Field Method

The results of the CSP blind test suggest that the methodology currently employed in crystal structure prediction can predict unknown crystal structures, possibly with higher accuracy than results obtained experimentally. However, it suffers from computational costs. The DFT-D method is a relatively high-precision method among first-principles calculations but it requires a computer with high computing power. Therefore, it is not a good strategy to adopt the first-principles calculation to determine polymorphs more efficiently.

Crystal force field calculations based on classical mechanics are an important potential solution. In general, the crystal energies and optimized crystal structures of the input crystal structures can be obtained 100–1000 times faster than the first-principles calculations. In other words, the structure optimization of several trial crystal structures generated by the crystal polymorphism search can be completed in a realistic calculation time. More accurate structures, energies, or properties based on electronic states can be obtained in a relatively short time by performing re-evaluation or structure optimization again using the DFT-D method. This is a more realistic and practical strategy.

The problem with the crystal force field calculation is its accuracy. The accuracy of the crystal force field, which is an extension of the molecular force field for a single molecule to the crystal structure, is almost the same or slightly worse than the experimental error [11]. The crystal energies do not correlate well with those of the DFT-D method. Although the DFT-D method can accurately be used to search for crystal polymorphs, the same accuracy cannot be obtained if the crystal force field used to optimize the trial crystal structure does not reproduce the appropriate structure and energy. In fact, the success of the Neumann group in the CSP blind test is largely due to the force field construction function (tailor-made force field) [13] introduced in their crystal structure prediction program GRACE. In their method, the crystal structure of a target molecule is optimized in advance by the corrected DFT method

and the crystal force field is automatically adjusted to reproduce the obtained crystal structure. Their success indicates that it is very effective in establishing molecular crystallography to obtain a crystal force field that better resembles the result obtained from the DFT method.

Crystal force field calculations have some challenges inherent to soft crystals. Since most of the molecules exhibiting soft crystal phenomena are metallic complexes, crystal force field calculations are not always available because of missing the force field parameters. In addition, as the force field method, in principle, describes molecules according to the valence bond rule, it may not be able to describe metal complexes properly. It is also difficult to geometrically define the coordination bonds (interactions) between the central metal ion and the organic ligands of metallic complexes and to describe how they change depending on the oxidation number of the central metal. Therefore, traditional molecular mechanics has not been actively treated for the coordinate compounds as one of the available methodologies, and it was not clear how to apply them in practice.

In Sect. 10.2, we review the classical mechanics-based crystalline force field calculations employed by us to analyze soft crystals. In Sect. 10.3, we present examples of our computational chemistry research on soft crystals and show how we have solved some of the aforementioned challenges. Section 10.4 outlines the approaches we are developing to analyze structural phase transitions, as exemplified by soft crystal phenomena, and describes new methodologies that will be developed in the future.

10.2 Crystal Force Field Calculation

Crystal force field calculations are an extension of molecular force fields, which have been developed mainly to reproduce three-dimensional structures, energies, and vibrational frequencies of isolated molecules, that make it possible to calculate crystal structures under periodic boundary conditions. Unlike first-principles calculations, molecular force fields do not treat electrons in an exposed manner but describe molecules using classical mechanical formulas for the "fields" that electrons rapidly form around atoms. This is called "molecular mechanics" [14]. To extend the molecular force field to a crystal force field, it is necessary to accurately calculate the crystal structure, crystal energies, and lattice vibrations, especially if the goal is to accurately reproduce the relative stability between crystal polymorphs [15]. Therefore, in crystal force field calculations, the force field functions for intermolecular interactions in crystals are usually the same as those for molecular force fields, even though some modifications are made to treat intermolecular interactions more rigorously [16]. Various force fields have been employed in crystal calculations under the requirement that they reproduce the crystal structure within less than the experimental error and allow the evaluation of the relative crystal energies of the stable and metastable phases. Furthermore, it should also be able to reproduce and analyze the observed crystal polymorphic structures and their behavior up to matching lattice vibrations ($k = 0$ phonons) [17].

In this section, we review the crystal energies, underlying crystal force fields, and their crystal structural predictions using the crystal force field calculation method [18–21] implemented in the computational chemistry program CONFLEX [22–24].

10.2.1 Crystal Energy

Given a molecular structure, space group, and lattice constant in an asymmetric unit, a crystal structure can be constructed on a computer. The crystal energy corresponding to the internal energy of the thermodynamic state for the crystal structure E_{crystal} can be defined as the energy per asymmetric unit in Eq. (10.1) [11, 21].

$$E_{\text{crystal}} = E_{\text{intra}} + E_{\text{lattice}} \tag{10.1}$$

where E_{intra} is the sum of the intramolecular interaction energies in the asymmetric unit and E_{lattice} is defined as

$$E_{\text{lattice}} = E_{\text{inter}}^{\text{AU}} + \frac{1}{2}\sum_{i}^{N}\sum_{S}^{M}\sum_{J}^{N} E_{\text{inter}}(i; S, J) \tag{10.2}$$

In Eq. (10.2), the first term $E_{\text{inter}}^{\text{AU}}$ is the sum of the intermolecular interaction energies in the asymmetric unit, which is zero if there is only one molecule in the asymmetric unit. The second term is the sum of the intermolecular interaction energies between the molecules in the asymmetric unit and the molecules replicated by the translational symmetry. In the CONFLEX crystal calculation model, the range for this sum is pre-specified by the nearest-neighbor interatomic distance between the molecules in the asymmetric unit and the replicated molecules (Fig. 10.1). In the crystal structure optimization, the coordinates of the atoms in the asymmetric unit and the lattice constants are used as parameters for structural optimization while maintaining the symmetry of the crystal to obtain the energy-minimal structure. For the evaluation of intra- and intermolecular interactions in the crystal, we employ the existing force field, MMFF94s [25–32].

In CONFLEX, we can calculate the crystal energy by inputting the crystal structure determined by X-ray crystallography, that is, the molecular structure and space group in the asymmetric unit and the lattice constant. In the same way, either or both the molecular structure and the lattice constant in the asymmetric unit of the crystal structure can be optimized. However, only the space group is kept constant during optimization. The crystal structure obtained by the optimization with minimal crystal energy agrees with the crystal structure determined by X-ray crystallography to the same extent as the experimental error [11]. Empirically, it is less than approximately 1.0 Å in root-mean-square deviation (RMSD) for a superposition of 15 molecules (RMSD_{15}) in a crystal. If the deviation from the experimental structure is large,

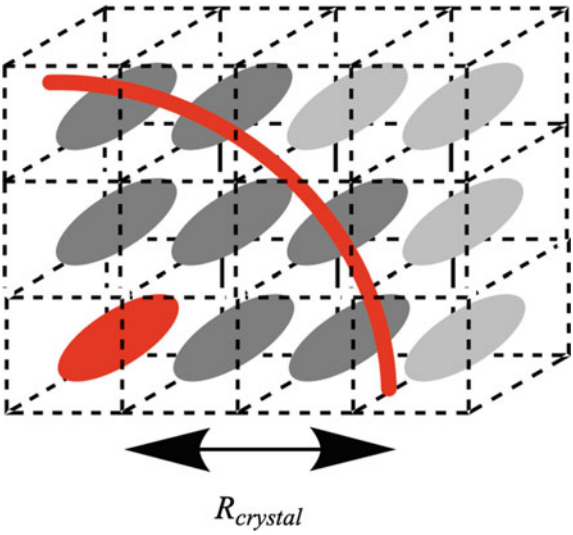

Fig. 10.1 Molecular crystal calculation model of CONFLEX (Reprinted (adapted) with permission from Ref. [42]. Copyright (2022) American Chemical Society.). The asymmetric unit is depicted in red and replicated molecules that the nearest-neighbor interatomic distance from molecules in asymmetric unit is less than $R_{crystal}$ are in dark gray. The molecules depicted in light grey are not including in the crystal energy calculation

likely, the crystal force field applied to the molecule is not appropriate. In such cases, it may be necessary to reconsider the force field parameters.

10.2.2 Crystal Force Field

In CONFLEX, the energy defined in Eq. (10.1) is calculated using the molecular force field based on classical mechanics. The MMFF94s potential energy function employed is constructed as described in Eq. (10.3) [25, 26, 32]:

$$E_{\mathrm{FF}} = E_{\mathrm{str}} + E_{\mathrm{bend}} + E_{\mathrm{tors}} + E_{\mathrm{oop}} + E_{\mathrm{str-bend}} + E_{\mathrm{vdW}} + E_{\mathrm{el}} \tag{10.3}$$

where E_{str} is the bond stretching, E_{bend} is the angle bending, E_{tors} is the bond torsion, E_{oop} is the out-of-plane angle, $E_{\mathrm{str-bend}}$ is the coupling of stretching and bending, and E_{vdW} and E_{el} correspond to the van der Waals (vdW) and electrostatic interactions, respectively. In CONFLEX, the force field, which has been developed mainly for the evaluation of single molecule structures, is extended to evaluate crystal energies. That is, the first term in Eq. (10.1), namely E_{intra}, is evaluated using Eq. (10.3). Furthermore, the last two terms in Eq. (10.3), namely E_{vdW} and E_{el}, are not only the force field potential function forms for the intramolecular non-bonded interactions in the asymmetric unit but also the intermolecular interaction energies E_{lattice} in Eq. (10.2) in the crystal force field calculations.

As MMFF94s has been developed to calculate potential energies for organic compounds, few force field parameters are available for the elements constituting metallic and inorganic materials. To perform crystal calculations for many metal

complexes that exhibit soft crystal phenomena, it is necessary to start by determining the force field parameters. In particular, the force field parameters for the vdW interactions are the most important factors that determine the accuracy of the crystal structure and energy optimized by the crystal force field.

The vdW interactions of the MMFF94s used for the crystal force field is obtained from Eq. (10.4):

$$E_{vdW_{ij}} = \varepsilon_{IJ}\left(\frac{1.07R^*_{IJ}}{R_{ij}+0.07R^*_{IJ}}\right)^7\left(\frac{1.12R^{*7}_{IJ}}{R^7_{ij}+0.12R^{*7}_{IJ}}-2\right) \tag{10.4}$$

where R_{ij} is the distance between atoms *i*-*j* in the crystal and R^*_{IJ} is a parameter determined by the combination of atom types *I*-*J*, which is obtained from the following equations:

$$R^*_{IJ} = 0.5\left(R^*_{II}+R^*_{JJ}\right)\left(1+0.2\left(1-\exp\left(-12\gamma^2_{IJ}\right)\right)\right) \tag{10.5}$$

$$\gamma_{IJ} = \left(R^*_{II}-R^*_{JJ}\right)/\left(R^*_{II}+R^*_{JJ}\right) \tag{10.6}$$

$$\varepsilon_{IJ} = \frac{181.16G_IG_J\alpha_I\alpha_J}{\left(\alpha_I/N_I\right)^{1/2}+\left(\alpha_J/N_J\right)^{1/2}}\frac{1}{R^{*6}_{IJ}} \tag{10.7}$$

where N_I of atom type I is the Slater–Kirkwood effective valence electron number, G_I is a scale factor determined to reproduce the experimental values for rare gasses, and R^*_{II} corresponds to the van der Waals radius of atom type I, which is defined using Eq. (10.8):

$$R^*_{II} = A_I\alpha_I^{1/4} \tag{10.8}$$

In Eq. (10.8), A_I is a scale factor describing the outermost electron spread. Thus, many force field parameters of the vdW interactions depend on the outermost-shell electron configuration and are optimized with reference to rare gas experiments [26, 32]. Therefore, to add a new atom type, the atomic polarization factor α must be calibrated. In our series of studies on soft crystals, we determined the force field parameters for several metal ions that are central to them. Specific examples are outlined in Sect. 10.3.

10.2.3 Crystal Structure Prediction

Predicting the crystal structure of a molecule from its structural formula is known as crystal structure prediction [6, 12, 33]. The method of crystal structure prediction in CONFLEX is essentially the same as those employed by other groups, with the

strategy of (1) generating possible crystal structures (Fig. 10.2a), (2) precise calculation of the relative energy of the crystal (Fig. 10.2b), and (3) selection of suitable predicted structures (Fig. 10.2c) [12].

The first step is to generate trial crystal structures with independent parameters describing the crystal structure as variables. The unique crystal polymorph obtained by structural optimization is considered as a possible crystal structure. This procedure is called "crystal polymorphism search." As the search space for polymorphs is large, the reliability of crystal structure prediction depends on the ability to search efficiently without missing any possible stable polymorphs.

In the CONFLEX search for polymorphs, the three-dimensional structure is first constructed based on the two-dimensional structural formula of the target molecule, and the structure of the isolated molecule is subsequently optimized. If the target molecule is flexible, conformational search is performed by local deformation of the molecular structure using corner flap, edge flip, and stepwise rotation and by

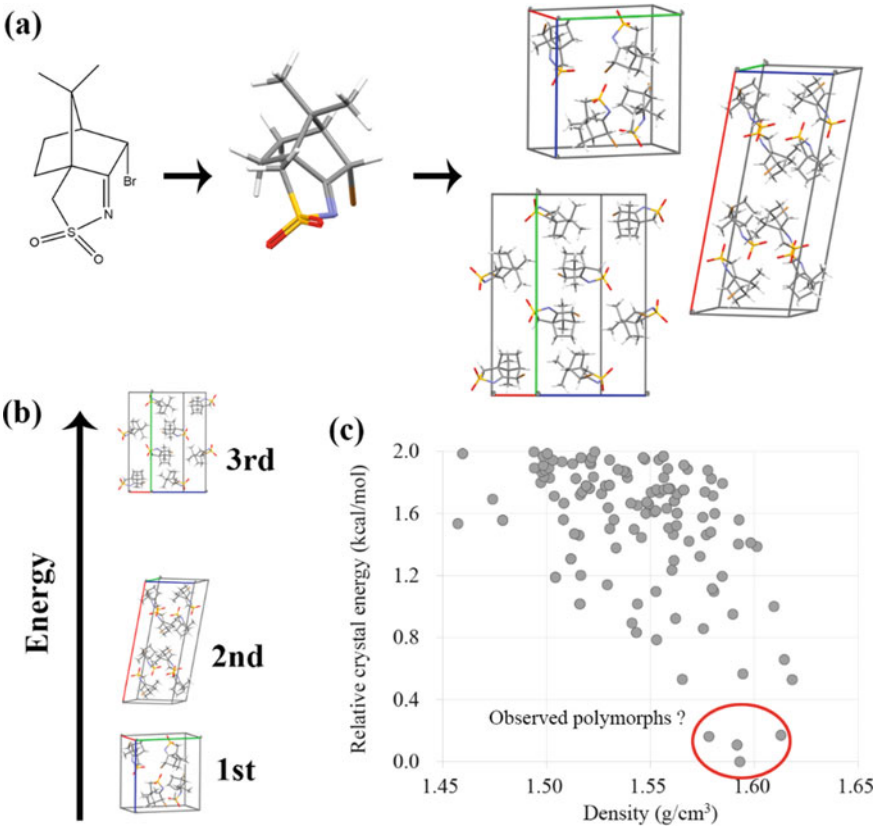

Fig. 10.2 Crystal structure prediction algorithm: **a** Generate possible crystal structures, **b** calculate accurate relative crystal energies, and **c** select the predicted structure based on their energies (Reprinted (adapted) with permission from Ref. [12])

reservoir-filling algorithm to obtain stable conformational isomers [22–24]. From the obtained conformational isomers, one or more conformational isomers are selected in principle in the order of their energies, considering the steric structures and energies, and trial crystal structures are generated for each of them as follows. According to the CSD Space Group Frequency Ordering [34], ten different space groups ($P2_1/c$, $P\bar{1}$, $C2/c$, $P2_12_12_1$, $P2_1$, $Pbca$, $Pna2_1$, Cc, $Pnma$, and $P1$) were determined to account for approximately 90% of organic crystals registered in the CSD. The choice of the space group must be flexible, and the symmetry of the target molecule and other factors must be considered as it determines the final crystal structure obtained [21]. The trial crystal structures generated are all subjected to crystal energy minimization and the unique optimized structure obtained is the possible crystal structure of the target molecule. We obtained a structure consistent with the experimental crystal structure [35]. We applied the method to ten different space groups, where the rotation angle of the molecular orientation was set to 20º increments for a single conformation. Approximately 100,000 trial crystal structures were generated. Although the crystal force field calculation can evaluate crystal energies faster than first-principles calculations, the computational load increases substantially owing to the expansion of the search space. Thus, it is important to develop more efficient search algorithms in the future.

In the second step, structures optimized by crystal force field calculations during the search are often re-evaluated for the relative energies between crystal polymorphs using ab initio calculations, especially the DFT-D method under periodic boundary conditions, which is considered superior. However, accurate evaluation is computationally expensive. Ideally, if the crystal structure optimized by the crystal force field calculation is sufficiently consistent with that of the DFT-D method, the large consumption of computation time can be avoided.

In the third step, we generally produce a ranking of the crystal polymorphs by crystal energy. It is desirable that the crystal structure observed in the experiment is consistent with the crystal polymorph with the lowest energy. However, even if we use the DFT-D method, we cannot be sure that the relative energies between the crystalline polymorphs are correctly evaluated. Indeed, in the fifth- and sixth-blind tests, the evaluation by the DFT-D method did not accurately predict the ranking of the crystal polymorphs, even though it could find structures consistent with the measured crystal structures [10, 11]. The accuracy of the evaluation by the crystal force field calculation was inferior to that by the DFT-D calculation. CONFLEX solves this problem by obtaining a ranking that considers the similarity of the crystal structures compared with the predicted crystal structure patterns when data of powder X-ray diffraction (PXRD) patterns are available, even if the crystal structures have not been determined. The ranking based on the similarity can be available for re-evaluation to be predicted polymorphic structure to produce a likely experimental structure [21].

10.3 Studies on Soft Crystals Using Crystal Force Field Calculations

In this section, we present our joint work on the application of crystal force field calculations to isocyanide-gold complexes, lanthanide (Ln) complexes, and disilane-bridged macrocycles belonging to soft crystals. For the gold isocyanide and Ln complex calculations, we have newly developed the necessary crystal force fields, which are also briefly introduced.

10.3.1 Force Field Parameters for Isocyanide Gold Complexes

The soft crystal phenomenon of phenyl(phenyl isocyanide)gold(I) (Fig. 10.3, $R^1 = R^2 = H$) synthesized by Ito et al. is very interesting that the two crystal structures of the isocyanide gold complex, namely Ib and IIy, induce a single crystal to undergo a single crystal phase transition from Ib to IIy simply by bringing them into contact with each other (Fig. 10.4) [36]. The blue Ib phase gradually changes to the yellow IIy phase upon ultraviolet (UV) irradiation. In addition, although the formed IIy does not revert to Ib by cooling, Ib can be obtained again by recrystallization in a solvent. Upon closer inspection of the difference between the two crystal structures, we notice that during the transition from Ib to IIy, a loose Au–Au bond is formed and the dihedral angle between the two Ph rings is changed. More interestingly, by introducing substituents at two ortho positions of this molecule, various combinations of luminescent colors can be observed before and after crystal rubbing [37].

To deal with this phenomenon using crystal force field calculations, the atomic type of Au was newly defined, the Au–C covalent and Au…CN coordination bonds between Au and C were considered (Fig. 10.3), and the force field parameters for Au, including bond stretching, angle bending, stretch-bend interactions, electrostatics, and vdW, for Au were developed [38]. The crystal structures Ib and IIy were optimized using the newly constructed crystal force field and the obtained lattice constants were compared with the measured values. These results are shown in Table 10.1. The difference in $RMSD_{20}$ [39, 40] from the experimental structure

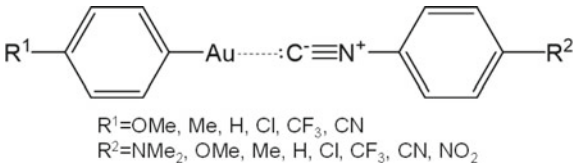

Fig. 10.3 Pheny(phenylisocyanide)gold(I) and its derivatives: The bond between the phenyl group and Au is assumed to be covalent-like, while the Au···CN bond is a coordination bond

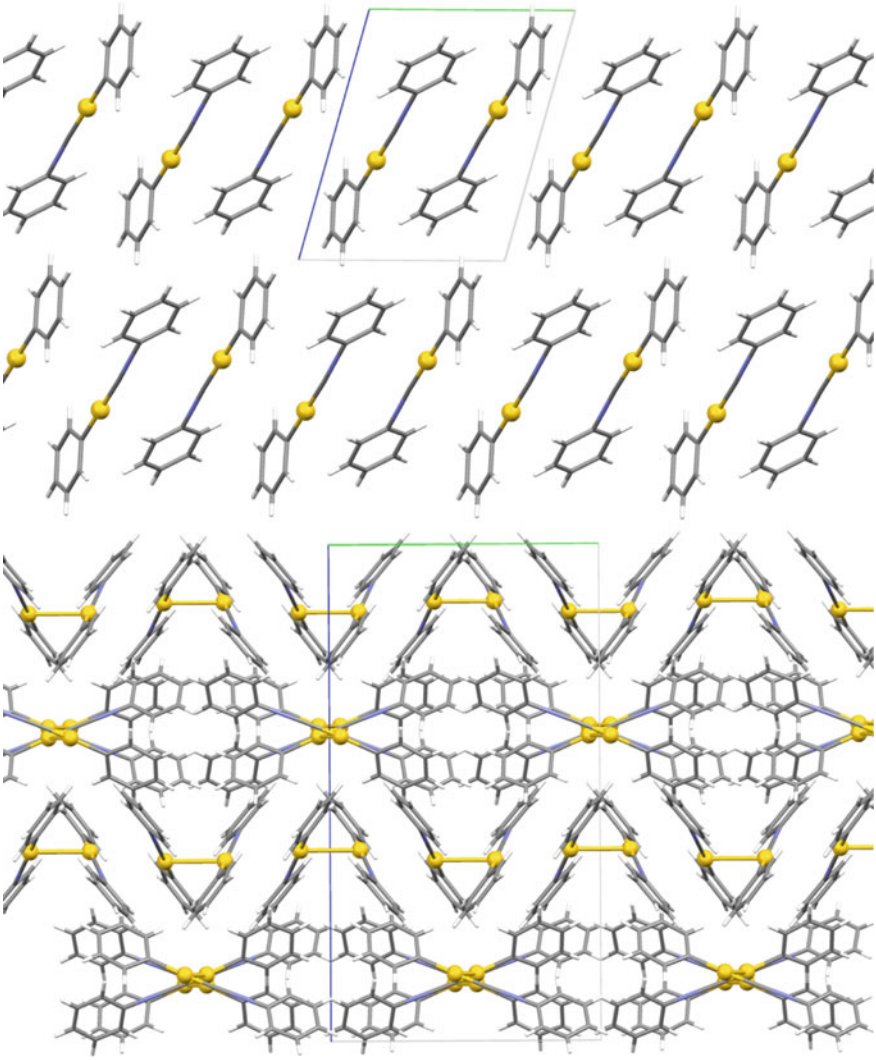

Fig. 10.4 Polymorphs of phenyl(phenylisocynide)gold(I) exhibiting Ib (upper) and IIy (lower) (Reprinted (adapted) with permission in Ref. [38])

by superposition of 20 molecules in the crystal is 0.468 Å for Ib and 0.595 Å for IIy. The Au…Au distance for IIy (Fig. 10.5) is also reproduced relatively well.

The RMSD of the lattice parameters from the experimental data for the 27 structures (including Ib and IIy) with substituents at the ortho-position were determined to be 0.70 Å for the lattice lengths a, b, and c and 3.3° for the lattice angle. Therefore, the newly developed crystal force field reproduced the crystal structure of gold isocyanide complexes.

Table 10.1 Experimental (Exptl.) and computational (Calcd.) lattice constants for phenyl(phenylisocynide)gold(I) complexes (Units are Å for a, b, c, and degrees for α, β, γ)

Form	Lattice constant	Exptl	Calcd
Ib	a	6.021	5.823
	b	9.073	9.934
	c	11.450	11.644
	α	102.2	103.4
	β	101.5	101.4
	γ	102.4	102.0
IIy	a	13.478	13.734
	c	24.808	27.638

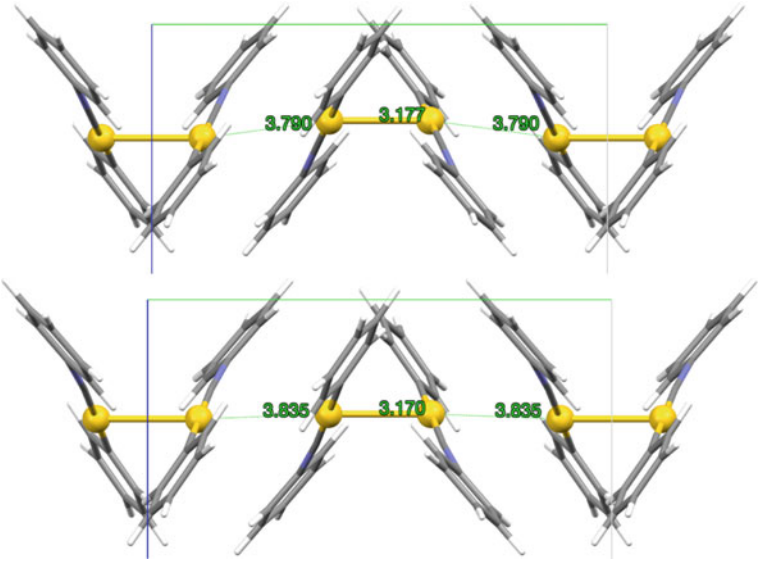

Fig. 10.5 Au···Au distances (Å) in experimental (upper) and computational (lower) crystal structures of IIy (Reprinted (adapted) with permission from Ref. [38])

10.3.2 Force Field Parameters for Helicate Lanthanide Complexes

Among the rare earth elements, the Ln series elements exhibit a unique phenomenon called Ln contraction, in which the ion size decreases as the atomic number increases. The six-coordinated Ln complexes with luminescent properties synthesized by Hasegawa et al. (Fig. 10.6, hereafter referred to as Ln**L** complexes) have a crystal structure in which ten types of Lns, namely Pr, Nd, Sm, Eu, Gd, Tb, Dy, Ho, Er, and Tm, adopt similar coordination structures [41, 42]. In these crystal structures, the distance between the N atom of the ligand ethylenediamine derivative and the

central metal Ln changes regularly, which is one of the cases where the effect of Ln contraction is manifested. It is also interesting to note that the chiral helical structure formed by the coordinating ligand changes with Ln, which is a very interesting aspect of the applicability of this material.

In the case of the isocyanide gold complex mentioned above, it was necessary to define both covalent and linear anisotropic coordination bonds between Au and C. However, in this Ln**L** complex, we decided to model it merely as a free Ln ion [42]. In other words, only isotropic non-bonded interactions need to be considered to determine the interaction between the Ln ion and ligand. In addition, if the Ln has a formal charge of +3, the electrostatic interaction can be calculated conventionally, so the only new parameter required is in terms of the vdW interaction. Then, among the force field parameters for the vdW interaction of Ln metal ions, N and G in Eq. (10.7) and A in Eq. (10.8) should be the same values as for the iodine atom common to the Ln series. Thus, 1.404, 6.95, and 3.08 must be adopted for N, G, and A, respectively, according to the outermost electron configuration rules described in Sect. 10.2.3. Thus, the only force field parameter we need to determine is the atomic polarization factor α. The optimized α to reproduce the X-ray crystal structures formed by the ten Ln complexes are listed in Table 10.2 [42]. The vdW radii R_{II}^{*} from Eq. (10.8) with the α of each Ln are smaller in order of atomic number and Ln contraction occurs.

Comparing the structure-optimized crystal structures with the experimental structures using the new force-field parameters, all the optimized structures are in agreement with the experimental structures, ranging from 0.32–0.46 Å in the $RMSD_{20}$ and from 0.031–0.064 Å in the absolute error of the distance between Ln···**L** (Fig. 10.7) [42]. To further verify the robustness of the optimized force-field parameters, we compared the force-field-optimized crystal structures with the experimental structures for the four Eu derivatives that were not used as reference structures for optimization. The results show that the absolute errors of the $RMSD_{20}$ and Ln···**L** distances are 0.40–0.61 Å and 0.018–0.041 Å, respectively.

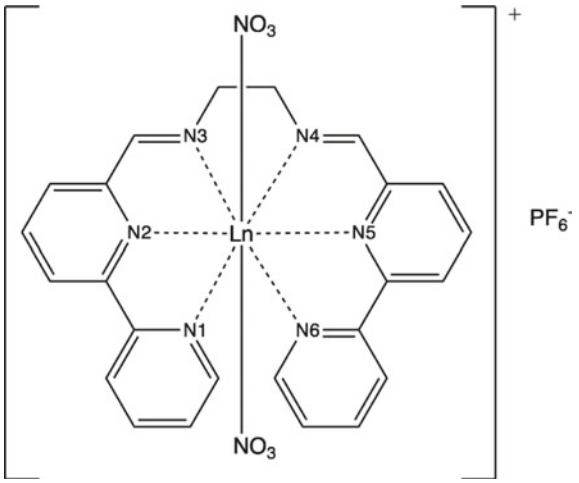

Fig. 10.6 Molecular structure of the helicate complex, Ln**L**

Table 10.2 Force field parameters and van der Waals radii of Lanthanide ions

Lanthanide	α_I	R^*_{II} (Å)
Pr^{3+}	2.05	3.685
Nd^{3+}	2.00	3.663
Sm^{3+}	1.85	3.592
Eu^{3+}	1.80	3.568
Gd^{3+}	1.75	3.543
Tb^{3+}	1.65	3.491
Dy^{3+}	1.35	3.320
Ho^{3+}	1.20	3.224
Er^{3+}	1.15	3.190
Tm^{3+}	1.10	3.154

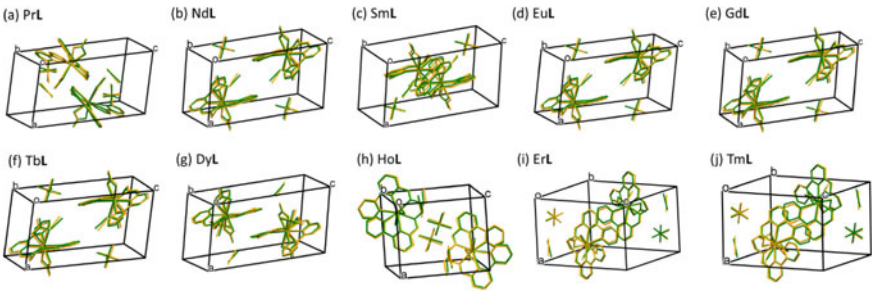

Fig. 10.7 Superimposed representation of observed (green) and optimized structures (yellow) of a series of Ln complexes with the helicate ligand **L** (Reprinted (adapted) with permission from Ref. [42])

This study is the first direct confirmation of Ln contraction by deriving a scientifically significant value of the vdW radius from the experimental structure. Although it is a recent trend to refer to high-precision first-principles calculations for determining force-field parameters, a large-scale computer is required to deal with this family of crystal structures by first-principles calculations. At present, the combination of experimental structure and crystal force field calculations is very useful for such a large system. It is also known that the Buffered 14–7 type function employed here to reproduce the vdW interaction is more accurate than the Lennard–Jones type function [26, 32]. As it can also be used in molecular dynamics simulations, it is expected to have applications in future developmental studies.

10.3.3 Prediction of the Vapochromic Crystal Structures of Ni(II)-Quinonoid Complexes

The Ni quinonoid complex crystal with a methyl group discovered by Kar et al. selectively adsorbs methanol vapor and changes its spin state to paramagnetic, and the solid exhibits vapochromism, changing its color from purple (MeP) to orange (MeO) (Fig. 10.8) [43]. Furthermore, the crystal with an ethyl group (EtP) is a purple solid as MeP and its structure and electronic state are similar to those of MeP. However, it does not adsorb methanol, as suggested by the experiment. The crystal structure of MeP is key to analyzing the methanol-selective adsorption mechanism but it has not yet been identified. Therefore, we attempted to construct crystal structure models of MeP based on the known crystal structures of MeO and EtP but we have not been able to find any crystal structure that is sufficiently consistent with the experimentally obtained PXRD patterns.

Therefore, we created new force field parameters for Ni to reproduce the three-dimensional structures of these complexes and modified the parameters of the ligands. Using the crystal force field with these updated parameters, we searched for crystal polymorphs of MeP, assuming the same space group $P1$ as the crystal structures of MeO and EtP, and obtained 18 crystal structures (Fig. 10.9). These structures were further optimized using the DFT-D method (PBE-D3, PAW), and structures that are lower in crystal energy than those modeled from known crystal structures (MeO and EtP) were determined to be in good agreement with the PXRD patterns [44].

In this study, we show that if appropriate force field parameters can be obtained to reproduce the molecular structure of a complex and estimate the space groups that the crystal structure of the complex can assume, it is possible to identify the crystal structure of a complex that is difficult to analyze by single crystal X-ray

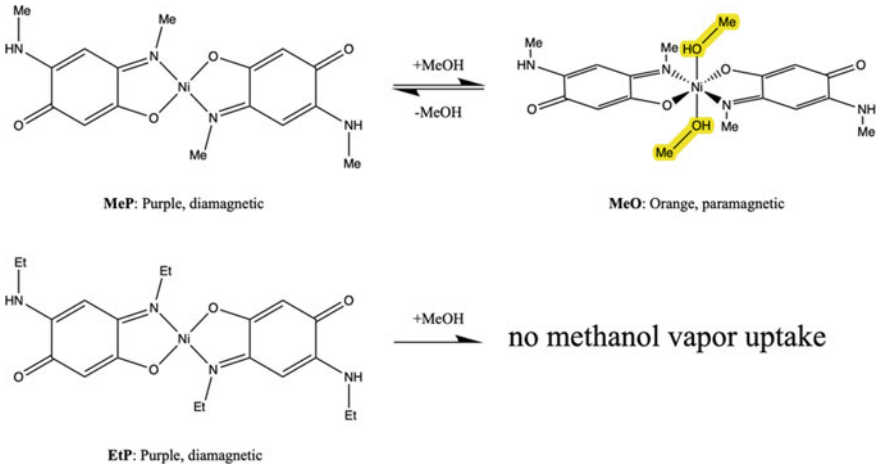

Fig. 10.8 Methanol vapor uptake of a Ni-quinonoid complex

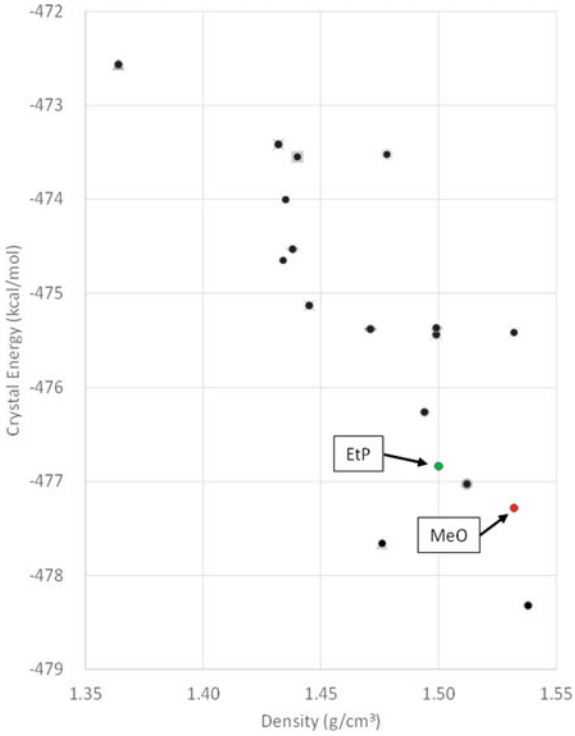

Fig. 10.9 Density-energy landscape of the polymorph search for MeP: A few crystal structures found in the crystal polymorph search are more common in energy and density than those derived from MeO (red) and EtP (green)

analysis through a crystal polymorph search. Furthermore, by performing electronic structure calculations on the obtained structures, we succeeded in evaluating the energies of adsorption processes and analyzing absorption spectra [44]. We believe that this study may be an opportunity to establish a new scheme for vapochromic complexes, for which it is sometimes difficult to identify the crystal structure before and after adsorption, by searching for the crystal structure using the classical force field and analyzing the luminescence mechanism by electronic structure calculation.

10.3.4 Structural and Energetic Evaluation of the Thermosalience in Disilanyl Macrocycles

The thermosalient effect is a phenomenon in which a crystal piece changes its shape remarkably when the temperature changes. The analysis of the states before and after this phenomenon, which is caused by the instantaneous structural change of molecules in a crystal, is important for clarifying the mechanism of phase transitions. Omoto et al. synthesized a cyclic molecule **C4** (Fig. 10.10) consisting of four

p-phenylenes bridged by disilane and concluded that its crystal undergoes a thermosalient phenomenon because of a phase transition under low temperature conditions [45].

In this system, the crystal structures of the **C4α** and **C4β** phases before and after the transition are known. The crystal structures of the **C4α** and **C4β** phases were optimized by CONFLEX crystal force field calculations while the respective lattice constants were maintained and the three-dimensional structures of the molecules in the crystals were reproduced. The energy difference between the two crystal structures is attributed to the intermolecular interactions. Furthermore, we optimized the crystal structure by stretching the lattice lengths *a, b,* and *c* separately and compared the crystal energies. This corresponds to the observation that the thermosalient phenomena are induced by crystal splitting along the (001) or (010) planes (Fig. 10.11) [45].

In this system, two crystal structures converge to the same structure when the crystal force field is used for structural optimization, including the lattice parameter. This result differs from experimental observations. To reproduce their crystal structures more accurately, we need to further improve the force field parameters. In particular, the refinement of the crystal force field around Si atoms will be important because of the wide range of applications of compounds with carbon-silicon (C–Si) bonds [46].

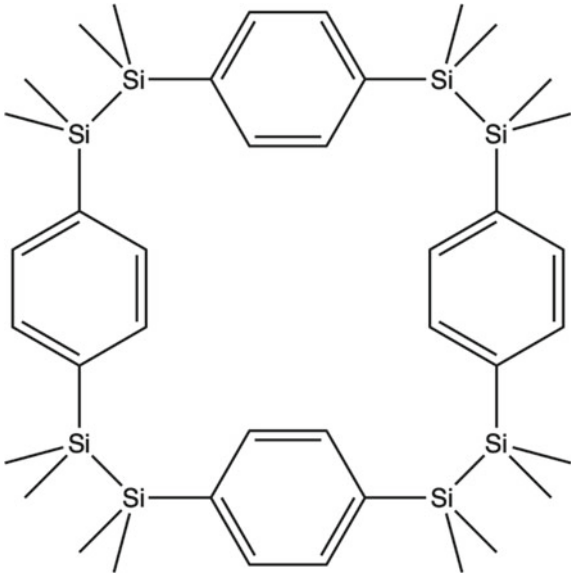

Fig. 10.10 Disilanyl macrocycle composed of four disilane (Si–Si) bonds and four *p*-phenylenes

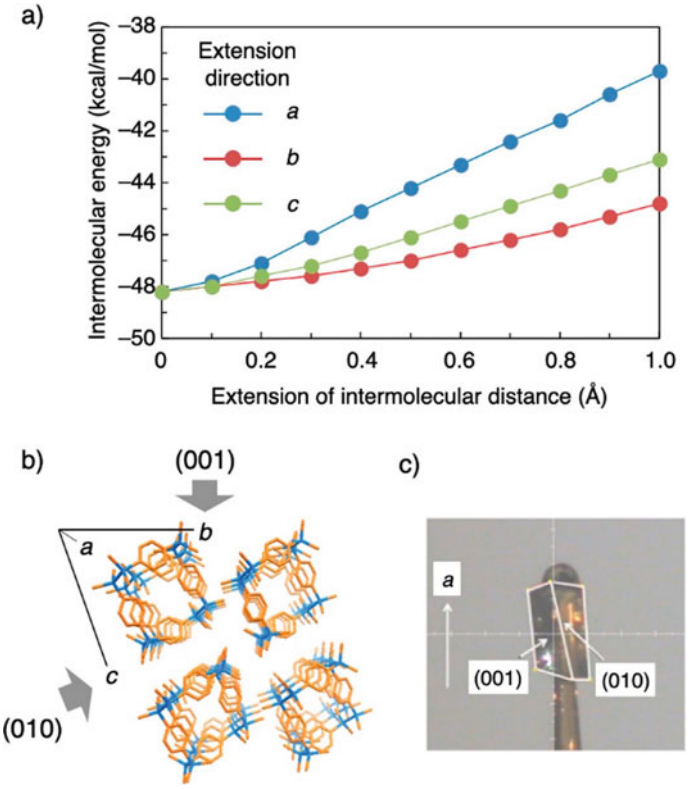

Fig. 10.11 **a** Changes in the intermolecular energy of the virtual crystals of C4α with an extension of the intermolecular distance. **b** Crystal packing with cell axes and **c** face-indexing graphics of C4α (Reprinted (adapted) with permission from Ref. [50]. Copyright (2020) American Chemical Society.)

10.3.5 Intermediate Formation by Pyridine Coordination for Lanthanide Complexes

The seven-coordinated Tb dinuclear complex $[Tb_2(tmh)_6(4,4'\text{-bpy})]$ (Tb-dinuclear), in which the green luminescent Tb ion is linked by a bipyridine (bpy), is converted under pyridine (py) vapor into an eight-coordinated Tb complex $[Tb(tmh)_3(py)_2]$ (Tb-pyr2) via an intermediate of the eight-coordinated Tb complex $[Tb(tmh)_3(4,4'\text{-bpy})]$ (Tb-polymer), as revealed by X-ray crystal structure analysis (Fig. 10.12). Hasegawa et al. discovered this three-step deformation and succeeded in linking it with a similarly generated yellow-luminescent Dy complex via a mononuclear intermediate, Tb-pyr2 [47]. The discovery of the rare properties of this rare-earth complex, such as its ability to link and combine two (or more) molecular crystals and transmit optical information in one direction, is extremely important for new developments, such as organic transistors and organic electro-luminescences (ELs).

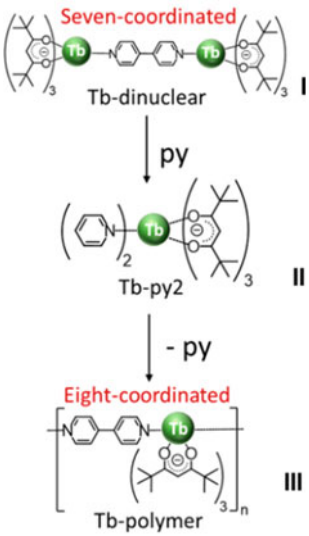

Fig. 10.12 Three-step deformation of the connected train-type Tb complex (Reprinted (adapted) with permission from Ref. [50])

This three-step transformation process contains several "obscurities". For example, the pathway py uses to approach Tb in the crystal of Tb-dinuclear, how bpy leaves Tb at that time and where it goes, when py leaves after Tb-pyr2 formation, and what pathway bpy uses to re-approach Tb to form a Tb-polymer. We investigated the dynamic pathways of py and bpy in the crystal by kinetic simulations based on crystal force field calculations using the rare-earth force field parameters developed above (Sect. 10.3.3). However, it was determined that the periodic boundary condition cannot be used for the migration of solvent molecules in the crystal because of symmetry breaking. Thus, it is necessary to construct a sufficiently large virtual lattice with some computational restrictions. Unfortunately, such a large-scale dynamics simulation could not be performed in a limited time.

We reserved the intracrystal dynamics of py to examine how py approaches Tb-dinuclear (Fig. 10.13). We decided to examine the unique four-way pattern in which the first py approaches. We applied the DFT method to the py…Tb-dinuclear in each pattern and evaluated the stability of the py…Tb-dinuclear by structure optimization in pyridine solvent with Polarizable Continuum Model (PCM). The results showed that the eight-coordinate Type 1 structure, such as Tb-pyr2 and the Tb-polymer, is stable and py predominantly approaches from the opposite side of bpy to Tb (Table 10.3). The Type 1 + 4 structure, in which the second py is coordinated from the top of the bpy, is the most stable (Fig. 10.14). From these results, the coordination process of py to Tb-nuclear can be determined, as shown in Fig. 10.15, even though the dynamics of py in the crystal is unknown.

The computational cost of analyzing the migration processes and pathways of solvent molecules in molecular crystals in a solvent vapor atmosphere, such as vapochromism, is very high, even if the force field method is employed. It is important to devise a simpler computational model, as in the case of the Tb complex, which can

Table 10.3 Energy differences (ΔE) of the first and second pyridine coordination for Tb-dinuclear

First coordination	ΔE (kcal/mol)	Second coordination	ΔE (kcal/mol)
Type 1	0.00		
Type 2	0.73	Type 1 + 2	1.00
Type 3	6.25	Type 1 + 3	1.29
Type 4	5.20	Type 1 + 4	0.00

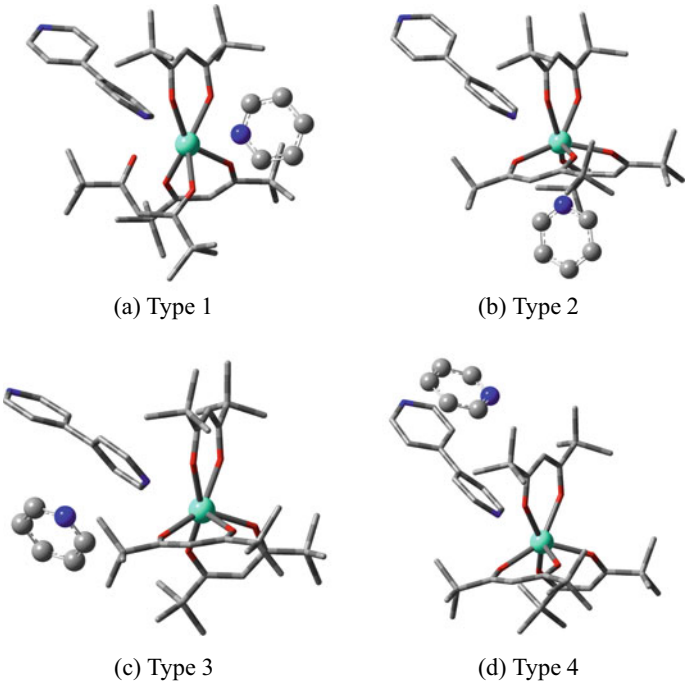

Fig. 10.13 Structures of one pyridine coordination approach to a Tb-dinuclear complex: **a** Type 1 is a pyridine approaching from the opposite side upward for Tb-ion, **b** Type 2 is from the opposite side downward, **c** Type 3 is from the same side downward, and **d** Type 4 is from the same side upward

be calculated without losing the essence of the problem through the ingenuity of the researcher. A well-conceived computational model will not only help us to solve the problem precisely but also amplify the interest of the research.

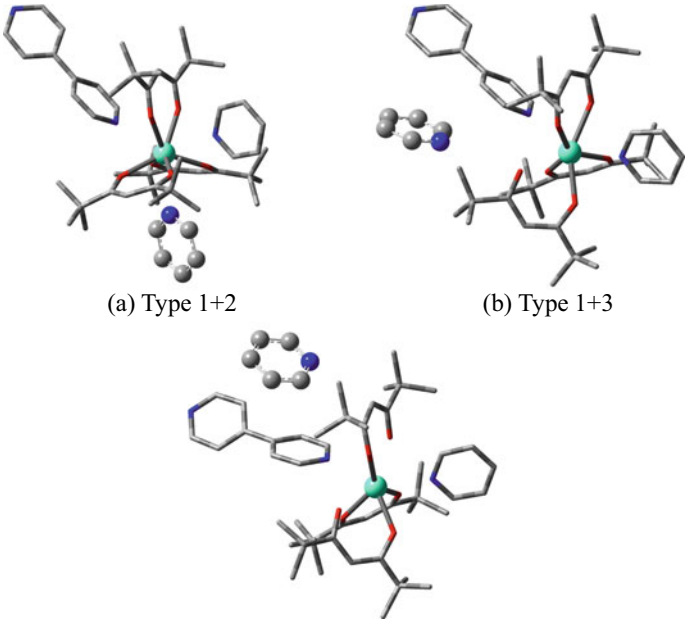

(a) Type 1+2 (b) Type 1+3

(c) Type 1+4

Fig. 10.14 Structures of another pyridine coordination for a py-coordinated Tb-dinuclear complex: **a** Type 1 is a second pyridine approaching from the opposite side downward to Tb-dinuclear, **b** Type 2 is from the same side downward, and **c** Type 3 is from the same side upward

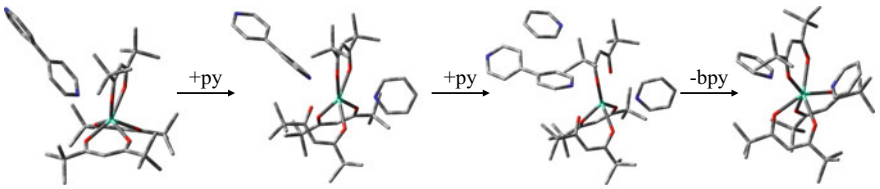

Fig. 10.15 Scheme of pyridine addition to the Tb-dinuclear complex

10.4 Perspectives on Computational Chemistry Methods for Molecular Crystals, Especially Soft Crystals

When soft crystals are dealt with computational chemistry, it is necessary to construct an appropriate computational model that describes how the external weak macroscopic stimuli that trigger the property change propagate into the crystal and what effects they have on the molecules. In the cases of the Ni(II)-quinonoid (Sect. 10.3.3) and Ln (Sect. 10.3.5) complexes, the existing crystal calculations could be applied to the macroscopic stimuli of "exposure to solvent vapor" by neglecting the dynamics

of solvent molecules penetrating the crystals. In the case of the disilanyl macrocycle (Sect. 10.3.4), which exhibits thermosalient effects, the tolerance of the crystal structure to sudden volume expansion or contraction upon heating or cooling can be discussed in terms of the lattice length and crystal energy. The model was constructed within the range of available computational methods, and if the obtained results agreed with the experimental results within the error range, it implies that the validity of the calculation is verified. However, verification of the calculation requires some discussion on the validity of the assumptions, hypotheses, and approximations that are the premises that the calculation model is based on, such as neglecting the dynamics of solvent molecules in the crystal or the deformation of the unit lattice. In particular, as traditional hypotheses and approximations are sometimes dependent on the computational capabilities of time, a bold update of these assumptions and approximations to match the current computational capabilities of current, large-scale, high-speed computers may lead to a major breakthrough.

10.4.1 Domino-Transformation of Isocyanide Gold Complexes

If the transition process between two single crystal polymorphs by structural phase transition is known, it will contribute to the construction of a new molecular design theory, such as control of the phase transition, improvement of the mutating properties, etc. In particular, if two crystal polymorphs are determined, the transition process may be inferred from their comparison. However, in the case of the mechanochromic isocyanide gold complexes described in Sect. 10.3.1, the two crystal structures are quite different and the changes and relationships between the polymorphs require sophisticated analysis techniques to be observed and interpreted accurately.

The metastable Ib of gold isocyanide complexes is triclinic $P\ \bar{1}$, while the most stable IIy is tetragonal $I\bar{4}2d$ (Fig. 10.4) [36]. Therefore, the structural transformation from Ib to IIy cannot be explained by a simple conformational change or molecular reorientation. Ito et al. suggested that the thermal phase transition may proceed via a mechanism similar to the proposed epitaxial mechanism [48]. This phase transition mechanism induced by mechanical stimuli is known as a "domino-like transformation" (Fig. 10.4 in ref. 37). The mechanism is based on the assumption that mechanical and thermal stimuli induce microcracks. The nucleation of the daughter phase (IIy) occurs in the microcracks parallel to the cleavage plane of the parent phase (Ib), and the molecules continuously move (like dominoes) from the opposite side of the microcracks to form the oriented nuclei of the daughter phase. Then, the more stable daughter phase grows inside the metastable parent phase.

In general crystal calculation models, imposing three-dimensional periodic boundary conditions can reasonably reduce the computational complexity, thereby allowing calculations to be performed within the available time. However, to construct a computational model according to this hypothesis, it is necessary to

create a virtual lattice that is large enough to allow cracks to form inside the crystal and perform the calculation under a two-dimensional periodic boundary condition. This can be accomplished using the atomic and molecular level dynamics simulations employed in the field of tribology for material surface phenomena. However, it would be computationally more expensive and large-scale than the three-dimensional periodic boundary conditions.

We departed from the hypothesis of a crack space in the crystal and focused on the thermal phase transition from Ib to IIy that occurs at 64.5–74.9 °C, assuming the repetition of many polymorphic interphase transitions, which have not been observed but are expected to be present. Forming period-free regions in the crystal with our available crystal calculation methods is challenging. Therefore, we developed a crystal dynamics method that can apply vibration vectors as heat by modifying the developed crystal structure optimization method.

We performed lattice-variable crystal dynamics simulations to follow the transformation process from Ib to IIy (Fig. 10.16) and generated a virtual lattice model in which the unit lattice of Ib is extended by a factor of 8 ($2 \times 2 \times 2$), 16 molecules are set to fit in the unit lattice as in IIy, and the space group is set to $P1$ to allow all degrees of freedom. The crystal dynamics simulation results show that following the deformation of the crystal structure along the lattice vibration modes of Ib, the crystal energy ΔE, the unit cell volume %CELL, and the rate of change (%) of the lattice constants a, b, c, α, β, and γ lead to a new polymorph III to appear in the region beyond the initial energy barrier and eventually return to Ib. By repeating the same procedure for other vibrational modes and new polymorphs, we may find stepwise pathways from Ib to IIy via multiple polymorphs (Fig. 10.16). Unfortunately, we have not been able to reach IIy from Ib presently but will publish the details and results of this methodology.

10.4.2 Approach to Organic Superelasticity of Terephthalamide

The organic superelasticity of terephthalamide, which was discovered by Takamizawa et al., is considered a soft crystal because it responds to macroscopic external stimuli. A single crystal phase fixed at one end is subjected to shear forces by pushing in the opposite end. When a shearing force is applied to an α phase with one end fixed by pushing in the opposite end, the intermediate region of the single crystal deforms and another single crystal β phase appears (Fig. 10.17). When the force is unloaded, the single crystal returns to its original α phase. From close observation of the shear surface of the single crystal, it was determined that the β phase gradually appears along the shear plane (Fig. 10.18) [4, 5, 49].

This phenomenon is different from any of the aforementioned soft crystal phenomena. The reason is that the β phase appears stably at room temperature in a shear deformation state, namely a state of continuously applied stress, and the stress

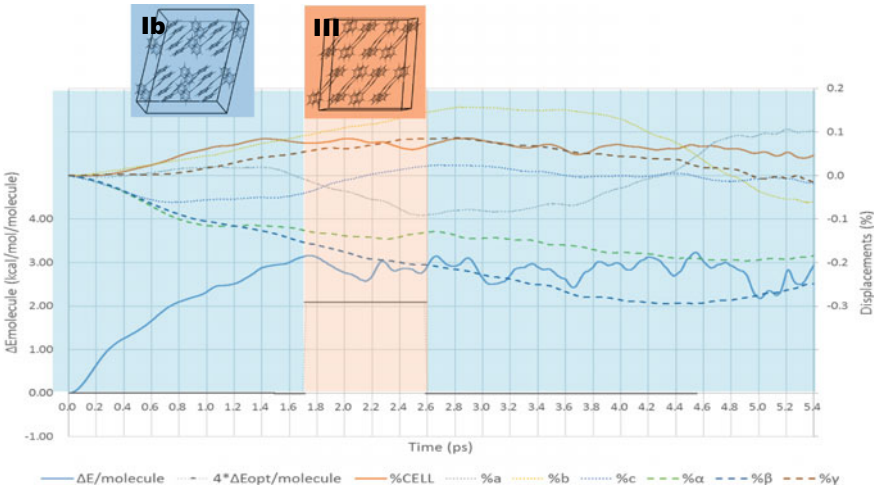

Fig. 10.16 Molecular crystal dynamics for the Ib form of an isocyanide gold complex: Following the changes in the crystal structure along the lattice vibrational modes of Ib, the potential energy (ΔE, bottom blue line), unit cell volume (%CELL, top line), and lattice constant also change, and new polymorphs of III appear in the intermediate region. Repeating this vibrational mode may help to find a transformation pathway to IIy

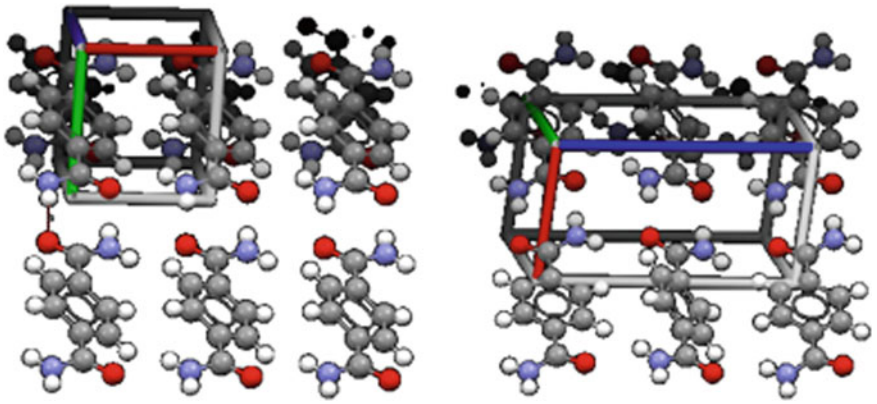

Fig. 10.17 Crystal structures of terephtalamide: α-form (left) and β-form (right) (Reprinted (adapted) with permission from Ref. [50])

inside the crystal in the β phase should have the same magnitude of shear stress applied externally and in the opposite direction [50]. To obtain the crystal structure under high pressure, the crystal enthalpy is defined in the CONFLEX crystal calculations (Eq. (10.9)).

$$H_{\text{crystal}} = E_{\text{crystal}} + pV \tag{10.9}$$

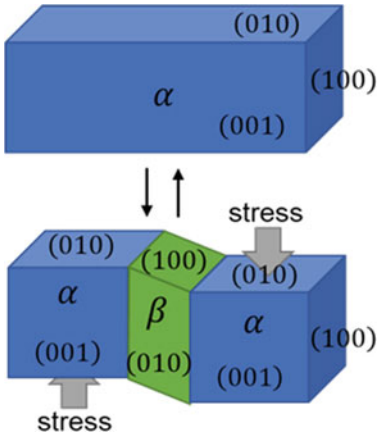

Fig. 10.18 Shear deformation of a terephthalamide crystal (Reprinted (adapted) with permission from Ref. [50])

where p is the pressure and V is the unit lattice volume. The crystal structure at a given pressure p can be obtained by performing structural optimization so that H_{crystal} (Eq. (10.9)) is minimized. Thus, a crystal structure can be obtained at a specified pressure p. Generally, under atmospheric pressure, the pV term can be neglected. However, under very high pressures, the effect of this term on the crystal structure is large.

Pressure, including atmospheric pressure, applies isotropic compressive (expansive) stress to the unit lattice and other stresses are anisotropic, which include tensile, compressive, bending, and torsional besides shear. From the macroscopic mechanical property tests of solid materials, we can deduce the type of deformations. To describe the state under general stresses, including pressure, the microscopic work per unit lattice associated with the microscopic deformation of the crystal structure ΔW is defined by Eq. (10.10):

$$\Delta W(\sigma, \varepsilon V) = \sum_{ij} \sigma_{ij} \varepsilon_{ij} V \tag{10.10}$$

where i and j denote the spatial coordinate axes x, y, and z, σ_{ij} is the stress tensor, and ε_{ij} is the strain tensor. The stress tensor σ_{ij} is decomposed into an isotropic stress term and a traceless (TL, sum of diagonal terms is zero) term, which is a shear stress, as in Eq. (10.11).

$$\sigma_{ij} = \mathrm{p}\delta_{ij} + \mathrm{q}\sigma_{ij}^{\mathrm{TL}} \tag{10.11}$$

The coefficient p corresponds to the pressure and q indicates the magnitude of the shear stress. In addition to shear stress, the traceless term can include volume-invariant vertical and rotational deformations, which can be combined to add various deformation stresses to the crystal structure. Thus, it considers the work performed by the externally applied stresses ΔW. The enthalpy of a crystal, considering the

work done by such externally applied stresses, can be defined as

$$H_{\text{crystal}} = E_{\text{crystal}} + \Delta W(\sigma, \varepsilon V) \tag{10.12}$$

If this equation holds, the crystal structure under external stress can be obtained by optimizing the crystal lattice so that H_{crystal} is minimized.

This methodology was applied to terephthalamide superelastic crystals. To define the difference in the number of molecules between the unit lattice and the disordered phase, the α phase was constructed as a virtual unit lattice (supercell) containing four molecules ($2 \times 2 \times 1$) and the β phase as $1 \times 1 \times 1$. The disordered phase is defined as the phase in which all four molecules have different conformations. Figure 10.19 shows the phase diagram when the crystal structure is optimized for different pressures (isotropic compressive stress) p and anisotropic shear stress q. Although the calculation is not refined, the phase transition from the α to β phase occurs simply by optimizing the crystal structure with a stress q of approximately 0.6. Figure 10.20 also shows the stress–strain diagram. The abscissa is the rate of volume change of the supercell (strain tensor norm) and the ordinate is the applied shear stress q. Similar to the pressure–stress phase diagram described above, the β phase appears at a q of approximately 0.6, and it can be seen that the crystal order is destroyed by applying only a small amount of stress above that value.

Such mechanical properties are used for quality testing performed when solid materials are made into market products and are well established in the field of mechanical engineering as macroscopic simulations, such as continuum approximations and finite element methods. The properties of soft crystals as solid materials are expected to be applied to Micro Electro Mechanical Systems (MEMS) and

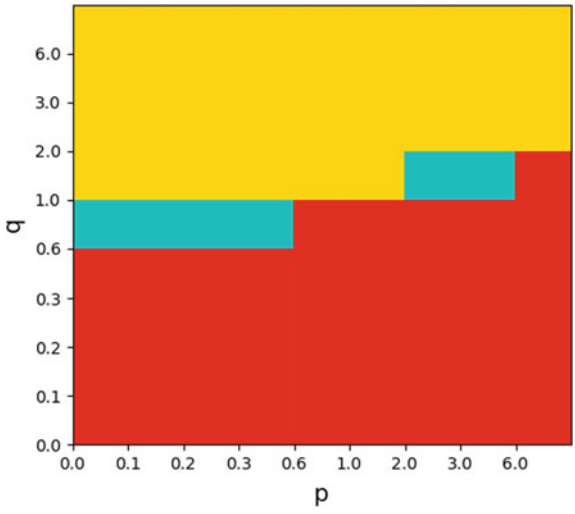

Fig. 10.19 Pressure (p)–stress (q) phase diagram of terephthalamide crystals: α, β, and disordered phases are represented by the red, blue, and yellow areas, respectively (Reprinted (adapted) with permission from Ref. [50])

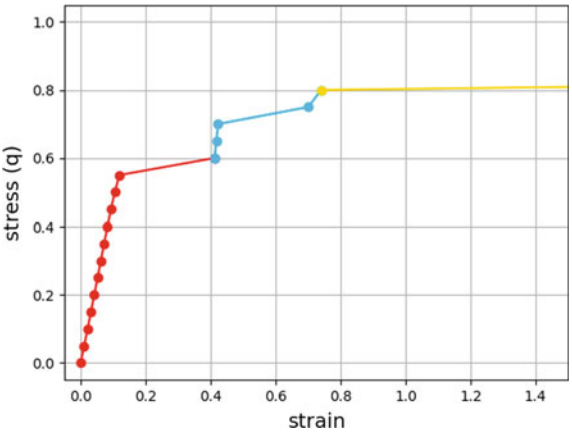

Fig. 10.20 Stress–strain diagram of terephthalamide crystals, where the pressure (p) was fixed at 0.3. α, β, fracture phases are represented by the red, blue, and yellow curves, respectively (Reprinted (adapted) with permission from Ref. [50])

nanomachines. In addition, computational methods for deriving atomistic mechanical properties, such as those presented in this chapter, could become essential in the future.

10.5 Conclusion

In this chapter, we described studies on computational chemistry that are useful for establishing the scientific theory of soft crystals. The contribution of the CCDC crystal structure prediction blind test has led to the improvement of the accuracy of first-principles calculations for molecular crystals. In particular, crystal structures optimized by the DFT-D method under periodic boundary conditions are more accurate than results obtained experimentally. However, the accuracy of the relative crystal energies among many crystal polymorphs, which is characteristic of molecular crystals, is not sufficient even with the DFT-D method, and further improvements are required to make it practically available. It is expected that the seventh blind test, which is now in progress, can predict crystal structures and energies with even higher accuracy. However, the computational cost of first-principles calculations is still high. To determine crystal polymorphs and crystal calculations of large molecules, we can rely on crystal force field calculations based on classical mechanics to accurately evaluate the crystal structure within the available computational time.

With regard to molecular crystals studies using crystal force field calculations, we introduced several collaborative works in which we applied our CONFLEX crystal force field calculations to various soft crystals. For isocyanide gold, Ln, and nickel complexes, we developed new force field parameters around metal ions, which are missing in the crystal force field, to enable crystal structure predictions and crystal dynamics simulations. In the application of the disilane-bridged macrocycle, the

triggering of the thermosalient effect was analyzed in terms of the energy increment associated with the lattice length elongation. For the three-step deformation of luminescent Ln complexes triggered by pyridine vapor spraying, the mechanism of the two-step pyridine-added coordination of pyridine was clarified by devising a computational model.

A common property of many soft crystals is that structural phase transitions, such as single-crystal-to-single-crystal phase transitions, are induced by weak external stimuli, resulting in significant changes in their characteristic properties. It is difficult to analyze all these phenomena by existing computational chemistry methods. Thus, it is necessary to develop new methodologies. In this chapter, we reviewed the crystal dynamics simulations of mechanochromic structural phase transitions in gold isocyanide complexes. Although it has not been clarified whether this phenomenon is epitaxial or multi-step structural phase transition, we believe that crystal dynamics simulation will be an important method to expand its application in the future. A stress-applied crystal structure optimization method for organic superelasticity of terephthalamide, in which the structural phase transition is induced by a continuous external force rather than an instantaneous external stimulus, is presented. This method extends the typical methodology for isotropic stresses, such as pressure, to handle anisotropic stresses. Although quantitative results have not been obtained, the method is expected to be applied to mechanical deformation tests of molecular crystals as solid materials.

In addition to the examples discussed here, various other soft crystals can be analyzed using computational chemistry applications. In particular, computational chemistry is expected to establish the science of soft crystals with many interesting properties, such as the internalization process of small molecules into porous crystals, the deformation mechanism of molecular machines, the properties of organic electronic devices, and anisotropic phonon dispersion analysis. For this, it is necessary to improve the existing methodologies and to further develop new methodologies, as well as to expect the availability of faster and cheaper computers.

This work was supported by Grant-in-Aid for Scientific Research (17H06373, 21K05105) from the Japanese Society for the Promotion of Science.

References

1. Kato M, Ito H, Hasegawa M, Ishii K (2019) Chem Eur J 25:5105–5112
2. Ohba T, Kobayashi A, Chang H-C, Kato M (2013) Dalton Trans 42:5514–5523
3. Ito H, Saito T, Oshima N, Kitamura N, Ishizaka S, Hinatsu Y, Wakeshima M, Kato M, Tsuge K, Sawamura M (2008) J Am Chem Soc 130:10044–10045
4. Takamizawa S, Miyamoto Y (2014) Angew Chem Int Ed 53:6970–6973
5. Takamizawa S, Takasaki Y, Sasaki T, Ozaki N (2018) Nat Commun 9:3984
6. Lommerse JP, Motherwell WD, Ammon HL, Dunitz JD, Gavezzotti A, Hofmann DW, Leusen FJ, Mooij WT, Price SL, Schweizer B, Schmidt MU, van Eijck BP, Verwer P, Williams DE (2000) Acta Crystallogr B 56:697–714

7. Motherwell WD, Ammon HL, Dunitz JD, Dzyabchenko A, Erk P, Gavezzotti A, Hofmann DW, Leusen FJ, Lommerse JP, Mooij WT, Price SL, Scheraga H, Schweizer B, Schmidt MU, van Eijck BP, Verwer P, Williams DE (2002) Acta Crystallogr B 58:647–661
8. Day GM, Motherwell WD, Ammon HL, Boerrigter SX, Della Valle RG, Venuti E, Dzyabchenko A, Dunitz JD, Schweizer B, van Eijck BP, Erk P, Facelli JC, Bazterra VE, Ferraro MB, Hofmann DW, Leusen FJ, Liang C, Pantelides CC, Karamertzanis PG, Price SL, Lewis TC, Nowell H, Torrisi A, Scheraga HA, Arnautova YA, Schmidt MU, Verwer P (2005) Acta Crystallogr B 61:511–527
9. Day GM, Cooper TG, Cruz-Cabeza AJ, Hejczyk KE, Ammon HL, Boerrigter SX, Tan JS, Della Valle RG, Venuti E, Jose J, Gadre SR, Desiraju GR, Thakur TS, van Eijck BP, Facelli JC, Bazterra VE, Ferraro MB, Hofmann DW, Neumann MA, Leusen FJ, Kendrick J, Price SL, Misquitta AJ, Karamertzanis PG, Welch GW, Scheraga HA, Arnautova YA, Schmidt MU, van de Streek J, Wolf AK, Schweizer B (2009) Acta Crystallogr B 65:107–125
10. Bardwell DA, Adjiman CS, Arnautova YA, Bartashevich E, Boerrigter SX, Braun DE, Cruz-Cabeza AJ, Day GM, Della Valle RG, Desiraju GR, van Eijck BP, Facelli JC, Ferraro MB, Grillo D, Habgood M, Hofmann DW, Hofmann F, Jose KV, Karamertzanis PG, Kazantsev AV, Kendrick J, Kuleshova LN, Leusen FJ, Maleev AV, Misquitta AJ, Mohamed S, Needs RJ, Neumann MA, Nikylov D, Orendt AM, Pal R, Pantelides CC, Pickard CJ, Price LS, Price SL, Scheraga HA, van de Streek J, Thakur TS, Tiwari S, Venuti E, Zhitkov IK (2011) Acta Crystallogr B 67:535–551
11. Reilly AM, Cooper RI, Adjiman CS, Bhattacharya S, Boese AD, Brandenburg JG, Bygrave PJ, Bylsma R, Campbell JE, Car R, Case DH, Chadha R, Cole JC, Cosburn K, Cuppen HM, Curtis F, Day GM, DiStasio RA Jr, Dzyabchenko A, van Eijck BP, Elking DM, van den Ende JA, Facelli JC, Ferraro MB, Fusti-Molnar L, Gatsiou CA, Gee TS, de Gelder R, Ghiringhelli LM, Goto H, Grimme S, Guo R, Hofmann DW, Hoja J, Hylton RK, Iuzzolino L, Jankiewicz W, de Jong DT, Kendrick J, de Klerk NJ, Ko HY, Kuleshova LN, Li X, Lohani S, Leusen FJ, Lund AM, Lv J, Ma Y, Marom N, Masunov AE, McCabe P, McMahon DP, Meekes H, Metz MP, Misquitta AJ, Mohamed S, Monserrat B, Needs RJ, Neumann MA, Nyman J, Obata S, Oberhofer H, Oganov AR, Orendt AM, Pagola GI, Pantelides CC, Pickard CJ, Podeszwa R, Price LS, Price SL, Pulido A, Read MG, Reuter K, Schneider E, Schober C, Shields GP, Singh P, Sugden IJ, Szalewicz K, Taylor CR, Tkatchenko A, Tuckerman ME, Vacarro F, Vasileiadis M, Vazquez- Mayagoitia A, Vogt L, Wang Y, Watson RE, de Wijs GA, Yang J, Zhu Q, Groom CR (2016) Acta Crystallogr B Struct Sci Cryst Eng Mater 72:439–459
12. Obata S, Nakayama N, Goto H (2020) Nihon Kessho Gakkaishi 62:260–268 in Japanese
13. Neumann MA (2008) J Phys Chem B 112:9810–9829
14. Burkert U, Allinger NL (1982) Molecular mechanics. American Chemical Society
15. Machida K (1999) Principles of molecular mechanics. Wiley-Kodansha
16. Price SL, Leslie M, Welch GWA, Habgood M, Price LS, Karamertzanis PG, Day GM (2010) Phys Chem Chem Phys 12:8478–8490
17. Marchese Robinson RL, Geatches D, Morris C, Mackenzie R, Maloney AGP, Roberts KJ, Moldovan A, Chow E, Pencheva K, Vatvani DRM (2019) J Chem Inf Model 59:4778–4792
18. Obata S, Goto H (2008) J Comput Chem Jpn 7:151–164 in Japanese
19. Obata S, Goto H (2008) J Comput Aided Chem 9:8–16 in Japanese
20. Obata S, Goto H (2015) AIP Conf Proc 1649:130–134
21. Ishii H, Obata S, Niitsu N, Watanabe S, Goto H, Hirose K, Kobayashi N, Okamoto T, Takeya (2020) Sci Rep 10:2524
22. Goto H, Obata S, Nakayama N, Ohta K (2020) CONFLEX 9. CONFLEX Corporation, Tokyo, Japan
23. Gotō H, Ōsawa E (1989) J Am Chem Soc 111:8950–8951
24. Gotō H, Ōsawa E (1993) J Chem Soc Perkin Trans 2:187–198
25. Halgren TA (1996) J Comput Chem 17:490–519
26. Halgren TA (1996) J Comput Chem 17:520–552
27. Halgren TA (1996) J Comput Chem 17:553–586
28. Halgren TA, Nachbar RB (1996) J Comput Chem 17:587–615

29. Halgren TA (1996) J Comput Chem 17:616–641
30. Halgren TA (1999) J Comput Chem 20:720–729
31. Halgren TA (1999) J Comput Chem 20:730–748
32. Halgren TA (1992) J Am Chem Soc 114:7827–7843
33. Nakanishi H Ed (2005) Yuuki Kesshou Zairyou No Saishin Gijyutsu, CMC Publishing, p 45 in Japanese
34. The Cambridge Crystallographic Data Centre (CCDC) (2022) CSD space group statistics—space group frequency ordering
35. Nakayama N, Obata S, Goto H (2020) Nihon Gazo Gakkaishi 59:308–315 in Japanese
36. Ito H, Muromoto M, Kurenuma S, Ishizaka S, Kitamura N, Sato H, Seki T (2013) Nat Commun 4:2009
37. Seki T, Takamatsu Y, Ito H (2016) J Am Chem Soc 138:6252–6260
38. Nakayama N, Obata S, Hori Y, Goto H, Seki T, Ito H (2018) J Comput Chem Jpn 17:155–157
39. Chisholm JA, Motherwell S (2005) J Appl Cryst 38:228–231
40. Macrae CF, Bruno IJ, Chisholm JA, Edgington PR, McCabe P, Pidcock E, Rodriguez-Monge L, Taylor R, van de Streek J, Wood PA (2008) J Appl Cryst 41:466–470
41. Hasegawa M, Sakurai S, Yamaguchi MA, Iwasawa D, Yajima N, Ogata S, Inazuka Y, Ishii A, Suzuki K (2020) Photochem Photobiol Sci 19:1054–1062
42. Nakayama N, Hijikata M, Ohmagari H, Tanaka H, Inazuka Y, Saito D, Obata S, Ohta K, Kato M, Goto H, Hasegawa M (2021) Bull Chem Soc Jpn 94(94):2973–2981
43. Kar P, Yoshida M, Shigeta Y, Usui A, Kobayashi A, Minamidate T, Matsunaga N, Kato M (2017) Angew Chem Int Ed 56:2345−2349
44. Nomiya K, Nakatani N, Nakayama N, Goto H, Nakagaki M, Sakaki S, Yoshida M, Kato MH (2022) J Phys Chem A 126:7687–7694
45. Omoto K, Nakae T, Nishio M, Yamanoi Y, Kasai H, Nishibori E, Mashimo T, Seki T, Ito H, Nakamura K, Kobayashi N, Nakayama N, Goto H, Nishihara H (2020) J Am Chem Soc 142:12651–12657
46. Nishio M, Shimada M, Omoto K, Nakae T, Maeda H, Miyachi M, Ya-manoi Y, Nishibori E, Nakayama N, Goto H, Matsushita T, Kondo T, Hat-tori M, Jimura K, Hayashi S, Nishihara H (2020) J Phys Chem C 124:17450–17458
47. Ferreira da Rosa PP, Kitagawa Y, Shoji S, Oyama H, Imaeda K, Nakayama N, Fushimi K, Uekusa H, Ueno K, Goto H, Hasegawa Y (2022) Nature Comm 13:3660
48. Herbstein FH (2006) Acta Crystallogr B 62:341–383
49. Mutai T, Sasaki T, Sakamoto S, Yoshikawa I, Houjou H, Takamizawa S (2020) Nat Commun 11:1824
50. Hamada S, Goto H (2021) Nihon Kessho Gakkaishi 63:63–68 (in Japanese)

Open Access This chapter is licensed under the terms of the Creative Commons Attribution 4.0 International License (http://creativecommons.org/licenses/by/4.0/), which permits use, sharing, adaptation, distribution and reproduction in any medium or format, as long as you give appropriate credit to the original author(s) and the source, provide a link to the Creative Commons license and indicate if changes were made.

The images or other third party material in this chapter are included in the chapter's Creative Commons license, unless indicated otherwise in a credit line to the material. If material is not included in the chapter's Creative Commons license and your intended use is not permitted by statutory regulation or exceeds the permitted use, you will need to obtain permission directly from the copyright holder.

Chapter 11
Approach of Electronic Structure Calculations to Crystal

Naoki Nakatani, Jia-Jia Zheng, and Shigeyoshi Sakaki

Abstract Nowadays, the importance of molecular crystals and solids with regular structures is increasing in both basic chemistry and applied fields. However, theoretical studies of those systems based on electronic structure theories have been limited. Although density functional theory (DFT) calculations using generalized gradient approximation type functional under periodic boundary condition is effective for such theoretical studies, we need some improvements for calculating the dispersion interaction and the excited state of crystals. Accordingly, in this chapter, two methods for calculating the electronic structures of molecular crystals are discussed: cluster-model/periodic-model (CM/PM)-combined method and quantum mechanics/periodic-molecular mechanics (QM/periodic-MM) method. In the CM/PM-combined method, an infinite crystal system is calculated by the DFT method under periodic boundary condition, and important moieties, which are represented by CMs, are calculated by either DFT method with hybrid-type functionals or wave function theories such as the Møller–Plesset second-order perturbation theory (MP2), spin-component-scaled-MP2, and coupled-cluster singles and doubles theory with perturbative triples (CCSD(T)). This method is useful for gas adsorption into crystals such as metal–organic frameworks. In the QM/periodic-MM method, an important moiety is calculated using a QM method such as the DFT method with hybrid-type functionals and wave function theories, where the effects of the crystal

N. Nakatani
Department of Chemistry, Tokyo Metropolitan University, Minami-Osawa 1-1, Hachiouji City, Tokyo 192-0397, Japan
e-mail: naokin@tmu.ac.jp

J.-J. Zheng
Laboratory of Theoretical and Computational Nanoscience, CAS Center for Excellence in Nanoscience, National Center for Nanoscience and Technology, Chinese Academy of Sciences, No. 11 Zhong Guan Cun Bei Yi Tiao, Beijing 100190, China
e-mail: zhengjj@nanoctr.cn

S. Sakaki (✉)
Institute for Cell-Material Sciences, Kyoto University, Kyoto-Daigaku-Katsura, Rohm Plaza R312, Kyoto 615-8246, Japan
e-mail: sakaki.shigeyoshi.47e@st.kyoto-u.ac.jp

© The Author(s) 2023

M. Kato and K. Ishii (eds.), *Soft Crystals*, The Materials Research Society Series,
https://doi.org/10.1007/978-981-99-0260-6_11

are incorporated into the QM calculation via the periodic MM method using a classical force field. This method is useful for theoretical studies of excited states and chemical reactions. The applications of these methods in the following processes are described in this chapter: adsorption of gas molecules on metal–organic frameworks, chemical reactions in crystals, and luminescence of the crystals of transition metal complexes. To the best of our knowledge, the theoretical calculations conducted in this chapter show one of the successful approaches of electronic structure theories to molecular crystals, because of the reasonable and practical approximations.

11.1 Introduction

In this section, we initially discuss the current stage of electronic structure theory from the viewpoint of its applications. Geometries of the molecules in the gas phase can be appropriately reproduced via electronic structure calculations. Difference between the relative energies of two compounds can be calculated with chemical accuracy (less than approximately 1 kcal mol^{-1}) at least using sufficiently suitable (nearly complete) basis sets and a high-quality wave function theory (for example, coupled-cluster singles and doubles theory with perturbative triples (CCSD(T)) [1] except for compounds possessing strong non-dynamical electron correlation effects (or static electron correlation effects), such as Cr dimer (Cr_2) and multinuclear Fe complexes with O_2 molecule(s). However, in experimental chemistry, target compounds very often exist in the solution phase. For the theoretical study of a compound and its chemical reaction in the solution phase, incorporation of solvent effects into electronic structure calculations is necessary. In many cases, the polarizable continuum model is used [2]. In this model, the solvent is considered as a continuous dielectric medium, and the electronic structure of the molecule(s) placed in its cavity is evaluated considering the polarization effect of the solvent. Solvent characteristics are represented by the sizes and polarizabilities of solvent molecules. In the reference interaction site model (RISM) [3], the solvent molecule is divided into interaction sites bearing charges, and the distribution of solvent molecules is determined based on statistical mechanics. In the RISM-self-consistent field (SCF) theory (RISM-SCF theory) [4–6], electronic structure of solute molecule is calculated by the quantum mechanics (QM) method taking into account the distribution of solvent molecules obtained by the RISM theory in a self-consistent manner between the electronic structure of the solute and the solvation structure. In the quantum mechanics/molecular mechanics (QM/MM) method, an important moiety is evaluated by the QM method, and steric and electrostatic effects of solvent molecules are taken into account in the QM calculation by representing the solvent molecules using the MM method. Although this method was proposed for theoretical calculations of biological systems such as proteins [7, 8], this method is effective to take into account solvent effects in electronic structure calculations. Thus, using this method, electronic structure calculations involving solvent effects can be performed in an approximate way.

Nowadays, electronic structure calculations of infinite systems, including crystals, with periodic structures are being actively conducted. Typically, the density functional theory (DFT) method with plane-wave basis sets under periodic boundary condition is employed for these calculations. For this type of calculation, several useful programs, for instance, the Vienna ab initio simulation package [9, 10] and Quantum ESPRESSO [11, 12], are already available. The main advantage of this type of computation method is that entire infinite systems can be evaluated by the QM method. Nevertheless, it has some limitations: when the unit cell is very small, hybrid DFT-type functionals and wave function theories can be used; however, when the unit cell is medium to large, the use of the hybrid-type functionals in the DFT calculations becomes difficult. Also, the use of the wave function theories is nearly impossible except for the system with very small unit cell. As most of the systems of interest in chemistry have large unit cells, DFT calculations have been performed using a generalized gradient approximation type (GGA-type) functional because of its low cost; various DFT functionals and their comparisons have been discussed in recent reviews [13, 14]. Although hybrid-type functionals can be used for single-point calculations without structural optimization, the applications of hybrid-type functionals in the geometry optimization of infinite systems with realistic unit cells are limited by their high costs. The GGA-type functional underestimates the activation barriers of chemical reactions and the energy gap between the highest occupied molecular orbital (HOMO) and the lowest unoccupied molecular orbital (LUMO) and overestimates the stabilities of low-spin states compared to high-spin states. Therefore, hybrid or range-separated type functionals are needed in the DFT calculations of molecules [13, 14]. Additionally, it should be noted that the DFT method is not very reliable for describing dispersion interaction and empirical parameters are used to evaluate the dispersion interaction, as described in the Sect. 11.2.1.

Recently, crystals, such as soft crystals and metal–organic frameworks (MOFs), have attracted significant interest [15]. They are considered molecular crystals; therefore, DFT calculations using at least a hybrid-type functional need to be conducted. Excited states and emission spectra of MOFs and soft crystals have been actively investigated experimentally. However, the application of electronic structure calculations under the periodic boundary condition in the calculation of excited states is impeded by the following shortcoming: as the population of molecules in the excited state is substantially smaller than that in the ground state, a unit cell consisting of a few molecules in the excited state and many molecules in the ground state surrounding the molecules in the excited state must be employed. This unit cell is very large for realistic computations of today. Even if we consider a minimal model in which an excited molecule is placed at the center of a cubic box and surrounded by the molecules in the ground state, the unit cell will comprise a total of 27 molecules. In the cases of transition metal complex, the size of such a unit cell becomes considerably large. Therefore, DFT calculations using GGA-type functionals under periodic boundary condition are not very sufficient for theoretical studies of molecular crystals and the use of better method is required.

In this chapter, we outline two methods involving crystal effects for the theoretical studies of molecular crystals, and discuss how to evaluate dispersion interactions and how to use hybrid DFT functional and/or post-Hartree–Fock (post-HF) methods. Then, we have examined the applications of these methods for the electronic structure calculations of molecular crystals. In the first method (namely, cluster-model/periodic-model combined method; abbreviated as CM/PM-combined method hereinafter), an infinite crystal system is evaluated via the DFT method under the periodic boundary condition, and the target moiety is calculated using wave function theories such as second-order Møller–Plesset perturbation theory (MP2), spin-component-scaled (SCS)-MP2, and coupled-cluster singles and doubles theory with perturbative triples (CCSD(T)). In the second method, the unit cell containing the main part under study is evaluated by the QM method, and the crystal effects from other unit cells are included in the calculation using classical MM method under periodic boundary condition. This method is named QM/periodic-MM method hereinafter. The CM/PM-combined method is suitable for the theoretical investigation of chemical events in the ground state and has been applied to the adsorption of gas molecules to MOFs or porous coordination polymers (PCPs). To apply the QM/MM method to a polymer, the problems of how to separate the QM and MM regions and how to connect them must be carefully solved. In contrast, these problems do not exist in the application of the QM/MM method to molecular crystals. Thus, the QM/periodic-MM method is appropriate for the theoretical study of molecular crystals. Particularly, this method is useful for geometry optimization of the transition states and intermediates of chemical reactions and molecules in excited states and evaluation of activation energy, reaction energy, absorption and emission spectra. As an example of the application of the CM/PM-combined method, we have described electronic structure calculations for the adsorption of gas molecules to MOFs/PCPs. Subsequently, as an example of the application of the QM/periodic-MM method, we have reported theoretical studies on the geometry optimization of the crystals of transition metal complexes, changes in the geometries and energies of the crystals of transition metal complexes induced by chemical reactions, and emission spectra of the crystals of transition metal complexes.

11.2 Computational Methods Based on Electronic Structure Theory for Molecular Crystals

For molecular crystals with flexible structures, such as soft crystals, both long-range periodic and short-range intermolecular interactions must be considered in a balanced manner. If the long-range periodic interactions are significantly stronger than the short-range intermolecular interactions, the crystal becomes stiff and inflexible. However, if the long-range periodic interactions are considerably weak, the long-range order is lost and the crystal becomes amorphous. Therefore, in the electronic

structure calculations of soft crystals, both long-range periodic and short-range intermolecular interactions should be appropriately evaluated. Long-range periodic interactions primarily originate from Coulombic interactions and nuclear repulsions, both of which decrease proportionately to the r^{-1} term (where r is the interatomic distance). Short-range interactions are mainly produced by nuclear repulsions and electrostatic, exchange-repulsion, and dispersion interactions, and charge-transfer (CT), and polarization interactions may also be involved, depending on the crystal type. Although electrostatic interactions, including point-charge–point-charge, point-charge–dipole-moment, and dipole-moment–dipole-moment interactions, are respectively correlated with r^{-1}, r^{-2} and r^{-3} terms, exchange-repulsion, dispersion, CT, and polarization interactions are approximately correlated with $\exp(-r)$. Thus, these interactions become important in the short distance case. Estimation of these interactions is difficult in a classical manner and requires quantum chemical calculations. We discuss the CM/PM-combined, QM/periodic-MM, and related methods in the following sections.

11.2.1 Cluster-Model/Periodic-Model Combined (CM/PM-Combined) Method

As abovementioned in Sect. 11.1, the DFT method was employed to calculate the electronic structures of crystals under periodic boundary condition. In this chapter, we have termed this method periodic-DFT. This method facilitates the treatment of periodic interactions of an infinite system in a quantum chemical manner. To the best of our knowledge, periodic-DFT calculations based on the Perdew–Burke–Ernzerhof (PBE) functional [16] with empirical dispersion correction [17, 18] reproduce experimental structures in many cases.

MOFs or PCPs, which are considered a type of molecular crystals, are expected to be applied for the separation, storage, and trapping of gas molecules [19–22]. In the adsorption of gas molecules on MOFs, the gas molecules form non-covalent interactions with the MOFs, and therefore, dispersion interactions are expected to play important roles. Specifically, for MOFs without unsaturated open metal sites, dispersion interactions are very crucial. Simultaneously, electrostatic interactions arising from infinite crystal effects should be appropriately considered in the electronic structure calculations because electrostatic interactions can also contribute to the interaction energies of gas molecules when the gas molecules have dipole and/or quadrupole moments. In the DFT calculations, the dispersion interactions are generally calculated using the empirical parameters proposed by Grimme et al. [17, 18]. Nevertheless, the dispersion interaction should be evaluated according to the electronic structures of the target gas molecule and the MOF. For this purpose, the post-HF methods, such as MP2, SCS-MP2, and CCSD(T), must be employed. However, when the unit cell is composed of several transition metal complexes, the use of post-HF methods in the electronic structure calculations under periodic

boundary condition is extremely difficult and impractical, as abovementioned, owing to the very long computation time and the need of huge work files.

To evaluate the interactions between gas molecules and MOFs with high accuracy, a hybrid approach has been proposed, in which the infinite system and the CM representing the important moiety of MOF are assessed by periodic-DFT and a post-HF method, respectively [23–25]. This method is similar to "our own N-layered integrated molecular orbital and molecular mechanics" (ONIOM) method [26] proposed by Morokuma et al. In this method, the infinite structure of a MOF (abbreviated as "IS") is calculated by period-DFT with the PBE functional [16] using the empirical correction for the dispersion interactions [17, 18] proposed by Grimme et al., and the CM (denoted as "C" in Eqs. 11.1 and 11.2) consisting of crucial moieties of the MOF and the target gas molecule(s) is evaluated using the post-HF methods such as MP2, SCS-MP2, and CCSD(T). For example, the entire MOF system comprising the unit cell shown by Scheme 11.1a was calculated by the periodic-DFT method with empirical dispersion correction, and the interaction between the gas molecules and the important moiety of the MOF shown by Scheme 11.1b was calculated by the post-HF method. In such a case, the binding energy (*BE*) of the gas molecule is represented by Eqs. (11.1) and (11.2):

$$BE(\text{post-HF:PBE} + \text{D}) = BE_{\text{pbc}}^{\text{PBE+D}}(\text{IS}) + \Delta BE^{\text{post-HF}}(\text{C}) \tag{11.1}$$

$$\Delta BE^{\text{post-HF}}(\text{C}) = BE^{\text{post-HF}}(\text{C}) - BE^{\text{PBE+D}}(\text{C}) \tag{11.2}$$

where BE(post-HF:PBE+D) is the binding energy (*BE*) of the gas molecule with the MOF; the subscript "pbc" of *BE* indicates that the calculation was performed under the periodic boundary condition; the superscripts "PBE+D" and "post-HF"

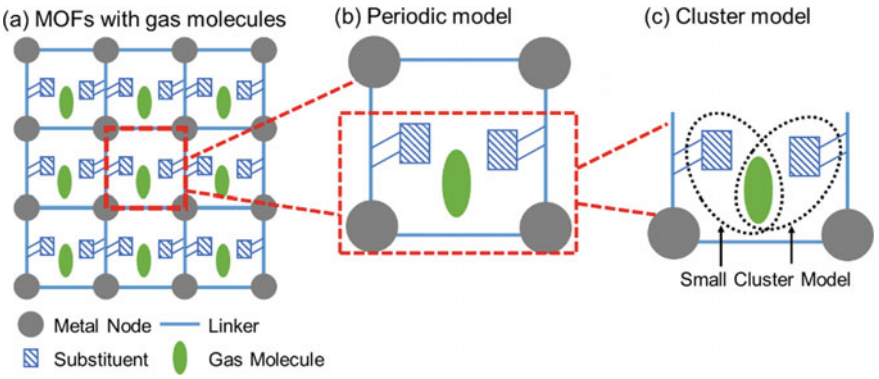

Scheme 11.1 Schematic representation of gas adsorption into MOF **(a)**, Periodic model (one unit cell of MOF with adsorbed gas molecule) for DFT calculation **(b)**, and cluster model for post-Hartree–Fock calculations **(c)**

represent DFT calculation using the PBE functional with dispersion correction and the post-HF calculation, respectively; and $\Delta BE^{\text{post-HF}}(\text{C})$ is the post-HF correction calculated using CM. These equations are essentially the same as those in the case of the ONIOM method. However, there is some difference; in the CM/PM-combined method, the correction term $\Delta BE^{\text{post-HF}}(\text{C})$ is evaluated as the sum of the correction terms calculated by several CMs (Scheme 11.1c), whereas in the two-layered ONIOM method, the correction term $\Delta BE^{\text{post-HF}}(\text{C})$ is evaluated using one model. Thus, the accuracy of the CM/PM-combined method is lower than that of the ONIOM method. However, the accuracy of Eq. 11.2 is adequate when the dispersion interaction is corrected by Eq. 11.2 [27]. As Eq. 11.2 is used to correct the dispersion interaction in the CM/PM-combined method, the accuracy of this method is considered sufficient.

In the CM/PM-combined method, the CM (for instance, it consists of gas molecule and important moiety of MOF) and the entire crystal (for example, it is the infinite MOF system including adsorbed gas molecules) are calculated by a quantum chemical method. The accuracy of this combined method in terms of the enthalpy of adsorption of the gas molecule on the MOF has been discussed in the next section. Nevertheless, this CM/PM-combined method has a limitation because the post-HF calculation of the CM does not include the crystal effects. This problem can be solved using a method, such as the QM/periodic-MM method, that incorporates the crystal effects using MM molecules, which is described in the next section. Despite the abovementioned limitation, the CM/PM-combined method is very useful and powerful for investigating the adsorption of gas molecules to MOFs, as explained in Sect. 11.4.

11.2.2 Quantum Mechanics/Periodic-Molecular Mechanics (QM/Periodic-MM) Method

As abovementioned in Sect. 11.1, the QM/MM method was proposed to calculate the electronic structures of biological systems including metalloenzymes and metalloproteins [7, 8], and many theoretical calculations have been conducted on the biological systems using the QM/MM method [28, 29]. Solvation effects can also be investigated using the QM/MM method. Additionally, the QM/MM method has been applied to crystals [30–36]. Herein, we have outlined a previously reported method [36] and explained similar related methods.

Briefly, in the QM/MM method for molecular crystals, one unit cell is quantum mechanically evaluated, whereas the other unit cells are calculated using a classical force field. In the quantum mechanical calculation of one unit cell, electrostatic interactions and steric effects of other unit cells are considered using the classical force field (MM). In the case of metalloenzymes, the target (that is, the metal and the important moiety of the protein, for instance) differs from other parts (namely, the protein moiety distant from the metal and solvent molecules). However, in molecular crystals, the target unit cell and other unit cells must have the same structure and the

same charge distribution. For this MM part, a periodic boundary condition can be used. The QM/periodic-MM method [36] was developed based on this concept.

Energy of the crystal (E_{Crystal}) is proportional to the sum of the energy $E_{\mathrm{QM}}(\mathrm{I})$ of the unit cell I acquired via the QM method and half of the energy of interaction $E_{\mathrm{QM/MM}}$ between the QM region (I) and the MM region (other unit cells) calculated by the MM method, as shown in Eqs. 11.3 and 11.4:

$$E_{\mathrm{Crystal}} \propto E_{\mathrm{QM}}(\mathrm{I}) + \frac{1}{2} E_{\mathrm{QM/MM}} \tag{11.3}$$

$E_{\mathrm{QM}}(\mathrm{I})$ is evaluated using the wave function of the unit cell I and the Hamiltonian in the gas phase.

$$E_{\mathrm{QM}}(\mathrm{I}) = \left\langle \Phi_{\mathrm{QM}}(\mathrm{I}) \middle| \hat{H}^{\mathrm{gas}} \middle| \Phi_{\mathrm{QM}}^{\mathrm{gas}}(\mathrm{I}) \right\rangle \tag{11.4}$$

where $\hat{H}^{\mathrm{gas}}$ is the Hamiltonian in the gas phase. $E_{\mathrm{QM/MM}}$ is calculated using the electrostatic interactions and the Lennard–Jones (LJ) potentials.

$$E_{\mathrm{QM/MM}} = E_{\mathrm{ES}} + E_{\mathrm{LJ}} \tag{11.5}$$

where the electrostatic energy E_{ES} of the entire crystal is evaluated via the Ewald summation. As indicated in Eq. 11.6, the electrostatic interaction E_{ES} is approximated as the sum of the electrostatic interactions between the point charges of the MM part and the wave function of the QM part in the case of a short distance (named inner region), the electrostatic interactions between the point charges of QM and MM parts in the case of a long distance (named outer region), and the value estimated by the switching function (Eq. 11.7) connecting the short- and long-distance values in the case of intermediate region (named switching region).

$$\begin{aligned} E_{\mathrm{ES}} = & \sum_{a \in \mathrm{MM}} q_a \left[-\sum_{\mu\nu} P_{\mu\nu} \int d\boldsymbol{r} \frac{\chi_\mu(\boldsymbol{r}) \chi_\nu(\boldsymbol{r})}{|\boldsymbol{r}_a - \boldsymbol{r}|} + \sum_{i \in \mathrm{QM}} \frac{Z_i}{|\boldsymbol{r}_a - \boldsymbol{r}_i|} \right] w(\boldsymbol{r}_a) \\ & + \sum_{a \in \mathrm{MM}} q_a \left[\sum_{i \in \mathrm{QM}} \frac{Q_i + Z_i}{|\boldsymbol{r}_a - \boldsymbol{r}_i|} \right] (1 - w(\boldsymbol{r}_a)) \end{aligned} \tag{11.6}$$

$$w(\boldsymbol{r}_a) = \begin{cases} 1 & \text{for inner region (I)} \\ Sw\left(\left| \boldsymbol{r}_0^a - \boldsymbol{r}_0^{\mathrm{QM}} \right|; \boldsymbol{r}_{\min}, \boldsymbol{r}_{\max} \right) & \text{for switching region (III)} \\ 0 & \text{for outer region (II)} \end{cases} \tag{11.7}$$

where $P_{\mu\nu}$ is the density matrix, q_a is the point charge of the a-th site of the MM part, $\chi_\mu(\boldsymbol{r})$ is the atomic orbital of the QM part, Z_i is the nuclear charge of the atom i in the QM part, and $\boldsymbol{r}_a$ represents the coordinates of the a-th site. Accordingly, the Fock matrix element $F_{\mu\nu}^{\mathrm{Crystal}}$ is represented by Eq. 11.8:

$$F_{\mu\nu}^{\text{Crystal}} = F_{\mu\nu}^{\text{gas}} - \frac{1}{2}\Bigg[\sum_{a\in\text{MM}} q_a \int d\boldsymbol{r}\frac{\chi_\mu(\boldsymbol{r})\chi_\nu(\boldsymbol{r})}{|\boldsymbol{r}_a-\boldsymbol{r}|}w(\boldsymbol{r}_a) + \sum_{a\in\text{MM}} Q_{\mu\nu,a}\left\{\sum_{\lambda\sigma}P_{\lambda\sigma}\int d\boldsymbol{r}\frac{\chi_\lambda(\boldsymbol{r})\chi_\sigma(\boldsymbol{r})}{|\boldsymbol{r}_a-\boldsymbol{r}|} - \sum_{i\in\text{QM}}\frac{Z_i}{|\boldsymbol{r}_a-\boldsymbol{r}_i|}\right\}w(\boldsymbol{r}_a) - \sum_{a\in\text{MM}}\sum_{i\in\text{QM}}\left\{q_a\frac{Q_{\mu\nu,i}}{|\boldsymbol{r}_a-\boldsymbol{r}_i|} + Q_{\mu\nu,a}\frac{Q_i+Z_i}{|\boldsymbol{r}_a-\boldsymbol{r}_i|}\right\}(1-w(\boldsymbol{r}_a))\Bigg] \quad (11.8)$$

The calculation is repeated until the charge of each atom in the target QM part becomes the same as the point charge assigned to each atom in the MM part. Equation 11.6 clearly implies that the differentiation of $Q_{\mu\nu,i}$ is necessary for geometry optimization; $Q_{\mu\nu,i} = \langle\chi_\mu(\boldsymbol{r})|\widehat{Q}_i|\chi_\nu(\boldsymbol{r})\rangle$ where $\widehat{Q}_i$ is a population operator acting on atom i. During geometry optimization, we must impose the condition that the geometry of the QM part is the same as that of the MM part. Although geometry optimization of crystals has rarely been performed except for that in one pioneering study [33], it is now feasible via the QM/periodic-MM method here [36].

Geometry optimization is initiated by hypothesizing a QM structure ($\boldsymbol{r}$), charges Q_i, and lattice vectors ($\boldsymbol{t}$). The structure and Q_i distribution of the MM part are created using those of the QM part. The first step is to conduct QM calculations. When the Q_i distribution of the QM part is different from that of the MM part, the QM calculation is repeated by assigning the newly obtained Q_i distribution of the QM part to the MM part. When the Q_i distributions of the QM and MM parts become the same, the next optimization of $\boldsymbol{t}$ is started. During this optimization, the Q_i distributions of the QM and MM parts must be equal. After the optimization of $\boldsymbol{t}$, geometry optimization of the QM part is performed using the new lattice vector $\boldsymbol{t}$. During this geometry optimization, the Q_i distributions and structures of the QM and MM parts must be equal. Thus, geometry optimization calculation must be conducted through three loops.

Accuracy of the QM/MM method for geometry optimization was confirmed by the crystal structures of Pt(IV) and Pt(II) complexes. $[Pt(CN)_4(H_2O)_2]$ is a six-coordinate Pt(IV) complex in which H_2O molecules are coordinated to a Pt atom via an O atom using the lone pair orbital on the O atom (Fig. 11.1a) [37]. $[PtCl_2(NH_3)$(L-glycine)$](H_2O)$ is a four-coordinate Pt(II) complex. Although the H_2O molecule is involved in the crystal structure, it is not coordinated to Pt(II) (Fig. 11.1b). The O atom of the H_2O molecule does not approach Pt(II); instead, the H atom with a δ+ charge unexpectedly approaches Pt(II) [38]. This approaching of H_2O molecules to Pt(II) is surprising because it is generally understood that the negatively charged O atom tends to approach the positively charged Pt(II) atom but the positively charged H atom does not like to approach Pt(II) in $[PtCl_2(NH_3)$(L-glycine)$](H_2O)$. However, this kind of interaction of H_2O molecule has been reported for similar Pt(II) complexes [39, 40]. This type of H-approaching H_2O molecule has also been theoretically discussed for

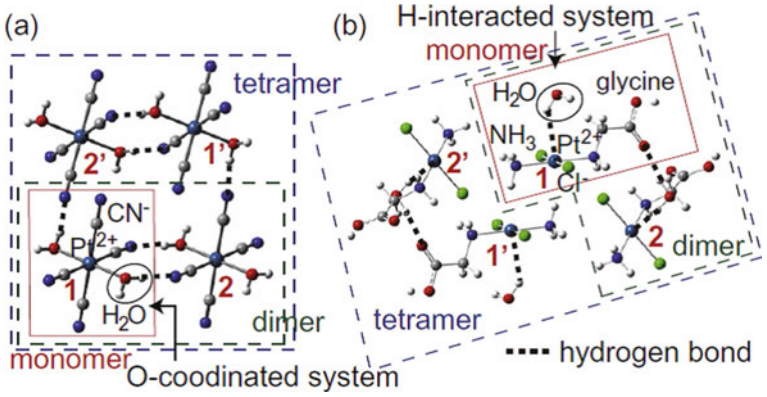

Fig. 11.1 Unit cells of crystals of $[Pt^{IV}(CN)_4(H_2O)_2]$ and $[Pt^{II}Cl_2(NH_3)(L\text{-glycine})]$. Cited from Ref. [36] with permission of Elsevier Co. Ltd.

Pt(II) complexes in aqueous solution [41]. Generally, this type of coordination structure is called a metal–hydrogen (or metal-H) bond [42]. Experimental and theoretical works revealed that the dispersion interaction instead of electrostatic interaction mainly contributes to the metal–H bond [39, 41, 42].

These two Pt complexes were theoretically investigated via QM/periodic-MM calculations, where DFT calculations with the B3LYP functional were utilized for the QM part. In the MM part, the AMBER force field [43] was used for the LJ parameters, except for the Pt atom. Because the LJ parameters for transition metal elements are not very appropriate, these parameters for the Pt atom were determined by fitting the potential energy curve obtained from the LJ parameters to the MP2-calculated curve. The results for $Pt(CN)_4(H_2O)_2$ are provided in Table 11.1a. The Pt–Pt distances acquired via the QM/Periodic-MM calculations, which correspond to the intermolecular distances in the crystal, are in better agreement with the experimental results than those in the case of the calculation of CM composed of four Pt complexes. Particularly, the Pt(1)–Pt(1′) distance significantly improved. The Pt(1)–Pt(2) and Pt(1′)–Pt(2′) distances were not bad even in the CM. This agreement was probably caused by the formation of a hydrogen bond between the H atom of the coordinated H_2O molecule of the Pt(1) complex and the terminal N atom of the CN ligand of the Pt(2) complex and that between the H atom of the Pt(1′) complex and the CN ligand of the Pt(2′) complex. However, this direct bonding interaction was absent between Pt(1) and Pt(1′) complexes, suggesting that the crystal packing and weak intermolecular interactions contribute to determine the Pt(1)–Pt(1′) distance. Consequently, the Pt(1)–Pt(1′) distance could not be appropriately calculated using the CM. The considerably improved Pt(1)–Pt(1′) distance obtained by the QM/periodic-MM method clearly shows that this method is powerful for the geometry optimization of molecular crystals. The lattice constants determined by the QM/periodic-MM method are also in suitable agreement with the experimental results.

Table 11.1 Optimized geometries (in Angstrom) of $Pt(CN)_4(H_2O)$ and $PtCl_2(NH_3)$(L-Glycine)(H_2O) by QM/Periodic-MM method[a]

(a) $Pt(CN)_4(H_2O)_2$					
	Cluster model		QM/Periodic-MM		Exp
R (in A)	2 QM	4 QM	2 QM	4 QM	
Pt(1)–Pt(2)	6.27	6.27	6.30	6.32	6.34
Pt(1)–Pt(1′)	–	7.06	7.60	7.63	7.70
Pt(1)–Pt(2′)	–		6.67	6.68	6.70
|a|, **|b|**, **|c|**	–	–	11.07, 6.41, 11.77	10.81, 6.60, 11.66	10.87, 6.53, 11.71
(b) $PtCl_2(NH_3)$(L-Glycine)					
Pt(1)–Pt(2)	6.27	6.48	6.49	6.71	6.54
Pt(1)–Pt(1′)		4.84	4.20	4.23	4.15
Pt(1)–Pt(2′)		6.75	6.87	6.90	6.83
Pt(1)–Hw	2.69, 3.60	3.09, 3.30	2.94, 3.77	2.97, 3.89	2.89, 3.83
Pt(1)–Ow	3.50	3.56	3.53	3.57	3.62
Pt(2)–Hw	2.39, 3.42	3.11, 4.51	2.87, 3.79	2.84, 3.94	2.89, 3.83
Pt(2)–Ow	3.32	3.67	3.53	3.58	3.62

[a] These values are taken from Ref. [36]

In $[PtCl_2(NH_3)$(L-glycine)$](H_2O)$, H_2O molecules are involved in the crystal structure; however, these H_2O molecules do not directly interact with Pt complexes. In the case of crystal H_2O molecules, the positions and orientations of H_2O molecules are flexible. Therefore, the optimization of these geometrical parameters is usually difficult. As presented in Table 11.2b, the Pt(1)–Pt(1′) distance in the case of the CM exhibits a substantial error; nevertheless, the distance optimized by the QM/periodic-MM method is in appropriate agreement with the experimental results. This appropriate agreement results from the facts that the relative positions of Pt(1) and Pt(1′) complexes depend on the overlap between the doubly occupied d_z^2 orbitals of these complexes, and in such a case, the exchange repulsion, dispersion interaction, short and long-range electrostatic interactions, and packing effects of the crystal play important roles in determining the relative positions of Pt and Pt′ complexes; in the CM case, the long-range electrostatic interaction and the packing effects are not evaluated well. The Pt(1)–H_w distance, where "Hw" represents the H atom of the H_2O molecule, should be the same as the Pt(2)–H_w distance. However, the Pt(1)–H_w distance is significantly different from the Pt(2)–H_w distance in the CM. There are two types of Pt(1)–H_w distances (Table 11.1b), which depend on the orientation of the H_2O molecule. Although these distances are not considerably different from the experimental values in the case of the CM consisting of two Pt complexes, they are significantly different for the CM comprising four Pt complexes. These results imply that the CM does not accurately determine the orientations of H_2O molecules in a crystal. In contrast, the QM/periodic-MM method appropriately reproduces the two

Pt (1)–H_w distances, which indicates that this method can reproduce the positions and orientations of the molecules adsorbed to a molecular crystal.

As above mentioned, using the QM/periodic-MM method, the structures of molecular crystals can be precisely determined. Note that the LJ parameters for transition metal elements are not very suitable and need to be reoptimized to reproduce the potential energy surface; for re-optimization, the potential energy surface obtained by MP2 calculation or DFT calculation including dispersion correction can be used as a reference.

11.2.3 Embedding Method Similar to QM/Periodic-MM Method

Several embedding methods similar to the QM/periodic-MM method have been proposed, where the main part is calculated by the quantum mechanics and the other moiety is represented by MM or density matrix. Herein, we introduced a method to embed the QM region in the distribution of point charges.

The method of embedding QM in point charges has been reported in numerous studies [41–53]. This method is beneficial for investigating chemical species adsorbed on metal oxide surfaces and the chemical events occurring on solid surfaces. Electronic structure calculations of solid surfaces are typically performed under periodic boundary conditions using a slab model (Scheme 11.2a). Nevertheless, the periodic-DFT calculation of the slab model using a hybrid-type functional is challenging because of the long computation time. Furthermore, the post-HF calculation is practically impossible when a unit cell is not very small. Thus, the CM (Scheme 11.2b) must be utilized for DFT calculations with a hybrid-type functional or post-HF calculations. However, a major issue in the application of a simple CM is that the electrostatic fields of other atoms on the surface are not considered in this CM. In metal oxides, each metal atom has a positive charge and each O atom has a negative charge. Therefore, these positive and negative charges must be included in the calculation of the CM. This electronic structure calculation can be conducted using a CM embedded in the distribution of the point charge placed on each atom of the solid surface (Scheme 11.2c). By arranging the slab model in three dimensions (Scheme 11.2d), the electrostatic field of the solid surface can be analytically represented. Thereafter, the electrostatic potential can be included in the Hamiltonian of the electronic structure calculation of CM. This potential is called the periodic electrostatic potential. This method was not employed for geometry optimization, but it was applied to single-point calculations using the geometry optimized by DFT calculations under periodic boundary condition.

Comparison of the interaction energies of Rh_2 supported on Al_2O_3 and $AlPO_4$ surfaces calculated via different methods is presented in Table 11.2. As expected, the interaction energy calculated using the bare CM is significantly different from that evaluated by the slab model, indicating that the calculation without point charges

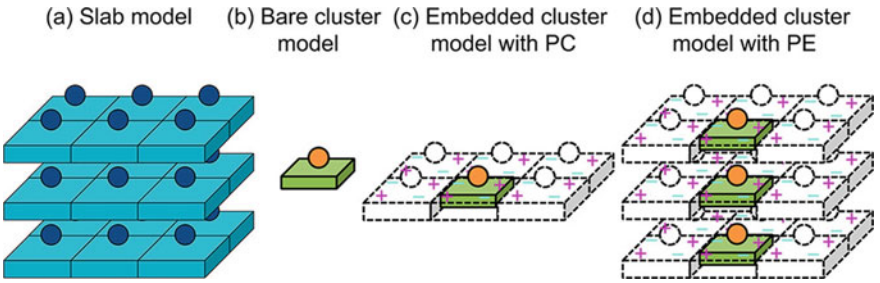

Scheme 11.2 Model for electronic structure calculations of metal clusters supported on the surface of a crystalline solid. This scheme is cited from Ref. [53] with permission of American Chemical Society

results in a large error. When approximately one-thousand point charges were placed on the surface, the error considerably decreased. When one-hundred-thousand point charges were put on the surface, the evaluated interaction energy converged to the value obtained using the periodic electrostatic interaction. In the case of Rh_2 on the $AlPO_4$ surface, the SCF convergence was not obtained in DFT calculations of the bare CM and the CM with a small number of point charges ($<7.55 \times 10^4$). Nevertheless, it is noted that the SCF convergence of the DFT calculation was obtained when a large number of point charges were added to the CM. The final interaction energy was overestimated, compared with that in the case of the slab model. A possible reason for this difference is the difficulty in determining the distribution of point charges in the boundary region of the CM to reproduce the electrostatic potential from an infinite system. Table 11.2 also demonstrates that the interaction energy differs between the GGA-type PBE and hybrid-type B3LYP functionals. These results indicate that the CM and DFT functional should be carefully selected for interaction energy calculation.

11.2.4 Quantum Embedding Theories

In this section, we have introduced two recent advances in embedding methods, which incorporate non-classical interactions between the main and other parts. In the abovementioned CM/PM-combined method, the effect of the ambient environment is not considered in the CM calculation of the main part. In the QM/periodic-MM method described in Sects. 11.2.2 and 11.2.3, the effects of periodic electrostatic interactions on the QM part can be treated within the scope of classical theory; in other words, it cannot capture the quantum interaction between the main part (that is the QM part) and other parts. To solve this problem, a new embedding method, collectively called quantum embedding theory, has recently attracted attention.

At first, we have presented the density functional embedding theory (DFET), which is based on the DFT viewpoint and treats the density of the entire system by

Table 11.2 Interaction energy[a] (in eV unit) of Rh_2 with Al_2O_3 and $AlPO_4$ surfaces

Model	Rh_2/Al_2O_3		$Rh_2/AlPO_4$	
	PBE	B3LYP	PBE	B3LYP
Slab model	−5.44	–	−5.29	–
Bare cluster	−7.18	−9.79	–	−12.36
VSP[b]	−6.44	−6.31	–	−9.53
SP[b]	−6.04	−5.56	–	−7.64
MP[b]	−6.00	−5.52	–	−5.09
LP[b]	−5.99	−5.51	−5.47	−5.35
VLP[b]	−5.99	−5.51	−5.55	−5.43
PE[c]	−6.02	−5.47	−5.71	−5.52

[a] The interaction energy is an intrinsic stabilization energy between Rh_2 and Al_2O_3 (or $AlPO_4$) surfaces, where geometries of Rh_2 and Al_2O_3 (or $AlPO_4$) surfaces are Al_2O_3 (or $AlPO_4$) surfaces are taken to be the same as those in the Rh_2 adsorbed Al_2O_3 (or $AlPO_4$) surfaces

[b] Numbers of point charges are 1060 ($24 \times 28 \times 15$ Å^3) for very small point charge model (VSP), 11,940 ($83 \times 83 \times 15$ Å^3) for small point charge model (SP), 1.079×10^5 ($250 \times 250 \times 15$ Å^3) for medial point charge model (MS), 5.879×10^5 ($590 \times 590 \times 15$ Å^3) for large point charge model (LS), and 1.452×10^6 ($920 \times 920 \times 15$ Å^3) for very large point Those are 2934 ($53 \times 50 \times 15$ Å^3), 8310 ($84 \times 84 \times 15$ Å^3), 7.551×10^4 ($270 \times 250 \times 15$ Å^3), 4.115×10^5 ($620 \times 580 \times 15$ Å)^3, and 1.016×10^6 ($970 \times 920 \times 15$ Å^3) for the $AlPO_4$ system. These values are taken from Ref. [53]

[c] PE represents periodic electrostatic potential proposed in Ref. [53]

dividing it into major and other parts. The original form of the DFET was proposed by Cortona [54, 55] in 1991 and by Wesolowski and Warshel [56] in 1993, and it was primarily developed by Carter et al. [57].

The DFT method is based on the concept that the energy of a system is a function of electron density $\rho(r)$ (denoted as $E_{\mathrm{DF}}[\rho]$). Herein, $E_{\mathrm{DF}}[\rho]$ is divided into three parts, each of which depends on the $\rho(r)$ of the main part $\rho_{\mathrm{A}}(r)$ (represented as $E_{\mathrm{A}}[\rho_{\mathrm{A}}]$), $\rho(r)$ of other parts $\rho_{\mathrm{B}}(r)$ (denoted as $E_{\mathrm{B}}[\rho_{\mathrm{B}}]$), and the interaction energy $\Delta E[\rho_{\mathrm{A}}, \rho_{\mathrm{B}}]$,

$$E_{\mathrm{DF}}[\rho] = E_{\mathrm{A}}[\rho_{\mathrm{A}}] + E_{\mathrm{B}}[\rho_{\mathrm{B}}] + \Delta E[\rho_{\mathrm{A}}, \rho_{\mathrm{B}}]. \tag{11.9}$$

Using this expression, the energy of the main part is replaced by, for example, that of the post-HF method $E_{\mathrm{WF}}[\rho_{\mathrm{A}}]$, which leads to the following expression of embedding energy:

$$E_{\mathrm{WF/DF}}[\rho] = E_{\mathrm{WF}}[\rho_{\mathrm{A}}] + E_{\mathrm{DF}}[\rho] - E_{\mathrm{A}}[\rho_{\mathrm{A}}] + \Delta E[\rho_{\mathrm{A}}, \rho_{\mathrm{B}}]. \tag{11.10}$$

To date, the DFET is substantially similar to the abovementioned CM/PM-combined and ONIOM methods; however, the most notable feature of the DFET is that $E_{\mathrm{WF}}[\rho_{\mathrm{A}}]$ is self-consistently solved under the potential provided by the surrounding part (V_{B}), where V_{B} is defined by Eq. 11.11 according to the concept of

the DFT method.

$$V_{\mathrm{B}} = \frac{\delta \Delta E[\rho_{\mathrm{A}}, \rho_{\mathrm{B}}]}{\delta \rho_{\mathrm{A}}} \tag{11.11}$$

If the Hamiltonian of the main part is defined by $\widehat{H}_{\mathrm{A}}$, the energy of the main part under V_{B} is presented as a solution of the following optimization problem:

$$E_{\mathrm{WF}}[\rho_{\mathrm{A}}] = \min_{\Psi_{\mathrm{A}}} \langle \Psi_{\mathrm{A}} | \widehat{H}_{\mathrm{A}} + V_{\mathrm{B}} | \Psi_{\mathrm{A}} \rangle = \min_{\Psi_{\mathrm{A}} \to \rho_{\mathrm{A}}} \langle \Psi_{\mathrm{A}} | \widehat{H}_{\mathrm{A}} | \Psi_{\mathrm{A}} \rangle. \tag{11.12}$$

In this optimization problem, V_{B} is determined such that the electron density ρ_{A} by the post-HF method for the main part is equal to that by the DFT method for the whole system. Consequently, the quantum interactions from the other parts can be at least qualitatively incorporated into the calculation of the main part.

The DFET, in combination with DFT calculations of periodic systems, enables natural incorporation of the quantum effects in the bulk of solids and periodic electrostatic interactions into the CM calculations of the main part of the system. Numerous applications of DFET to ionic and metal oxide crystals [54, 57] and to molecular adsorption on metal surfaces and metal nanoparticles [58–62] have been reported. Although DFET can be easily applied to molecular crystals, to date, few applications of DFET in the electronic structure calculations of molecular crystals have been reported. The number of applications of DFET in molecular crystals may increase in the future with an increase in the practicality of DFET.

The disadvantage of DFET is that the interaction between the main part and other parts is treated only at the DFT level. Thus, the accuracy of the calculation degrades, when interactions, such as dispersion interactions, charge-transfer interactions, and higher-order electron correlation effects are involved, because dispersion interaction and higher-order electron correlation effect cannot be described well within the theoretical framework of the DFT method, and because charge-transfer interaction between the main part and the remaining is only approximately evaluated in the DFET method. However, similar to the DFT method, DFET is certainly a powerful tool for most molecular systems and materials.

Herein, we have introduced the density matrix embedding theory (DMET) [63, 64], which was proposed by Knizia and Chan in 2012 as a method similar to DFET. DMET is based on the concept of decomposing the wave function of the entire system into many-body basis functions of the main part and bath, which has the same dimensions as the main part;

$$|\Psi\rangle = \sum_i \lambda_i |\alpha_i\rangle |\beta_i\rangle \tag{11.13}$$

where α_i is the i-th state of the main part and β_i is the i-th state of the bath, which couples with α_i. The coefficient λ_i is a positive real number (singular value) related to the weight of the i-th product state. In this case, regardless of the size of the non-main part, the dimension of β_i is equal to that of α_i (that is, states in the main part).

Therefore, the size of a problem can be reduced to at most twice that for the main part.

Nevertheless, to precisely calculate β_i, solving an exact wave function of the whole system is necessary, and thus, β_i can only be obtained approximately in practice. In the original study of DMET, mean-field approximation was utilized to construct the wave function of the entire system, which was used as a reference system to approximately compute β_i. That is, similar to the case of DFET, the many-body wave function can be optimized so that the one-electron $P_{\mu\nu}$ of the main part reproduces the one-particle $P_{\mu\nu}$ of the main part obtained from the mean-field wave function of the entire system.

The advantage of DMET is that it facilitates exact calculations "in principle" regardless of how the main part is defined. Certainly, the exact solution cannot be acquired because of the approximation used in the construction of the reference system; however, even a fragment where the covalent bond is cleaved can be possibly defined, for instance, by considering the two C atoms (the ethylene fragment) of the benzene ring as the main part (Scheme 11.3).

Thus, basically, DMET can be used to treat all quantum interactions in a partitioned manner and has attracted substantial attention as a beneficial tool to treat strongly correlated electron systems, including the two-dimensional Hubbard model of high-T_c superconductivity, in condensed matter physics [63, 65, 66]. DMET in combination with response theory has also been applied to the calculation of bulk spectra of solids and has successfully reproduced the bulk spectra of solids with a few major sites in a demonstrative calculation using the Hubbard model [67]. Recently, DMET has been gradually linked with the molecular orbital method, and the resulting method has been utilized for two-dimensional crystal systems of boron nitride and nickel oxide [68].

DFET and DMET discussed in this section are still under development and have few practical applications. Nevertheless, the non-classical treatment of the interaction between the main part and the other parts had not been considered in the conventional embedding methods. Thus, these quantum embedding methods are expected to be

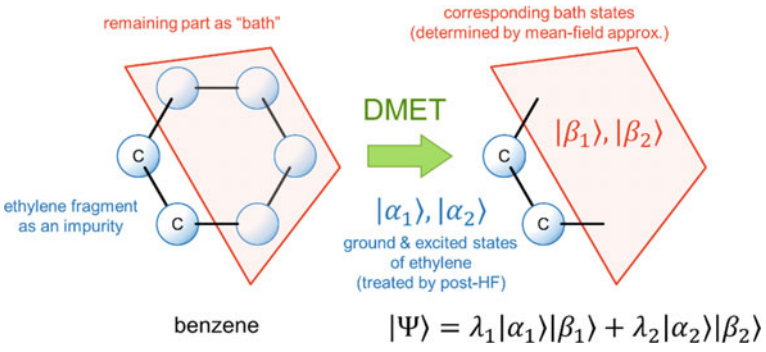

Scheme 11.3 Schematic explanation of the density matrix embedding theory (DMET) in quantum chemistry. An ethylene fragment of the benzene molecule can be accurately solved by considering that the bath size of the DMET wave function is only twice the sizes of the quantum states in the ethylene fragment

promising calculation methods for complex systems including crystals and solid surfaces.

11.3 Application of Cluster Model/Periodic-Model (CM/PM) Combined Method to Metal-Organic-Frameworks (MOFs)

11.3.1 Gas Adsorption and Lateral Interaction

Methane (CH_4), the main component of natural gas, has attracted significant attention as a fuel because of low CO_2 production during its combustion. However, due to the very low boiling point of CH_4, efficient transportation and storage of CH_4 are necessary for its application as a fuel. MOFs can be used for the transportation and storage of CH_4 because of their large specific surface areas [69]. Nevertheless, unlike olefins and other substances, CH_4 weakly interacts with materials due to its nonpolar electronic structure, spherical shape, and the absence of any functional group useful for intermolecular interaction. To effectively adsorb CH_4 to MOFs, knowledge of the strength and character of the interaction of CH_4 with MOFs and the mechanism of adsorption of CH_4 to MOFs is required. For this purpose, a theoretical study with the correct estimation of the dispersion interaction is necessary. This is true because CH_4 does not have any functional groups that can interact with transition metal complexes and the dispersion interaction seems to play important roles in the interaction of CH_4 with other materials.

MOFs, for example, CPO-27-Mg and CPO-27-Ni, consisting of 2,5-dihydroxyterephthalate (hdtp) and divalent metal ions demonstrate high adsorption performances for CH_4 [70]. Sauer et al. theoretically investigated the adsorption of CH_4 to CPO-27-Mg [23]. Considering the importance of the dispersion interaction, they used periodic-DFT for a whole infinite system and the post-HF method for CMs, as discussed in Sect. 11.2.1. Neutron diffraction results reveal that CPO-27-Mg has a honeycomb-like structure with large one-dimensional pores of 11–12 Å diameter (Fig. 11.2a). There are two types of CH_4 adsorption sites in CPO-27-Mg:Mg^{2+} site (denoted as Mg-site) and linker site (that is, hdtp ligand site, abbreviated as L-site) (Fig. 11.2b). In addition to these two sites, the vacant space above these sites, which is called the second-layer site (denoted as 2'nd L-site), can be useful for CH_4 adsorption. To calculate the *BE*s of CH_4 molecules at these sites on CPO-27-Mg, periodic-DFT calculations using the PBE+D functional were performed as the first step, followed by correction at the post-HF level with MP2 calculations using the CMs shown in Fig. 11.2c, d and CCSD(T) calculations using the smaller CM shown in Fig. 11.2e. The calculations indicated that totally six CH_4 molecules were adsorbed (one CH_4 molecule per site) on the Mg-, L-, and 2'nd L-sites in one unit cell (Fig. 11.2b) comprising six Mg-, L-, and 2'nd L-sites.

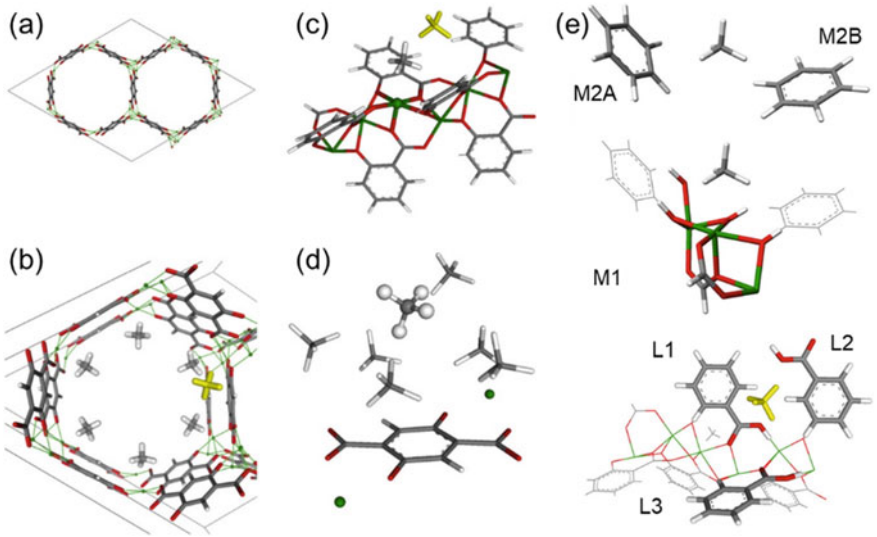

Fig. 11.2 Model systems used in the calculations. Conventional unit cell of CPO-27-Mg viewed along the c direction **(a)**, part of the MOF with six CH_4 molecules at Mg-site and one (yellow) at a linker (L) site **(b)**, cluster model **6B** adopted for MP2 calculations for CH_4 adsorption on the Mg- and L-sites **(c)**, cluster model **Mg_2dhtp** adopted for MP2 calculations **(d)**, where CH_4 adsorption occurs on the second layer site, cluster models adopted for CCSD(T) calculations for CH_4 adsorption on the Mg- and L-sites **(e)**. Cited from Ref. [23] with permission of the American Chemical Society

Table 11.3 presents the adsorption energies of CH_4 molecules at the three sites of CPO-27-Mg calculated by several methods. At the Mg-site, the periodic-DFT-calculated *BE* of the infinite model was slightly different from the DFT-calculated *BE* of the CM (**6B**, Fig. 11.2c). Corrections at the MP2 and CCSD(T) levels using the CMs were also small. At the L-site, the *BE* of the CM (**6B**) was different from the periodic-DFT-calculated *BE* by 5.2 kJ mol^{-1}. Additionally, the *BE*s calculated for the CM by the DFT and MP2 methods differed by 1.3 kJ mol^{-1}. At the 2'nd L-site, the *BE* of the CM (**Mg_2dhtp**, Fig. 11.2d) and the periodic-DFT-calculated *BE* differed by 3.1 kJ mol^{-1}. The *BE* obtained by the periodic-DFT calculations using the PBE+D functional increased in the following order: 2'nd L-site $\leq$ L-site < Mg-site; this trend was the same as that of the *BE* corrected by the post-HF calculations. However, the difference between the *BE*s at the 2'nd L- and L-sites increased to 3.2 kJ mol^{-1} upon correction by the post-HF calculations. This implies that the post-HF correction increases the *BE* at the L-site as compared to that at the 2'nd L-site, suggesting the need for the correct evaluation of dispersion interactions at these sites. This seems reasonable because the dispersion interaction substantially contributes to the *BE*s at these sites. The computational result demonstrating that the adsorption energy at the Mg site is the largest is consistent with the general understanding that metal ions exhibit strong binding interactions with gas molecules. Moreover, the

Table 11.3 Binding energy (in kJ mol^{-1}) of CH_4 with CPO-27-Mg at different sites calculated with different methods on periodic PBE+D structures and cluster models cut out from these periodic PBE+D structures

	Mg-site			L-site			2'nd L-site		
	6B[a]	pbc[b]	LR[c]	**6B**[a]	pbc[b]	LR[c]	**Mg_2dhtp**[a]	pbc[b]	LR[c]
BE^{PBE+D}	−27.1	−27.1	0.0	−12.8	−18.0	−5.2	−14.6	−17.7	−3.1
$BE^{MP2:PBE+D}$	−28.3			−14.1			−10.8		
$BE^{Final\ d}$	−27.8			−18.3			−15.1		

[a] **6B** represents a cluster model for CH_4 adsorption at the Mg^{2+} and L sites (Fig. 11.2c); **Mg_2dhtp** represents a cluster model (Fig. 11.2d) for CH_4 adsorption at the second layer site

[b] DFT calculation under periodic boundary conditions

[c] Long-range correction defined by the difference in binding energy between periodic and cluster models

[d] Binding energy estimated using the PM/CM-Combined method with the MP2:PBE+D with ΔCCSD(T) correction. These values are taken from Ref. [23]

*BE*s determined by the dispersion (D) part of the PBE+D functional are considerably larger than those evaluated by the PBE functional for all the three sites, indicating that the dispersion interaction significantly contributes to the adsorption energy. The large *BE* at the Mg-site and small *BE*s at the L- and 2'nd L-sites imply that CH_4 initially adsorbs on the Mg-site of CPO-27-Mg followed by on the L- and 2'nd L-sites.

Because a large number of CH_4 molecules are adsorbed in one unit cell, the intermolecular interactions between CH_4 molecules (termed the lateral interaction in Ref. [23]) are expected to affect the adsorption energy and enthalpy. Thus, in the theoretical study, the interaction energies between two CH_4 molecules in the gas phase and between two CH_4 molecules adsorbed on different sites of CPO-27-Mg were compared. In the gas phase, the distance between two CH_4 molecules was optimized to be 3.64 Å by MP2/aug-cc-pVTZ, which was moderately smaller than that optimized by PBE+D (3.82 Å). The CH_4–CH_4 intermolecular interaction energy calculated by CCSD(T)/aug-cc-pVTZ was −1.7 and −2.3 kJ mol^{-1} at these distances, respectively. When all six Mg-sites of this MOF are occupied by CH_4 molecules, the distances between CH_4 molecules on two adjacent Mg-sites are 5.17 (a/b direction) and 6.89 Å (c direction). As the distance between CH_4 molecules adsorbed on these sites is slightly longer than that in the gas phase, the interaction energies of CH_4 molecules become weaker (−0.5 kJ mol^{-1}). The interaction energies of the two CH_4 molecules in the gas phase and the two CH_4 molecules adsorbed on the Mg- and L-sites (−1.7 kJ mol^{-1}) are comparable. The distances and interaction energies between the CH_4 molecules adsorbed on adjacent L-sites are 4.44 Å and −1.2 kJ mol^{-1}, respectively. Because the adsorbed CH_4 molecules are adjacent to other CH_4 molecules, the contributions of the lateral interaction energy to the adsorption energies of CH_4 molecules at the Mg- and L-sites are −2.1 and −2.7 kJ mol^{-1}, respectively. These values indicate that the effect of lateral interaction cannot be neglected in the calculation of adsorption isotherm.

The adsorption energies of CH_4 at the Mg-, L-, and 2'nd L-sites and the enthalpy change of CH_4 adsorption can be evaluated using Eq. 11.14.

$$\frac{1}{6}(CH_4)_{6n}/MOF + CH_4 \rightarrow \frac{1}{6}(CH_4)_{6n+6}/MOF \tag{11.14}$$

The thermodynamic quantities of CH_4 adsorption calculated by the DFT method with corrections by MP2 and CCSD(T) calculations are presented in Table 11.4. The CH_4 molecule in the gas phase has six degrees of freedom for translational and rotational movements. In contrast, the movements of CH_4 molecule adsorbed to MOFs with respect to the adsorption site is described as oscillations with six low frequencies. However, the adsorbed CH_4 molecule may retain the rotational degrees of freedom because of the weak adsorption interaction, whereas the translational degrees of freedom are lost. Table 11.4 provides a comparison between the results obtained via these two different calculations; in the former one, the six degrees of freedom are completely lost, and in the latter one, the three rotational degrees of freedom are retained. Note that not only the entropy, but also the zero-point energy (ZPE) and thermal energy (E_{therm}) vary with the change in the number of degrees of freedom. Consequently, the Gibbs energy change (ΔG) for adsorption becomes more negative by approximately 4 kJ mol^{-1} when the rotational degrees of freedom are retained as compared to the case when they are lost. Using these changes in the thermodynamic quantities, the adsorption isotherm for CH_4 to CPO-27-Mg was calculated utilizing the multi-site Langmuir equation (Eq. 11.15):

$$\theta = \sum_{\text{site}} K_{\text{site}} P \Big/ (1 + K_{\text{site}} P) \tag{11.15}$$

where θ and P are the coverage and pressure, respectively, and K is the equilibrium constant for the adsorption of CH_4 at a site of CPO-27-Mg.

As shown by the dotted line in Fig. 11.3, if the degrees of freedom of the adsorbed CH_4 molecule are completely frozen (that is, all translational and rotational degrees of freedom are changed to vibrational degrees of freedom), the adsorption amount of CH_4 is significantly underestimated. If we consider that three rotational degrees of

Table 11.4 Adsorption enthalpy change, (ΔH) and zero-point energy change (ZPE), thermal energy change (ΔE_{therm}) and adsorption entropy term ($T\Delta S$) calculated for CH_4 adsorption at different sites using the PM/CM-Combined Method (all in kJ mol^{-1} at 179 K)

Site	3 Rotational and 3 vibrational degrees of freedom					6 Vibrational degrees of freedom				
	ΔH	ΔE_{ZPE}	ΔE_{therm}	$T\Delta S$	ΔG	ΔH	ΔE_{ZPE}	ΔE_{therm}	$T\Delta S$	ΔG
Mg	−26.7	2.0	0.6	−18.5	−8.2	−24.1	4.2	1.0	−19.8	−4.3
L	−17.5	1.4	0.9	−17.1	−0.4	−14.9	3.6	1.3	−18.6	+3.7
2'nd L	−13.6	2.6	0.4	−18.6	+5.0	−10.8	5.2	0.6	−20.1	+9.3

These values are taken from Ref. [23]

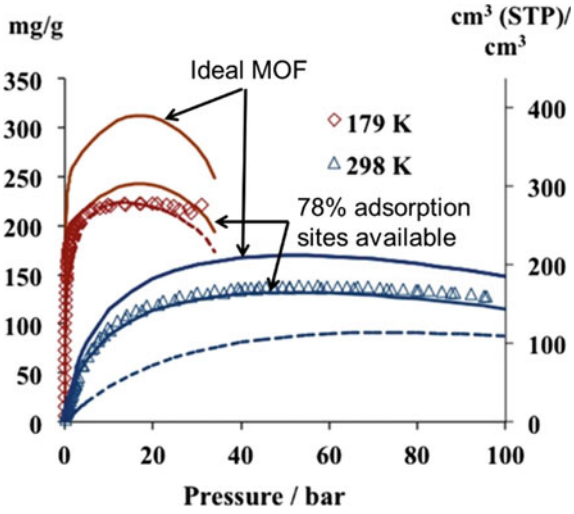

Fig. 11.3 Calculated excess adsorption isotherms for CH_4 adsorption in CPO-27-Mg for which experimentally determined availability (78%) of adsorption sites is assumed. Data points are experimentally determined amounts of adsorbed CH_4. Dashed lines: isotherms for adsorbed CH_4 with six vibrational motions of adsorbed CH_4 molecule. Solid lines: isotherm calculated with three rotational degrees of freedom for adsorbed CH_4 molecule. This figure is cited from Ref. [23] with permission of American Chemical Society

freedom remain in the adsorbed CH_4 molecule, the calculated adsorption amount of CH_4 is higher than the experimental value, as indicated by the solid line in Fig. 11.3. This calculation is for the case where all the sites of MOFs are available for the adsorption of CH_4 molecules (denoted as ideal MOF; solid line). Nevertheless, the experimentally determined availability of the adsorption sites of CPO-27-Mg is approximately 78%. Based on this availability, the calculated adsorption amount of CH_4 is in appropriate agreement with the experimental data acquired at both 179 and 298 K.

Similarly, the adsorptions of CO and N_2 molecules on CPO-27-Mg have been theoretically investigated, and the adsorption isotherms have been calculated [24].

In conclusion, via the periodic-DFT calculation of the entire infinite system with post-HF correction using the cluster model the interaction between the adsorption sites of MOFs and the adsorbed gas molecules can be accurately evaluated. This method is expected to be a powerful tool for analyzing and understanding the gas adsorption behaviors of MOFs.

11.3.2 Gas Adsorption to Flexible MOF with Gate-Opening Mechanism

Flexible MOFs are a type of soft crystals. The flexibilities of MOFs were predicted by Kitagawa et al. in 1998 [71] and experimentally reported in 2002 [72] by the same group. Thereafter, many efforts have been devoted to creating flexible MOFs and developing their applications. Gate-opening adsorption of gas molecules is one of the characteristic features of flexible MOFs, in which structural transformations induced by adsorbed gas molecules accelerate the subsequent adsorption of gas molecules. This is contrary to our intuitive expectation that adsorbed gas molecules generally suppress the successive adsorption of gas molecules. Interestingly, a unique sigmoidal isotherm has been observed for the gate-opening adsorption of gas molecules, which is different from the typical Langmuir-type isotherm. Various theoretical approaches have been applied to the adsorption of gas molecules to flexible MOFs to understand the dynamic behaviours of flexible MOFs and the sigmoidal adsorption isotherm at the molecular level [73–76]. However, precise knowledge of the gate-opening adsorption mechanism is limited.

In a recent theoretical study [25], the CM/PM-combined method (Sect. 11.2.1) was applied to the gate-opening adsorption of gas molecules to a flexible MOF to elucidate the characteristic features of gate-opening gas adsorption and the origin of the sigmoidal adsorption isotherm. As examples, CO_2 adsorptions to $[Fe(ppt)_2]_n$ (**PCP-N**, Hppt = 3-(2-pyrazinyl)-5-(4-pyridyl)-1,2,4-triazole) and its isostructural analogue $[Fe(dpt)_2]_n$ (**PCP-C**, Hdpt = 3-(2-pyridinyl)-5-(4-pyridyl)-1,2,4-triazole) [77] were investigated. Although these two MOFs have similar structures (Fig. 11.4a, b), they exhibit completely different adsorption features (Fig. 11.4c), as summarized below: (i) gate-opening CO_2 adsorption occurs in the case of **PCP-N**, (ii) CO_2 adsorption to **PCP-N** takes place with a sigmoidal adsorption isotherm, and (iii) non-gate-opening CO_2 adsorption with the Langmuir-type isotherm occurs in the case of **PCP-C**.

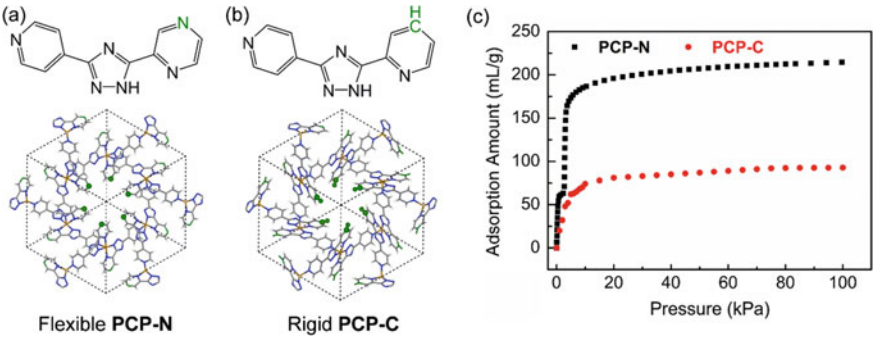

Fig. 11.4 Experimental crystal structures of flexible MOF **PCP-N** (**a**), rigid MOF **PCP-C** (**b**), and adsorption isotherms of **PCP-N** and **PCP-C** at 195 K (**c**). Cited from Refs. [25, 77] with permission of the American Chemical Society

Figure 11.5 depicts one unit cell of the periodic structure of **PCP-N** and the cluster models (CMs) employed in the study. Single-crystal X-ray diffraction study reported that CO_2 adsorption occurred at three different sites: a large cage (site I), a small aperture next to site I (site II), and a small pore around Fe^{2+} (site III) (Fig. 11.5a) [77]. The positions and orientations of CO_2 molecules in one unit cell could not be clearly observed experimentally. Therefore, their positions and orientations were refined by periodic-DFT calculations using plane-wave basis sets. The number of adsorbed CO_2 molecules was calculated to be six, six, and three for sites I, II, and III, respectively. *BE*s of the CO_2 molecule at these sites of **PCP-N** were evaluated using periodic-DFT with the PBE functional [16], where the Grimme's "D3" [17, 18] dispersion correction was used. Then, the post-HF correction at the SCS-MP2 level was performed using the CMs shown in Fig. 11.5b–d (CM^A, CM^B, and CM^C for sites I, II, and III, respectively). The geometries of the CMs were obtained from the PBE-D3-optimized infinite system (IS), where the dangling bonds of CMs were capped by H atoms. Subsequently, the CCSD(T) correction was conducted using the smaller CMs (SCMs) such as $SCM^{A1–A18}$, $SCM^{B1–B7}$, and $SCM^{C1–C4}$ (Fig. 11.5e–g).

Table 11.5 presents a comparison between the *BE*s of CO_2 on the different sites of **PCP-N** calculated by periodic-DFT and CM/PM-combined methods. The *BE* decreases in the order site I > site III > site II in both the PBE-D3 calculations of the infinite (IS) system and the CM/PM-combined calculations. The *BE*s calculated using these two methods were slightly different; apparently, the PBE-D3 overestimated the *BE*s (Table 11.5a), whereas the SCS-MP2 correction underestimated the *BE*s.

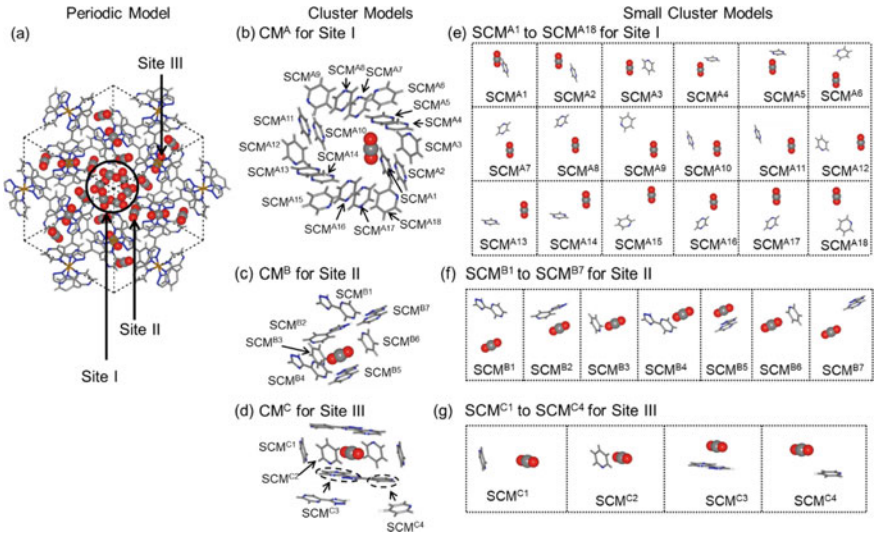

Fig. 11.5 Periodic model of MOF with adsorbed CO_2 molecules at three different sites (**a**), cluster models used in SCS-MP2 correction (**b–d**) and small cluster models (**e**) used in CCSD(T) correction for CO_2 adsorptions at sites I, II, and III, respectively. Cited from Ref. [25] with permission of the American Chemical Society

Table 11.5 Comparison between CO_2 binding energy (BE, kcal mol^{-1}) with **PCP-N** at different sites calculated by periodic DFT and hybrid methods

(a) Comparison among sites I, II, and III when one CO_2 molecule is adsorbed

	Site I	Site II	Site III
$BE^{\text{SCS-MP2:PBE-D3}} + \Delta\text{CCSD(T)}$	–6.51	–2.30	–4.52
$BE^{\text{SCS-MP2:PBE-D3}}$	–5.41	–1.21	–3.16
$BE^{\text{PBE-D3}}$	–7.37	–2.94	–4.03

(b) Binding energy (BE, kcal mol^{-1}) and adsorption enthalpy (ΔH) of CO_2 at the sites I of **PCP-N** depending on the number of adsorbed CO_2 molecules

Number (n) of CO_2 molecule	1	2	3	4	5	6
$BE^{\text{SCS-MP2:PBE-D3}}$[a]	–5.41	–5.65	–5.71	–5.92	–6.01	–6.10
$E_{\text{DEF}}^{\text{PBE-D3}}$[b]	0.35	0.24	0.23	0.21	0.20	0.17
$E_{\text{INT}}^{\text{SCS-MP2:PBE-D3}}$(H-G)[c]	–5.75	–5.68	–5.44	–5.44	–5.36	–5.21
$E_{\text{INT}}^{\text{SCS-MP2}}$(G-G)[c]	0.00	–0.13	–0.51	–0.68	–0.85	–1.05
$\Delta H^{\text{PBE-D3}}$	–6.53	–6.90	–7.23	–7.54	–7.79	–8.04
$\Delta H^{\text{SCS-MP2:PBE-D3}}$	–4.57	–4.81	–4.87	–5.09	–5.18	–5.20
$\Delta H^{\text{SCS-MP2:PBE-D3}}+\Delta\text{BE}^{\text{CCSD(T)}}$	–5.67	–5.97	–6.18	–6.46	–6.67	–6.89

[a] $\text{BE}^{\text{SCS-MP2:PBE-D3}}$ represents average CO_2 binding energy at site I, which is defined by $\text{BE}^{\text{SCS-MP2:PBE-D3}} = [E(\text{PCP} \cdot (n)\ CO_2) - E(\text{PCP})]/n - E(CO_2)$

[b] $E_{\text{DEF}}^{\text{PBE-D3}}$ represents average crystal deformation energy of **PCP-N** per one CO_2 molecule induced by CO_2 adsorption at site I

[c] $E_{\text{INT}}^{\text{SCS-MP2:PBE-D3}}$(H-G) and $E_{\text{INT}}^{\text{SCS-MP2}}$(G-G) represent stabilization energy between deformed CO_2 and **PCP-N** and between CO_2 molecules. These values are taken from Ref. [25]

However, the underestimation of BEs by the SCS-MP2 calculation was moderately overcome by the CCSD(T) correction. These results demonstrate that the post-HF correction using SCS-MP2 and CCSD(T) is needed to quantitatively calculate the BEs of the gas molecules adsorbed to MOFs.

Herein, we have compared the calculated ΔH_{ads} values with the experimental values. The ΔH_{ads} value was experimentally evaluated to be -5.71 to -6.45 kcal mol^{-1} for the adsorption of one to four CO_2 molecules at site I. As presented in Table 11.5b, the $\Delta H^{\text{PBE-D3}}$ value is larger than the experimental value, and $\Delta H^{\text{SCS-MP2:PBE-D3}}$ is smaller than the experimental value; However, the CCSD(T):SCS-MP2 corrected value, $\Delta H^{\text{SCS-MP2:PBE-D3}} + \Delta BE^{\text{CCSD(T)}}$, is in agreement with the experimental value. This comparison clearly shows that the CP/PM-combined method is effective for calculating ΔH_{ads} and a post-HF correction is required.

The results in Table 11.5a indicate that CO_2 initially adsorbs on site I followed by on sites II and III. In the case of continuous CO_2 adsorption on site I, the BE gradually increased from -5.41 to -6.10 kcal mol^{-1} at the SCS-MP2:PBE-D3 level with an increase in the number of adsorbed CO_2 molecules from one to six (Table 11.5b). The interaction energy E_{INT}(H–G) between CO_2 and **PCP-N** slightly changed with

an increase in the number of adsorbed CO_2 molecules from one to six, where G and H represent a guest molecule (gas molecule) and a host system (MOF), respectively. However, the CO_2-CO_2 interaction energy E_{INT}(G–G) slowly increased (became more negative) from 0.0 to -1.05 kcal mol^{-1}. Additionally, the framework deformation energy E_{DEF} per one CO_2 molecule gradually decreased from 0.35 to 0.17 kcal mol^{-1} with an increase in the number of adsorbed CO_2 molecules from one to six. Consequently, the *BE* per CO_2 molecule at site I increased with an increase in the number of adsorbed CO_2 molecules.

Because a total of fifteen CO_2 molecules were experimentally observed in **PCP-N**, theoretical study investigated if CO_2 molecules further adsorbed on **PCP-N** after site I was completely occupied by six CO_2 molecules. Notably, the *BE* of the seventh CO_2 molecule was positive (repulsive) at site II and very small at site III (Table 11.6), suggesting that the seventh CO_2 molecule could not adsorb on sites II and III when site I was occupied by six CO_2 molecules. This is reasonable because the six CO_2 molecules at site I suppress the geometric deformations of sites II and III, which are required for CO_2 adsorption at sites II and III. However, the *BE*s increased (that is, became more negative) from 1.20 to –4.77 kcal mol^{-1} at site II and from –0.62 to –5.26 kcal mol^{-1} at site III with an increase in the number of adsorbed CO_2 molecules from one to six at site II and from one to three at site III. This increase in the *BE* is rational because E_{DEF} per one CO_2 molecule considerably decreases with an increase in the number of adsorbed CO_2 molecules, whereas E_{INT} per CO_2 molecule slightly changes (E_{DEF} and E_{INT} are defined in footnotes b and c of Table 11.5). Therefore, the sum of the *BE*s of the six CO_2 molecules at site II and those of the three CO_2 molecules at site III becomes negative. These results show that one CO_2 molecule cannot adsorb at sites II and III when site I is occupied by six CO_2 molecules, but totally nine (six + three) CO_2 molecules can simultaneously adsorb at sites II and III even when the site I is occupied by six CO_2 molecules. Note that the *BE*s of CO_2 molecules at sites II and III were similar, strongly suggesting the simultaneous adsorption of a total of nine CO_2 molecules occurs on sites II and III. This phenomenon corresponds to the gate-opening adsorption mechanism, as discussed below.

Summarising the abovementioned results, the equilibrium equations for CO_2 adsorption are presented as follows:

PCP-N:

$$\text{At site I:}\quad CO_2 + \textbf{PCP-N}\cdot(CO_2)_n \rightleftarrows \textbf{PCP-N}\cdot(CO_2)_{n+1} \quad n = 0{-}5, \tag{11.16}$$

$$\text{At sites II and III:}\quad 9\,CO_2 + \textbf{PCP-N}\cdot(CO_2)_6 \rightleftarrows \textbf{PCP-N}\cdot(CO_2)_{15} \tag{11.17}$$

The equilibrium constant K of these equations was evaluated using the Gibbs energy change by adsorption of gas molecule ΔG^{o} calculated by the CM/PM-combined method:

Table 11.6 Binding energy (BE, kcal mol^{-1}) of CO_2 at the sites II and III of **PCP-N** in the presence six CO_2 molecules at the site I

	Site II						Site III		
Number (n) of CO_2 molecules	1	2	3	4	5	6	1	2	3
$BE^{\text{SCS-MP2:PBE-D3}}$ [a]	1.20	–2.19	–3.33	–4.00	–4.41	–4.77	–0.62	–4.15	–5.26
$E_{\text{DEF}}^{\text{PBE-D3}}$ [b]	7.52	4.41	3.34	2.76	2.37	2.12	7.46	3.97	2.95
$E_{\text{INT}}^{\text{SCS-MP2:PBE-D3}}$(H-G) [c]	–5.52	–5.76	–5.84	–5.92	–5.99	–6.04	–7.93	–7.96	–8.04
$E_{\text{INT}}^{\text{SCS-MP2}}$(G-G) [c]	–0.80	–0.84	–0.82	–0.83	–0.80	–0.84	–0.15	–0.16	– 0.16

[a] $BE^{\text{SCS-MP2:PBE-D3}}$ here represents CO_2 binding energy at the sites II and III in the presence of six CO_2 molecules at site I, which is defined by $BE^{\text{SCS-MP2:PBE-D3}} = [E(\text{PCP}\cdot(n+6)\text{CO}_2) - E(\text{PCP}\cdot 6\text{CO}_2)]/n - E(\text{CO}_2)$

[b] $E_{\text{DEF}}^{\text{PBE-D3}}$ represents average crystal deformation energy of **PCP-N** per one CO_2 molecule induced by CO_2 adsorption at site II or III

[c] $E_{\text{INT}}^{\text{SCS-MP2:PBE-D3}}$(H-G) represents interaction energy between CO_2 and **PCP-N** framework. $E_{\text{INT}}^{\text{SCS-MP2}}$(G-G) is the sum of CO_2–CO_2 interaction energy at sites I, II, and III
These values are taken from Ref. [25]

PCP-N:

$$\text{At site I: } K_1 = \exp\left(-\Delta G_{\text{ads},1}^{\circ} / RT\right) \tag{11.18}$$

$$\text{At sites II and III: } K_2 = \exp\left(-9\Delta G_{\text{ads},2}^{\circ} / RT\right) \tag{11.19}$$

As **PCP-C** is isostructural to **PCP-N**, **PCP-C** also has three possible sites for CO_2 adsorption. The calculated BE for the adsorption of CO_2 on **PCP-C** decreases in the following order: site I (−4.55) > III (−2.12) > II (−2.00), where the values in parentheses are SCS-MP2:PBE-D3-calculated BEs in kcal mol^{-1}. This result indicates that CO_2 initially adsorbs at site I of **PCP-C**, similar to the case of **PCP-N**. After site I is fully occupied by six CO_2 molecules, further adsorption of CO_2 molecules at sites II and III of **PCP-C** is difficult because the BEs for the adsorption of CO_2 molecules at sites II and III significantly decrease (–0.27 and –0.15 kcal mol^{-1}, respectively) after the adsorption of six CO_2 molecules at site I. These small BE values arise from the large E_{DEF} values for CO_2 adsorptions at sites II and III of **PCP-C**; actually, the E_{DEF} value is 6.23 and 7.83 kcal mol^{-1} for sites II and III, respectively. Even when six and three CO_2 molecules simultaneously adsorb at sites II and III, these large E_{DEF} values cannot be overcome by the sum of E_{INT} values. Thus, in the case of **PCP-C**, CO_2 adsorption occurs only at site I and does not take place at sites II and III.

For CO_2 adsorption on **PCP-C**, the equilibrium equation and K are represented by Eqs. 11.20 and 11.21, which are the same as those at site I in the case of **PCP-N** (Eqs. 11.16 and 11.18):

$$\text{PCP-C site I:} \quad CO_2 + \textbf{PCP-C} \cdot (CO_2)_n \leftrightarrows \textbf{PCP-C} \cdot (CO_2)_{n+1}, \quad n = 0\text{–}5 \tag{11.20}$$

$$K = \exp\left(-\Delta G^{\circ}_{ads} / RT\right) \tag{11.21}$$

At sites I of **PCP-N** and **PCP-C**, CO_2 adsorption occurs according to Eqs. 11.16 and 11.20, respectively. In this case, the adsorption coverage θ under a certain pressure (P) can be expressed by the Langmuir equation (Eq. 11.22):

$$\theta = K\left(p / p_0\right)\left[1 + K\left(p / p_0\right)\right] \tag{11.22}$$

where p_0 is the standard pressure and K is the equilibrium constant of Eqs. 11.18 and 11.21. At sites II and III of **PCP-N**, nine CO_2 molecules instead of one CO_2 molecule can be simultaneously adsorbed because the sum of nine E_{INT} values is sufficient to overcome the sum of the E_{DEF} values of nine CO_2 molecules; in contrast, the BE of one CO_2 molecule is not enough to overcome the E_{DEF} value. Therefore, the adsorption isotherm can be described by Eq. 11.23:

$$\theta = K\left(p / p_0\right)^9\left[1 + K\left(p / p_0\right)^9\right] \tag{11.23}$$

This equation is essentially the same as that of the Langmuir–Freundlich adsorption isotherm, where the order "9" of the $\left(p / p_0\right)$ term is valuable depending on the adsorption equilibrium; it must be larger than 1.0 for the Langmuir–Freundlich equation, whereas it must be 1.0 for the usual Langmuir equation.

Using Eqs. 11.22 and 11.23, the isotherms for the adsorptions of CO_2 on **PCP-N** and **PCP-C** were calculated (Fig. 11.6). Evidently, the calculated amount of adsorbed CO_2 molecules was smaller than the experimental value under low pressure. This is appropriate because the ΔG°_{ads} value for the adsorption of gas molecules on the MOF is often underestimated by the assumption that the rotational and translational movements of the gas molecules adsorbed to the MOF are completely frozen, as discussed in Sect. 11.3.1. However, the gas molecules adsorbed to the MOF easily move. Thus, it is likely that one to two freedoms of rotational movement remain [23]. In this case, the ΔG°_{ads} value for CO_2 adsorption may increase by 1.0–1.5 kcal mol^{-1} from the value obtained for the case of totally frozen rotational movements. The CO_2 adsorption isotherms for **PCP-N** and **PCP-C** calculated using the modified ΔG°_{ads} values are in suitable agreement with the experimentally observed results (Fig. 11.6a, b). Experiments revealed that the adsorption of CO_2 on **PCP-N** occurred with a stepwise isotherm, whereas that on **PCP-C** took place with a non-stepwise isotherm (black and red lines, respectively, in Fig. 11.4). This stepwise adsorption isotherm for **PCP-N** was appropriately reproduced via calculation. As comprehensively shown in Fig. 11.6c, the adsorption of CO_2 at site I (red line) starts at $p_0 = 0.0$, which is a normal feature observed in the Langmuir-type isotherm without a sigmoidal curve. In contrast, the adsorptions of CO_2 at sites II and III (blue line) do not start at p

$= 0.0$; instead, they start at approximately $p = 3$ kPa with sigmoidal feature. This isotherm indicates that CO_2 adsorption does not occur at sites II and III when $p <$ 3 kPa, whereas it suddenly starts at approximately $p = 3$ kPa. That is, gate-opening adsorption with a sigmoidal adsorption isotherm originates from the equilibrium represented by Eq. 11.23. The Eq. 11.23 is presented when two or more gas molecules simultaneously adsorb to the MOF rather than only one gas molecule. This leads to gate-opening adsorption with a sigmoidal adsorption isotherm.

In summary, the CM/PM-combined method is a powerful computational method for calculating the *BE* of a gas molecule with a flexible MOF. Using this combined method, the mechanism and key factors of gate-opening adsorption with the sigmoidal adsorption isotherm have been clearly elucidated; adsorption of one gas molecule cannot occur because the large E_{DEF} cannot be overcome by the E_{INT} of one gas molecule. Nevertheless, there is a possibility that the sum of E_{INT} values overcomes the total E_{DEF}, when an E_{DEF} value per one gas molecule decreases but an E_{INT} value per one gas molecule decreases little as the number of adsorbed gas molecules increases. These are true in the case of flexible MOFs. In this case, simultaneous adsorption of more than one gas molecule can occur. This is the case for the adsorptions of gas molecules on sites II and III of **PCP-N**. On the other hand, if E_{DEF} is significantly large such that the simultaneous adsorption of more than one gas molecule cannot overcome the total E_{DEF}, gas adsorption does not take place. This is the case for the adsorptions of gas molecules on sites II and III of **PCP-C**. These findings show that E_{DEF} must be accurately calculated to better understand the gate-opening gas adsorption. Therefore, a simple cluster model is not useful; instead, the CM/PM-combined method must be employed in theoretical calculations of infinite system.

Here, we need to mention one weak point of the CM/PM-combined method. Although E_{INT} of a gas molecule is evaluated using the post-HF correction, E_{DEF} is calculated using the DFT method without the post-HF correction. If the post-HF correction is applied to the calculation of E_{DEF} using a reasonable CM, the quality of the CP/PM-combined method will improve.

11.4 Application of QM/Periodic-MM Method to Molecular Crystal

11.4.1 Isomerization of Ruthenium(II) Sulfur Dioxide Complex in Crystal

Photoinduced linkage isomerization occurs when a ligand coordinates to a metal atom in several metastable structures different from an equilibrium structure. This linkage isomerization is expected to be useful for optical data storage [78–80] because the

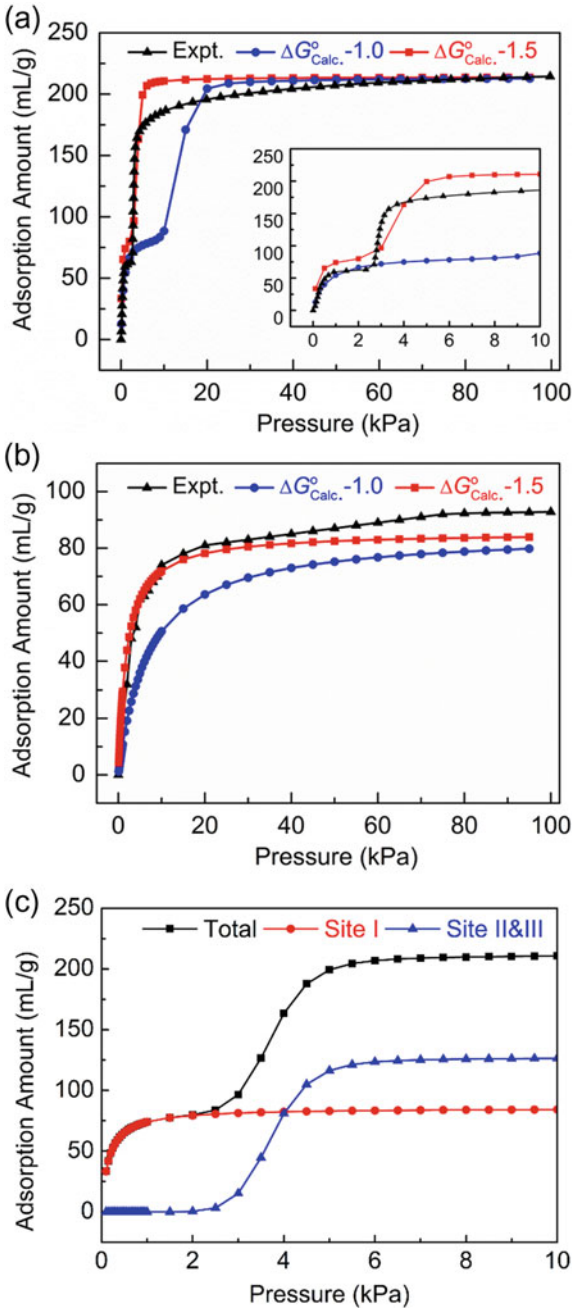

Fig. 11.6 Calculated CO_2 adsorption isotherms at 195 K by **PCP-N** (**a**), that by **PCP-C** (**b**) and that by **PCP-N** at low pressure (**c**). The black lines represent experimental isotherms; blue and red lines represent isotherms calculated by increasing the adsorption Gibbs energy change by 1.0 and 1. 5 kcal mol^{-1}, respectively. Inset represents the expansion at low pressure region. Cited from Ref. [25] with permission of the American Chemical Society

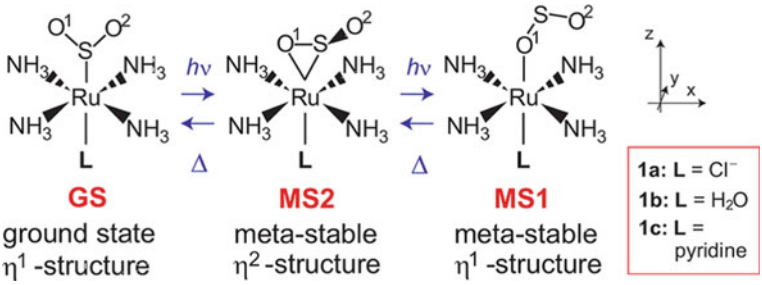

Scheme 11.4 Ground state of $[Ru(NH_3)_4(SO_2)L]^{n+}$ (n = 1 for L = Cl; n = 2 for L = H_2O or pyridine) and its meta-stable states produced by photo-irradiation. Cited from Ref. [91] with permission of the American Chemical Society

ground state of the isomer can be assigned as "0" and the metastable state can be designated as "1". Metastable structures can be experimentally detected by photocrystallography [81–83]. Thus, photoinduced linkage isomerization has attracted considerable interest as a prototype of molecular memories. A suitable example is the photoinduced linkage isomerization of the crystals of the ruthenium(II) sulfur dioxide complexes $[Ru(NH_3)_4(SO_2)L]^{n+}$ **1** (n = 1 for L = Cl^- and n = 2 for L = H_2O (**w**) or pyridine (**py**)) [84–90] (Scheme 11.4). In the ground state, the SO_2 ligand coordinates to the Ru atom via the S atom (η^1-S form; **GS**). Under photoirradiation, **GS** isomerizes to a metastable η^2-SO-coordinated form (η^2-SO form; **MS2**) and then to another metastable η^1-O-coordinated form (η^1-O form; **MS1**). After photoirradiation, **MS1** thermally returns to **GS** in the ground state via **MS2**. To apply this material to molecular memory, controlling the thermal isomerization of **MS1** to **GS** is necessary. However, to date, the details of thermal isomerization in crystal are unclear. As we do not have an appropriate understanding of the chemical reactions occurring in crystals, currently, theoretical knowledge of the chemical reactions taking place in crystals is primarily important.

Thermal isomerization occurs when the crystal is not extremely rigid. If the crystal is highly rigid, thermal isomerization is difficult to occur. In contrast, if the crystal is extremely flexible, thermal isomerization quickly takes place as in solution, which is not suitable for application in molecular memory. Therefore, the crystal must be appropriately rigid (or flexible). This indicates that theoretical calculations must be performed by accurately considering the crystal effects.

Because the isomerization of a Ru complex in a crystal is different from the phase transition of the crystal, the transition state must be optimized for one Ru complex in the presence of other Ru complexes that do not simultaneously undergo isomerization. This theoretical study has recently been reported using the QM/periodic-MM method [91].

The QM/periodic-MM calculation was conducted using a QM region composed of one target complex ($[Ru(NH_3)_4(SO_2)Py]^{2+}$, $\mathbf{1_{Py}}$ (**QM0**) (Py = pyridine)), two nearest-neighboring Ru complexes (**1Py** (**QM1**)), five Cl^- counter ions, and one crystal H_2O molecule (**QM2**). A similar QM region was employed for

$[Ru(NH_3)_4(SO_2)(H_2O)]^{2+}$ ($\mathbf{1_W}$) and $[Ru(NH_3)_4(SO_2)Cl]^{+}$ ($\mathbf{1_{Cl}}$). For the MM moiety, the LJ parameters of the AMBER force field were used, except for the Ru atom. As discussed in Sect. 11.2.2, the LJ parameters for the Ru atom were readjusted such that the acquired LJ parameters reproduced the B3PW91-calculated potential energy curve.

At first, the geometries of the **GS-**, **MS1-**, and **MS2-**crystals were optimized. Thereafter, the transition states and intermediates were optimized for the **GS-**, **MS1-**, and **MS2**-crystals to explore the influence of the crystal structure on the transition state and activation barrier of isomerization. Because it is interesting to know differences in geometry among gas phase, solution, and crystal, the geometry changes were compared among gas phase, solution, and crystal (Fig. 11.7), where $\delta r = R(Ru\text{-}S) - R(Ru\text{-}O)$ is taken as an approximate reaction coordinate. This δr is a suitable measure representing the extent of the progress of isomerization as it is highly negative for **GS**, close to zero for **MS2**, and highly positive for **MS1**. Interestingly, the geometries change in similar manner among gas phase, aqueous solution, and crystal. These moderate differences suggest that the chemical reaction occurs in a similar cavity in both the solution and the crystal. Nevertheless, the energy changes were moderately different, as shown in Fig. 11.8, where the energy zero was taken for the equilibrium geometry of **GS** in the gas phase. As the orientations of ligands are slightly different in the crystal and gas phases, the geometries in this figure were optimized starting from those in the crystal phase. Particularly, the energy changes in the gas phase differed from those in the solution and crystal phases. In the gas phase, **MS1A** is at a lower energy than those of **MS2A** in $\mathbf{1_W}$ and $\mathbf{1_{Py}}$. This relative energy implies that isomerization does not occur from **MS1A** to **MS2A** in the gas phase, which is contrary to the experimentally observed result for the crystal phase, showing that **MS1A** → **MS2A** isomerization takes place in the crystal phase. Only **MS1A** of $\mathbf{1_{Cl}}$ is at a higher energy than that of **MS2A**, indicating that **MS1A** → **MS2A** isomerization can occur in $\mathbf{1_{Cl}}$. These results suggest that the reactions taking place in the crystal phase cannot be investigated in the gas phase, as expected.

In the aqueous solution phase, the geometry and energy changes were calculated using the three-dimensional (3D)-RISM-SCF method by combining the solvation effects obtained by the 3D-RISM method [92, 93] with the electronic structure theory in a self-consistent manner [4–6]. The 3D-RISM-SCF method is effective for incorporating solvation effects when the target solute is large, highly polarizable, and charged like a transition metal complex bearing molecular charge(s) [94]. In the aqueous solution phase, **MS1A** of all the complexes is at a higher energy than that of **MS2A**, and **MS2A** is at a higher energy than that of **GSA** (Fig. 11.8b). Furthermore, the activation energy of **MS1A** → **MS2A** isomerization is smaller than that of **MS2A** → **GSA** isomerization. These results indicate that **MS1A** → **MS2A** isomerization occurs at low temperatures, whereas **MS2A** → **GSA** isomerization takes place at higher temperatures, as experimentally observed in the crystal phase.

For **GS-**, **MS1-**, and **MS2**-crystals, unexpectedly, the relative energies of **GS**, **MS1A**, and **MS2A** and the activation energies for the two isomerization steps were not different so much, as shown in Fig. 11.9, where the results of **MS2**-geometries have been omitted to save space because the energy changes for the **MS2**-geometries

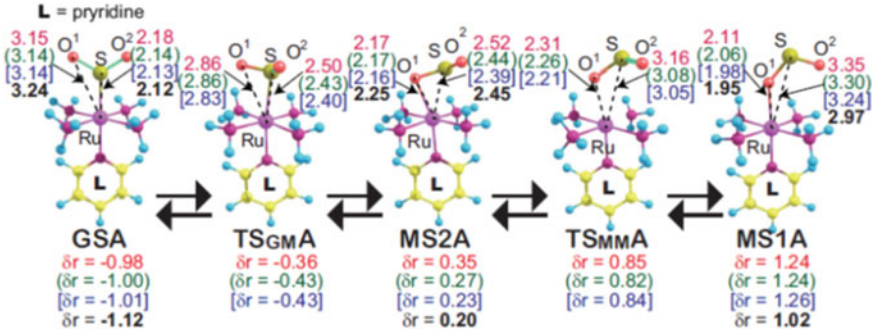

Fig. 11.7 Geometry changes in thermal isomerization of $[Ru(NH_3)_4(SO_2)L]^{n+}$ (n = 1 for L = Cl; n = 2 for L = H_2O or pyridine) from meta-stable state (η^1-O coordinated form **MS1**) to ground state (η^1-S coordinated form **GS**) through the second meta-stable state (η^2-SO coordinated form **MS2**). (Red); Gas phase, (Green); Aqueous solution, (Blue); Crystal, and (Black bold); experimental values. Cited from the SI of Ref. [91] with permission of the American Chemical Society

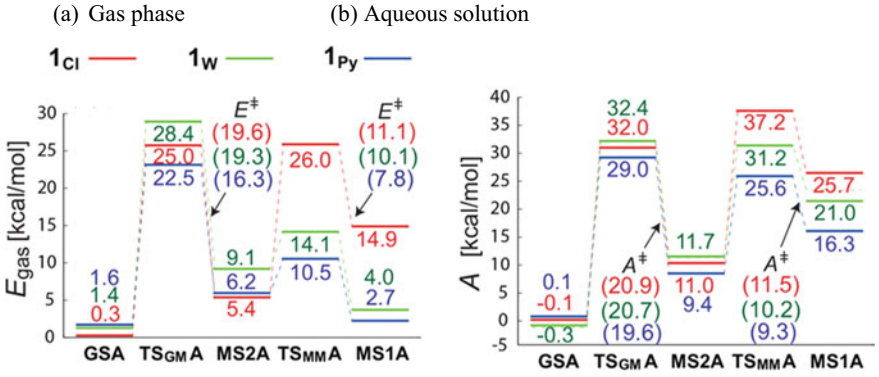

Fig. 11.8 Energy changes (in kcal/mol) in thermal isomerization of $[Ru(NH_3)_4(SO_2)L]^{n+}$ (n = 1 for L = Cl; n = 2 for L = H_2O or pyridine) from meta-stable state (η^1-O coordinated form **MS1**) to ground state (η^1-S coordinated form **GS**) through the second meta-stable state (η^2-SO coordinated form **MS2**) in gas phase and aqueous solution, where the most stable structure in gas phase was taken as reference (energy zero) and **GSA** was optimized starting from the orientations of NH_3 and L ligands taken in the crystal. Values without parenthesis are relative energy to the most stable species. In parenthesis is activation energy. Cited from Ref. [91] with permission of the American Chemical Society

are similar to those for the **MS1**-geometries. However, the energy levels of all isomers and transition states depend on lattice vectors. Their energy levels relative to **GS** are lower in the crystal phases with lattice vectors at lower temperatures, whereas they become higher in the crystal phases with lattice vectors at higher temperatures. These results imply that the differences in crystal packing between at low and high temperatures lead to differences in relative energies. In all the lattice vectors, however, **MS1** of all the complexes is at a higher energy than that of **MS2A**, and **MS2** is at a higher

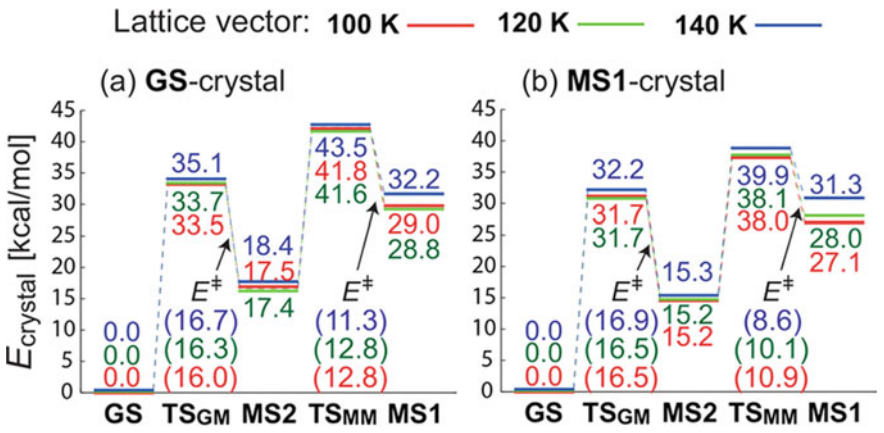

Fig. 11.9 Energy changes (in kcal/mol) in thermal isomerization of $[Ru(NH_3)_4(SO_2)L]^{n+}$ (n = 1 for L = Cl; n = 2 for L = H_2O or pyridine) from meta-stable state (η^1-O coordinated form **MS1**) to ground state (η^1-S coordinated form **GS**) through the second meta-stable state (η^2-SO coordinated form **MS2**) in crystal. Values without parenthesis are relative energy to the most stable species. In parenthesis is activation energy. Cited from Ref. [91] with permission of the American Chemical Society

energy than that of **GSA**. The activation energy of **MS1A** → **MS2A** isomerization is smaller than that of **MS2A** → **GSA** isomerization in all the lattice vectors. These results are in agreement with the experimentally observed results, demonstrating that **MS1A** → **MS2A** isomerization occurs at low temperatures, whereas **MS2A** → **GSA** isomerization takes place at higher temperatures in the crystal phase.

Interestingly, these results are qualitatively similar to those obtained for the solution phase, indicating that the reaction behaviors of $[Ru(NH_3)_4(SO_2)L]^{n+}$ in the solution phase are not significantly different from those in the crystal phase. This is one of the surprising results. The similar reaction behaviors of $[Ru(NH_3)_4(SO_2)L]^{n+}$ in the solution and crystal phases suggest that the reaction in the solution phase occurs in the solvation cage, whereas that in the crystal phase takes place in the crystal cavity. Nevertheless, all the metastable intermediates and transition states are at higher energies relative to that of **GSA** in the crystal phase than in the solution phase. These results imply that the metastable intermediates and transition states suffer from larger steric repulsion with crystal than the ground state **GSA** does. This is consistent with our general understanding that unstable intermediates and transition states have longer Ru–SO_2 distances. Accordingly, in the crystal phase, the activation barrier of isomerization is not always larger than that in the solution phase.

In summary, the QM/periodic-MM calculations revealed that the chemical reaction in the crystal phase occurs in a crystal cavity similar to the solvation cage in the solution phase; however, the crystal effects are larger in the metastable intermediate and transition state of the crystal reaction than the solvation effects in the solution reaction. Although the achieved results are not surprising, they are important because to date, no clear theoretical result of chemical reactions in crystals has been reported

with evidence. These results demonstrate that the QM/periodic-MM method is a powerful tool for the theoretical study of chemical reactions in crystals.

11.4.2 Meta-Metal to Ligand Charge-Transfer (MMLCT) Excited State of Transition Metal Complexes in Crystal

Recently, theoretical studies of the excited states in the molecular crystals of a gold(I) phenyl(phenyl isocyanide)gold(I), (Ph)Au^{I}(NCPh), and a platinum(II) dicyanobipyridine complex, $Pt^{II}(CN)_2$(bpy), have been performed using the QM/periodic-MM method [95, 96]. As these studies have been summarized in a recent review [97], we have only provided a brief overview of these studies here.

(1) Excited states and emission spectra in the crystal of gold(I) phenyl phenylisocyanide complex: This complex has attracted considerable interest ever since Ito et al. have reported that the absorption and emission spectra were changed by mechanical stimulation [98]. This phenomenon is attributed to the single-crystal-to-single-crystal transition induced by mechanical stimulation. Nevertheless, it is not easy to investigate experimentally the influences of the changes in the crystal phase on the excited state of the complex, the mechanism behind the changes in the excited state with the occurrence of phase transition, and the extent of changes in the excited state because of the very small population of excited molecules.

When the emission spectra of metal complexes in the crystal phases or in highly concentrated solution phases significantly change from those in dilute solution, it is generally understood that a metal–metal (M–M) bond is formed in the excited state and CT excitation occurs from the antibonding orbital of the M–M bond to the π^*-orbital of the ligand. When Au(I) complexes with d^{10} electron configuration approach each other, d–d bonding and antibonding molecular orbitals are formed between those two Au(I) complex (Scheme 11.5). Pt(II) has a d^8 electron configuration. When four ligands are located on the x and y axes in the Pt(II) complex, the $d_z{}^2$ orbital is doubly occupied; thus, the $d_z{}^2$ orbital of one Pt(II) complex forms bonding and antibonding molecular orbitals with that of the neighboring Pt(II) complex, as in the case of Au(I), and a similar CT transition occurs. This CT transition is called metal-metal to ligand CT (MMLCT) excitation because CT occurs from the M–M bond to the ligand. Consequently, an M–M bond with a formal bond order of 0.5 is produced between these two M atoms in the MMLCT excited state; that is, exciplexes of Au(I) and Pt(II) complexes are generated by photoexcitation in the crystal phase and/or the concentrated solution phase. The emission from this MMLCT excited state should be considerably different from that of a single molecule. However, there are several open questions: Is this exciplex actually produced in the crystal phase? And can the MMLCT emission be observed? Evaluating the geometries of the excited states and emission energies in molecular crystals via theoretical calculations can provide answers to those questions but challenging.

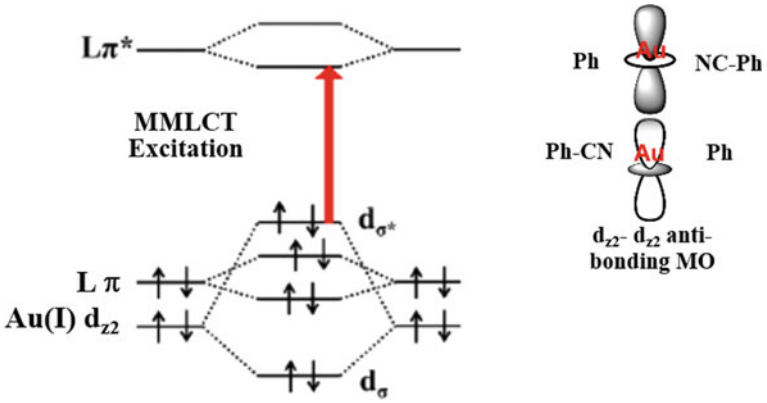

Scheme 11.5 Metal–metal to ligand charge-transfer (MMLCT) excitation

(Ph)Au^{I}(NCPh) has two crystal phases: **1y**, which demonstrates yellow luminescence, and **1b**, which exhibits blue luminescence [98]. The optimized geometries of these phases are depicted in Fig. 11.10. In **1y**, the Au–Au distance is long (4.73 and 5.73 Å), and CH–π interactions are developed between Au complexes, whereas π–π interactions do not exist. In **1b**, the Au–Au distance is short (3.18 and 3.79 Å), and both CH–π and π–π interactions are formed between Au complexes. Moreover, the **1b**-to-**1y** phase transition occurs. The differential scanning calorimetry (DSC) analysis has revealed that **1b** is more stable than **1y** by 7 kJ mol^{-1}, consistent with the experimental fact showing that **1b**-to-**1y** phase transition occurs.

The relative stabilities of **1b** and **1y** were theoretically analyzed by the QM/periodic-MM method using four Au complexes as the QM part in **1b** and six Au complexes as the QM part in **1y** (Scheme 11.6). These models were employed for the following reasons: In **1y**, which has alternating short and long Au–Au intervals, the MMLCT excited state is possibly formed by the two Au complexes with short

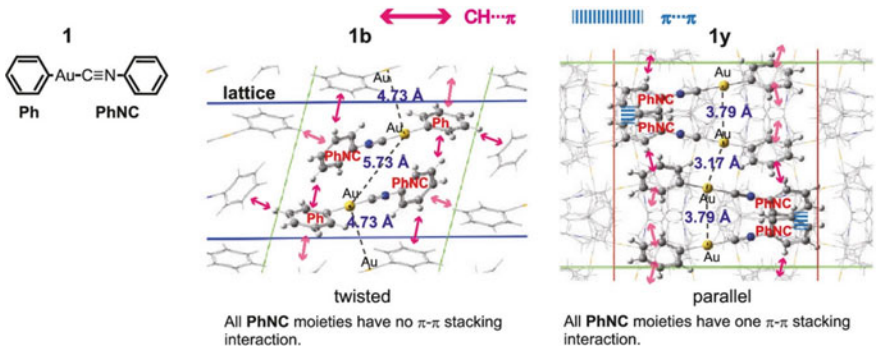

Fig. 11.10 Two crystal phases of phenyl(phenyl isocyanide)gold(I) complex. Cited from Ref. [95] with permission of the American Chemical Society

interval. When the two central Au complexes participate in exciplex formation, the other two Au complexes with short Au–Au intervals exist above the exciplex and the remaining two Au complexes with short Au–Au interval exist below the exciplex. That is, the exciplex contacts with two pairs of two Au complexes in the ground state, when six Au(I) complexes are involved in the QM region (Scheme 11.6b). In **1b**, the distance between all Au complexes is long. When the two Au complexes at the central position form the MMLCT excited state, one Au complex in the ground state is located above the exciplex and the other Au complex in the ground state is located below the exciplex such that the exciplex is sandwiched with the Au complexes in the ground state. When four Au complexes are involved in the QM region, therefore, the exciplex is surrounded by two Au complexes at the ground state in the QM region (Scheme 11.6a). Using these models, the relative stabilities of **1b** and **1y** have been investigated by considering the energy per molecule of the Au complex. Using the positions of the Au nuclei determined in the experiment, the rotations of the Ph and PhNC ligands, orientations of the Au complexes, and geometries of the ligand moieties have been optimized. The optimized geometries reveal that the CH–π interaction is indeed present in **1b** and the π–π interaction does not exist (Fig. 11.10a), whereas the CH–π and π–π interactions are present in **1y** (Fig. 11.10b).

Additionally, the calculations indicated that **1b** was more stable than **1y** and the relative stabilities of **1b** and **1y** were governed by the QM–MM and MM–MM interactions but were not by the QM part. These results suggest that long-range interactions are critical for determining the relative stabilities of molecular crystals. The QM–QM interaction has been corrected by the MP2 method; nevertheless, the

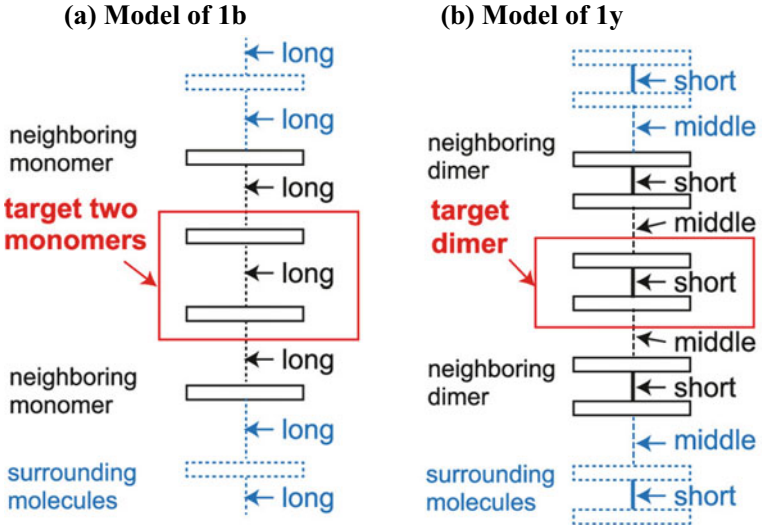

Scheme 11.6 Models of crystal structures of phenyl(phenyl isocyanide)gold(I) complex employed for QM/Periodic-MM calculation of 1b (**a**) and 1y (**b**). Cited from Ref. [95] with permission of the American Chemical Society

stability of the molecular crystal of this Au(I) complex is not changed very much by the MP2 correction. Using these ground-state structures, QM/periodic-MM calculations were conducted by applying time-dependent (TD)-DFT with the B3LYP-D3 functional to evaluate the excitation energies. The lowest-energy excitation was an intramolecular CT excitation from the π-orbital of the Ph ligand to the π*-orbital of the PhNC ligand. The excitation energy was obtained with an error of about 0.5 eV from the experimental value. Adsorption energies of the surface Au complex and the internal Au complex were also compared using the slab model and were found to be significantly different.

Geometry optimization of the excited state was performed by the QM/periodic-MM method using the B3LYP functional. **1b** does not form an exciplex consisting of two Au complexes. This is reasonable because of the long Au–Au distances of 4.69 and 5.87 Å at the ground state (Fig. 11.11a). Instead, the lowest-energy excited state is formed through triplet π–π* excitation in one PhNC ligand. In contrast, for **1y**, the Au–Au distance is shorter at the ground state (2.85 Å), suggesting that d_z^2–d_z^2 bonding and antibonding molecular orbitals are formed between two Au complexes and one-electron excitation occurs from the d_z^2–d_z^2 antibonding molecular orbital to the π* orbital of PhNC ligand. In fact, these two molecular orbitals are singly occupied in the excited state (Fig. 11.11b). Table 11.7 presents a comparison of the emission spectra and the experimental results. In the case of **1b**, the energy of the emission spectrum is in appropriate agreement with the experimental value, with an error of 0.2 eV. The emission spectra of the Au(I) complex on the surface and the interior of the crystal have been compared, which exhibit a slight difference as compared to the cases of the adsorption spectra. This slight difference originates from the fact that the adsorption spectrum is induced by CT excitation from the Ph ligand to the PhNC ligand, as discussed above, whereas emission occurs from the π–π* excited state in one PhNC ligand; in other words, the Ph and PhNC ligands are influenced in a different manner by the atmosphere, leading to the difference in the absorption spectrum between at the surface and interior, whereas both π and π* orbitals of the PhNC ligand are affected to a similar extent by the crystal atmosphere, leading to the similar emission spectrum between at the surface and interior. In **1y**, ^{3}MMLCT1 is the first excited state (Fig. 11.11b), and ^{3}MMLCT2 is observed at different positions (Fig. 11.11b). The emission energies of ^{3}MMLCT1 and ^{3}MMLCT2 are moderately different. This is an artificial error originating from the small size of the QM region: ^{3}MMLCT1 is produced at one place in the QM region, whereas ^{3}MMLCT2 is generated in two different Au complexes. If the size of the QM region is sufficiently increased, both ^{3}MMLCT1 and ^{3}MMLCT2 should have the same structure and the same energy. Because of the small QM region, the circumstances of the ^{3}MMLCT1 state moderately differ from those of the ^{3}MMLCT2. For ^{3}MMLCT, almost no difference was observed between the energies of the emission spectra of the complex at the surface and the interior of the crystal. Furthermore, the theoretically calculated emission energy is in suitable agreement with the experimental results for ^{3}MMLCT. In these calculations of emission spectra, the ΔSCF method was used instead of TD-DFT. Certainly, although the emission spectra can be calculated by the TD-DFT using

the excited-state structure, the results of the ΔSCF method are in better agreement with the experimental results in our experience.

(2) Temperature effects on the excited state structure and emission spectrum of [$Pt^{II}(CN)_2$(bpy)] (bpy = 2,2′-bipyridine) complex in crystals: Planar four-coordinate Pt(II) complexes exhibit weak or no emission in dilute solution phase; however, they often demonstrate strong emission spectra in the concentrated solution or crystal phase. This phenomenon is called aggregation-induced phosphorescence or assembly-induced phosphorescence (abbreviated as AIP) [99–101]. Generally, when metal complexes are located in close proximity to each other in the high-concentration solution or crystal phase, MMLCT (Scheme 11.5) is produced, and thus, a new emission spectrum is observed. This emission spectrum becomes broad with an increase in temperature, and the emission peak shifts to a higher energy

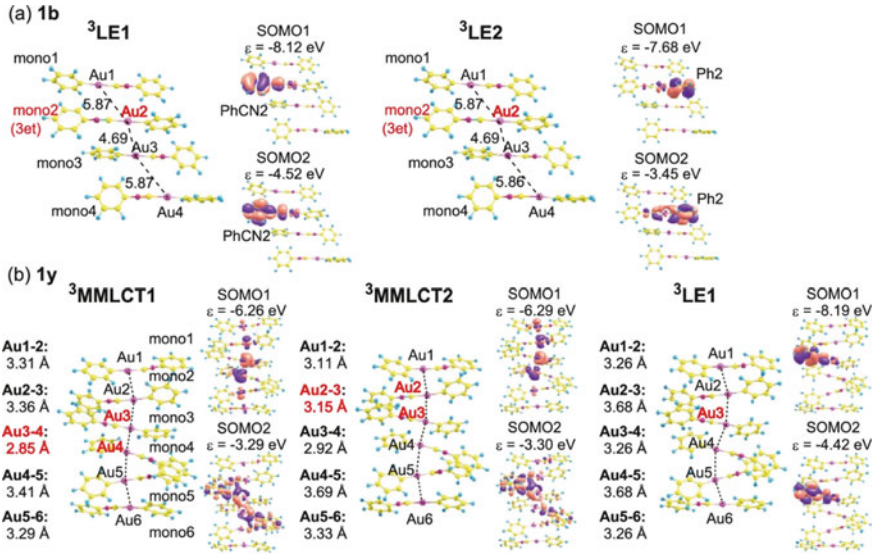

Fig. 11.11 The optimized geometries of the triplet excited state of phenyl(phenyl isocyanide)gold(I) complex in crystal phases **1b** and **1y**. Cited from Ref. [95] with permission of the American Chemical Society

Table 11.7 Emission energies of Au(Ph)(PhNC) in crystal phases **1b** and **1y**

Crystal phase	**1b** (with Long Au–Au distance)			**1y** (with short Au–Au distance)				
	^{3}**L1**[a]	^{3}**L2**[b]	expt[c]	^{3}**MMLCT1**[d]	^{3}**MMLCT2**[e]	^{3}**L1**[f]	^{3}**L2**[g]	Expt.[c]
Surface	2.73	3.08		2.30	2.33	2.73	2.79	
Bulk	2.71	3.10	2.53, 2.72	2.37	2.35	2.72	2.77	2.19

[a] The local * excited state of PhNC ligand. The [b] local * excited state of Ph ligand excited state of Ph ligand. The calculated values are taken from Ref. [95]

in many cases. A typical example is depicted in Fig. 11.12 [102]. The emission spectrum of the $[Pt^{II}(CN)_2(bpy)]$ complex in the crystal phase was measured at various temperatures ranging from low (15 K) to room temperature. At 15 K, a sharp emission spectrum was noticed at approximately 660 nm, whereas at room temperature, a broad spectrum was observed at approximately 620–630 nm [102]. Figure 11.12b shows the Pt–Pt distances at different temperatures. Clearly, the Pt–Pt distance increased with an increase in temperature, indicating that the d_{z2}–d_{z2} antibonding molecular orbital between two Pt(II) complexes shifted to a lower energy and the MMLCT excitation energy shifted to a higher energy with an increase in the Pt–Pt distance in MMLCT. Nevertheless, whether the crystal structure in the ground state is reflected in the structure of the excited state is still unclear. Additionally, the reason for the broadening of the spectrum has not yet been clarified.

A QM/periodic-MM theoretical study of $[Pt^{II}(CN)_2(bpy)]$ molecular crystal was conducted [96], in which the temperature dependences of the excited-state structure and emission spectrum were discussed. A unit cell comprising n QM and (225-n) MM molecules was used for calculation, and three kinds of QM regions were considered. The first type of QM region included the central two molecules, and the second and third kinds of QM regions comprised the central three and four molecules, respectively. Using these models, QM/periodic-MM calculations were performed. The excited-state structures of $[Pt^{II}(CN)_2(bpy)]$ in the gas and crystal phases were different; for instance, in the crystal phase, the orientations of bpy and CN in the ground and excited states were the same. However, in the gas phase, bpy and CN were twisted around each other and formed a staggard structure. Originally, the staggard structure of the ligands was stable due to steric repulsion between the two ligands; on the other hand, in the crystal phase, the eclipsed orientation was probably induced by the crystal packing effect, and the orientation change upon excitation was suppressed by the crystal effect. When two Pt complexes were used in the QM region, the MMLCT excited state (denoted as ^{3}**[Pt-MMLCT]$_2$**) was

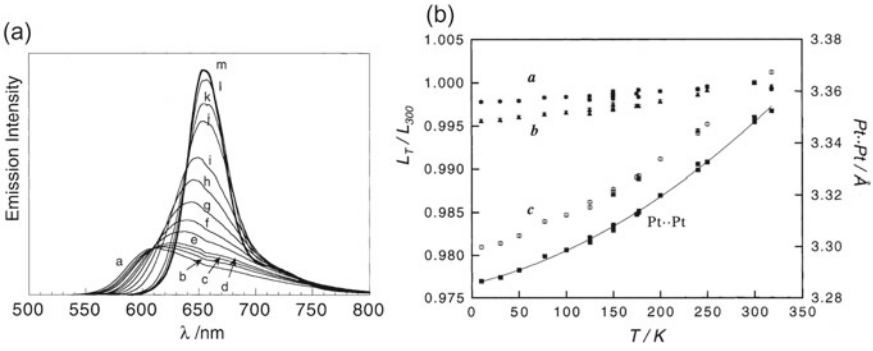

Fig. 11.12 Emission spectrum of $Pt(CN)_2(bpy)$ (bpy = 2,2′-bipyridine) at various temperatures (**a**) and the lattice vectors with Pt–Pt distance a to m in (**b**) represent 292, 260, 240, 220, 180, 160, 140, 120, 100, 60, 45, 30, 15 K, respectively. λ_{ex} = 514.5 nm. Cited from Ref. [102] with permission of the American Chemical Society

Table 11.8 Relative energies (in kcal/mol) of dimer, trimer, and tetramer MMLCT excited states and their populations (in %)

	10 K			293 K		
	dimer	trimer	tetramer	dimer	trimer	tetramer
e^{a}	3.3	0.4	0.0	2.4	0.0	0.3
$E + \mathrm{ZPE}^{b}$	2.1	0.03	0.0	1.6	0.0	0.7
Pop.[c]	0.0	20.6	79.4	4.6	74.0	21.4

[a] Relative potential energy
[b] Relative zero-point energy of the Pt–Pt vibration
[c] Population at 10 or 293 K

formed by these two Pt complexes. When three Pt complexes were used in the QM region, the excited state (denoted as ^{3}**[Pt-MMLCT]$_3$**) was delocalized into three Pt(II) complexes. When four Pt complexes were used in the QM region, the excited state (denoted as ^{3}**[Pt-MMLCT]$_4$**) was delocalized into four QM Pt(II) complexes, where the excited state character was stronger and the spin density was larger in the central two Pt molecules than those in the terminal two Pt molecules. Because of this delocalization, the energies of the three excited states, namely, ^{3}**[Pt-MMLCT]$_2$**, ^{3}**[Pt-MMLCT]$_3$**, and ^{3}**[Pt-MMLCT]$_4$**, were different (Table 11.8). Therefore, the populations of these excited states varied with respect to temperature.

The potential energy curve with respect to the Pt–Pt distance in the excited state was shallow; thus, the vibrational frequency was small. This implies that the populations of vibrationally excited states are large. In this study, the vibrational wave function was obtained by solving the Schrödinger equation for the Pt–Pt vibration, and the population of each vibrationally excited state was calculated at low and room temperatures based on the Boltzmann distribution law. For vibrational wave functions with higher quantum numbers, the probability of a structure deviating from the equilibrium nuclear configuration is large. At low temperatures, the populations of the vibrationally excited states are small, which leads to a small probability of structure deviated from the equilibrium nuclear configuration and therefore results in a sharp spectrum. At room temperature, the populations of the vibrationally excited states are large; therefore, the probability of deviating structure is large and a broadened spectrum is presented at room temperature, compared with that at low temperature (Fig. 11.13a). This feature resembles the phenomenon that the symmetry-forbidden d–d transition can have an oscillator strength at room temperatures owing to the probabilities of the vibrationally excited states [103]. However, the peak of the spectrum was almost equal to that obtained at a low temperature when only the probability of deviating structure was considered. As abovementioned, the populations of ^{3}**[Pt-MMLCT]$_2$**, ^{3}**[Pt-MMLCT]$_3$**, and ^{3}**[Pt-MMLCT]$_4$** change with an increase in temperature because of the variation in their energies; their populations were evaluated using the Boltzmann distribution law (Table 11.8): the population of ^{3}**[Pt-MMLCT]$_4$** was 80% at 10 K, whereas that of ^{3}**[Pt-MMLCT]$_3$** was 74% at room temperature. This change is induced by not only the Boltzmann distribution,

but also the fact that the Pt–Pt distance in the crystal phase becomes shorter at low temperature and longer at room temperature (Fig. 11.12b). In fact, the tetramer exciplex becomes more stable at low temperature and less stable at room temperature than other exciplexes because the three Pt–Pt distances become shorter in the tetramer exciplex and the tetramer exciplex formation easily occurs when the intermolecular distance is short. Instead, the trimer exciplex becomes more stable than the tetramer exciplex at room temperature because the intermolecular distance becomes longer at room temperature than that at low temperature. Even at room temperature, the trimer exciplex is more stable than the dimer exciplex because the delocalization of the electronic structure of the trimer is larger than that of the dimer and significantly stabilized the trimer compared to the dimer. Considering the change in the population of the exciplex and the deviation of the structure of the vibrationally excited state from the equilibrium structure, the emission spectrum was calculated to be sharp at a low energy (1.95 eV) when temperature is low, and broad at a high energy (2.01 eV) when room temperature (Fig. 11.13b). These computational results (Fig. 11.13b) are in appropriate agreement with the experimental results shown in Fig. 11.12a.

In summary, the broadening of the emission spectrum induced by an increase in temperature is explained by the fact that the population of the vibrationally excited state increases at high temperature, and the high-energy shift of the emission spectrum is understood by the change in the populations of several exciplexes. These results indicate that the QM/periodic-MM method is promising for the theoretical study of the excited states in crystals.

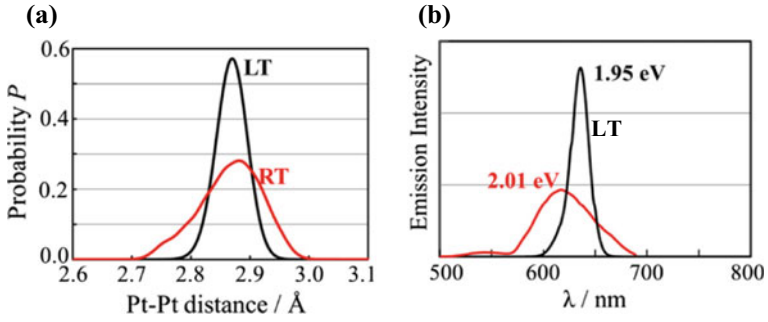

Fig. 11.13 Theoretically calculated emission spectrum of $[Pt(CN)_2(bpy)]$ (bpy = 2,2′-bipyridine) from the MMLCT excited state consisting of dimer (**a**) and that calculated using the Boltzmann distribution of dimer, trimer, and tetramer excited states (**b**). Cited from Ref. [96] with permission of the American Chemical Society

11.5 Advantages and Disadvantages of CM/PM-Combined and QM/Periodic-MM Methods from the Viewpoint of Application

Herein, we have compared the CM/PM-combined and QM/periodic-MM methods from the viewpoints of their applications to molecular crystals. The CM/PM-combined method was applied to the adsorption of gas molecules to MOFs [23–25]; the enthalpy of adsorption could be evaluated with adequate accuracy and the adsorption isotherm could be reproduced well, as described in Sect. 11.3. In the theoretical studies, structural optimization was performed via periodic-DFT calculation of the entire crystal system, and the adsorption energy was evaluated using periodic-DFT calculation of the entire system and post-HF correction for appropriate cluster models.

This CM/PM-combined method is not suitable for geometry optimization of excited state and calculation of emission spectrum of excited state because a very large unit cell is required for the geometry optimization and the emission spectrum calculation owing to the considerably smaller population of molecules at excited state than that of molecules at ground state. In the theoretical study of chemical reactions in crystals, we must also utilize a large unit cell because of the following reasons: if we calculate the intermediate and transition state using one unit cell, the reaction simultaneously occurs in all other unit cells; these geometry and energy changes correspond to phase transitions. In a chemical reaction, the simultaneous occurrence of reactions in all the unit cells is improbable; that is, the chemical reaction takes place in one unit cell, whereas no reaction occurs in many other unit cells.

Considering these features of the excited state and chemical reaction, the CM/PM-combined method is appropriate for theoretical calculations of the chemical events, such as the adsorption of gas molecules to MOFs or zeolites and adsorption of molecules to solid surfaces with regular structures, occurring in the ground states of molecular crystals.

In contrast, in the QM/periodic-MM method, the main part of a molecular crystal is calculated by the QM method and the remaining parts are evaluated via the classical force field (MM). The QM part at excited state can possibly be assessed in the presence of MM molecules bearing the structure and charge distribution in the ground state, as discussed in Sect. 11.4.2. Similar calculations can be conducted to investigate chemical reactions in crystals (Sect. 11.4.1). When the target is a solid, including MOFs and zeolites, with an infinite series of bonds, defining the QM and MM parts by cutting some of the infinite series of bonds is necessary. Particularly, the application of this method is challenging when the cutting procedure cannot be easily performed; For instance, cutting procedure is very difficult for extended and/or conjugated systems such as graphite. On the other hand, the QM/periodic-MM method can be facilely applied to a molecular crystal because the molecular crystal is clearly and reasonably separated into the QM and MM parts without any problem. For instance, the QM/periodic-MM method is suitable for theoretical studies of absorption spectra, excited-state structures, emission spectra [95, 96], and the structural

and energy changes induced by chemical reactions in molecular crystals because the cutting procedure is not required in the case of molecular crystals.

In summary, these methods can be improved as follows: In the CP/PM-combined method, cutting out appropriate cluster models (CMs) is necessary. Also, in the high-quality calculation of the CM, the crystal effect is not considered currently, which is a limitation of this method. This limitation can be overcome using the QM/periodic-MM method for the calculation of CM, as abovementioned. In this case, charge distribution in the boundary region between the QM and MM parts must be carefully set.

In the QM/periodic-MM method, the excited-state, intermediate, and transition-state in the QM part directly interact with MM molecules when the QM part is small. As well known, the QM–MM interaction is less accurately evaluated than the QM–QM interaction. Moreover, relaxations of the geometries and electronic structures of MM molecules are not considered in this method because they are taken to be the same as those for the molecular crystal in the ground state or before the chemical reaction. In fact, the relaxations of the geometries and electronic structures occur during chemical reactions and excitations. Therefore, we need to employ a QM region composed of an important moiety, in which chemical events, such as excitation and chemical reactions, occur, and other QM molecules that do not directly participate in the events but surround the important moiety. The idea of fragment molecular orbital [104] proposed by Kitaura et al. may be applicable to this case; however, its combination with the QM/periodic-MM method has not yet been carried out. Additionally, non-dynamical (or static) electron correlation often needs to be considered to calculate the excited state and conical intersection by this method. In this case, we employed the multireference wave function method. When exciplex consists of several transition-metal complexes, the active space becomes large and the usual complete active space self-consistent-field (CASSCF) calculation cannot cope with it. In such a case, the density matrix renormalization group (DMRG) method [105] can be applied to the multireference wave function method. If the quantum embedding theory outlined in Sect. 11.3.2 can be easily implemented, these theoretical calculations incorporating the non-dynamical electron correlation effects can be performed using a combination of DMRG and quantum embedding procedures.

Recently, the photochemistry of infinite system has attracted significant attention in the experimental field. Herein, we have discussed the theoretical study of the photochemistry of crystalline materials. This computational subject is gaining importance in connection with solar cells, photochemical reactions, and so on. Photochemistry is also of much interest in MOFs [106]. For theoretical studies of excited states in crystalline materials, at least the use of DFT methods with hybrid-type functionals is required, and in many cases, the use of post-HF methods, for example, CASSCF, symmetry-adapted-cluster/configuration interaction method (SAC-CI), and equation-of-motion coupled-cluster (EOM-CC), is desirable. Nevertheless, the application of these methods for periodic-DFT calculations of infinite systems is difficult from the viewpoint of computational time, indicating that we need to improve the approach to photochemistry of infinite systems.

In this regard, the following practical procedure can be conducted: we can obtain the ground-state structure using periodic-DFT calculations, which is not difficult. Using the ground-state geometry, we can acquire the excitation energy through the TD-DFT calculation with the GGA-type functional, where an entire system is employed. Then, corrections using hybrid DFT functional or post-HF methods such as SAC-CI, EOM-CC, and state-averaged CASSCF, are added. These calculations can be performed using an appropriate CM. Then, the excitation energy can be corrected using the ONIOM procedure. These calculations can be conducted by placing the QM part in the MM part of the ground state obtained by periodic-DFT calculation of the infinite system. Although to date, theoretical calculations of this type have not been performed, this is a practical approximation and seems reasonable.

11.6 Conclusions and Perspectives

In this chapter, two methods, namely, the CM/PM-combined method and the QM/periodic-MM method, for theoretical studies of the electronic structures of molecular crystals are outlined and their applications are presented. The CM/PM-combined method was applied to the theoretical study of the adsorption of gas molecules to MOFs. In the study, the adsorption isotherms of gas molecules were appropriately reproduced. The QM/periodic-MM method was employed for the theoretical studies of the crystal structures of transition metal complexes, structural and energy changes induced by chemical reactions in crystals, and the excited-state structures and emission spectra of molecular crystals. Similar embedding methods proposed for the theoretical studies of solids and solid surfaces are discussed.

Nevertheless, these methods have several limitations, some of which can be overcome, as described in Sect. 11.5. The importance of molecular crystals and solids with regular structures is increasing in both basic chemistry and applied fields. Thus, theoretical studies of these materials are required to obtain theoretical knowledge and correct understanding of the various chemical phenomena occurring in solid systems and the properties of solid systems.

Furthermore, amorphous solids will become more important in a near future. Amorphous systems consist of several different microstructures. Theoretical calculations of this type of systems without periodic structures are very difficult. In such a case, considering their Boltzmann distributions is necessary. A hybrid Monte Carlo (MC)/MD reaction method (named Red-Moon method), recently proposed by Nagaoka et al. [107], has been applied to amorphous materials such as solid electrolyte interphase (SEI) film in secondary batteries. Thus, progress in the theoretical studies of large amorphous systems consisting of microstructures has also started.

Currently, knowledge of the structures, functions, and electronic properties of molecules in solids, whether crystalline or amorphous, is crucially important and will increase more in a near future. The electronic structure theory in solid-state chemistry needs to be further developed, which is challenging from the viewpoints of both method development and application.

References

1. Bartlett RJ, Musial M (2007) Rev Mod Phys 79:291
2. Tomasi J, Mennucci B, Cammi R (2005) Chem Rev 105:2999
3. Hirata F (2003) Molecular theory of solvation. Kluwer, Dordrecht
4. Ten-no S, Hirata F, Kato S (1993) Chem Phys Lett 214:391
5. Ten-no S, Hirata F, Kato S (1994) J Chem Phys 100:7443
6. Sato H, Hirata F, Kato S (1996) J Chem Phys 105:1546
7. Warshel A, Levitt M (1976) J Mol Biol 103:227
8. Field MJ, Bash PA, Karplus M (1990) J Comput Chem 11:700
9. Kresse G, Furthmüller J (1996) J Comput Mater Sci 6:15
10. Kresse G, Furthmüller J (1996) Phys Rev B 54:11169
11. Giannozzi P, Baroni S, Bonini N, Calandra M, Car R, Cavazzoni C, Ceresoli D, Chiarotti GL, Cococcioni M, Dabo I, Dal Corso A, Fabris S, Fratesi G, de Gironcoli S, Gebauer R, Gerstmann U, Gougoussis C, Kokalj A, Lazzeri M, Martin-Samos L, Marzari N, Mauri F, Mazzarello R, Paolini S, Pasquarello A, Paulatto L, Sbraccia C, Scandolo S, Sclauzero G, Seitsonen AP, Smogunov A, Umari P, Wentzcovitch RM (2009) J Phys: Condens Matter 21:395502
12. Giannozzi P, Andreussi O, Brumme T, Bunau O, Nardelli MB, Calandra M, Car R, Cavazzoni C, Ceresoli D, Cococcioni M, Colonna N, Carnimeo I, Dal Corso A, de Gironcoli S, Delugas P, DiStasio RA Jr, Ferretti A, Floris A, Fratesi G, Fugallo G, Gebauer R, Gerstmann U, Giustino F, Gorni T, Jia J, Kawamura M, Ko H-Y, Kokalj A, Küçükbenli E, Lazzeri M, Marsili M, Marzari M, Mauri F, Nguyen NL, Nguyen HV, Otero-de-la-Roza O, Paulatto L, Poncé S, Rocca D, Sabatini R, Santra B, Schlipf M, Seitsonen AP, Smogunov A, Timrov I, Thonhauser T, Umari P, Vast N, Wu X, Baroni S (2017) J Phys: Condens Matter 29:465901
13. Mardirossian N, Head-Gordon M (2017) Mol Phys 115:2315
14. Verma P, Truhlar DG (2020) Trends Chem 2 SI:302
15. Kato M, Ito H, Hasegawa M, Ishii K (2019) Chem Eur J 25:5105
16. Perdew JP, Burke K, Ernzerhof M (1996) Phys Rev Lett 77:3865; Erratum Phys Rev Lett 78:1396 (1997)
17. Grimme S (2006) J Comput Chem 27:1787
18. Grimme S, Antony J, Ehrlich S, Krieg H (2020) J Chem Phys 132:154104
19. Kitagawa S, Kitaura R, Noro S (2004) Angew Chem Int Ed 43:2334
20. Kitagawa S (2015) Angew Chem Int Ed 54:10686
21. Kitagawa S (2017) Acc Chem Res 50:514
22. Krause S, Hosono N, Kitagawa S (2020) Angew Chem Int Ed 59:15325
23. Sillar K, Sauer J (2012) J Am Chem Soc 134:18354
24. Kundu A, Piccini G, Sillar K, Sauer J (2016) J Am Chem Soc 138:14047
25. Zheng J-J, Kusaka S, Matsuda R, Kitagawa S, Sakaki S (2018) J Am Chem Soc 140:13958
26. Chung LW, Sameera WMC, Ramozzi R, Page AJ, Hatanaka M, Petrova GP, Harris TV, Li S, Ke Z, Liu F, Li H-B, Ding L, Morokuma K (2015) Chem Rev 5:5678
27. Deshmukh MM, Sakaki SS (2012) J Comput Chem 33:617–628
28. Alonso-Cotchico L, Rodriguez-Guerra J, Lledos A, Marechal JD (2020) Acc Chem Res 53:896
29. Mennucci B, Corni S (2019) Nat Rev Chem 3:315
30. Stueber D (2006) Concepts Magn Reson A 28A:347
31. Weber J, Schmedt auf der Günne J (2010) Phys Chem Chem Phys12:583
32. Götz K, Meier F, Gatti C, Burow AB, Sierka M, Sauer J, Kaup M (2010) J Comput Chem 31:2568
33. Bjornsson R, Bühl M (2012) J Chem Theory Comput 8:498–508
34. Iwano K, Shimoi Y (2008) Phys Rev B: Condens Matter Mater B 77:075120
35. Iwano K, Shimoi Y (2013) Rev Lett 110:116401
36. Aono S, Sakaki S (2012) Chem Phys Lett 544:77

37. Mühle C, Nuss J, Jansen MZ (2009) Kristallogr NCS 224:9–10
38. Rizzato S, Berges J, Mason SA, Albinati A, Kozelka J (2010) Angew Chem Int Ed 49:7440
39. Brammer L, Charnock JM, Goggin PL, Goodfellow R, Orpen AG, Koetzle TF (1991) J Chem Soc Dalton Trans 1789
40. Albinati A, Lianza F, Pregosin PS, Müller B (1994) Inorg Chem 33:2522
41. Aono S, Mori T, Sakaki S (2016) J Chem Theory Comput 12:1189
42. Brammer L (2003) Dalton Trans 3145
43. Cornell WD, Cieplak P, Bayly CI, Gould IR, Merz KM Jr, Ferguson DM, Spellmeyer DC, Fox T, Caldwell JW, Kollman PAA (1995) J Am Chem Soc 117:5179
44. Nygren MA, Pettersson LGM (1996) J Phys Chem 100:1874
45. Vollmer JM, Stefanovich EV, Truong TN (1999) J Phys Chem B 03:9415
46. Herschend B, Baudin M, Hermansson K (2004) J Chem Phys 120:4939
47. Teunissen EH, Jansen AP, van Santen RA, Orlando R, Dovesi R (1994) J Chem Phys 101:5865
48. Kudin KN, Scuseria GE (1998) Chem Phys Lett 283:61
49. Kudin KN, Scuseria GE (2004) J Chem Phys 121:2886
50. Burow AM, Sierka M, Döbler J, Sauer J (2009) J Chem Phys 130:174710
51. Kanan DK, Sharifzadeh S, Carter EA (2002) Chem Phys Lett 519–520:18
52. Wellington JPW, Kerridge A, Jonathan A, Nikolas N (2006) J Nucl Mat 482:124
53. Matsui M, Sakaki S (2007) J Phys Chem C 121:20242–20253
54. Cortona P (1991) Phys Rev B 44:8454
55. Cortona P (1992) Phys Rev B 46:2008
56. Wesolowski TA, Warshel A (1993) J Phys Chem 97:8050
57. Huang C, Pavone M, Carter EA (2011) J Chem Phys 134:154110
58. Libisch F, Huang C, Liao P, Pavone M, Carter EA (2012) Phys Rev Lett 109:198303
59. Libisch F, Cheng J, Carter EA, Phys Z (2013) CHEM 227:1455
60. Mukherjee S, Libisch F, Large N, Neumann O, Brown LV, Cheng J, Lassiter JB, Carter EA, Nordlander P, Halas NJ (2013) Nano Lett 13:240
61. Cheng J, Libisch F, Carter EA (2015) J Phys Chem Lett 6:1661
62. Martirez JMP, Carter EA (2017) J Am Chem Soc 139:4390
63. Knizia G, Chan GKL (2012) Phys Rev Lett 109:186404
64. Knizia G, Chan GKL (2013) J Chem Theory Comput 9:1428
65. Bulik IW, Scuseria GE, Dukelsky J (2014) Phys Rev B 89:035140
66. Zheng BX, Chan GKL (2016) Phys Rev B 93:035126
67. Booth GH, Chan GKL (2015) Phys Rev B 91:15510
68. Cui ZH, Zhu T, Chan GKL (2020) J Chem Theory Comput 16:119
69. Li B, Wen HM, Zhou W, Xu JQ, Chen BL (2016) CHEM 1:557–580
70. Dietzel PDC, Besikiotis V, Blom R (2009) J Mater Chem 19:7362
71. Kitagawa S, Kondo M (1998) Bull Chem Soc Jpn 71:1739–1753
72. Kitaura R, Fujimoto K, Noro S, Kondo M, Kitagawa S (2002) Angew Chem Int Ed 41:133
73. Coudert FX, Boutin A, Jeffroy M, Mellot-Draznieks C, Fuchs AH (2011) Chem Phys Chem 12:247
74. Yang Q, Liu D, Zhong C, Li J-R (2013) Chem Rev 113:8261
75. Odoh SO, Cramer CJ, Truhlar DG, Gagliardi L (2015) Chem Rev 115:6051
76. Fraux G, Coudert FX (2017) Chem Commun 53:7211
77. Ma Y, Matsuda R, Sato H, Hijikata Y, Li L, Kusaka S, Foo M, Xue F, Akiyama G, Yuan R, Kitagawa S (2015) J Am Chem Soc 137:15825
78. Coppens P, Novozhilova I, Kovalevsky A (2002) Chem Rev 102:861
79. Schaniel D, Imlau M, Weisemoeller T, Woike T, Krämer KW, Güdel HU (2007) Adv Mater 19:723
80. Bitterwolf TE (2006) Coord Chem Rev 250:1196
81. Coppens P, Fomitchev DV, Carducci MD, Culp K (1998) J Chem Soc Dalton Trans 865
82. Imlau M, Haussühl S, Woike T, Schieder P, Angelov V, Rupp RA, Schwarz K (1999) Appl Phys B: Lasers Opt 68:877
83. Cole M (2008) Acta Crystallogr Sect A Found Crystallogr 64:259

84. Kovalevsky AY, Bagley KA, Coppens PJ (2002) J Am Chem Soc 124:9241
85. Kovalevsky AY, Bagley KA, Cole JM, Coppens P (2003) Inorg Chem 42:140
86. Bowes KF, Cole JM, Husheer SLG, Raithby PR, Savarese TL, Sparkes HA, Teat SJ, Warren JE (2006) Chem Commun 23:2448
87. Phillips AE, Cole JM, d'Almeida T, Low KS (2010) Phys Rev B: Condens Matter Mater Phys 82:155118
88. Phillips AE, Cole JM, d'Almeida T, Low KS (2012) Inorg Chem 51:1204
89. Sylvester SO, Cole JM, Waddell PJ (2012) J Am Chem Soc 134:11860
90. Sylvester SO, Cole JM, Waddell PJ, Nowell H, Wilson C (2014) J Phys Chem C 118:16003
91. Aono S, Sakaki S (2018) J Phys Chem C 122:20701
92. Kovalenko A, Hirata F (2000) J Chem Phys 112:10391
93. Kovalenko A, Hirata F (2000) J Chem Phys 112:10403
94. Aono S, Sakaki S (2012) J Phys Chem B 116:13045
95. Aono S, Seki T, Ito H, Sakaki S (2019) J Phys Chem C 123:4773
96. Nakagaki M, Aono S, Kato M, Sakaki S (2020) J Phys Chem C 124:10453
97. Zheng J-J, Sakaki S (2022) J Photochem Photobio C 51:100482
98. Ito H, Muromoto M, Kurenuma S, Ishizaka S, Kitamura N, Sato H, Seki T (2013) Nat Commun 4:2009
99. Wong KM-C, Yam VW-W (2011) Acc Chem Res 44:424
100. Sathish V, Ramdass A, Thanasekaran P, Lu K-L, Rajagopal S (2015) J Photochem Photobiol C 23:25
101. Yoshida M, Kato M (2018) Coord Chem Rev 355:101
102. Kato M, Kosuge C, Morii K, Ahn JS, Kitagawa H, Mitani T, Matsushita M, Kato T, Yano S, Kimura M (1999) Inorg Chem 38:1638
103. Saito K, Eishiro Y, Nakao Y, Sato H, Sakaki S (2012) Inorg Chem 51:2785
104. Fedorov DG, Asada N, Nakanishi I, Kitaura K (2014) Acc Chem Res 47 SI:2846
105. Chan G-L, Head-Gordon M (2002) J Chem Phys 116:4462
106. Allison MR, Martin CR, Galitskiy VA, Berseneva AA, Leith GA, Shustova NB (2020) Chem Rev 120:8790
107. Suzuki Y, Nagaoka M (2017) J Chem Phys 146:204102

Open Access This chapter is licensed under the terms of the Creative Commons Attribution 4.0 International License (http://creativecommons.org/licenses/by/4.0/), which permits use, sharing, adaptation, distribution and reproduction in any medium or format, as long as you give appropriate credit to the original author(s) and the source, provide a link to the Creative Commons license and indicate if changes were made.

The images or other third party material in this chapter are included in the chapter's Creative Commons license, unless indicated otherwise in a credit line to the material. If material is not included in the chapter's Creative Commons license and your intended use is not permitted by statutory regulation or exceeds the permitted use, you will need to obtain permission directly from the copyright holder.

Part III
Scope

Chapter 12
Toward the Applications of Soft Crystals

Kazuyuki Ishii and Masako Kato

Abstract In this chapter, to design functions of soft crystals, the relationships between gentle stimuli and the corresponding responses are classified based on the photofunctions, and the key terms are linked and then systematized. Also, trials of functionalization based on soft crystal-related phenomena are introduced toward the functionalization of soft crystals.

Keywords Classification and systematization · Photofunction · Functionalization of soft crystals

12.1 Functions and Prospects of Soft Crystals

Soft crystals are advantageous since their nm-order molecular structural changes can be precisely monitored by X-ray crystal structural analyses, and their sub-μm-order crystalline changes reflecting various intermolecular interactions can be observed by optical microscopy analyses. Also, soft crystals show the following properties: (1) their molecules can move with a certain degree of flexibility, (2) small molecules can be adsorbed and desorbed, and (3) chemical reactions can occur. All of these properties can help in the understanding of various chemical reactions by the combination with theoretical and computational sciences.

Furthermore, soft crystals are expected to be molecular functional materials. At this stage, the die shrink based on top-down technology, in accordance with Moore's law, is approaching its limit [1]. On the other hand, chemicals dramatically increase in recent decades [2]. Thus, the utilization of molecular materials has been gaining attention. Although molecular crystals are essential materials for the development

K. Ishii (✉)
Institute of Industrial Science, The University of Tokyo, 4-6-1 Komaba Meguro-Ku, Tokyo 153-8505, Japan
e-mail: k-ishii@iis.u-tokyo.ac.jp

M. Kato
Department of Applied Chemistry for Environment, Kwansei Gakuin University, 1 Gakuen Uegahara, Sanda 669-1330, Japan
e-mail: katom@kwansei.ac.jp

© The Author(s) 2023

M. Kato and K. Ishii (eds.), *Soft Crystals*, The Materials Research Society Series,
https://doi.org/10.1007/978-981-99-0260-6_12

of molecular devices, they are not yet regarded as the best candidate materials by engineers. The excellent mechanical properties and softness of soft crystals can be beneficial in applications requiring flexibility and mechanical compliance. While the mass production of soft crystals is still difficult, "Soft Crystals" could add values advantageous to metals or ceramics and polymers due to the lightweight and the long-range structural ordering or anisotropy, respectively.

The control of soft crystals is expected to help in the development of unexplored functional materials with phase transition phenomena linked to various properties such as optical properties, dielectric properties, electrical conductivity, and magnetism. With reference to the historical development of liquid crystals and organic electroluminescence, innovations based on the development of new materials using soft crystals will significantly impact the society.

Consequently, the classification of soft crystals in terms of the gentle stimuli and the corresponding response is important. Gentle stimuli-responsive structural transformations with highly ordered structures, which are the characteristics of soft crystals, are advantageous for controlling electronic structures; thus, the relationships between gentle stimuli and the corresponding responses are classified based on the photofunctions (Table 12.1). The color change (including luminescence color change) and shape change are observed as responses to gentle stimuli such as grinding, hitting, heat, light, and small molecule. Thus, initial typical responses of soft crystals, such as vapochromism, mechanochromism, and superelasticity, can be classified into these categories. Furthermore, recent studies have shown that soft crystals can show almost all types of responses against stimuli. Although these phenomena can be observed in other materials, soft crystals have characteristics such as the movability of molecules and the adsorption/desorption of small molecules due to their flexible molecular structure and substituents, large voids, small intermolecular interactions, and/or small activation energy for transitions. This type of classification is possible not only for photofunctions but also for other functions, which will be beneficial for the design and development of new functions.

In order to tailor the functions, it is important to systematize the key terms of soft crystals. As described in Sect. 2.1, various key terms have been associated to soft crystals: formation of many crystal polymorphs, phase transition and/or structural transformation by gentle stimuli, intermolecular electronic interactions such as d-π, d-d, or π-π, existence of large voids in crystals, adsorption/desorption of molecules, and chemical conversions or chemical reaction-based chemiluminescence. Furthermore, the highly ordered structures in soft crystals are considered to be advantageous for controlling electrons and excitons. These key terms can be classified as "Essences", "Phenomena", and "Functions" and can be thus systematized by linking them (Fig. 12.1). Some functions can be also designed on demand by tracing connection lines.

Table 12.1 Relationships between gentle stimuli and the corresponding responses

		Gentle stimulus			
		Grinding, Hitting	Heat	Light	Small molecule
Response	Color change	Mechanochromism	Thermochromism	Photochromism	Vapochromism
	Luminescence	Triboluminescence	Chemiluminescence	Photoluminescence	–
	Shape change	Superelasticity, Ferroelasticity	Thermosalient, Shape memory	Photosalient	–

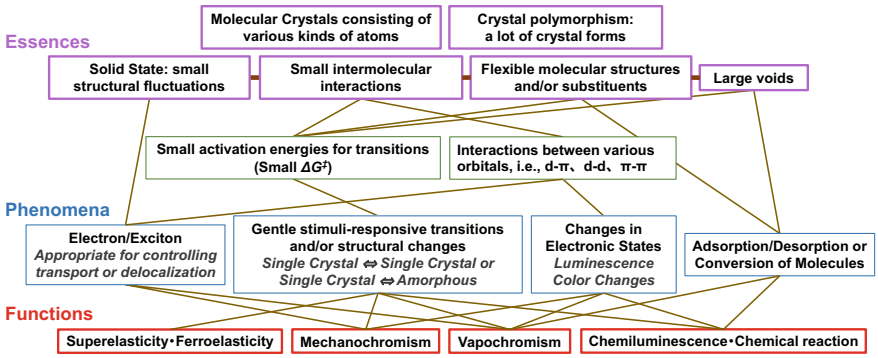

Fig. 12.1 Systematization of the key terms of "soft crystals"

12.2 Toward the Functionalization of Soft Crystals

Several trials of functionalization based on soft crystal-related phenomena, such as phase transition, crystallization, and organic vapor response, have been conducted with reference to the boundary region between crystals, liquid crystals, and polymers. Since these are important steps toward the functionalization of soft crystals, three examples are introduced.

12.2.1 Organic Thin-Film Transistor Memory with a Highly Oriented Molecular Layer as a Dielectric Gate

Kobayashi et al. investigated organic thin-film transistor (OTFT) memory using highly oriented molecular arrangements [3]. The device consisted of poly(γ-methyl-L-glutamic acid) (PMLG) and pentacene as a dielectric gate layer and an active layer, respectively, as well as gold source-drain electrodes (Fig. 12.2 inset). The PMLG layer showed ferroelectric properties based on the highly oriented molecular arrangements, and consequently the device showed a clear electric hysteresis (Fig. 12.2, black line). This study indicates that highly oriented molecular arrangements with ferroelectric properties can be applied to the memory function of OTFTs.

12.2.2 Heat Shielding Materials Based on Phase Transition

Soft crystals are promising smart materials that respond to gentle stimuli in the surrounding environmental changes. Ishii et al. proposed novel heat-shielding materials based on the thermochromic phase transition of a composite of silicon phthalocyanine dye ($SiPc(OH)_2$) and liquid crystalline 4′-*n*-octyloxy-4-biphenylcarbonitrile

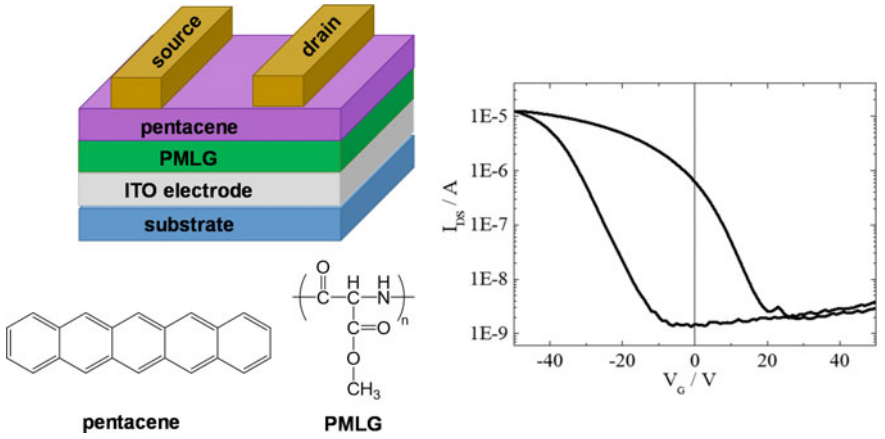

Fig. 12.2 OTFT device using a PMLG film and its transfer characteristics. Reprinted with permission from Ref. [3] Copyright 2020 MDPI, All Rights Reserved

(8OCB) molecules [1]. When $SiPc(OH)_2$ was dissolved in an excess of liquid crystal molecules, it existed as a monomer and showed a sharp Q absorption band (FWHM ~20 nm) at around 700 nm, in the temperature region where the liquid crystal molecules are in the liquid or liquid crystal (LC) phase (Fig. 12.3). On the other hand, in the temperature region of the crystalline (Cr) phase, 8OCB crystallized, and $SiPc(OH)_2$ aggregated, thus resulting in a very broad Q absorption band (FWHM > 200 nm). The temperature of this dramatic thermochromism could be controlled by changing the phase-transition temperature of the liquid crystalline molecules. This thermochromic material has been investigated as a potential heat shield material by encapsulating the composites; at low temperatures, $SiPc(OH)_2$ aggregates broadly absorbed sunlight and the material's temperature increased, whereas at high temperatures, the monomeric $SiPc(OH)_2$ absorbed only red light and prevented the temperature rise by the backside reflector. The combined use of the phase transition and aggregation/dissociation behavior is promising in terms of stability and the easy control of temperature or color, in comparison with thermochromic leuco dyes whose color is changed by the formation/cleavage of chemical bonds.

12.2.3 Agents for the Collection of Volatile Organic Compounds (VOCs)

As the development of soft crystals researches, when investigating vapochromism, the solid → liquid changes that occurred in response to organic solvent vapors were observed in the crystals of the molecular salts. Systematic experiments revealed that this phenomenon was in fact deliquescence caused by the VOCs and was consequently named organic deliquescence [4]. Deliquescence is a well-known

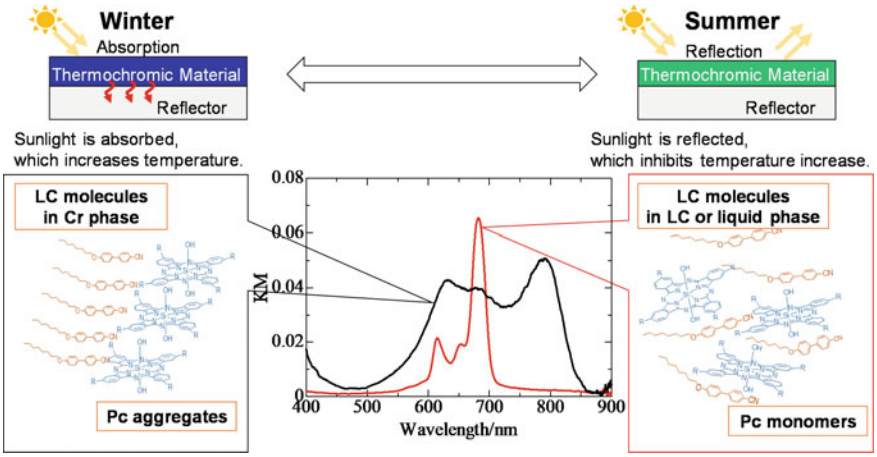

Fig. 12.3 Temperature-dependent heat shielding effects using the thermochromic behaviors of the composite of $SiPc(OH)_2$ dye and liquid crystalline 8OCB molecules

phenomenon in which substances such as citric acid, sodium hydroxide, potassium carbonate, magnesium chloride, and calcium chloride absorb water vapor from the air and spontaneously form an aqueous solution. On the other hand, organic deliquescence had not been reported.

In the case of chloroform ($CHCl_3$) widely used as a solvent in the chemical industry, organic deliquescence was observed in tetrabutylammonium hexafluorophosphate ((n-Bu_4N)PF_6), which is highly soluble in $CHCl_3$. For dimethylformamide (DMF), which is a highly polar solvent that can dissolve various salts, organic deliquescence was observed in (n-Bu_4N)PF_6, NH_4PF_6, and NH_4BF_4 soluble in DMF. When using toluene, which has a low polarity, organic deliquescence was observed in tetrabutylammonium benzoate according to the well-known principle of "like dissolves like", in contrast to the non-organic deliquescence in (n-Bu_4N)PF_6, NH_4PF_6, NH_4BF_4, and NaCl, which are insoluble in toluene. These results indicated that it is possible to design the organic deliquescence phenomenon for target specific VOCs based on the principle of "like dissolves like".

One of important features of organic deliquescence compared to conventional adsorption phenomena is that the amount of collected solvent can be much higher than that of the salt. Since calcium chloride is practically used as a desiccant, the organic deliquescence behavior can enhance the development of agents for the collection of VOCs (Fig. 12.4).

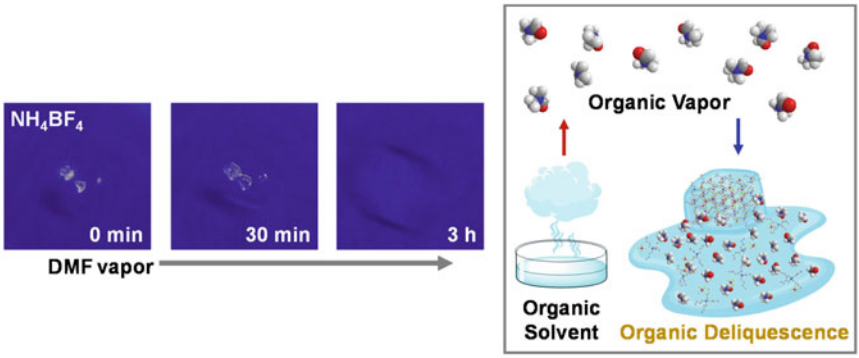

Fig. 12.4 Organic deliquescent behavior of NH_4BF_4 exposed to DMF (left) and the mechanism (right). Reprinted with permission from Ref. [4], Copyright 2022 Royal Society of Chemistry, All Rights Reserved

References

1. Moore G (1965) Electron Mag 38(8)
2. Ishii K (2019) Chem Lett 48:1452
3. Liang L, He W, Cao R, Wei X, Uemura S, Kamata T, Nakamura K, Ding C, Liu X, Kobayashi N (2020) Molecules 25:499
4. Ishii K, Yokomori K, Murata K, Nakamura S, Enomoto K (2022) RSC Adv 29:18307

Open Access This chapter is licensed under the terms of the Creative Commons Attribution 4.0 International License (http://creativecommons.org/licenses/by/4.0/), which permits use, sharing, adaptation, distribution and reproduction in any medium or format, as long as you give appropriate credit to the original author(s) and the source, provide a link to the Creative Commons license and indicate if changes were made.

The images or other third party material in this chapter are included in the chapter's Creative Commons license, unless indicated otherwise in a credit line to the material. If material is not included in the chapter's Creative Commons license and your intended use is not permitted by statutory regulation or exceeds the permitted use, you will need to obtain permission directly from the copyright holder.